

Recent Advances on Analysis Methods and Modelling Approaches for Seismic Assessment and Design of Infilled RC Buildings

Lead Guest Editor: André Furtado

Guest Editors: Hemchandra Chaulagain, Ibrahim S. Misir, Maria T. de Risi, and Tanja K. Šipoš





**Recent Advances on Analysis Methods and
Modelling Approaches for Seismic Assessment
and Design of Infilled RC Buildings**

Advances in Civil Engineering

**Recent Advances on Analysis Methods
and Modelling Approaches for Seismic
Assessment and Design of Infilled RC
Buildings**

Lead Guest Editor: André Furtado

Guest Editors: Hemchandra Chaulagain, Ibrahim S.
Misir, Maria T. de Risi, and Tanja K. Šipoš



Copyright © 2020 Hindawi Limited. All rights reserved.

This is a special issue published in "Advances in Civil Engineering." All articles are open access articles distributed under the Creative Commons Attribution License, which permits unrestricted use, distribution, and reproduction in any medium, provided the original work is properly cited.

Chief Editor

Cumaraswamy Vipulanandan, USA

Editorial Board

Glenda Abate, Italy
Khalid Abdel-Rahman, Germany
Abdul Aziz bin Abdul Samad, Malaysia
Musa Adamu, Malaysia
Ali Mardani Aghabaglou, Turkey
José Aguiar, Portugal
Reza Akhavian, USA
Luigi Aldieri, Italy
Maria Cruz Alonso, Spain
Serji N. Amirkhanian, USA
Eleftherios K. Anastasiou, Greece
Panagiotis Ch. Anastasopoulos, USA
Venu G. M. Annamdas, Singapore
Farhad Aslani, Australia
Paul Awoyera, Nigeria
Qingsheng Bai, Canada
Daniele Baraldi, Italy
Ozgur BASKAN, Turkey
Emilio Bastidas-Arteaga, France
Chiara Bedon, Italy
Rita Bento, Portugal
Rafael J. Bergillos, Spain
Han-bing Bian, China
Xia Bian, China
Giovanni Biondi, Italy
Hugo C. Biscaia, Portugal
Giosuè Boscato, Italy
Melina Bosco, Italy
Jorge Branco, Portugal
Bruno Briseghella, China
Brian M. Broderick, Ireland
Emanuele Brunesi, Italy
Quoc-Bao Bui, Vietnam
Gladis Camarini, Brazil
Alberto Campisano, Italy
Francesco Canestrari, Italy
Alessio Cascardi, Italy
Paolo Castaldo, Italy
Giulio Castori, Italy
Liborio Cavaleri, Italy
Robert Černý, Czech Republic
Constantin Chalioris, Greece
Wen-Shao Chang, United Kingdom
Carlos Chastre, Portugal

Ghassan Chehab, Lebanon
Wensu Chen, Australia
Hang Chen, China
Po-Han Chen, Taiwan
Li Chen, China
Nicholas Chileshe, Australia
Prinya Chindaprasirt, Thailand
Wanjei Cho, Republic of Korea
Se Jin Choi, Republic of Korea
Heap-Yih (John) Chong, Australia
Gian Paolo Cimellaro, Italy
Francesco Colangelo, Italy
Ottavia Corbi, Italy
Marco Corradi, Italy
Andrzej Cwirzen, Sweden
Mario D'Aniello, Italy
Amos Darko, Hong Kong
Gianmarco de Felice, Italy
Stefano de Miranda, Italy
Maria T. de Risi, Italy
Tayfun Dede, Turkey
Sadik O. Degertekin, Turkey
Camelia Delcea, Romania
Cristoforo Demartino, China
Antonio Di Cesare, Italy
Angelo Di Egidio, Italy
Luigi Di Sarno, Italy
Fabio Di Trapani, Italy
Aboelkasim Diab, Egypt
Giulio Dondi, Italy
Jiangfeng Dong, China
Chao Dou, China
Jingtao Du, China
Mohamed ElGawady, USA
Ahmed Elghazouli, United Kingdom
Francesco Fabbrocino, Italy
Flora Faleschini, Italy
Xueping Fan, China
Cheng Fang, China
Qian Fang, China
Ilenia Farina, Italy
Yingbin Feng, Australia
Guang-Liang Feng, China
Massimiliano Ferraioli, Italy

Marco Filippo Ferrotto, Italy
Antonio Formisano, Italy
Guoyang Fu, Australia
André Furtado, Portugal
Meng Gao, China
Giovanni Garcea, Italy
Emilio García-Taengua, United Kingdom
DongDong Ge, USA
Elhem Ghorbel, France
Agathoklis Giaralis, United Kingdom
Rodrigo Gonçalves, Portugal
Belén González-Fonteboa, Spain
Salvatore Grasso, Italy
Fan Gu, USA
Esra Mete Güneyisi, Turkey
Pingye Guo, China
Ankit Gupta, India
Husnain Haider, Saudi Arabia
Yifei Hao, China
Hadi Hasanzadehshooili, Iran
Mostafa Fahmi Hassanein, Egypt
Kirk Hatfield, USA
Amir Ahmad Hedayat, Iran
Khandaker Hossain, Canada
Zahid Hossain, USA
Mohammad R. Hosseini, Australia
Jiang Hu, China
Xiaodong Hu, China
Lei Huang, China
Bon-Gang Hwang, Singapore
Süleyman İpek, Turkey
Pitthaya Jamsawang, Thailand
Dong-Sheng Jeng, Australia
Jian Ji, China
Lishuai Jiang, China
Jiang Jin, China
Peerapong Jitsangiam, Thailand
Mosbeh Kaloop, Egypt
Murat Kankal, Turkey
John Kechagias, Greece
Manoj Khandelwal, Australia
Vaclav Koci, Czech Republic
Kyriakos I. Kourousis, Ireland
Moacir Kripka, Brazil
Emma La Malfa Ribolla, Czech Republic
Andreas Lampropoulos, United Kingdom
Raffaele Landolfo, Italy

Massimo Latour, Italy
Eul-Bum Lee, Republic of Korea
Bang Yeon Lee, Republic of Korea
Bobo Li, China
Li Li, Canada
Dongsheng Li, China
Chun-Qing Li, Australia
Yingchun Li, China
Minghui Li, China
Jiale Li, China
Xiaoli Liu, China
Pengfei Liu, Germany
Xuemei Liu, Australia
Zaobao Liu, China
Zhuang-Zhuang Liu, China
Davide Lo Presti, United Kingdom
Diego Lopez-Garcia, Chile
Cristiano Loss, Canada
Lyan-Ywan Lu, Taiwan
Yanbin Luo, China
Dan Ma, China
Zhongguo John Ma, USA
Yann Malecot, France
Prabhat Kumar Mandal, India
John Mander, USA
Iman Mansouri, Iran
Giuseppe Carlo Marano, Italy
Enzo Martinelli, Italy
Maria Rossella Massimino, Italy
Vasant Matsagar, India
Fabio Mazza, Italy
Claudio Mazzotti, Italy
Ahmed Mebarki, France
Shazim A. Memon, Kazakhstan
Giovanni Minafò, Italy
Hossein Moayedi, Vietnam
Abbas Mohajerani, Australia
Fabrizio Mollaioli, Italy
Rosario Montuori, Italy
Ayman S. Mosallam, USA
H. Naderpour, Iran
Roberto Nascimbene, Italy
Hassan Nasir, Pakistan
Behzad Nematollahi, Australia
Luís C. Neves, United Kingdom
Trung Ngo, Australia
Mehdi Nikoo, Iran

Sanjay Nimbalkar, Australia
Timothy O. Olawumi, Hong Kong
Giuseppe Oliveto, Italy
Alejandro Orfila, Spain
Maurizio Orlando, Italy
Walid Oueslati, Tunisia
Hayri Baytan Ozmen, Turkey
Alessandro Palmeri, United Kingdom
Fabrizio Paolacci, Italy
Fulvio Parisi, Italy
SUVASH PAUL, Bangladesh
Arnaud Perrot, France
Giuseppe Piccardo, Italy
Waldemar Pichór, Poland
Keerthan Poologanathan, United Kingdom
Doddy Prayogo, Indonesia
Chongchong Qi, China
Giuseppe Quaranta, Italy
Carlo Rainieri, Italy
Damien Rangeard, France
Rizal Rashid, Malaysia
Qing-Xin Ren, China
Giuseppe Ricciardi, Italy
Dimitris Rizos, USA
Geoffrey W. Rodgers, New Zealand
Hugo Rodrigues, Portugal
Pier Paolo Rossi, Italy
Anna Saetta, Italy
Timo Saksala, Finland
Filipe Santos, Portugal
Evangelos J. Sapountzakis, Greece
Vassilis Sarhosis, United Kingdom
Navaratnarajah Sathiparan, Sri Lanka
Halil Sezen, USA
Payam Shafiqh, Malaysia
M. Shahria Alam, Canada
Faiz U.A. Shaikh, Australia
JUNLONG SHANG, Singapore
Mostafa Sharifzadeh, Australia
Zhifu Shen, China
Wei Shen, China
Sara Shirowzhan, Australia
Sanjay Kumar Shukla, Australia
Amir Si Larbi, France
Rui Song, China
Stefano Sorace, Italy
Flavio Stochino, Italy






Piti Sukontasukkul, Thailand
Andrea Sulis, Italy
Shengwen Tang, China
Yinshan Tang, United Kingdom
Patrick W.C. Tang, Australia
Weerachart Tangchirapat, Thailand
Piergiorgio Tataranni, Italy
Jing-Zhong Tong, China
Antonello Troncone, Italy
Filippo Ubertini, Italy
Humberto Varum, Portugal
Castorina S. Vieira, Portugal
Valeria Vignali, Italy
Claudia Vitone, Italy
Wayne Yu Wang, United Kingdom
Hao Wang, USA
Lei Wang, USA
Chao Wang, China
Zhenjun Wang, China
Xiuling Wang, China
Chaohui Wang, China
Roman Wan-Wendner, Austria
Xin-Jiang Wei, China
Weiping Wen, China
Yu Wu, China
Bangbiao Wu, China
Wenbing Wu, China
Chao Wu, China
Bo Xia, Australia
Nuwen Xu, China
Rongchao Xu, China
Jian Xu, China
Michael Yam, Hong Kong
Libo Yan, Germany
Jian Yang, China
Xu Yang, Australia
Shangtong Yang, United Kingdom
Xu-Xu Yang, China
Hui Yao, China
Zaher Mundher Yaseen, Vietnam
Xinyu Ye, China
Victor Yepes, Spain
Gürol Yildirim, Turkey
Doo-Yeol Yoo, Republic of Korea
Zhanping You, USA
Xinbao Yu, USA
Bingxiang Yuan, China



Hyun-Do Yun, Republic of Korea
Geun Y. Yun, Republic of Korea
Mariano Angelo Zanini, Italy
Yuqing Zhang, United Kingdom
Jiu Peng Zhang, USA
Yu Zhang, China
Zetian Zhang, China, China
Zhiguo Zhang, China
Zhigang Zhang, China
Yi Zhang, China
Yi Zhang, China
Chun-Shun Zhang, Australia
Junhui Zhang, China
Dong Zhao, USA
Xianbo Zhao, Australia
Annan Zhou, Australia
Jia-wen Zhou, China
Gang Zhou, China
Jian ZHOU, China
Hai-Tao Zhu, China
Wenjun Zhu, China
Jianbo Zhu, China
QuanJie Zhu, China

Contents

Recent Advances on Analysis Methods and Modelling Approaches for Seismic Assessment and Design of Infilled RC Buildings

André Furtado , Maria Teresa De Risi , Hemchandra Chaulagain , Ibrahim Misir , and Tanja Šipoš 

Editorial (1 page), Article ID 4101826, Volume 2020 (2020)

Numerical Modelling and Simulation of the In-Plane Response of a Three-Storey Masonry-Infilled RC Frame Retrofitted with TRM

Christiana A. Filippou , Nicholas C. Kyriakides, and Christis Z. Chrysostomou 

Research Article (19 pages), Article ID 6279049, Volume 2020 (2020)

Recent Findings and Open Issues concerning the Seismic Behaviour of Masonry Infill Walls in RC Buildings

André Furtado  and Maria Teresa de Risi


Review Article (20 pages), Article ID 9261716, Volume 2020 (2020)

Numerical Investigation on the Influence of In-Plane Damage on the Out-of-Plane Behavior of Masonry Infill Walls

Xiaomin Wang , Weitong Zhao , Jingchang Kong , and Tiejun Zhao

Research Article (16 pages), Article ID 6276803, Volume 2020 (2020)

Seismic Performance Evaluation of Modern Bare and Masonry-Infilled RC SMRF Structures

M. E. Ahmad, N. Ahmad , S. Pervez, A. Iqbal, A. Z. Khan, M. E. Rahim, W. Hassan, K. Umer, and K. Khan


Research Article (15 pages), Article ID 6572465, Volume 2019 (2019)

Shaking Table Test Study on Seismic Performance of Hollow Rectangular Piers

Yanli Shen  and Bo Wei


Research Article (14 pages), Article ID 7508759, Volume 2019 (2019)

Shake Table Response of Unreinforced Masonry and Reinforced Concrete Elements of Special Moment Resisting Frame

Syed Azmat Ali Shah, Junaid Shah Khan , Syed Muhammad Ali, Khan Shahzada, Waqar Ahmad, and Junaid Shah

Research Article (17 pages), Article ID 7670813, Volume 2019 (2019)

Building Earthquake Damage Analysis Using Terrestrial Laser Scanning Data

Qisong Jiao , Hongbo Jiang, and Qiang Li

Research Article (12 pages), Article ID 8308104, Volume 2019 (2019)

Editorial

Recent Advances on Analysis Methods and Modelling Approaches for Seismic Assessment and Design of Infilled RC Buildings

André Furtado ¹, Maria Teresa De Risi ², Hemchandra Chaulagain ³,
Ibrahim Misir ⁴ and Tanja Šipoš ⁵

¹CONSTRUCT-LESE, Faculdade de Engenharia da Universidade do Porto, Porto, Portugal

²Department of Structures for Engineering and Architecture, University of Naples Federico II, Naples, Italy

³School of Engineering, Pokhara University, Pokhara, Nepal

⁴Dokuz Eylul University, School of Engineering, Izmir, Turkey

⁵Faculty of Civil Engineering and Architecture, Osijek, Croatia

Correspondence should be addressed to André Furtado; afurtado@fe.up.pt

Received 31 October 2019; Accepted 1 November 2019; Published 6 August 2020

Copyright © 2020 André Furtado et al. This is an open access article distributed under the Creative Commons Attribution License, which permits unrestricted use, distribution, and reproduction in any medium, provided the original work is properly cited.

One major challenge of earthquake risk mitigation is the assessment of existing buildings not designed with modern codes and the development of effective strengthening techniques. The design of new building structures is also of paramount importance since infills are still currently neglected (or a lot of information is missing) by most of the seismic codes. Special attention should be paid to reinforced concrete (RC) frame structures with masonry infill panels, as proved by their poor performance in recent earthquakes. Accurate modelling strategies and appropriate seismic assessment methodologies for new or existing infilled buildings are crucial to understand their behaviour and to develop efficient and appropriate mitigation measures to prevent high level of damage, casualties, and economic losses. The effect of the combined in-plane and out-of-plane behaviour interaction of the infill masonry walls in the RC structure seismic behaviour, the local shear interaction between the RC frame and the masonry infill, the development of analytical formulations that could help design engineers are still open issues, among others, on this topic.

The focus of this Special Issue is on recent advances on analysis methods and modelling approaches for seismic assessment of infilled RC buildings. Some of the most significant recent developments in the topic of computational methods to simulate infilled RC structure seismic behaviour and their applications in structural and seismic engineering problems are herein presented. Furthermore, experimental

works in the field of as-built and/or retrofitted infilled RC frames are also part of the Special Issue.

A total of 14 papers were submitted, from which a total of 6 papers have been finally selected to integrate the present issue, which accentuates the need, the interest, and the importance of this topic. The topics addressed in the papers belong to different subtopics across the seismic behaviour of infilled RC structures, such as the seismic performance of bare frame and infilled RC frame structures, the shaking table test of hollow rectangular RC columns, the building earthquake damage analysis using terrestrial laser scanning data, the shake table response of unreinforced masonry and reinforced concrete elements of special moment resisting frame, and a literature review on the experimental studies carried out on infilled RC frames focusing in particular the seismic behaviour of the masonry infill walls.

Conflicts of Interest

The guest editors have no conflicts of interest regarding the publication of this special issue.

André Furtado
Maria Teresa De Risi
Hemchandra Chaulagain
Ibrahim Misir
Tanja Šipoš

Research Article

Numerical Modelling and Simulation of the In-Plane Response of a Three-Storey Masonry-Infilled RC Frame Retrofitted with TRM

Christiana A. Filippou , Nicholas C. Kyriakides, and Christis Z. Chrysostomou 

Department of Civil Engineering and Geomatics, Cyprus University of Technology, Limassol, Cyprus

Correspondence should be addressed to Christiana A. Filippou; ca.filippou@edu.cut.ac.cy

Received 2 August 2019; Revised 20 December 2019; Accepted 14 February 2020; Published 29 June 2020

Academic Editor: Stefano de Miranda

Copyright © 2020 Christiana A. Filippou et al. This is an open access article distributed under the Creative Commons Attribution License, which permits unrestricted use, distribution, and reproduction in any medium, provided the original work is properly cited.

A numerical study was conducted to investigate the in-plane behavior of a masonry-infilled reinforced concrete (RC) frame retrofitted with textile-reinforced mortar (TRM). A two-dimensional finite element model was developed using DIANA finite element analysis (FEA) software to simulate the 2 : 3 scaled three-storey masonry-infilled RC frame retrofitted with TRM that was studied experimentally in the past. The three-storey structure used in the test was with a nonseismic design and detailing, and was subjected to in-plane displacement-control cyclic loading. The current study evaluates the capabilities of a representative numerical model to simulate the results of the experimental test, and after the calibration of the numerical model sensitivity analysis and parametric study were performed. In order to create an accurate numerical model, suitable constitutive models, based on the smeared crack approach, were used to characterize the nonlinear response of concrete, masonry infill, and TRM. The calibration of the models was based on the experimental results or inverse fitting based on optimizing the simulation of the response. The numerical model proved capable of simulating the in-plane behavior of the retrofitted masonry-infilled RC frame with good accuracy in terms of initial stiffness, and its deterioration, shear capacity, and cracking patterns. The calibrated model was then used to perform sensitivity analysis in order to examine the influence of infill-frame interface properties (tangential and normal stiffness) on the behavior of the retrofitted infilled frame. The numerical results showed that the gap opening is influenced significantly by the stiffness of the interface. In addition, a parametric study was performed in order to evaluate the importance of the full-bond condition between the TRM and the masonry-infilled RC frame. The numerical results indicate that the composite action between the TRM and the masonry-infilled RC frame improves the global stiffness and lateral resistance of the infilled frame, and it reduces the gap opening between the masonry infill and the RC frame.

1. Introduction

Masonry-infilled RC frame structures are widely dispersed around the world, and most of them are located in the seismic region while they were built before the development of new seismic design codes. Therefore, seismic retrofitting of existing masonry structures is nowadays a challenging engineering problem, since the most significant seismic risk in the world today is associated with existing buildings. Several rehabilitation techniques have been developed over the years [1, 2] in order to improve the performance of masonry-infilled RC frame structures. Masonry infills are usually treated as a nonstructural element, and their

interaction with the bounding frame is ignored in the design. This interaction may or may not be beneficial to the performance of the structure [3, 4]. For instance, the existence of masonry infill in an RC frame can increase the strength, stiffness, and lateral capacity of the building [5–7]. On the contrary, the existence of masonry infill can introduce brittle shear failure mechanisms associated with the wall-frame interaction [8]. The irregularities of infill in plan and elevation cause different types of failure mechanisms due to large concentration demand in a few members of the structure. The most typical failure mechanisms are the *soft-storey mechanism* [9] where the stiffness at the lower floor is smaller than the stiffness at the storey above, the *short-*

column mechanism [10] where the infill wall in the RC frame is shorter than the column height, and *plan torsion effect* where the infills are located in the plan asymmetrically [11, 12]. The failure mechanism and the load resistance of the masonry-infilled RC frame depend on a number of parameters such as geometry of the wall (height/width ratio and openings), geometrical plane and elevation distribution of the infills in a structure, quality of the materials, stiffness and ductility of the frame, type of loading, detailing, relative infill-frame stiffness and strength, and quality of the workmanship. In a seismic event, however, they carry in-plane shear loads or out-of-plane flexural loads [13, 14]. Past earthquakes showed that the out-of-plane failures are more disastrous than the in-plane ones [15–17]. Most of the previous studies categorized the failure modes of masonry-infilled frames into five distinct modes such as frame failure, sliding shear, diagonal compression, corner crushing, and diagonal cracking failure [17].

Retrofit or repair structures built before any provision for an earthquake is one of the most serious problems faced by the engineers today. Several rehabilitation techniques have been developed over the years so that the masonry-infilled frame structures can be enhanced to satisfy modern seismic design codes [1, 2]. Amongst them, fiber-reinforced polymers (FRP) [18–22] have received extensive attention in the recent years due to their high mechanical strength and ease of application. The use of ductile fiber-reinforced cementitious matrix composites (FRCM) [23, 24] has recently received attention as a sustainable, and more compatible solution for retrofitting concrete structures compared to the traditional method of concrete jacketing. Owing to the need for introducing innovative materials, more recently, the research community has focused on the use of textile-reinforced mortar (TRM) for retrofitting the masonry and cultural heritage structures. TRM is a composite material consisting of inorganic matrix (lime-based or cement-based) and the fiber reinforcing textile. The variety of fibers and mortar type leads to a wide range of possible mechanical properties for the TRM. The use of the inorganic matrix instead of epoxy resins as in the case of FRPs overcomes some of their drawbacks [25, 26]. The information regarding the effectiveness of TRM in retrofitting masonry infills under static monotonic and cyclic loading is still very limited [27–33]. Papanicolaou et al. [34, 35] concluded that TRM jacketing is an extremely promising solution for retrofitting masonry walls subjected to either out-of-plane or in-plane loading. Particularly, it was stated that TRM confining jackets provide an increase in compressive strength and deformation capacity of the masonry wall. Bernat et al. [36, 37] carried out a study aiming at investigating the influence of three different types of mortar, two different types of fiber (glass and carbon grids), and the possible benefit of using anchors to improve the connection between the walls and the external reinforcement on the performance of masonry walls retrofitted with the TRM. The results showed that the application of TRM provides 100% increase in the initial load-bearing capacity of the wall under an eccentric axial load. Moreover, a stiffer and more homogeneous behavior is noticed when TRM is applied. Later, Koutas et al.

[31, 32] performed an experimental and numerical study to investigate the behavior of TRM-retrofitted masonry-infilled RC frames under cyclic loading. The study showed that in the retrofitted specimen, an approximately 56% increase in the lateral strength, accompanied by a 52% higher deformation capacity at the top of the structure at the ultimate strength state compared to the unretrofitted one. In addition, the retrofitted specimen dissipated 22.5% more energy compared to the unretrofitted one, for the same loading history. Recently, Akhoundi et al. [38] studied the performance of TRM-retrofitted masonry-infilled RC frames using two half-scale specimens subjected to in-plane cyclic loading. A similar application of the TRM retrofitting technique to that of Koutas et al. [31, 32] was used. Based on their results, retrofitting of masonry infills and connecting them to the RC frame by simply extending the retrofitting layers to the faces of the columns and the beam yielded an increase in lateral stiffness and ultimate strength of about 40%. Koutas et al. [26] presented an overview of studies which used the TRM for flexural and shear confinement of RC structures and for seismic retrofitting of masonry structures, while the key parameters of each study were examined. The authors concluded that the TRM technique was highly effective in increasing load-carrying capacity and the stiffness of columns, beams, and the infill walls.

Numerical studies aiming for predicting the behavior of retrofitted masonry infill wall are limited and most of them used the macromodelling approach and focused on the simulation of the behaviour of TRM-retrofitted masonry infill wall under monotonic loading. Koutas et al. [32] proposed a macromodel using a single strut to represent the infill panel to capture the in-plane response of masonry-infilled RC frame retrofitted with TRM. Other studies also proposed macromodelling techniques to study the effectiveness of the TRM retrofitting method on the behavior of the masonry infill wall under monotonic loading [39, 40]. On the contrary, several numerical studies were conducted to investigate the effectiveness of FRP on the in-plane and out-of-plane behavior of the masonry-infilled RC frame [41, 42]. In addition, detailed micromodels have been developed to simulate the behavior of TRM-retrofitted masonry walls, using a microscopic smeared crack approach for modelling the masonry wall, while pushover analyses were performed for these models [39, 43, 44]. Only one study can be found in the literature concerning detailed numerical modelling of retrofitted masonry wall at a structural level, which focuses on the static monotonic nonlinear response of the TRM-masonry infill [45]. It is important to note that a number of numerical studies using a macromodelling approach have been performed in order to investigate the influence of masonry infills (with and without openings) on the structural capacity of the RC frame structure [46–48]. Numerical modelling of masonry-infilled structures retrofitted with TRM is a complex task due to the combination of many materials governed by very different constitutive relationships resulting in a complex response but comprises a vital step towards understanding the parameters that influence the performance of retrofitted structures and evaluating the effectiveness of this technique in greater depth.

Focusing on the numerical modelling of masonry-infilled frame structures retrofitted with TRM, initially, an efficient technique for modelling the behavior of masonry infill is chosen, followed by the determination of adequate constitutive models for each component of the structural system. In the literature, different modelling techniques that simulate the behavior of the infill wall can be found and can be divided into three categories [49, 50] as follows: detailed or simplified micromodelling approach, where the bricks, mortar, and the interface between them are modelled separately by continuum elements or the bricks are modeled by continuum elements and the interaction between brick units and mortar with interface elements with an effective thickness [51–53], macromodelling where the bricks and mortar are modeled by a continuum element or the infill wall is represented by a diagonal equivalent strut (or multiple diagonal) element which is described by a constitutive nonlinear monotonic or cyclic law [54–59], and mesomodelling which combines the advantages of the above-mentioned models such as computational efficiency of the macromodel and numerical accuracy of micromodels [50]. In the mesomodelling approach, the masonry infill walls are modelled using continuous elements and the interaction between brick units and mortar is taken into account, the possible failure in tension and shear [60].

This paper presents a numerical model that represents the in-plane behavior of a three-storey TRM-retrofitted masonry-infilled RC frame under cyclic loading, following the mesomodelling approach to simulate the masonry infill wall. A two-dimensional FE model was developed in the DIANA FEA software, and an eigenvalue analysis, followed by a nonlinear displacement-based cyclic analysis was performed to simulate the experimental test conducted by Koutas et al. [31]. The three-storey structure used in the experimental test was with a nonseismic design and detailing and it was subjected to in-plane cyclic loading. The current study evaluates the capabilities of a representative numerical model to simulate the results of the experimental test and investigates some of the parameters that are able to affect the behavior of masonry-infilled RC frames retrofitted with TRM through sensitivity analysis and parametric study. In order to create an accurate numerical model, suitable constitutive models, based on the smeared crack approach, were used to characterize the nonlinear response of concrete, masonry infill, and TRM. The calibration of the models was based on the experimental results or inverse fitting based on optimizing the simulation of the response. The numerical model proved to be capable of simulating the in-plane behavior of the retrofitted masonry-infilled RC frame with good accuracy in terms of initial stiffness, and its deterioration, shear capacity, and cracking patterns. Sensitivity analysis was performed in order to examine the influence of infill-frame interface properties (tangential and normal stiffness) on the behaviour of the retrofitted infilled frame. The numerical results showed that the gap opening is influenced significantly by the stiffness of the infill-frame interface. In addition, a parametric study was performed in order to evaluate the importance of the full-bond condition between the TRM and the masonry-infilled RC frame. The

numerical results indicate that composite action between the TRM and the masonry-infilled RC frame improves the global stiffness and lateral resistance of the infilled frame, and it reduces the gap opening between the masonry infill and the RC frame.

2. Brief Review of the Experimental Test

Koutas et al. [31] performed an experimental study to investigate the effectiveness of the TRM technique for retrofitting a 2:3 scaled three-storey masonry-infilled RC frame with nonseismic design and detailing under in-plane cyclic loading. Two masonry-infilled frames were designed and built with and without TRM. In this section, a short description of the experimental case study is presented for the benefit of the reader. Full details about the case study can be found in Koutas et al. [31].

Figure 1(a) shows the geometry of the masonry-infilled RC frame specimen. The C16/20 class of concrete (according to Eurocode (2)) was used for columns (rectangular cross section) and for beams (T-section). The modulus of elasticity and the compressive strength of concrete were 24.1 GPa and 27.8 MPa, respectively. The longitudinal ribbed reinforcement had 12 mm diameter and mean yield stress equal to 550 MPa, while smooth steel stirrups with a mean value of yield stress equal to 270 MPa were used as transverse reinforcement for all concrete members. Perforated, fired clay bricks were used for the construction of masonry infill, while the perforation of the brick was running parallel to the unit's length in the x -direction. The modulus of elasticity of the masonry infill wall perpendicular to the bed joints and the compressive strength were equal to 3.37 GPa and 5.1 MPa, respectively. The mean value of the shear modulus was 1.38 GPa, while the value of diagonal cracking strength of masonry infill ranges from 0.30 to 0.8 MPa. As shown in Figure 1(a), the masonry infill wall was supported rigidly by the foundation RC beam plate at the bottom of the frame. In addition, Figure 1(b) presents the TRM strengthening scheme for the retrofitted specimen. Glass TRM externally bonded on the face of the masonry wall was used (due to its limited width, the textile was applied with an overlap of about 300 mm along the entire length of each bay, near the bottom part of each storey), and six and eight anchors (the straight part of it was inserted into predrilled holes filled with injected epoxy resin and the fanned parts are bonded by hand pressure on the top of the first TRM layer) were placed along the beam-infill interface of the first and the second floors, respectively, as shown in Figure 1(b). At the ends of RC columns, carbon TRM was used. Commercial fiber-reinforced cement-based mortar was used for TRM with compressive and flexural strength equal to 18.9 and 4.3 MPa, respectively. In addition, the modulus of elasticity of carbon and glass textile was 225 GPa and 73 GPa, respectively, while their tensile strength per running meter was equal to 157 kN/m and 115 kN/m, respectively.

In order to provide full clamping between the foundation beam and the laboratory floor, prestressing rods were placed, as shown in Figure 1(c). The specimen was subjected to a sequence of quasistatic cycles of a

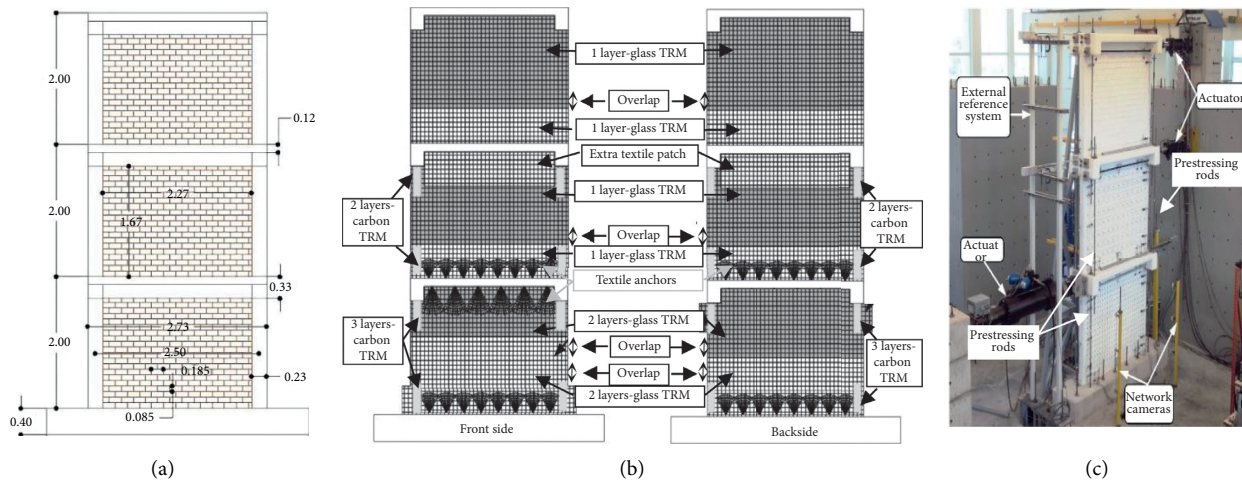


FIGURE 1: (a) Geometry of the masonry-infilled RC frame and (b) the strengthening scheme: textile anchors of the first and the second storeys and the TRM layer on the faces of masonry infill at the first, second, and third storeys. (c) Test setup. [31].

predefined force pattern. A history of imposed cycles of displacements was defined to be applied at the top, while maintaining an inverted triangular distribution of forces to the three levels until failure occurred. The displacement history for all storeys is shown in Figure 2. Permanent load is considered in the test by applying a vertical load of 80 kN per storey, concurrent to the lateral loading action. The experimental results showed that for the retrofitted specimen, the maximum base-shear force was attained during the fourth cycle of loading. After this cycle of loading, the lateral strength was decreasing due to complete debonding of the TRM from the beam surface on the backside of the first storey. In addition, the six TRM anchors placed at the top of the front side of the first storey were completely debonded during the sixth cycle of loading due to local crushing of the masonry infill at the two upper ends of the columns at the first storey.

3. Finite Element Modelling of TRM Masonry-Infilled RC Frame

A two-dimensional numerical model was developed to simulate the nonlinear behavior of the TRM-retrofitted masonry-infilled RC frame described above. The DIANA FEA software Version 10.2 was used for the purpose of this study. The following sections describe the element type, size of meshing, boundary conditions, and loading sequence that were used in this numerical model. In addition, the appropriate constitutive material models which were selected to characterize the nonlinear response of concrete, masonry infill, and TRM are also presented. DIANA FEA was selected for modelling this structural system since it provides the elements and constitutive models needed for the TRM composite material, concrete, reinforcement, and masonry infill [61].

3.1. Geometry, Mesh, Boundary Constraints, and Loading Scheme. The geometry of the TRM-retrofitted masonry-

infilled RC frame model was similar as possible to the experimental one, as shown in Figure 2. A regular squared mesh [62] with the discretization as indicated in Figure 2 was used. Three different types of elements were used in this numerical model: (1) eight-node quadrilateral isoperimetric plane-stress elements (CQ16M) for simulating the concrete frame, masonry infill wall, and TRM composite material; (2) the steel reinforcement was modelled with two-node bar elements, and they were connected to the eight-node concrete elements at the two external nodes; (3) three-point line interface element (CL12I) was used in order to simulate the gap opening and sliding at the infill-frame interface.

The interaction between masonry infill and bounding frame was modelled using the line interface element in order to take into account the gap opening and the sliding along the interface which was observed in the experiment. In addition, in this numerical model, the glass and carbon TRM were perfectly bonded to the masonry infill wall and to concrete elements, respectively, since in the experimental test, no debonding of the TRM surface from the masonry and the RC frame was observed. The bond condition provided by the existence of anchors at the top and bottom sides of the first and the second floor beams (Figure 2), was also accounted in the numerical model. In the experimental case study, textile-based anchors were used to provide a composite action of the TRM with masonry-infilled RC frame at the first and the second floors, as shown in Figure 2. More specifically, the anchors at the top and bottom sides of the first and the second floors did not fail during the experiment, therefore, composite action of the TRM at the beam-infill interfaces can be considered, so this connection is modelled assuming full bond connection between the layer of the TRM of the wall and concrete elements of the beam (full bond). In the case where the anchors failed (no composite action is provided), this connection is modelled with no bond between the TRM layer of the wall and the concrete elements of the beam (no bond).

In addition, the strong foundation RC-beam plate that was used at the bottom of the frame in the experiment was

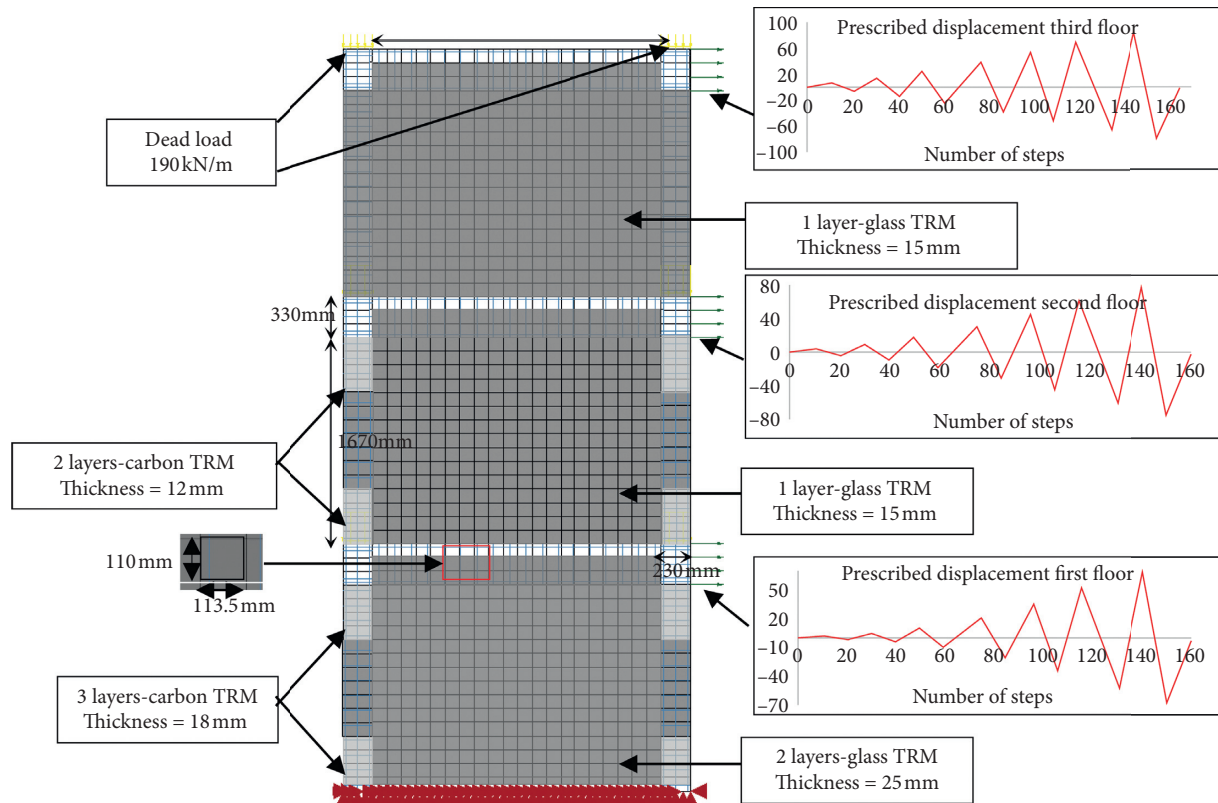


FIGURE 2: Geometry and mesh details of the FE model.

simulated by restraining all nodes at the base of the first floor of the masonry infill by preventing any translation in the x - and y -directions.

Two types of loads, representing the vertical compression and horizontal cyclic load, have been applied on the model. The dead load of the structure was simulated with a constant axial load equal to 0.174 kN/mm on the top of each column. In addition, for the horizontal cyclic loading, prescribed deformation load at the top of each floor was applied to simulate as closely as possible the experimental loading as shown in Figure 2.

3.2. Material Models. Four constitutive models are considered in this numerical model to reproduce the nonlinear behaviour of (1) concrete, (2) steel reinforcement, (3) masonry infill, and (4) TRM composite material. In addition, the interface between the masonry infill and the RC frame is modelled as described below. In this study, most of the material properties are taken from the experimental case study as described in Section 2 of this paper, and other properties were taken from the literature as described in the following paragraphs. The numerical results were compared to the experimental results, and some material properties were adjusted to enhance the accuracy of the simulation results.

The Total Strain Crack model was adopted for the concrete since this model can simulate in detail the nonlinear response of concrete with a limited number of parameters. Nevertheless, concrete members are expected to undergo low nonlinear deformations and the use of a more

complicated model was not deemed necessary. Figure 3 presents the Total Strain Crack model in terms of stress-strain for one cycle of loading and unloading (tension and compression) [43]. Limited parameters are required for the Total Strain Crack model such as Young modulus, tensile (2.15 MPa), and compressive strength (27.2 MPa) based on the Maekawa–Fukuura model [63, 64]. The fracture energy (G_F) (N/mm) was determined based on the expression that was included in the *fib* model code [65] as follows:

$$G_F = 73 * f_{cm}^{0.18}, \quad (1)$$

where f_{cm} is the compressive strength of the concrete in MPa. The fracture energy in tension is equal to 130 N/m. In addition, the modulus of elasticity was reduced to 9.1 GPa since the Total Strain Crack model does not take into account the reduction in stiffness due to the early cracking of the concrete section. In order to define cracking orientation in this numerical model, the rotating crack model is used [66].

The Menegotto–Pinto model was selected for simulating the nonlinear behaviour of steel bar reinforcement since this model is available for embedded reinforcements including the cyclic behavior of steel bar reinforcement [67]. More details regarding the Menegotto–Pinto model are presented in Filippou et al. [68]. The parameters adopted for this model are the modulus of elasticity (207 GPa) and the yield tensile stress for longitudinal reinforcement and stirrups equal to 549 MPa and 295 MPa, respectively.

The infill wall material was modelled using the Engineering Masonry model to simulate the nonlinear behavior

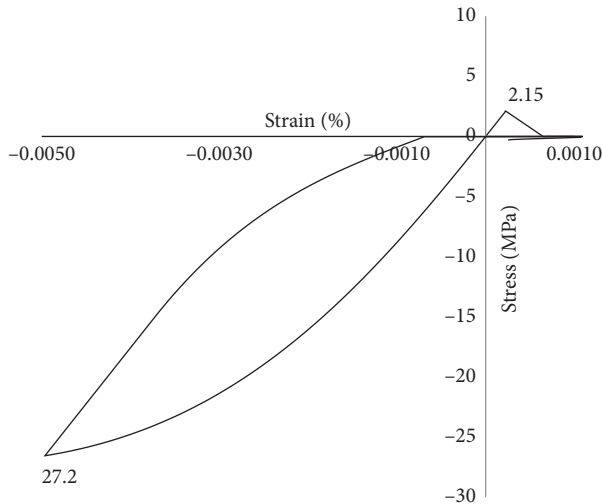


FIGURE 3: Typical uniaxial stress-strain curve as defined by the Total Strain Crack model with Maekawa–Fukuura compressive behavior.

of the masonry infill at mesolevel [69]. The Engineering Masonry model is a smeared failure model comprising a total strain-based continuum model that covers tensile, shear, and compression failure modes as shown in Figure 4. The Total Strain Crack model can be also used for modelling the masonry infill at the mesolevel since this model is used for capturing of failure of brittle materials such as masonry infill and concrete. According to Rots et al. [69], the Total Strain Crack model underestimated the stiffness degradation and energy dissipation of the masonry infill under cyclic loading compared to the Engineering Masonry model although the first one requires a small number of material properties. In addition, the Total Strain Crack model cannot simulate adequately the shear failure of the masonry infill [69]. On the contrary, the Engineering Masonry model is a material model that can simulate the behavior of the masonry infill under cyclic loading with good accuracy in terms of stiffness, energy dissipation, cracking orientation, and shear failure (Figure 4(c)). The Engineering Masonry model includes the standard Coulomb friction failure criterion for the shear failure mechanism. In addition, in this model, the unloading behaviour of the masonry infill is described with the assumption of linear unloading for compressive stresses with initial elastic stiffness (Figure 4(a)). The parameters adopted for the Engineering Masonry model are taken from the literature as previously mentioned since this material model requires a large number of material properties, and most of them were not provided by the experimental case study. The parameters adopted for the Engineering Masonry model are given in Table 1. The modulus of elasticity in the direction normal to bed joints (y -direction) was obtained from the experimental test. Where other information was not available for Young's modulus in the direction parallel to the bed joints, it was estimated according to the ratio between Young's modulus in the x -direction and Young's modulus in the y -direction which ranging from 1.5 to 2, this ratio is often found for masonry units [70, 71]. The tensile strength of the joint is still a subject of research, and therefore the tensile behavior parameters have been assumed according to the

information provided by the respective experimental testing reports or related references. The tensile strength normal to the bed joints ranging from 0.1 to 1 MPa for different brick unit-mortar combination [72–74]. The residual tensile strength was calculated as 40% of the tensile strength, while the tensile strength normal to the bed joint is equal to 0.5 MPa according to Lourenço and Rots [70, 71]. In the experimental case study, the value of the fracture energy in compression and tension was not provided. The value of the fracture energy can be obtained from the literature for similar types of masonry walls [72, 75]. In this study, the compressive fracture energy (G_{fc}) and the tensile fracture energy (G_{ft}) (N/mm) have been determined according to the following formulation (equations (2) and (3), respectively), as proposed by Rots [69]:

$$G_{fc} = 15 + 0.43 f_c - 0.0036 f_c^2, \quad (2)$$

$$G_{ft} = 0.025 (2f_t)^{0.7}, \quad (3)$$

where f_c is the compressive strength of the masonry in MPa and f_t is the tensile strength of the masonry normal to the bed joint in MPa. Reviewing the literature, it can be concluded that the cohesion ranges from 0.2–1.2 MPa for different brick unit-mortar combination. In this study, the cohesion was obtained 1.5 times greater than the tensile strength according to the relation proposed by Cur [76]. Following the Mohr–Coulomb failure criterion and considering the value of the shear strength of the masonry infill as was obtained from the experimental results (Section 2 of this paper), the friction angle (φ) is equal to 20 degrees. In the Engineering Masonry model, the cohesion, c , and the friction angle are specified as shown in Table 1. These values are then used to calculate the shear fracture energy according to equations included in DIANA FEA.

The gap opening and sliding occurred due to interaction between the frame and the masonry infill significantly influence the overall behavior of the masonry-infilled RC frame as described by Filippou et al. [68]. Therefore, in order to model the interaction between the masonry infill wall and the bounding RC frame, an interface gap, plasticity-based model was used as proposed by Lourenço and Rots [77]. A tension cutoff tensile failure criterion (mode I), a Coulomb friction shear failure criterion (mode II), and a gap mode compressive failure criterion are included in this model as shown in Figure 5. The interface is controlled by tension, shear (Coulomb friction), and crushing failure. One drawback regarding the use of an interface model is the lack of material properties since no experimental test was available regarding the direct measurement of the required parameters for this model. However, data regarding the gap opening and sliding at the interface which were obtained from the experimental test conducted by Koutas et al. [31] can be used for calibrating the required parameters for this model. Therefore, in this study, it was decided to define the required material properties of the interface model using recommendations (equations) available in the literature and at the same time to fit the global and local numerical results to the results obtained from the experimental case study. The mechanical properties of the interface between the masonry infill and the RC frame depend on infill wall-frame relative stiffness and infill

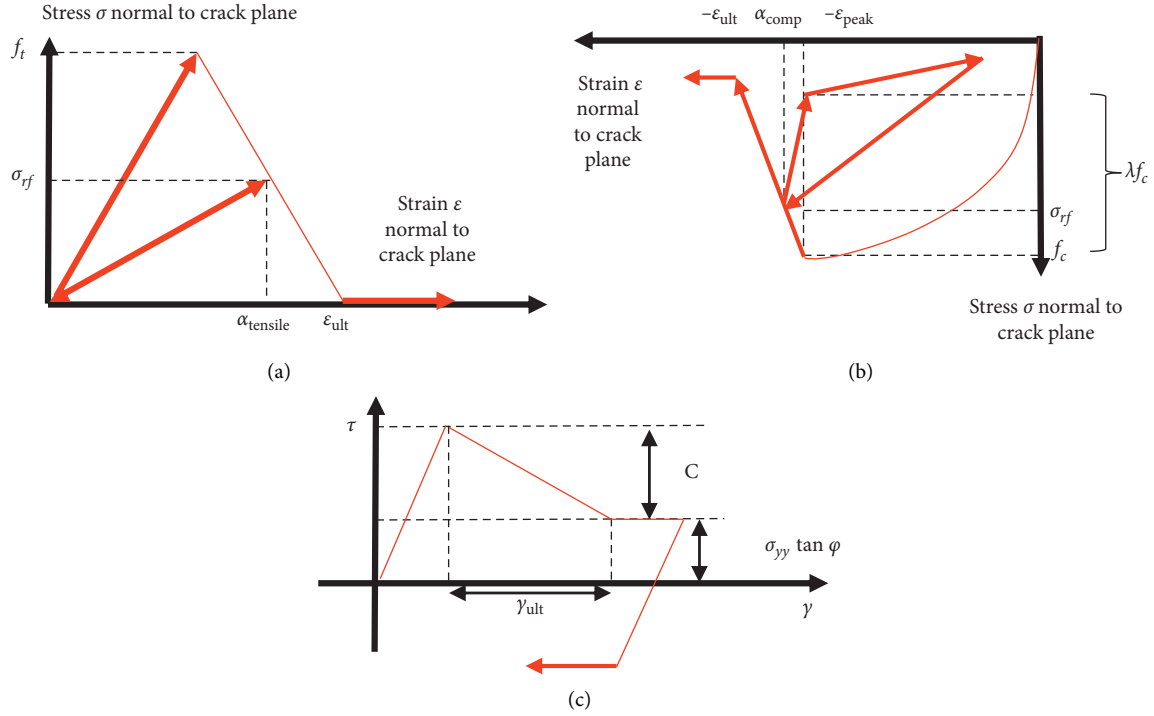


FIGURE 4: Engineering masonry model (a) behavior in traction, (b) behavior in compression, and (c) shear behavior [69].

TABLE 1: Material properties of the engineering masonry model.

Modulus of elasticity— x -direction (GPa)	7
Modulus of elasticity— y -direction (GPa)	3.37
Shear modulus (GPa)	1.38
Mass density (kg/m^3)	800
Cracking: head joint failure	
Tensile strength normal to the bed joint (MPa)	0.5
Residual tensile strength (MPa)	0.2
Fracture energy in tension (N/mm)	0.05
Crushing parameters	
Compressive strength (MPa)	5.1
Fracture energy (N/mm)	40
Compressive unloading factor	0.2
Shear failure parameters	
Cohesion (MPa)	0.71
Friction angle (degree)	20

wall-frame friction and bond strength. In this study, a recommendation by DIANA FEA, which is based on the equations proposed by Lourenco et al. [78], is used for calculating the value of the normal stress (equation (4)) and shear stiffness (equation (5)) as follows:

$$K_{\text{normal}} = (100 - 1000) \frac{E_x}{l_{\text{element}}}, \quad (4)$$

$$K_{\text{tangential}} = \frac{K_{\text{normal}}}{(10 - 100)}, \quad (5)$$

where E_x is the Young's modulus of masonry infill parallel to the bed joint in GPa and l_{element} is the length of the masonry infill plane-stress element in mm. The above recommendation shows that the normal and shear stiffness of the

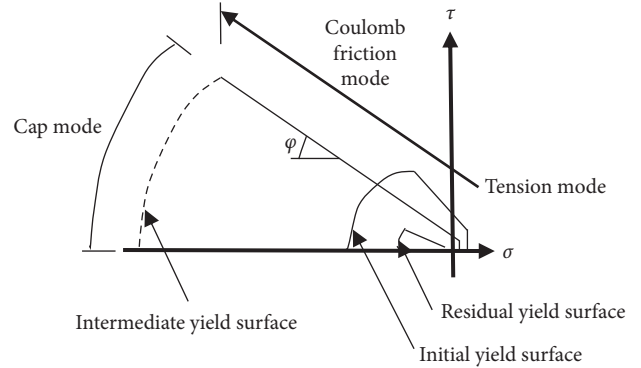


FIGURE 5: Coulomb friction interface model [77].

interface depend on the modulus of elasticity of the masonry infill in each direction. The cohesion (c) (MPa) associated with the Coulomb friction interface model has been determined based on the relation (equation (6)) proposed by Sarhosis et al. [79] as follows:

$$c = 0.1065 f_c + 0.531, \quad (6)$$

where f_c is the compressive strength of the masonry infill in MPa. The interface friction angle associated with the Coulomb friction model ranges from 20 to 50 degrees [76, 78]. In addition, it is difficult to relate the tensile strength of the interface with other parameters of the interface, and therefore it was decided to define the tensile strength of the interface by fitting the numerical results to the results obtained from the experimental case study. The interface Coulomb friction model is defined in DIANA FEA using the parameters as shown in Table 2.

For the simulation of the TRM composite material, the Total Strain Crack model with the Fiber-Reinforced Concrete model for tensile behavior [65] was chosen as well as the *fib* model code 2010 model for its compressive behavior. This Total Strain Crack model requires parameters for the tensile and compressive behavior of the composite material. Therefore, the required input parameters were obtained from the TRM-coupon tests conducted by Koutas et al. [31]. The Fiber-Reinforced Concrete model was specified as a function of the strains where the cracking of composite is initiated at the strain where its tensile strength is reached. In addition, the maximum compressive and ultimate strains were obtained from the *fib* model code [65]. The parameters adopted in the DIANA FEA software for the TRM model are given in Table 3.

Numerical monotonic and cyclic tensile tests were performed in order to validate the nonlinear response of the TRM composite material. The validation was performed by comparing the numerical results with those obtained from monotonic tensile TRM-coupon tests conducted by Koutas et al. [31] and taking into account the results obtained by cyclic available experimental tests [80, 81]. Koutas et al. [31] performed in total six coupon tests of two layers of glass-TRM under uniaxial tensile load. Considering the macromodelling approach, the TRM composite material is modelled with the assumption of having a homogenized layer of mortar and textile using the quadrilateral isoperimetric plane-stress element since the current study is not intended to reproduce the TRM behaviour in a very detailed way but to describe its structural response in a simple and sufficiently accurate manner. The two layers of glass TRM were characterized through a numerical tension test with a nominal size of $500 \times 100 \times 10$ mm subjected to uniaxial and cyclic tension loading. The main focus of the numerical modelling of this composite is on the validation of its tensile response using the selected constitutive model with particular attention to the cyclic behavior of the composite material. The numerical stress-strain curves are shown and compared with the envelope of the experimental results [31] in Figure 6(a) while Figure 6(b) shows the numerical results obtained for the cyclic test of two layers of glass TRM in terms of stress-strain.

The numerical results show good agreement with the experiment data in terms of peak and ultimate stress and strain, stiffness, and postcracking behavior. Previous studies concluded that the TRM nonlinear stress-strain curve is divided into three states: State I (the uncracked matrix), State II (the crack formation), and State III (the crack stabilization and failure) [82–88] as shown in Figure 6(b). Experimental studies conducted by Jesse and Keer [80, 81] showed that as the loading/unloading continues, the modulus of elasticity of the composite material decreases in State III. Therefore, high residual strain is obtained after the failure of the mortar (State III). The numerical results using the Total Strain Crack model with the Fiber-Reinforced Concrete model show that no residual strain is adopted in State III. As shown in Figure 6(b), which illustrates the loading and unloading of the above-mentioned numerical TRM-coupon test, the unloading branch of the curve at State III directs towards zero residual strain. Therefore, the selected constitutive model for TRM is not

TABLE 2: Material properties of the interface Coulomb friction model.

	y -direction	x -direction
Normal stiffness (kN)	6000 N/mm ³	3000 N/mm ³
Shear stiffness (ks)	60 N/mm ³	30 N/mm ³
Friction angle (φ)	30 degree	30 degree
Dilatancy (ψ)	0	0
Model for gap appearance	Brittle	Brittle
Tensile strength	$1e - 10$ N/mm ²	$1e - 10$ N/mm ²

TABLE 3: Material properties of total strain crack model for glass and carbon TRM.

	Glass TRM	Carbon TRM
Elastic modulus (GPa)	30.00	34.00
Poison ratio	0.2	0.2
Mass density (kg/m ³)	2400	2400
Total crack strain model	Crack orientation rotating	
Tensile behavior	<i>Fib</i> fiber-reinforced concrete	
Tensile strength (MPa)	2.72	5.57
Tensile stress point I (MPa)	2.72	5.57
Strain at point I (%)	0.009	0.017
Tensile stress point J (MPa)	2.72	5.57
Tensile strain point J (%)	0.21	0.1
Tensile stress point k (MPa)	12	15
Tensile strain point K (%)	1.5	0.7
Ultimate strain (%)	1.5	0.7
Crack band width	Rotating	
Compressive behavior	<i>Fib</i> model code for concrete structure 2010	
Compressive strength (MPa)	18	18
Strain at maximum stress (%)	0.21	0.21
Strain at ultimate stress (%)	0.35	0.35

simulating exactly the cyclic behavior of TRM; however, in this case study, the behavior of TRM at State III does not influence the behavior of the masonry-infilled RC frame retrofitted with TRM because this type of masonry-infilled structure cannot reach a high value of strains, i.e., behavior is limited to early stage of loading of TRM (State II), thus very limited residual strain is anticipated. It can be concluded that there is still a lack of information on a suitable constitutive model for simulating the cyclic nonlinear response of the TRM composite. The large variety of mortars and fiber textile used in real application has made the characterization and constitutive modelling challenging.

4. Simulation of the Response of a Masonry-Infilled RC Frame Retrofitted with TRM

In this section, the calibration of the numerical model is presented, by comparing the numerical results of the eigenvalue and nonlinear cyclic analysis with experimental ones. Nonlinear cyclic analysis was performed (displacement control analysis) with the secant iteration scheme and the automatic incrementation procedure, in which both the number of steps and the corresponding step size are automatically computed. The energy-based convergence criterion was applied with the standard tolerance value (0.0001).

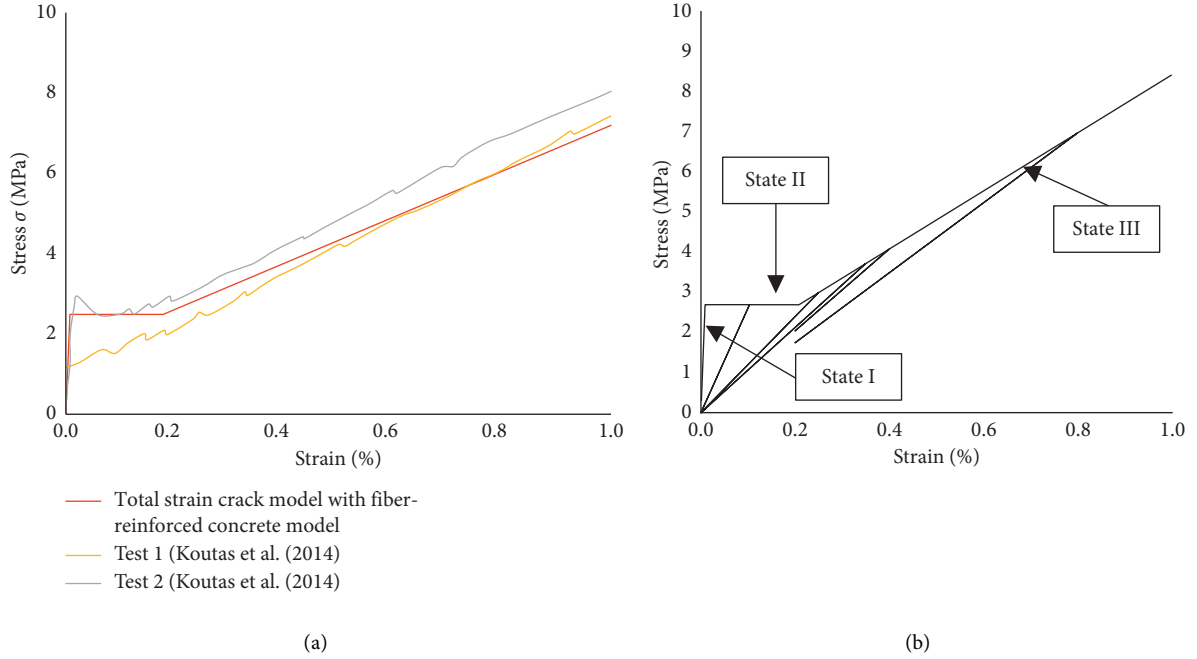


FIGURE 6: (a) Comparison of the results between the numerical model using the total strain crack model with the fiber-reinforced concrete model (*fib*) and the experimental test and (b) numerical results for the cyclic behavior of two layers of glass TRM in terms of stress-strain.

The fundamental period of the bare frame and for the masonry-infilled RC frame with and without TRM is presented in Table 4, and they are in good agreement with the experimental ones.

The comparison between the experimental (black line) and numerical (red line) results concerning the global performance of the TRM-retrofitted masonry-infilled RC frame subjected to cyclic loading is presented in Figures 7 and 8. Figure 7(a) shows the base shear versus top floor displacement, and Figures 7(b) and 7(c) show the base shear in relation to the load step and the top storey displacement versus the load step, respectively.

Figures 8(a) and 8(b) illustrate a comparison between experimental and numerical results for the TRM masonry-infilled RC frame in terms of global stiffness and hysteric energy, respectively. The secant stiffness degradation is expressed by the following equation:

$$K_i = \frac{|+V_{\max,i}| + |-V_{\max,j}|}{|+X_{\max,i}| + |-X_{\max,j}|}, \quad (7)$$

where $j = i + 1$, $|\pm V_{\max,i}|$ is the absolute value of the positive and negative peak base shear values of the i^{th} cycle, and $|\pm X_{\max,i}|$ is the absolute value of the displacement corresponding to the positive and negative peak base shear values of the i^{th} cycle.

The energy dissipated at each cycle of loading is obtained by calculating the area enclosed by the loop in the base shear versus the top floor displacement diagram. The dissipated energy is associated with the propagation of damage through the wall (crack opening) and with the increase of the lateral capacity which leads to a higher area inside the hysteric loop.

TABLE 4: Comparison of experimental and numerical fundamental periods.

Fundamental period (seconds)	Bare frame	Masonry-infilled RC frame	TRM strengthened masonry-infilled RC frame
Experiment	0.24	0.06	0.047
Model	0.23	0.062	0.049

For easy calculations, the evolution of the dissipated energy is expressed by the following equation:

$$S_i = S_{i-1} + 0.5 * (V_{b,i} + V_{b,i-1}) * (X_{b,i} - X_{b,i-1}), \quad (8)$$

where $(V_{b,i}, V_{b,i-1})$ is the base shear in two consecutive points of the response and $(X_{b,i}, X_{b,i-1})$ is the corresponding displacement.

Numerical results and experimental data of the TRM-masonry-infilled RC frame have been compared (Figures 7 and 8) and are in good agreement with the experimental ones regarding initial stiffness, stiffness degradation, maximum shear force, and energy dissipation in each cycle of loading. Based on the results from Figures 7(c) and 8(b), the shear force capacity and the energy dissipation for the last cycle of unloading are overestimated by 15% and 16%, respectively. The energy dissipated at the last cycle of loading and unloading obtained by calculating the area enclosed by the loop in the base shear versus the top floor displacement diagram is overestimated by about 20% (Figure 6(a)). This might depend on the analysis convergence and on the nonlinearities that were introduced in the last cycle of loading during the experiment (soft-storey failure of the ground floor wall). In addition, no discrepancy appears for the first three

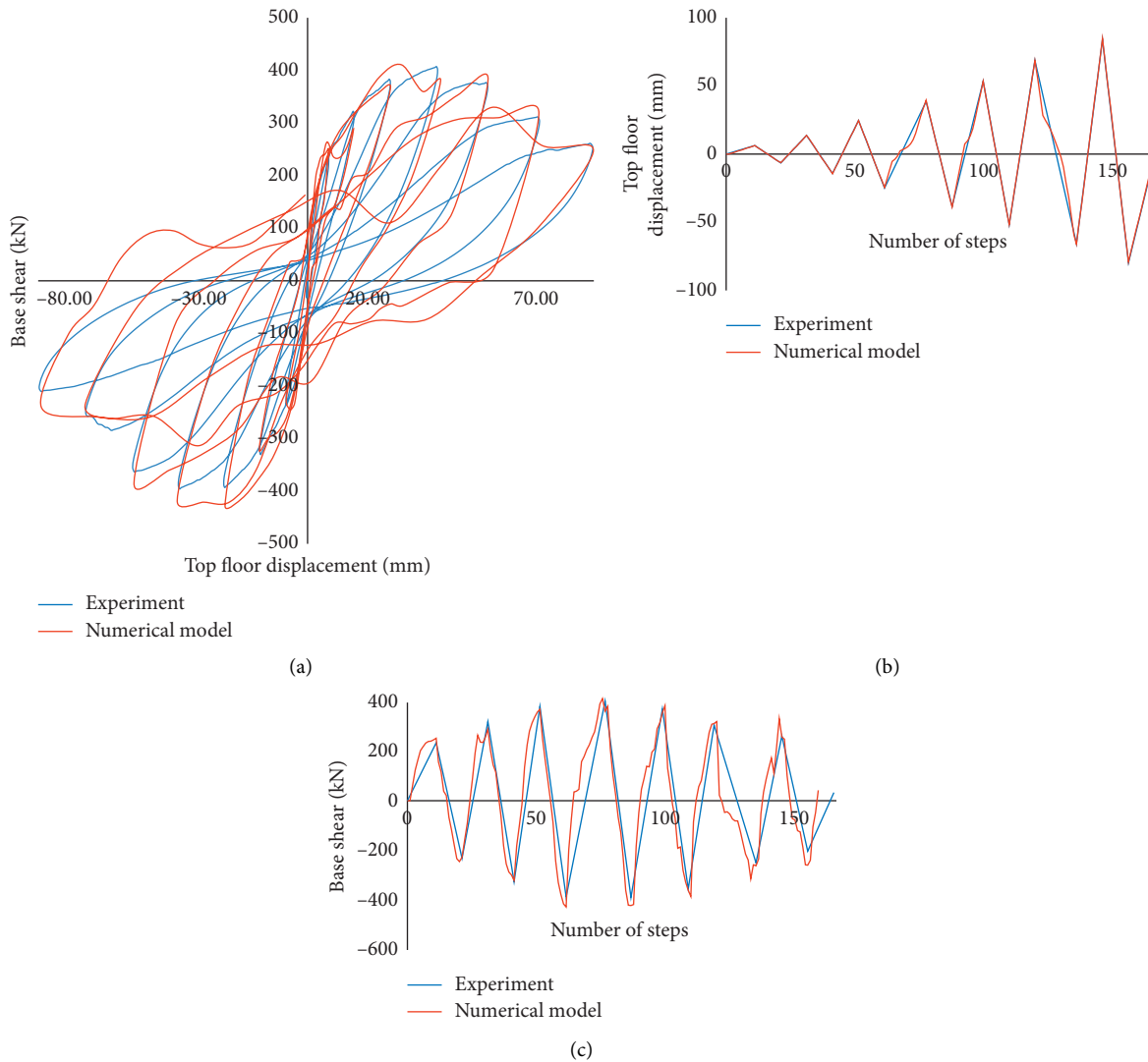


FIGURE 7: Comparison between experimental and numerical model results in terms of (a) base shear and top floor displacement hysteric curves, (b) base shear in relation to the load step, and (c) and top floor displacement in relation to the load step.

cycles of loading between numerical and experimental results in terms of base shear, stiffness, and hysteric energy.

In addition, the comparison between the experimental and numerical results in terms of crack patterns is presented in Figure 9. Figures 9(a) and 9(b) show the cracking that occurred at the first storey east column and at the retrofitted masonry infill of the first storey, respectively, in the experimental case study at the end of the test. Figure 9(c) shows the crack patterns in the numerical model on external face of TRM at the masonry infill at the first floor at the end of the test. It is important to mention that the TRM plane-stress elements overlay the masonry plane-stress elements, and therefore the crack propagation of masonry cannot be graphically presented.

In the TRM-retrofitted masonry-infilled RC frame model, flexural and tensile cracks occurred on external face of TRM both in the diagonal and horizontal directions at the first floor where these cracks have the same location as observed in the experiment. In addition, in the numerical model, shear and

tensile cracks appear at the top of the first storey east column, which resembles the rupture of the TRM at the experimental study. It can be concluded that the crack pattern is well reproduced by a numerical model since the same damage is observed in the experiment upon test completion. It is observed that the proposed numerical model is capable of detecting the major features of the real behavior of the TRM-retrofitted masonry-infilled RC frame. The crack propagation and the global performance of retrofitted masonry-infilled RC frame in terms of base shear, stiffness, and energy are well reproduced by the numerical model. The discrepancy between numerical and experimental results is due to the nonlinearities that are introduced in the last cycle during the experiment (soft-storey failure of the ground floor wall).

5. Sensitivity Analysis and Parametric Study

After the calibration of the numerical model, sensitivity analysis is performed in order to examine how the stiffness properties

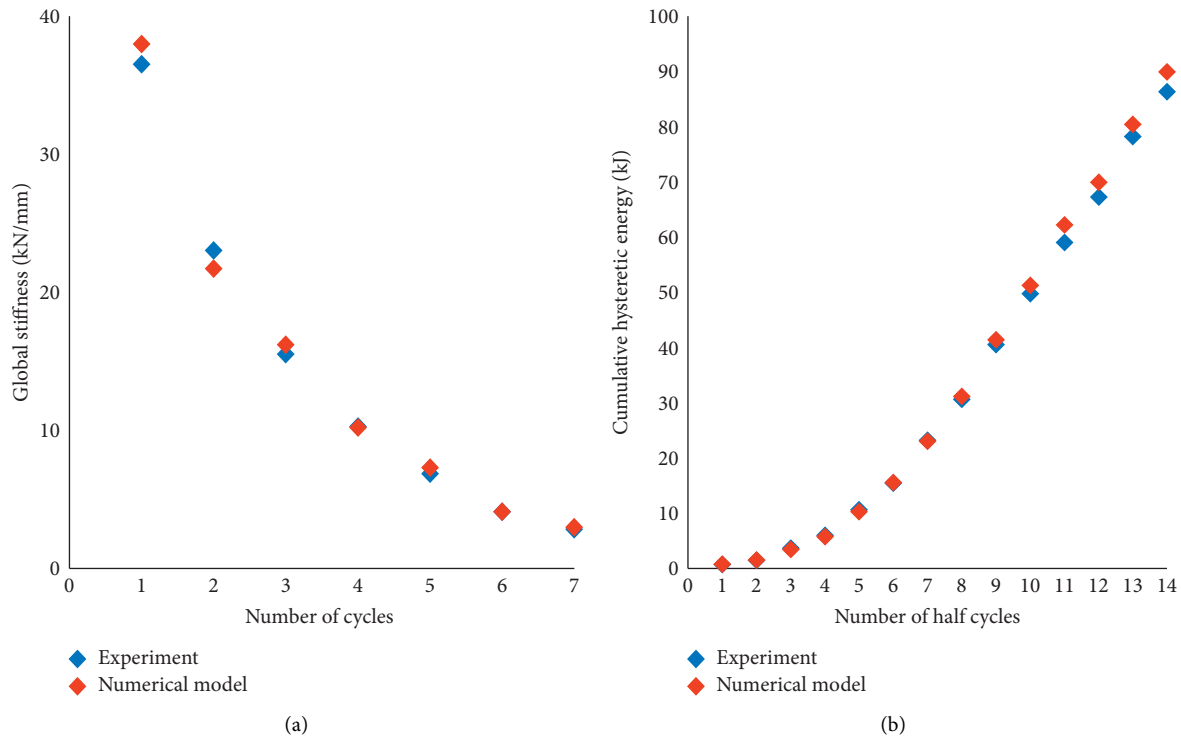


FIGURE 8: Comparison between the numerical model and the experimental results for the TRM masonry-infilled frame in terms of the (a) global lateral stiffness per cycle and (b) cumulative global hysteretic energy per half cycle.

(tangential and normal) of the infill-frame interface element affect the behavior of the retrofitted infilled frame. In addition, numerical experiments through a parametric study are performed to evaluate how important is the full-bond condition between the TRM and the masonry-infilled RC frame.

5.1. Effect of Stiffness Properties (Normal and Tangential) of the Infill-Frame Interface on the Behavior of TRM Masonry-Infilled RC Frame. As mentioned in Section 3.2, the interface between the masonry infill and the frame is modelled with an interface element which has zero thickness, and a plasticity-based model is adopted for modelling the interface as shown in Figure 5. Sensitivity analysis was performed in order to examine how the stiffness properties (tangential and normal) of the infill-frame interface element affect the behaviour of the retrofitted infilled frame. The required normal and shear (tangential) stiffness of the interface are estimated using the equations (4) and (5), respectively, as mentioned in Section 3.2. Therefore, following these approximations, three different analyses were performed in this sensitivity analysis as shown in Table 5.

The comparison between the numerical results from the three analyses concerning the global and local performance of the TRM-retrofitted masonry-infilled RC frame subjected to cyclic loading is presented in Figures 10 and 11, respectively.

From Figures 10 and 11, it is observed that by increasing the normal and tangential stiffness of the interface, the average gap opening decreases while the energy dissipation and the global stiffness increase. In the case where

the tangential stiffness is 10 times higher (Case 1) than the tangential stiffness used in the calibrated model (Case 0), the gap opening between the masonry infill and the beam decreases about two times while the stiffness and energy dissipation increase by about 50–87% and 20–40%, respectively. In addition, comparing the results from Case 2 with those obtained from Case 1 (where the normal stiffness in Case 2 is ten times higher than in Case 1), the average gap opening between the masonry infill with the beam and with the column decreases about 7–9 times while the stiffness and the energy dissipation increase by about 5% and 10%, respectively. Therefore, as the normal and shear stiffness increase (Case 2 and Case 3), the gap opening tends to zero, causing almost a monolithic behavior of the masonry-infilled RC frame. Furthermore, comparing the results from Case 2 and Case 3 (where the normal and shear stiffness are ten and hundred times higher than the normal and shear stiffness used in Case 0, respectively), with that obtained from Case 0 it seems that the stiffness and the energy dissipation increase by 70–100% and 45–75%, respectively, in the last cycles of the test. Comparing the results obtained from Case 2 and with that obtained from Case 3, the average gap opening between the masonry infill and the RC frame (beam and column) is almost the same. Therefore, in the case where the infill-frame interface stiffness is high, then a small gap opening will occur.

From the sensitivity analysis, it is concluded that the nonlinear response of the masonry-infilled RC frame retrofitted with TRM is sensitive to the normal and shear stiffness of the infill-frame interface because the interaction between the frame

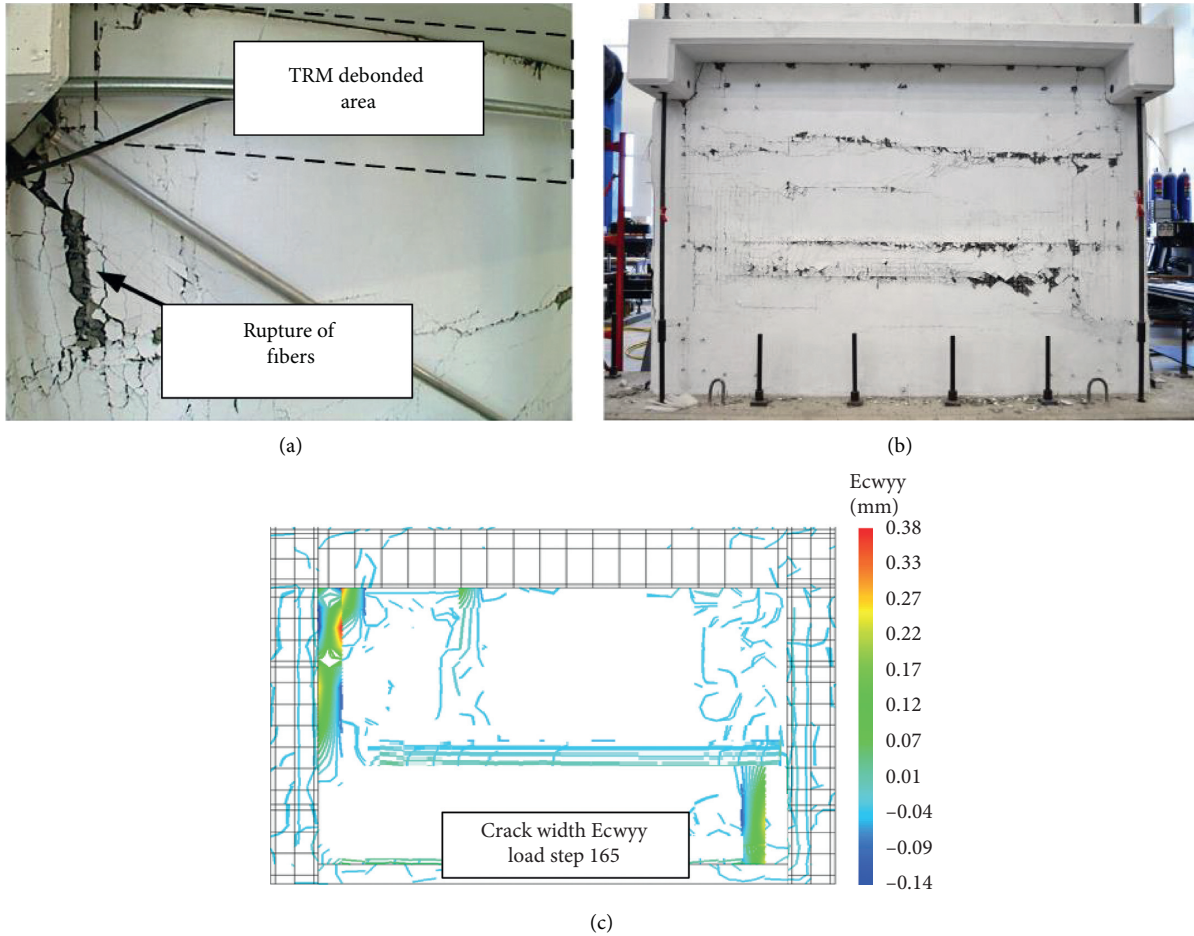


FIGURE 9: (a) Damage at the first storey on the east column in the experimental study, (b) cracking of the masonry at the first storey in the experimental study, and (c) crack patterns in the numerical model in the masonry infill in the first floor at the end of the test.

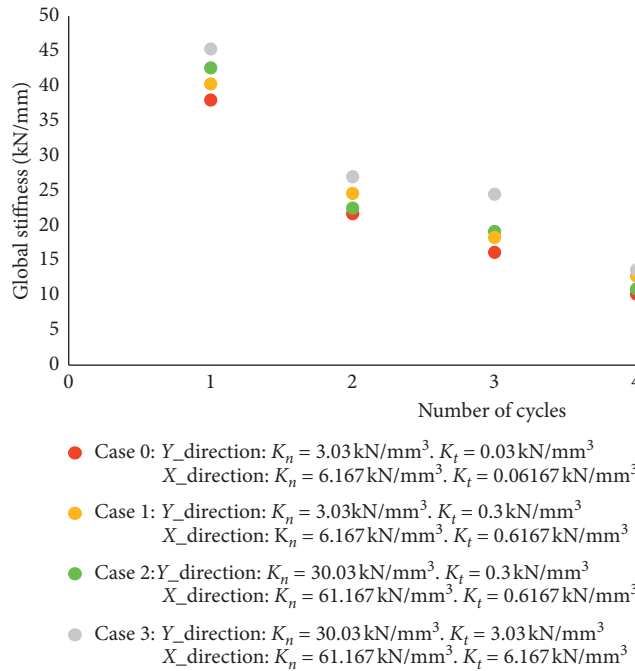
TABLE 5: Number of trials for normal and tangential stiffness of the interface.

Name of analysis	K_{normal} (kN/mm ³)	$K_{\text{tangential}}$ (kN/mm ³)	Interface between masonry infill and column	
			K_{normal} (kN/mm ³)	$K_{\text{tangential}}$ (kN/mm ³)
	Interface between masonry infill and column (y-direction)		Interface between masonry infill and beam (x-direction)	
Case 0 (calibrated model)	3.03	0.030	6.167	0.06167
Case 1	3.03	0.30	6.167	0.6167
Case 2	30.03	0.30	61.67	0.617
Case 3	30.03	3.03	61.67	6.67

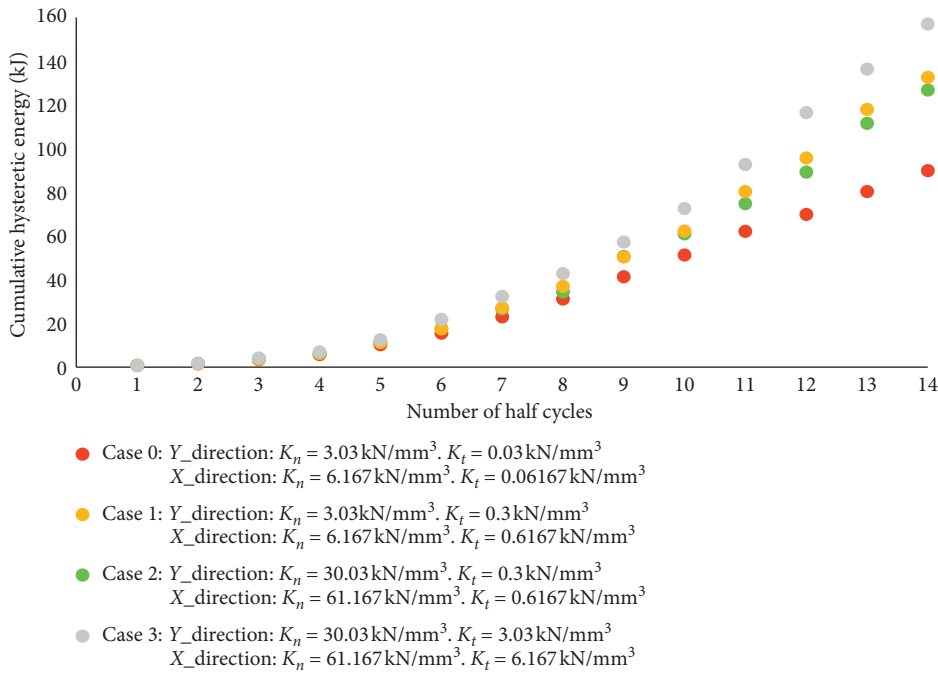
and the infilled panel is considered as the major cause of the nonlinear behaviour of this type of structure [89–96]. Therefore, the infill-to-frame interaction depends on infill-frame relative stiffness since this relative stiffness (normal and tangential stiffness properties of the interface) describes the stress deformation characteristics of the interface between the masonry infill and the RC frame. Although the normal and tangential stiffness properties of the infill-frame interface model do not represent actual masonry infill parameters, they are required parameters for simulating the interface between the masonry

infill and the RC frame because they can control the gap opening and the sliding of adjacent elements in the model.

5.2. Effect of Bonding of TRM on the Behavior of TRM Masonry-Infilled RC Frame. In this section, numerical experiments are performed using the calibrated model in order to evaluate the importance of full-bond condition between the TRM and the masonry-infilled RC frame on global and local response of the retrofitted infilled frame under cyclic



(a)



(b)

FIGURE 10: Comparison between numerical model results using different values in the stiffness of the interface for the TRM masonry-infilled frame in terms of the (a) global lateral stiffness per cycle and (b) cumulative global hysteretic energy per half cycle.

loading. A parametric investigation of the response of the calibrated model is undertaken in order to assess the effectiveness of considering full bond condition between the retrofitted wall and the surrounding frame. Two different configurations of connection were examined in order to evaluate the importance of the full-bond condition between the TRM and the masonry-infilled RC frame that the anchors provide: (1) full bond, where the glass TRM layer of the

wall is fully bonded (Section 3.1) to the beam at the first and the second floors, and (2) no bond (Section 3.1), where the glass TRM of the wall is not fully bonded to the beams at the first and the second floors.

The numerical results of the two different configurations (full bond and no bond) are compared with the results obtained from the calibrated model in terms of stiffness and energy dissipation as shown in Figures 12(a) and 12(b), respectively.

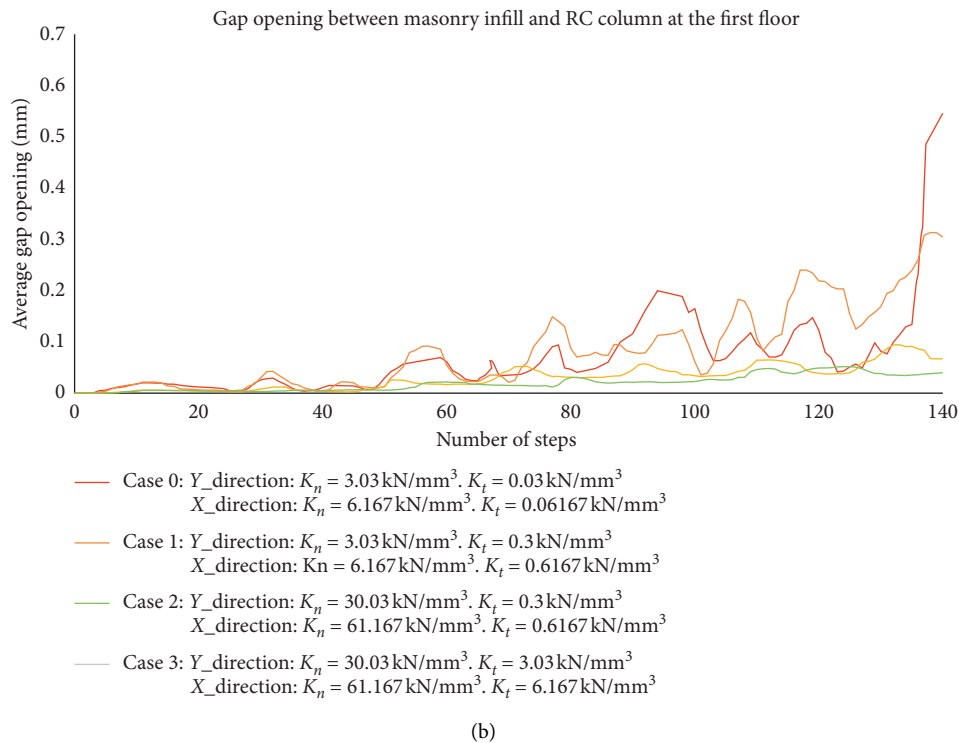
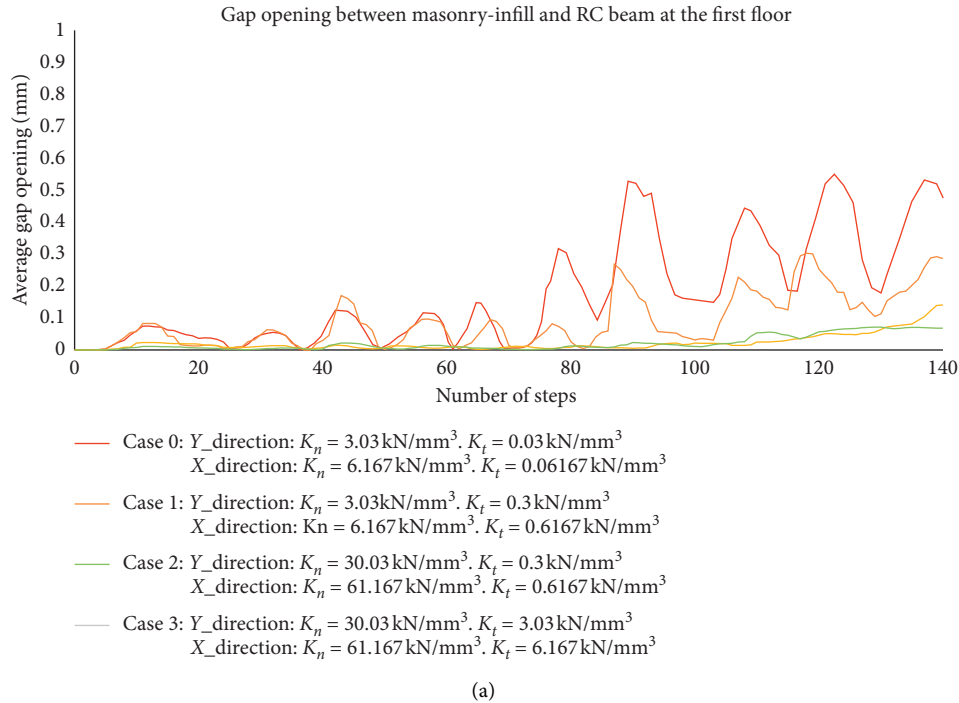


FIGURE 11: Comparison between numerical model results using different values in the stiffness of the interface for the TRM masonry-infilled frame in terms of gap opening between the masonry infill and (a) the beam and (b) the column.

The results show that in the case where the full-bond condition is considered, the global stiffness and the hysteric energy increase by about 15% at the first three cycles of loading compared to the corresponding ones obtained from the calibrated numerical model. In addition, at the maximum lateral capacity (fourth cycle of loading), the energy and the stiffness of the structure as obtained from the full-bond case increase equal to

35% compared to those obtained from the calibrated numerical model. Therefore, composite action of the TRM jacket at the beam-infilled interfaces (full bond) contributes to provide a substantial gain in the shear capacity and the hysteric energy of the TRM masonry-infilled RC frame. In the case of no bond, reduction of the stiffness (15%) is observed compared to the stiffness obtained from the full-bond case at the fourth and fifth

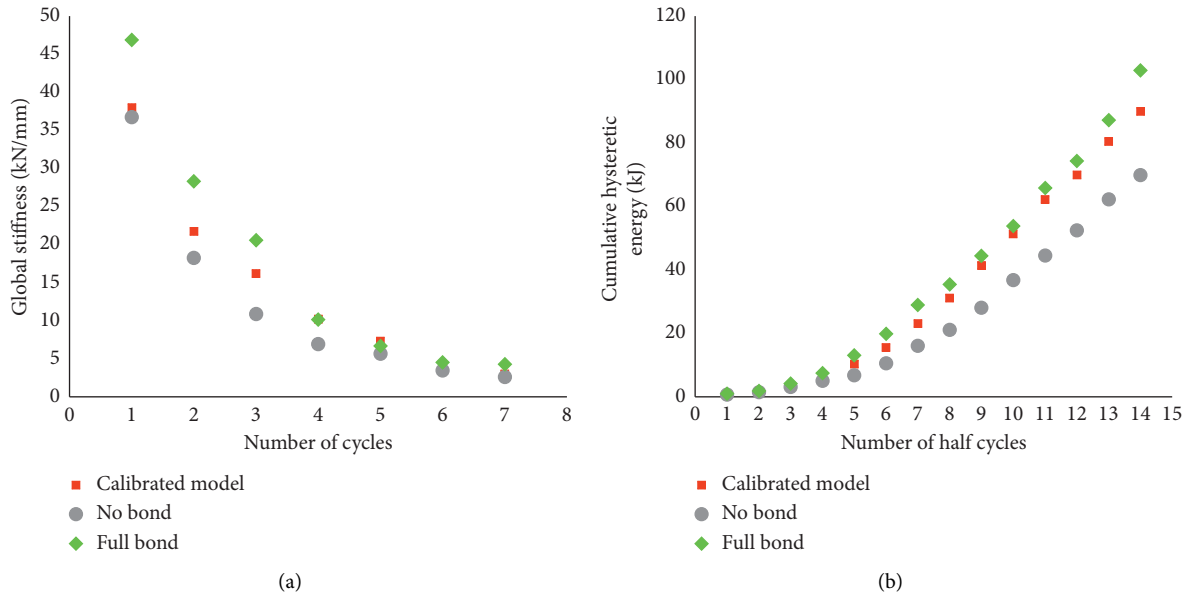


FIGURE 12: Comparison of the results in terms of (a) stiffness and (b) hysteretic energy between the numerical model results considering full bond, no bond, and calibrated model bond conditions.

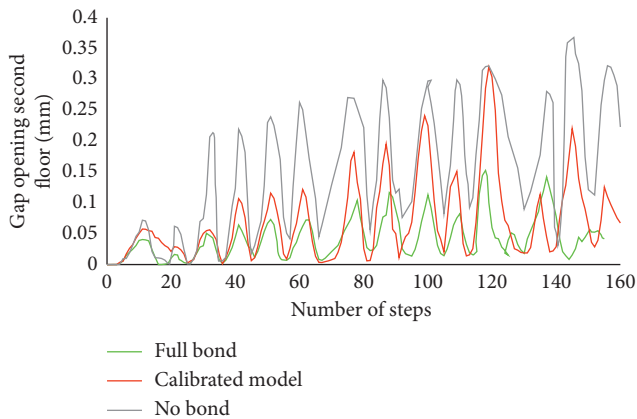


FIGURE 13: Comparison of the results in terms of gap opening between the numerical model results considering full bond, no bond, and calibrated model conditions.

cycles of loading, while the energy after the third cycle of loading decreases by 30% compared to that obtained from the full-bond case. The numerical results show that improving the bond condition between the TRM layer and masonry-infilled frame, especially at the beam-infilled interface would enhance the performance of this structural system.

In order to investigate the effect of bond condition between the TRM and the masonry-infilled RC frame on the behaviour of the retrofitted infilled frame structure, the local results are presented in terms of gap opening between the infill wall and the beam (Figure 13). The infill-frame separation occurred at the very early stages of loading in the experiment and in the numerical model. The corresponding gap at the left side of the interface between the masonry wall and the bottom side of the beam at the first floor is 1.2 mm in the no bond case, 0.6 mm in the calibrated model (Section 3.2), and 0.2 mm in the case

of full-bond. From Figure 13, it can be concluded that composite action of the TRM layer at the beam-infilled interfaces (full bond) contributes to influence the interaction of masonry infill with the beam since the gap opening decreases. More specifically, the results show that when full-bond condition is considered, the gap opening decreases about two times compared to that obtained from the calibrated numerical model. In addition, in the no bond case, the gap opening increases about three times compared to that obtained from the full-bond case.

From the experimental study performed by Koutas et al. [31] and from the current parametric study, it can be concluded that improved bond condition between the TRM and the masonry-infilled frame contributes to improve the performance of the retrofitted infilled frame. Further numerical and experimental studies must be performed to find the optimal retrofit strategies using textile-based anchors including the investigation of adequate anchorage of the TRM jacket around the perimeter of the masonry (bond length, different types of the textile, different angle of anchors, and different application of the anchorage). In addition, further studies are needed in order to explore other types of connectors that should be used in the TRM-retrofitted masonry-infilled RC frame.

6. Conclusion

A numerical model that simulates the in-plane nonlinear behavior of a masonry-infilled RC frame retrofitted with TRM under cyclic loading using the DIANA FEA software is presented in this paper. The test was conducted on a 2:3 scale three-storey infilled frame structure with nonseismic design and detailing, subjected to in-plane cyclic loading through the displacement control load. In this study, constitutive models based on the smeared crack approach for each component of the structural system were selected and

calibrated based on the experimental results or inverse fitting with clear identification and justification. It is important to note that the anchors are not modelled in this numerical study so their failure is not predicted. The bond condition that the anchors provide between the masonry infill and the frame is taken into account in the model.

The numerical model was capable of simulating the in-plane nonlinear behavior of the TRM-retrofitted masonry-infilled RC frame with good accuracy in terms of initial stiffness and its deterioration, and shear capacity. In particular, the energy absorption and maximum shear force capacity in the last cycle of loading are overestimated compared to experimental results, due to high nonlinearities that are introduced in the last cycle of loading in the experiment (soft-storey failure of the ground floor wall). The crack patterns observed numerically show good agreement with the ones observed at the end of the experiment, concerning the location and propagation of the cracks.

After the calibration of the numerical model, sensitivity analysis was performed in order to examine the influence of infill-frame interface properties (tangential and normal stiffness) on the behaviour of the retrofitted infilled frame under cyclic loading. In addition, a parametric study was performed in order to evaluate the importance of the full-bond condition between the TRM and the masonry-infilled RC frame. From the sensitivity analysis, it can be concluded that the nonlinear response of the masonry-infilled RC frame retrofitted with TRM is sensitive to the normal and shear stiffness of the infill-frame interface, and these parameters are essential for simulating the infill-frame interface since they are able to control the gap opening and the sliding of adjacent elements in the model. The results from the parametric study showed that the composite action of the TRM jacket at the beam-infill interface (full bond) contributes to increase the load capacity and the hysteric energy of the TRM masonry-infilled RC frame, and to reduce the gap opening between the masonry infill and the RC frame. The numerical results show that improving the bond condition between the TRM and the interface between the masonry infill and the RC frame the performance of this structural system is improved. Further numerical and experimental studies are needed to find the optimal retrofitting strategies using the TRM composite material in a large-scale structure and to find an adequate configuration of textile-based anchors. This will expand the results' database and will allow the development of design guidelines for a new strengthening technique on masonry-infilled RC frames using TRM.

Data Availability

All data related to the numerical work included in the submission can be made available upon request.

Conflicts of Interest

The authors declare that they have no conflicts of interest.

References

- [1] R. Kumar, Y. Singh, and R. Deoliya, "Review of retrofitting techniques for masonry infilled RC frame buildings," *Trends and Challenges in Structural Engineering and Construction Technologies*, vol. 1, pp. 284–296, 2009.
- [2] H. Kaplan and Y. Salih, "Seismic strengthening of reinforced concrete buildings," in *Earthquake-Resistant Structures—Design, Assessment and Rehabilitation*, pp. 407–428, Intechopen, London, UK, 2012.
- [3] A. Stavridis, I. Koutromanos, and P. B. Shing, "Shake-table tests of a three-story reinforced concrete frame with masonry infill walls," *Earthquake Engineering & Structural Dynamics*, vol. 41, no. 6, pp. 1089–1108, 2012.
- [4] H. Baghi, A. Oliveira, J. Valença, E. Cavaco, L. Neves, and E. Júlio, "Behavior of reinforced concrete frame with masonry infill wall subjected to vertical load," *Engineering Structures*, vol. 171, pp. 476–487, 2018.
- [5] L. Decanini, F. Mollaioli, A. Mura, and G. Rodolfo Saragoni, "Seismic performance of masonry infilled R/C frames," in *Proceedings of the 13th World Conference on Earthquake Engineering*, p. 165, Vancouver, Canada, August 2004.
- [6] M. N. Fardis and T. B. Panagiotakos, "Seismic design and response of bare and masonry-infilled reinforced concrete buildings. Part II: bare structures," *Journal of Earthquake Engineering*, vol. 1, no. 1, pp. 219–256, 1997.
- [7] A. B. Mehrabi, P. B. Shing, M. P. Schuller, and J. L. Noland, "Experimental evaluation of masonry-infilled RC frames," *Journal of Structural Engineering*, vol. 122, no. 3, pp. 228–237, 1996.
- [8] J. Yu, Y.-P. Gan, J. Wu, and H. Wu, "Effect of concrete masonry infill walls on progressive collapse performance of reinforced concrete infilled frames," *Engineering Structures*, vol. 191, pp. 179–193, 2019.
- [9] C. A. Syrmakizis and P. G. Asteris, "Influence of infilled walls with openings to the seismic response of plane frames," in *Proceedings of the 9th Canadian Masonry Symposium.*, Athens, Greece, 2001.
- [10] Y.-J. Chiou, J.-C. Tzeng, and Y.-W. Liou, "Experimental and analytical study of masonry infilled frames," *Journal of Structural Engineering*, vol. 125, no. 10, pp. 1109–1117, 1999.
- [11] A. A. Costa, M. A. Ferreira, and C. S. Oliveira, "O grande sismo de sichuan: impactos e lições para futuro," in *8o Congresso De Sismologia E Engenharia Sismica*, pp. 1–31, Porto, Portugal, 2010.
- [12] X. Romão, A. A. Costa, E. Paupério et al., "Field observations and interpretation of the structural performance of constructions after the 11 May 2011 Lorca earthquake," *Engineering Failure Analysis*, vol. 34, pp. 670–692, 2013.
- [13] V. Palieraki, C. Zeris, E. Vintzileou, and C.-E. Adami, "In-plane and out-of plane response of currently constructed masonry infills," *Engineering Structures*, vol. 177, pp. 103–116, 2018.
- [14] M. Donà, M. Minotto, E. Saler, G. Tecchio, and F. da Porto, "Combined in-plane and out-of-plane seismic effects on masonry infills in RC frames," *Ingegneria Sismica*, vol. 34, pp. 157–173, 2017.
- [15] Federal Emergency Management Agency, "Evaluation of earthquake damaged concrete and masonry wall buildings," in *FEMA 306, Applied Technology Council (ATC-43 Project)*, Federal Emergency Management Agency, Washington, DC, USA, 1998.

- [16] P. G. Asteris, D. J. Kakaletsis, C. Z. Chrysostomou, and E. E. Smyrou, "Failure modes of in-filled frames," *Electronic Journal of Structural Engineering*, vol. 11, pp. 11–20, 2011.
- [17] C. Z. Chrysostomou and P. G. Asteris, "On the in-plane properties and capacities of infilled frames," *Engineering Structures*, vol. 41, pp. 385–402, 2012.
- [18] M. A. Elgawady, P. Lestuzzi, and M. Badoux, "Rehabilitation of unreinforced brick masonry walls using composites," *Geotechnical and Geological Engineering*, vol. 1, pp. 413–422, 1986.
- [19] T. C. Triantafillou, "Strengthening of masonry structures using epoxy-bonded FRP laminates," *Journal of Structural Engineering*, vol. 2, pp. 104–111, 1998.
- [20] M. L. Albert, A. E. Elwi, and J. J. R. Cheng, "Strengthening of unreinforced masonry walls using FRPs," *Journal of Composites for Construction*, vol. 5, no. 2, pp. 76–84, 2001.
- [21] T. H. Almusallam and Y. A. Al-Salloum, "Behavior of FRP strengthened infill walls under in-plane seismic loading," *Journal of Composites for Construction*, vol. 11, no. 3, pp. 308–318, 2007.
- [22] F. Akhoundi, P. B. Lourenço, and G. Vasconcelos, *Numerical Modelling of Masonry-Infilled Reinforced Concrete Frames: Model Calibration and Parametric Study*, pp. 1–13, University of Minho, Braga, Portugal, 2014.
- [23] Y. Y. Kim, H. J. Kong, and V. C. Li, "Design of engineered cementitious composite suitable for wet-mixture shotcreting," *ACI Materials Journal*, vol. 100, no. 6, pp. 511–518, 2003.
- [24] M. A. Kyriakides and S. L. Billington, "Seismic retrofit of masonry-infilled non-ductile reinforced concrete frames using sprayable ductile fiber-reinforced cementitious composites," in *Proceedings of the 14 World Conference Earthquake Engineering*, Beijing, China, October 2008, <http://www.14wcee.org/Proceedings/14w7/main.htm>.
- [25] T. Triantafillou, "Innovative textile-based composites for strengthening and seismic retrofitting of concrete and masonry structures," in *Advances in FRP Composites in Civil Engineering*, Springer, Berlin, Germany, 2011, http://link.springer.com/chapter/10.1007/978-3-642-17487-2_1.
- [26] L. N. Koutas, Z. Tetta, D. A. Bournas, and T. C. Triantafillou, "Strengthening of concrete structures with textile reinforced mortars: state-of-the-art review," *Journal of Composites for Construction*, vol. 23, no. 1, Article ID 03118001, 2019.
- [27] B. Christos, "Comparative study of masonry infill walls retrofitted with TRM," Thesis Dissertation, University of Patras, Patras, Greece, 2005.
- [28] A. Prota, G. Marcari, G. Fabbrocino, G. Manfredi, and C. Aldea, "Experimental in-plane behavior of tuff masonry strengthened with cementitious matrix-grid composites," *Journal of Composites for Construction*, vol. 10, no. 3, pp. 223–233, 2006.
- [29] M. Harajli, H. Elkhatib, and J. T. San-Jose, "Static and cyclic out-of-plane response of masonry walls strengthened using textile-mortar system," *Journal of Materials in Civil Engineering*, vol. 22, no. 11, pp. 1171–1180, 2010.
- [30] F. Parisi, I. Iovinella, A. Balsamo, N. Augenti, and A. Prota, "In-plane behaviour of tuff masonry strengthened with inorganic matrix-grid composites," *Composites Part B: Engineering*, vol. 45, no. 1, pp. 1657–1666, 2013.
- [31] L. Koutas, S. N. Bousias, and T. C. Triantafillou, "Seismic strengthening of masonry-infilled RC frames with TRM: experimental study," *Journal of Composites for Construction*, vol. 19, no. 2, Article ID 04014048, 2015.
- [32] L. Koutas, S. N. Bousias, and T. C. Triantafillou, "Analytical modeling of masonry-infilled RC frames retrofitted with textile-reinforced mortar," *Journal of Composites for Construction*, vol. 19, no. 5, Article ID 04014082, 2014.
- [33] F. Akhoundi, P. B. Lourenço, and G. Vasconcelos, "Numerically based proposals for the stiffness and strength of masonry infills with openings in reinforced concrete frames," *Earthquake Engineering & Structural Dynamics*, vol. 45, no. 6, pp. 869–891, 2016.
- [34] C. G. Papanicolaou, T. C. Triantafillou, K. Karlos, and M. Papatthanasidou, "Textile-reinforced mortar (TRM) versus FRP as strengthening material of URM walls: in-plane cyclic loading," *Materials and Structures*, vol. 40, no. 10, pp. 1081–1097, 2007.
- [35] C. Papanicolaou, T. Triantafillou, and M. Lekka, "Externally bonded grids as strengthening and seismic retrofitting materials of masonry panels," *Construction and Building Materials*, vol. 25, no. 2, pp. 504–514, 2011.
- [36] E. Bernat, L. Gil, P. Roca, and C. Escrig, "Experimental and analytical study of TRM strengthened brickwork walls under eccentric compressive loading," *Construction and Building Materials*, vol. 44, pp. 35–47, 2013.
- [37] E. Bernat, C. Escrig, C. A. Aranha, and L. Gil, "Experimental assessment of Textile Reinforced Sprayed Mortar strengthening system for brickwork wallettes," *Construction and Building Materials*, vol. 50, pp. 226–236, 2014.
- [38] F. Akhoundi, G. Vasconcelos, P. Lourenço, L. M. Silva, F. Cunha, and R. Figueiro, "In-plane behavior of cavity masonry infills and strengthening with textile reinforced mortar," *Engineering Structures*, vol. 156, pp. 145–160, 2018.
- [39] F. Parisi, G. P. Lignola, N. Augenti, A. Prota, and G. Manfredi, "Nonlinear behavior of a masonry subassembly before and after strengthening with inorganic matrix-grid composites," *Journal of Composites for Construction*, vol. 15, no. 5, pp. 821–832, 2011.
- [40] S. Babaeidarabad, D. Arboleda, G. Loreto, and A. Nanni, "Shear strengthening of un-reinforced concrete masonry walls with fabric-reinforced-cementitious-matrix," *Construction and Building Materials*, vol. 65, pp. 243–253, 2014.
- [41] G. Milani and P. B. Lourenço, "Simple homogenized model for the nonlinear analysis of FRP-strengthened masonry structures. II: structural applications," *Journal of Engineering Mechanics*, vol. 139, no. 1, pp. 77–93, 2013.
- [42] B. Pantò, F. Cannizzaro, S. Caddemi, I. Calì, C. Chàcara, and P. Lourenço, "Nonlinear modelling of curved masonry structures after seismic retrofit through FRP reinforcing," *Buildings*, vol. 7, no. 4, pp. 79–17, 2017.
- [43] M. Basili, G. Marcari, and F. Vestroni, "Nonlinear analysis of masonry panels strengthened with textile reinforced mortar," *Engineering Structures*, vol. 113, pp. 245–258, 2016.
- [44] G. P. Lignola, A. Prota, and G. Manfredi, "Nonlinear analyses of tuff masonry walls strengthened with cementitious matrix-grid composites," *Journal of Composites for Construction*, vol. 13, no. 4, pp. 243–251, 2009.
- [45] X. Wang, B. Ghiassi, D. V. Oliveira, and C. C. Lam, "Modelling the nonlinear behaviour of masonry walls strengthened with textile reinforced mortars," *Engineering Structures*, vol. 134, pp. 11–24, 2017.
- [46] A. Fiore, F. Porco, D. Raffaele, and G. Uva, "About the influence of the infill panels over the collapse mechanisms activated under pushover analyses: two case studies," *Soil Dynamics and Earthquake Engineering*, vol. 39, pp. 11–22, 2012.
- [47] P. G. Asteris, L. Cavaleri, F. Di Trapani, and V. Sarhosis, "A macro-modelling approach for the analysis of infilled frame structures considering the effects of openings and vertical

- loads," *Structure and Infrastructure Engineering*, vol. 12, no. 5, pp. 551–566, 2016.
- [48] B. Pantò, I. Calìò, and P. B. Lourenço, "Seismic safety evaluation of reinforced concrete masonry infilled frames using macro modelling approach," *Bulletin of Earthquake Engineering*, vol. 15, no. 9, pp. 3871–3895, 2017.
- [49] P. B. Lourenço, *Computational Strategies for Masonry Structures*, Delft University of Technology, Delft, Netherlands, 1996.
- [50] F. J. Crisafulli, A. J. Carr, and R. Park, "Analytical modelling of infilled frame structures," *Bulletin of the New Zealand Society for Earthquake Engineering*, vol. 33, no. 1, pp. 30–47, 2000.
- [51] P. B. Lourenço, "Computations on historic masonry structures," *Progress in Structural Engineering and Materials*, vol. 4, no. 3, pp. 301–319, 2002.
- [52] A. Tzatzis and P. Asteris, "Finite element analysis of masonry structures: part I—review of previous work," in *Proceedings of the 9th Ninth North American Masonry Conference*, pp. 101–111, Clemson, SC, USA, June 2003.
- [53] P. G. Asteris, D. M. Cotsovos, C. Z. Chrysostomou, A. Mohebbkhah, and G. K. Al-Chaar, "Mathematical micro-modeling of infilled frames: state of the art," *Engineering Structures*, vol. 56, pp. 1905–1921, 2013.
- [54] P. B. K. Mbewe and G. P. A. G. Van Zijl, "A simplified non-linear structural analysis of reinforced concrete frames with masonry infill subjected to seismic loading," *Engineering Structures*, vol. 177, pp. 630–640, 2018.
- [55] S. V. Polyakov, "On the interaction between masonry filler walls and enclosing frame when loaded in the plane of the wall," in *Translation in Earthquake Engineering*, pp. 36–42, Earthquake Engineering Research Institute (EERI), San Francisco, CA, USA, 1960.
- [56] M. Holmes, "Steel frames with brickwork and concrete infilling," *Proceedings of the Institution of Civil Engineers*, vol. 19, no. 4, pp. 473–478, 1961.
- [57] B. Stafford-Smith, "Lateral stiffness of infilled frames," *Journal of the Structural Division*, vol. 88, no. 6, pp. 183–226, 1962.
- [58] R. J. Mainstone, *Supplementary Note on the Stiffness and Strength of Infilled Frames*, Building Research Station, Watford, UK, 1974.
- [59] M. Panagiotakos and M. N. Fardis, "Seismic response of infilled RC frame structures," in *Proceedings of the 11th World Conference on Earthquake Engineering*, Acapulco, Mexico, June 1996.
- [60] L. Macorini and B. A. Izzuddin, "A non-linear interface element for 3D mesoscale analysis of brick-masonry structures," *International Journal for Numerical Methods in Engineering*, vol. 85, no. 12, pp. 1885–1891, 2011.
- [61] S. Johnson, *Comparison of Nonlinear Finite Element Modeling Tools for Structural Concrete*, pp. 1–56, University of Illinois, Champaign, IL, USA, 2006.
- [62] K. Ho-Le, "Finite element mesh generation methods: a review and classification," *Computer-Aided Design*, vol. 20, no. 1, pp. 27–38, 1988.
- [63] J. Izumo Okamura and M. Kohichi, "Reinforced concrete plate element subjected to cyclic loading," *Journal of Composites for Construction*, pp. 575–590, 2016.
- [64] R. P. Prasad and K. Maekawa, "Path-dependent cyclic stress—strain relationship of reinforcing bar including buckling," *Engineering Structures*, vol. 24, no. 11, pp. 1383–1396, 2002.
- [65] Fib Model Code 2010 Vol. 1, 2010 247–278.
- [66] J. G. Rots, "Smearred and discrete representations of localized fracture," *Current Trends in Concrete Fracture Research*, vol. 51, pp. 45–59, 1991.
- [67] W. Yu, *Inelastic Modeling of Reinforcing Bars and Blind Analysis of the Benchmark Tests on Beam-Column Joints under Cyclic Loading*, Università degli Studi di Pavia, Pavia, Italy, 2006.
- [68] C. A. Filippou, N. C. Kyriakides, and C. Z. Chrysostomou, "Numerical modeling of masonry-infilled RC frame," *The Open Construction & Building Technology Journal*, vol. 13, no. 1, pp. 135–148, 2019.
- [69] G. Rots, DIANA Validation Report for Masonry Modelling, Netherlands, 2017.
- [70] P. B. Lourenço, P. De Borst, and J. G. Rots, "A plane stress softening plasticity model for orthotropic materials," *International Journal for Numerical Methods in Engineering*, vol. 40, no. 21, pp. 4033–4057, 1997.
- [71] P. B. Lourenço and J. G. Rots, "Multisurface interface model for analysis of masonry structures," *Journal of Engineering Mechanics*, vol. 123, no. 7, pp. 660–668, 1997.
- [72] C. Sandoval and O. Arnau, "Experimental characterization and detailed micro-modeling of multi-perforated clay brick masonry structural response," *Materials and Structures*, vol. 50, no. 1, 2017.
- [73] M. Dhanasekar, "The influence of brick masonry fill properties on the behavior of infilled frames," *Journal of Civil Engineering*, vol. 81, pp. 593–605, 1986.
- [74] P. B. Lourenço, J. G. Rots, and J. Blaauwendraad, "Continuum model for masonry: parameter estimation and validation," *Journal of Structural Engineering*, vol. 124, no. 6, pp. 642–652, 1998.
- [75] A. Drougkas, P. Roca, and C. Molins, "Numerical prediction of the behavior, strength and elasticity of masonry in compression," *Engineering Structures*, vol. 90, pp. 15–28, 2015.
- [76] C. Cur, *Structural Masonry: An Experimental/numerical Basis for Practical Design Rules*, Cur, Gouda, The Netherlands, 1994.
- [77] P. B. Lourenço and J. G. Rots, "Multisurface interface model for analysis of masonry structures," *Journal of Engineering Mechanics*, vol. 123, no. 7, pp. 660–668, 1997.
- [78] P. B. Lourenço, "A user/programmer guide for the micro-modelling of masonry structures," *TNO Building and Construction Research—Computational Mechanics*, 1996.
- [79] V. Sarhosis, K. Bagi, J. V. Lemos, and G. Milani, "Computational modeling of masonry structures using the discrete element method," *Advances in Civil and Industrial Engineering*, vol. 1, p. 505, 2016.
- [80] F. Jesse, *Load Bearing Behaviour of Filament Yarns in Cementitious Matrix*, vol. 39, IGI Global, Hershey, PA, USA, 2004.
- [81] J. G. Keer, "Behaviour of cracked fibre composites under limited cyclic loading," *International Journal of Cement Composites and Lightweight Concrete*, vol. 3, no. 3, pp. 179–186, 1981.
- [82] B. Mobasher, *Mechanics of Fiber and Textile Reinforced Cement Composites*, CRC press, Boca Raton, FL, USA, 2011.
- [83] F. Jesse, N. Will, M. Curbach, J. Hegger, Load-Bearing Behavior of Textile-Reinforced Concrete, 250, 2008, 59–68.
- [84] J. Hegger, N. Will, O. Bruckermann, and S. Voss, "Load-bearing behaviour and simulation of textile reinforced concrete," *Materials and Structures*, vol. 39, no. 8, pp. 765–776, 2006.
- [85] S. V. J. Hegger, "Textile reinforced concrete under biaxial loading," in *6th International RILEM Symposium on Fibre Reinforced Concretes*, pp. 1463–1472, RILEM Publications SARL, Guildford, UK, 2004.
- [86] F. Jesse, R. Ortlepp, and M. Curbach, "Tensile stress-strain behaviour of textile reinforced concrete," *IABSE Symposium Report*, vol. 86, no. 7, pp. 127–134, 2002.

- [87] M. Molter, *Zum Tragverhalten von textildbewehrtem Beton*, Ph.D. thesis, RWTH Aachen University, Aachen, Germany, 2005.
- [88] Voss S. A., Techn. Hochsch., Diss., Ingenieurmodelle zum Tragverhalten von textildbewehrtem Beton = Engineering models for the load-bearing behaviour of textile reinforced concrete, 2008.
- [89] J. L. Dawe and C. K. Seah, "Dawe and, Behaviour of masonry infilled steel frames," *Canadian Journal of Civil Engineering*, vol. 16, no. 6, pp. 865–876, 1989.
- [90] M. R. A. Kadir, *The structural behavior of masonry-iniflled panels in framed structures*, Ph.D. thesis, The University of Edinburgh, Edinburgh, Scotland, 1974.
- [91] T. C. Yong, "Shear strength of masonry panels in steel frames," M.S. thesis, New Brunswick Canada, Fredericton, Canada, 1984.
- [92] M. A. Nazief, *Finite element characterization of the behaviour of masonry infill shear walls with and without openings*, Ph.D. thesis, University of Alberta, Edmonton, Canada, 2014.
- [93] R. D. Flanagan and R. M. Bennett, "In-plane behavior of structural clay tile infilled frames," *Journal of Structural Engineering*, vol. 125, no. 6, pp. 590–599, 1999.
- [94] M. Teguh, "Experimental evaluation of masonry infill walls of RC frame buildings subjected to cyclic loads," *Procedia Engineering*, vol. 171, pp. 191–200, 2017.
- [95] X. Gao, A. Stavridis, V. Bolis, and M. Preti, "Experimental study on the seismic performance of non-ductile rc frames infilled with sliding frames infilled with sliding subpanels," in *Proceedings of the 11th U.S. National Conference on Earthquake Engineering*, Los Angeles, CA, USA, June 2018.
- [96] A. D. Dautaj, Q. Kadiri, and N. Kabashi, "Experimental study on the contribution of masonry infill in the behavior of RC frame under seismic loading," *Engineering Structures*, vol. 165, pp. 27–37, 2018.

Review Article

Recent Findings and Open Issues concerning the Seismic Behaviour of Masonry Infill Walls in RC Buildings

André Furtado ¹ and Maria Teresa de Risi²

¹CONSTRUCT-LESE, Faculdade de Engenharia da Universidade do Porto, Porto, Portugal

²Department of Structures for Engineering and Architecture, University of Naples Federico II, Via Claudio 21, 80125 Naples, Italy

Correspondence should be addressed to André Furtado; afurtado@fe.up.pt

Received 4 October 2019; Accepted 19 February 2020; Published 13 March 2020

Academic Editor: Chongchong Qi

Copyright © 2020 André Furtado and Maria Teresa de Risi. This is an open access article distributed under the Creative Commons Attribution License, which permits unrestricted use, distribution, and reproduction in any medium, provided the original work is properly cited.

The extension of the damages observed after the last major earthquakes shows that the seismic risk mitigation of infilled reinforced concrete structures is a paramount topic in seismic prone regions. In the assessment of existing structures and the design of new ones, the infill walls are considered as nonstructural elements by most of the seismic codes and, generally, comprehensive provisions for practitioners are missing. However, nowadays, it is well recognized by the community the importance of the infills in the seismic behaviour of the reinforced concrete structures. Accurate modelling strategies and appropriate seismic assessment methodologies are crucial to understand the behaviour of existing buildings and to develop efficient and appropriate mitigation measures to prevent high level of damages, casualties, and economic losses. The development of effective strengthening solutions to improve the infill seismic behaviour and proper analytical formulations that could help design engineers are still open issues, among others, on this topic. The main aim of this paper is to provide a state-of-the-art review concerning the typologies of damages observed in the last earthquakes where the causes and possible solutions are discussed. After that, a review of in-plane and out-of-plane testing campaigns from the literature on infilled reinforced concrete frames are presented as well as their relevant findings. The most common strengthening solutions to improve the seismic behaviour are presented, and some examples are discussed. Finally, a brief summary of the modelling strategies available in the literature is presented.

1. Introduction

The seismic vulnerability assessment of existing buildings that were not designed according to the recent and modern codes and the development of effective strengthening techniques are, nowadays, a paramount topic in the seismic engineering field. Over the last few years, it is visible a great interest regarding the study of the masonry infill walls and their influence in the response of reinforced concrete (RC) buildings when subjected to earthquakes, proved by the number of numerical and experimental studies available in the literature [1–4]. Their presence can be favorable or not for the seismic performance of the building, depending on several phenomena such as their plan and height distribution, existence or not of connection to the surrounding frame, boundary conditions, relative stiffness and strength

between the infill panel and the frame elements, and the infills' material and mechanical properties, among others.

Recent postearthquake survey damage assessment reports recognized that the infill masonry (IM) walls played an important role in the seismic response of the RC buildings [5–7]. The infill panels' seismic behaviour was also characterized by extensive level of damages and collapses, due to combined in-plane and out-of-plane loadings, as reported in [8, 9]. The collapse of many infill panels was responsible for several fatalities, direct and indirect economic losses [10, 11]. It is recognized that their in-plane (IP) behaviour affects with their out-of-plane (OOP) performance, since extensive damages caused by IP demands, such as the panel detachment, diagonal cracking, or shear failure, increase the infill panel OOP vulnerability [12, 13]. Different authors [1, 9, 14] reported that the masonry infill walls' OOP behaviour is

strongly affected by existence or not of connection between the panel and the reinforced concrete frame elements; existence or not of connection between leaves (in case of double-leaf infill walls); inadequate panel support width (very common constructive procedure adopted for thermal bridges' prevention); boundary conditions, panel slenderness, and inadequate execution of the upper bed joint; and lastly, the existence of previous damage. The infill panels' collapse can also result in plan and/or vertical irregularities, which can trigger global failure mechanisms such as torsion or soft storey.

Considering the number of experimental and numerical studies investigating the vulnerability issues of infilled RC frames, the missing of proper prescriptions by codes, and based on the well common masonry infill walls' presence in the RC buildings in the southern European countries, it is fundamental to carry out studies to characterize the seismic behaviour of these panels and to develop efficient strengthening strategies to improve their performance and prevent their collapse when subjected to earthquakes.

The present research work aims at presenting a global state-of-the-art review concerning the infilled RC frame seismic behaviour. First, a damage reconnaissance report from the last major earthquakes is presented. Observations of the RC structure performance during strong earthquakes represent a mean of teaching builders and engineers and proper and improper construction of earthquake load resisting systems. In regions that have long been inhabited, and which are subjected to relatively frequent strong ground shaking, design procedures have evolved, resulting in relatively good performance of engineered structures [15, 16]. Although such design procedures are not universally applicable because of regional differences in construction materials and techniques, structural engineers can learn much by studying such procedures. Additionally, the postearthquake damage reconnaissance highlighted the importance of the infill walls in the seismic performance of RC structures. Many authors pointed out that these elements (used to be called as "nonstructural") are very important and are responsible for a significant part of the human, material, and economic losses [7, 17].

Second, a deep state-of-the-art review of the experiments carried out on infilled RC frames is presented, where the major findings by each author are discussed. This section is very important to associate those findings with the damages observed in postearthquake scenarios. Finally, a brief presentation of modelling strategies of the masonry infill walls is provided, from the macromodelling approaches to micro-modelling approaches.

2. The Role of the Masonry Infill Walls in the Recent Seismic Events over the World

The RC structure behaviour depends on the strength and stiffness characteristics of the structural elements. The structural strength is provided by each of the structural members and by the interaction among them. Their response is controlled by the loading redistribution capacity that results in the failure of some members and/or in the

possibility of those members to be not able to suffer high levels of deformation demands until it fails. The insufficient strength capacity or incapacity of the structural elements to face seismic actions, which is several times higher than the value considered in the design process and results in shear loads higher than their strength capacity, is very common in existing low-standard buildings. The structures should be designed according to the seismic loading demand defined in the codes and to have stiffness, strength, and ductility balanced between the elements, joints, and supports. Similarly, the strength and stiffness contribution of the infill panels should be considered since these elements can significantly affect the whole structural behaviour.

This section aims at presenting the major learnings and findings concerning the typical damages from the last major earthquake in the Mediterranean area. They are presented and discussed, and a particular focus is dedicated to the masonry infill wall seismic behaviour and participation in the structural response.

2.1. Damage Typology Definition in Infilled RC Structures.

The Eurocode 8 [18] classifies the building elements as structural or nonstructural. Concerning the structural elements, they are subdivided into primary members (SP) and secondary members (SS). The primary members (SP) are considered as part of the structural system that resists to the seismic demands, modelled in the analysis for the seismic design situation, and fully designed and detailed for earthquake resistance. On the other hand, the secondary elements are members which are not considered as part of the seismic action resisting system and whose strength and stiffness against seismic actions are neglected; they are not required to comply with all the capacity design rules according to Eurocode 8 [18], but are designed and detailed to support gravity loads when subjected to the displacements caused by the seismic design condition. Last, nonstructural elements (NS) comprising architectural, mechanical, or electrical elements, systems, and components, whether due to lack of strength or to the way they are connected to the structure, are not considered in the seismic design as load carrying elements.

During the last major earthquakes all over the world, different types of damages, being the most representative ones listed above, affected the RC structures according to several authors and postearthquake survey damage assessments [5–8, 19]:

Damage Type 1: damages associated with stirrups and hoops (inadequate quantity and detailing, regarding the required ductility)

Damage Type 2: damages associated with detailing (bond, anchorage, and bond splitting)

Damage Type 3: damages associated with shear and flexural capacity of beam/column/wall elements

Damage Type 4: damages associated with the inadequate shear capacity of RC joints

Damage Type 5: damages associated with strong-beam weak-column mechanism

Damage Type 6: damages associated with short-column mechanism

Damage Type 7: damages associated with structural irregularities (in plan and/or in elevation: torsion, “weak storey,” and “soft storey”)

Damage Type 8: damages associated with pounding

Damage Type 9: damages in secondary elements (cantilevers, stair, etc.)

Damage Type 10: damages in nonstructural elements.

From the list, the first eight damages are related to primary members (SP), the ninth is related to secondary elements (SP), and finally, the tenth is related to nonstructural elements (SS). According to the after-earthquake damage survey assessment, it was concluded that there is an interaction among the last five types of damages. This interaction is related to the contribution/participation of the nonstructural elements or secondary elements in the global response of the infilled RC structure [20]. The existence of buildings with different (in plan or vertical) irregularities results in different responses than those expected; part of them are related to the disposition of the nonstructural elements [21]. Damages observed in postearthquake field missions highlighted that masonry infills, the main core of this work, cannot be generally regarded as nonstructural or secondary elements, as better discussed in Section 2.2, but should be considered as primary members, especially if they were built in full contact with the surrounding frame.

2.2. Most Common Damages in Masonry Infill Walls in Recent Earthquakes. Infills represent the external skin of the RC structures; they are generally used as interior partitions and to separate the inner spaces for the outside with constructive techniques that strongly depend on the construction practice typical of each country (double- or single-leaf infill, connection system between infill panel and surrounding frame, workmanship, etc.). This aspect can introduce a significant heterogeneity in the influence of the infills on the RC building seismic performance. Nevertheless, some similarities in the main vulnerability issues can be identified and observed in postearthquake reconnaissance field missions, especially if the more recent seismic events in the Mediterranean area are considered. The presence of infill panels generally leads to an increase of the IP lateral stiffness and strength, at least at low displacement demand, and a beneficial increase of the dissipated energy during a ground motion. Under higher displacement demand, infill panels, above all traditional (slender) panels, generally reduce their contribution to the lateral load and stiffness, thus producing a strength drop in the global lateral response of the whole infilled frame [22]. Some significant detrimental effects can be induced by the infill panels, certainly affecting the damage limitation performance level, but also potentially dangerous for the life safety, as discussed in the following remarks.

As well known, due to horizontal action parallel to their plane, infill panels generally exhibit a diagonal damage pattern, as shown in Figure 1. Such damage can be more or less diffused across the building and generally concentrated

at the lowest floors, where the relative displacement demand is generally higher. Such kind of damage is the clear evidence of the cooperation of infills in the seismic response of the building, so that their typical definition of “nonstructural” components can be considered as not appropriate. Additionally, as anticipated above, this damage, which is often particularly severe also under quite moderate seismic shaking, considerably affects the economic seismic losses for RC buildings [17], in terms of repair costs, downtime, and casualties, thus reducing the seismic resilience of the communities in seismic prone areas.

A structural irregularity can be induced by a nonuniform distribution of the infill panel along the height. As a matter of fact, due to severe seismic actions, a soft-storey collapse mechanism can be induced by the (quite common) absence of panels at the ground floor (see, for example, Figure 2(a)). Another kind of “irregularity” is the presence of frames with ribbon windows that are only partially infilled: such a situation generates very squat columns, which are extremely vulnerable to shear failures (see, for example, Figure 2(b)). These vulnerability issues clearly assume a crucial role since they are related to the life-safety performance level.

One of the big problems for life-safety purposes due to the infills is their OOP collapses (or overturning), which can be produced by the absence of proper connection systems between the “nonstructural” panel and the RC frame, as typical in existing buildings. In these cases, the problem becomes also more severe due to the typical high slenderness of the infills in existing buildings, generally realised in two (not properly connected to each other) leaves. As a result, the overturning of the infills is generally observed in post-earthquake field missions, as shown in Figure 3, enhanced by the combination between the damage due to in-plane actions and the transverse acceleration demand during a seismic event [6, 7].

A further issue affecting the life-safety performance level concerns the local shear interaction between the infill panels and the surrounding RC members. As well known, due to horizontal actions, an infill panel locally produces a shear action on the surrounding RC columns/beams concentrated in a squat portion of the RC member [26]. Such an action can lead to the shear failure of the RC structural members, especially in existing buildings, not designed according to capacity design principals, thus affecting the integrity and safety level of the whole building. Some examples of local shear interaction, from L’Aquila (Italy) 2009 [24] and Lorca (Spain) 2011 [7] earthquakes, are reported in Figure 4.

3. Literature Review on Recent Developments on Experimental Testing of Infilled RC Frames

The postearthquake damage analyses reported in the previous section highlight that a comprehensive knowledge of all the vulnerability aspects related to the seismic behaviour of infilled framed structures, of their nonstructural components, and of the phenomena related to the interaction between structural and “nonstructural” elements is

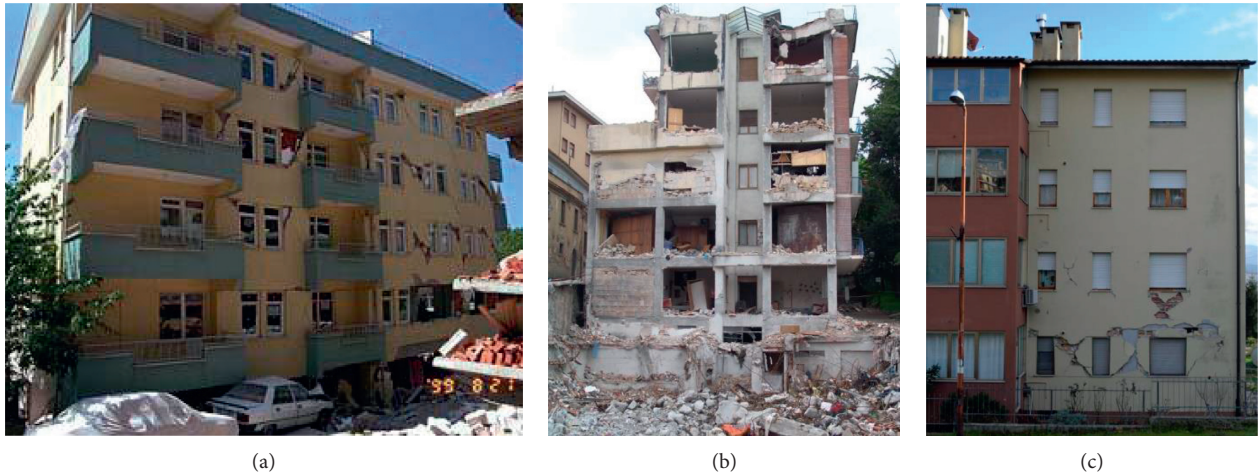


FIGURE 1: Example of medium-severe in-plane damage to infills (adapted from [23]). (a) Izmit (1999). (b) L'Aquila (2009). (c) Centre Italy (2016).

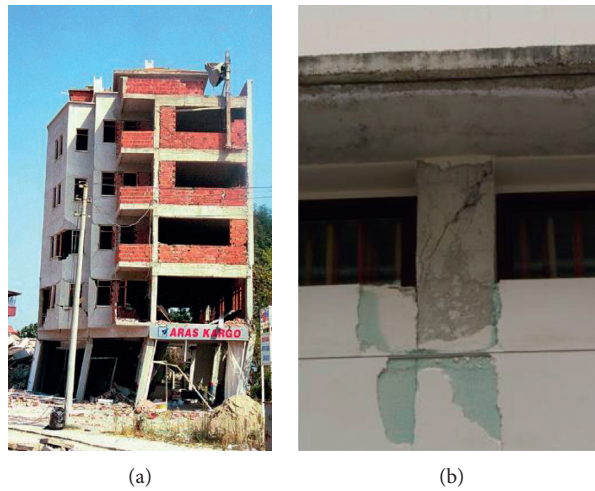


FIGURE 2: Example of structural irregularities induced by the infill panel (adapted from [7, 23]). (a) Izmit (1999). (b) Lorca (2011).

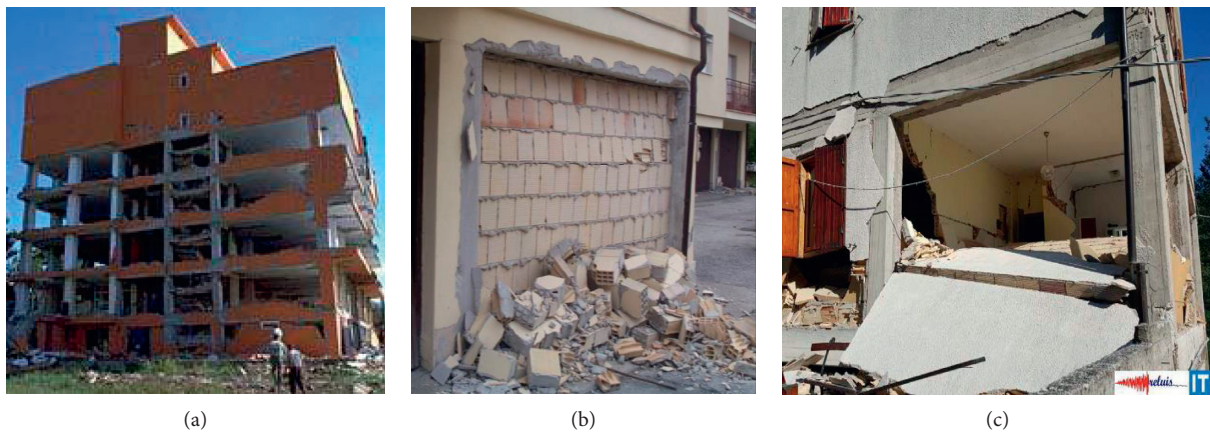


FIGURE 3: Example of out-of-plane collapses (adapted from [23–25]). (a) Izmit (1999). (b) L'Aquila (2009). (c) Centre Italy (2016).



FIGURE 4: Example of in-plane shear interaction between infill panels and RC frames adapted from [7, 24]. (a) L'Aquila (2009). (b) L'Aquila (2009). (c) Lorca (2011).

necessary. To this aim, the experimental testing allows understanding and characterizing the structural behaviour of given elements under different loading conditions reproducing the damage due to real earthquakes in lab. This is a key point to achieve the knowledge that is necessary to improve the codes with the capability of designing safer structures and with lower risk. Different types of experiments can be found over the literature concerning the infilled RC structures, which can be classified in in-plane (loading acting in the infill plane) and the out-of-plane (loading acting perpendicularly to the infill plane) testing of masonry infill walls. Section 3.1 presents a literature review about the in-plane (IP) tests, and Section 3.2 presents the out-of-plane (OOP) testing review and, lastly, a revision of strengthening techniques is presented in Section 3.3.

3.1. In-Plane Tests. Numerous tests have been performed in the literature to study the behaviour of infilled RC frames under in-plane actions in the last sixty years (see Table 1). Each experimental campaign investigated the influence of the infill panel on the lateral response of the whole frame depending on the brick typology (e.g., hollow or solid clay bricks, concrete or autoclaved aerated concrete (AAC) blocks, or other material typologies), on the infill-to-frame relative stiffness and strength, and on the presence of openings with different opening ratios and eccentricities, among other investigated parameters. Tested specimens were generally one-bay one-storey scaled infilled frames (e.g., [13, 34, 58] among many others—see Table 1). More rarely two- or three-storey frames (e.g., [29, 64]) or full-scale infilled frames [33, 40, 49] were tested in lab. Different typologies of test have been performed, by means of the application of monotonic or cyclic actions and pseudostatic or pseudodynamic actions or, more rarely, by means of shake table tests. Overall, about two hundred tests performed on RC frames with various typologies of infills can be collected from the literature [4, 65–67]. The main findings of these experimental campaigns on unreinforced masonry infills under in-plane actions are discussed in what follows.

A complete list of these campaigns can be found in Table 1 for infilled without openings (i.e., doors or windows).

For these tests, the experimentally observed failure mode has been different depending on the main geometrical and mechanical features of infills and frames. More in detail, the failure modes, specifically related to the infill panel, can be classified as follows [68]: (i) sliding shear failure, characterized by the horizontal sliding along mortar bed joints—typical in weak mortar infills and strong frame; (ii) diagonal cracking failure, characterized by cracks along the infill diagonals—typical of weak frame infilled with a strong infill; (iii) diagonal compression failure, characterized by the infill crushing in the centre of the panel—typical of slender infills; and (iv) corner crushing failure, characterized by the infill crushing in the corners—typical of weak masonry infills and frames with weak joints and strong members.

Although the significant heterogeneity of the tests is due to their differences in mechanical properties or material brick units (see Table 1), some general conclusions can be carried out.

From a phenomenological point of view, the evolution of damage affecting the infill panel under increasing in-plane lateral load goes from a hairline cracking along mortar bed joints or in bricks (“Slight Damage”), to more severe diagonal cracking and bricks crushing, often in the corners (“Moderate Damage”), until the complete “Collapse” of the panel [69], as shown in Figure 5. Starting from the analysis of the in-plane collected tests, the displacement capacity thresholds of the infills can be obtained for given Damage States (DS), from Slight Damage to Collapse, depending on their material typology, as recognized in Del Gaudio et al. [10]. It was found that, for infills with clay bricks, the median interstorey drift capacity is equal to 0.08%, 0.33%, and 1.6%, respectively, at Slight Damage level, at Moderate Damage, and at Collapse. Infills with concrete blocks showed a higher median drift capacity with respect to the infills with clay bricks, whereas, generally, a smaller drift capacity characterized infills with solid clay bricks with respect to infills with hollow clay bricks at more severe DSs [10].

TABLE 1: Literature review of IP experimental tests of infill walls depending on infill material typology: subset of tests on 1-bay 1-storey frames infilled without opening (adapted from [4]).

Author	Number of tests	Masonry unit	Scale factor
Aly and Mooty [27]	2	Solid clay unit	1:2
Akhoundi et al. [28]	1	Hollow clay unit	1:2
Al-Chaar et al. [29]	2	Solid clay unit-solid concrete unit	1:2
Angel et al. [13]	7	Solid clay unit-solid concrete unit	1:2
Baran and Sevil [30]	3	Hollow clay unit	1:3
Basha and Kaushik [31]	4	Solid fly ash unit	1:2
Bergami and Nuti [32]	2	Hollow clay unit	1:2
Calvi and Bolognini [33]	2	Hollow clay unit	1:1
Cavaleri and Di Trapani [34]	12	Hollow clay or concrete unit-solid calcarenite unit	1:2
Centeno et al. [35]	1	Hollow concrete unit	1:2
Chiou and Hwang [36]	2	Solid clay unit	1:1
Colangelo [37]	11	Hollow clay unit	1:2
Combesure and Pegon [38]	4	Hollow clay unit	2:3
Gazic and Sigmund [39]	10	Hollow clay unit-solid clay unit	1:2
Guidi et al. [40]	2	Hollow clay unit	1:1
Haider [41]	3	Hollow clay unit	1:1
Hashemi and Mosalam [42]	1	Solid clay unit	1:1
Kakaletsis and Karayannis [26]	2	Hollow clay unit-vitrified clay unit	1:3
Khoshnoud and Marsono [43]	1	Solid clay unit	1:4
Kyriakides and Billington [44]	1	Solid clay unit	1:5
Lafuente and Molina [45]	10	Solid clay unit	1:3
Mansouri et al. [46]	1	Solid clay unit	1:2
Mehrabi et al. [47]	11	Solid or hollow concrete unit	1:2
Misir et al. [48]	4	Hollow clay unit-solid AAC unit-hollow pomice unit	4:5
Morandi et al. [49]	1	Hollow clay unit	1:1
Parducci and Checchi [50]	6	Hollow clay unit	1:2
Pereira et al. [51]	1	Hollow clay unit	2:3
Pires [52]	6	Hollow clay unit	2:3
Schwarz et al. [53]	5	Solid AAC unit	1:2
Sigmund and Penava [54]	1	Hollow clay unit	1:2
Shing et al. [55]	1	Solid clay unit	2:3
Stylianidis [56]	11	Hollow clay unit	1:3
Suzuki et al. [57]	2	Hollow concrete unit	1:4
Verderame et al. [58]	2	Hollow clay unit	1:2
Waly [59]	2	Hollow clay unit	1:2
Yuksel and Teymur [60]	1	Hollow clay unit	1:2
Zarnic and Tomažević [61]	1	Semisolid clay unit	1:3
Zhai et al. [62]	1	Hollow concrete unit	1:1
Zovkic et al. [63]	3	Hollow clay unit-solid AAC unit	1:2

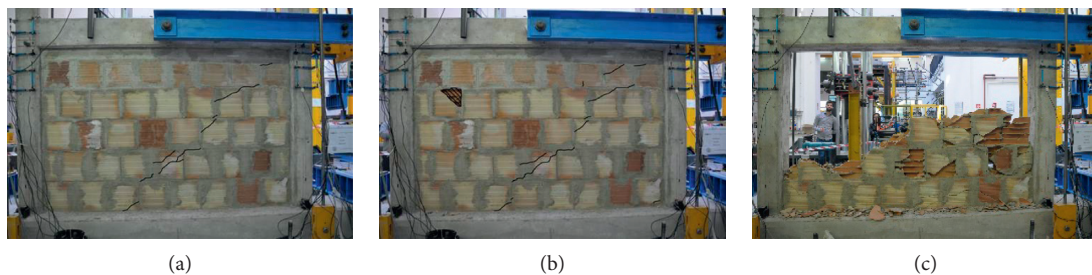


FIGURE 5: Example of damage evolution (adapted form De Risi et al. (2018)). (a) Slight. (b) Moderate. (c) Collapse.

Concerning the lateral response of the infilled frame, the analysed experimental responses for RC frames where the infill is well connected to the frame, under increasing lateral in-plane loading, generally showed an initial detachment of

the infill panel from the frame, until the born of a diagonal compressive stress flow—often reproduced in numerical analyses by means of one single- or multistrut (only resisting to compressive) [70], as better explained in Section 4. A high

initial stiffness until first cracking occurrence is generally observed, depending on the in-plane stiffness (thickness and material) of the infill panel. After the first macrocracking, a subsequent lateral stiffness degradation generally occurred up to the peak load. After the achievement of the maximum in-plane load, a degrading branch can be easily recognized until the residual strength of the frame, when the infill panel is no more able to contribute in terms of strength and stiffness [4]. The in-plane response and particularly the peak load and the subsequent softening branch were found to be dependent on the failure mode of the panel. Additionally, a significant portion of the experimental results indicated that, at least for one-bay one-storey frames under in-plane actions, (i) the presence of the infills can improve the lateral strength, stiffness, ductility, and energy dissipation capacity with respect to bare frames, and (ii) specimens with strong infills can exhibit a higher strength, stiffness, and energy dissipation capacity than those with weak infills [26].

Nevertheless, the estimation of the lateral load of the infill is important to define the shear action produced by the panel on the surrounding structural members. During the in-plane testing on infilled frames, some tests exhibited a shear failure in beams or columns due to their interaction with the infill panel. The analysis of the experimental campaigns revealed that such phenomenon, often observed also after seismic events as described in Section 2, was more likely for specimens with infills relatively strong with respect to the frame [68], as typical when the former is made up of strong concrete blocks or solid clay bricks and the latter is representative of existing low-standard buildings. Unfortunately, very few experimental studies [58, 71] are available from the literature to reproduce the local shear interaction between infill and frame, even less if masonry panels made of hollow clay units (typical of light nonstructural masonry in European and Mediterranean countries) are considered. More experimental tests on these units should be carried out to provide a useful support for a comparison with more or less simplified nonlinear modelling approaches [58], from FEM-based micromodelling to macromodelling, and the choice/proposal of a proper modelling tool.

Additionally, few tests exist in the literature about the study of the in-plane behaviour of infills with openings, taking into account their possible differences in void ratio, aspect ratio, or eccentricity (e.g., [26, 38, 54], among others). As expected, the presence of openings leads to a reduction in infill lateral strength and stiffness and energy dissipation capacity, mainly depending on the opening size [26]. Nevertheless, openings with an opening percentage (i.e., opening area divided by the whole frame area) lower than 40% can improve the lateral strength, stiffness, and energy dissipation capacity under in-plane actions with respect to bare frames [4, 25]. More frequently, the presence of openings is investigated only numerically (e.g., [2], among others), and therefore, additional real data should be provided by further experimental campaigns to be compared with the numerical results.

A higher number of experimental results should be still produced also to investigate about the effect of the level of restraint between the panel and the surrounding frame,

which can be strictly dependent on the construction practice adopted country by country, and which can strongly affect the in-plane response of the whole frame (as recently carried out by [72, 73]). Lastly, quite few tests from the literature studied the in-plane behaviour of infilled frame considering all the above-mentioned critical issues by means of shake table tests (as in [42]; or [74], one of the most recent study). It should be desirable to carry out new and further data from shake table tests to more realistically reproduce the ground shaking for the investigation of the seismic response of infilled frames.

3.2. Out-of-Plane Tests. Over the literature, few testing campaigns can be found where it was carried out the study and characterization of the OOP behaviour of infill panels in steel or RC frames, considering or disregarding their interaction with the IP loading demand [13, 33, 51, 75–86]. Part of these testing campaigns were based on shaking table tests of single IM panels or scaled infilled RC structures [87–94].

Dawe and Seah [76] started in 1989 the study of the OOP seismic behaviour of masonry infill walls surrounded by a steel frame. The authors performed eight full-scale infill panels made with concrete blocks. The loading on the wall was transferred with a system of airbags against a reaction frame, uniformly inflating to impose a displacement history. The objectives were to study the horizontal connections with reinforcement, other with mortar interface of infill frame, the influence of the wall's thickness, openings, among other parameters. Some of the conclusions were as follows: (1) the interface's reinforcement provided higher OOP deformation capacity of the system, (2) interface reinforcement sustained more OOP loading before appearance of the first crack, (3) higher thickness allowed the limitation of OOP arch mechanism, resulting in stronger loadings for collapse, (4) the opening did not reduce significantly the OOP capacity, and (5) the connections with reinforcement are introducing stress concentrations when connectors transmit in-plane loads. This causes premature damage to the infill, which reduces the infill's out-of-plane capacity. Thereafter, Frederiksen [95] tested fifteen scaled infill panels surrounded by steel frames under OOP loading using an airbag. Three types of brick were used in their experiment, and the main objective was to study the effect of infill-to-frame boundary condition by placing different materials in gaps between the infill and the frame at all boundaries instead of mortar. They concluded that the effect of bound type on the OOP strength and cracking pattern is negligible so long as the infill is in tight contact with the bounding frame. Angel et al. [13] performed thirteen full-scale infill walls made with concrete blocks and with brick masonry walls. They tested the combination of IP-OOP loading sequence. The OOP forces were applied with an airbag system following monotonic loading protocol. Some of the conclusions were as follows: (1) the OOP strength was affected by the thickness of the wall and by the compressive strength of the masonry, and (2) IP loading increased the OOP secant stiffness. Calvi and Bolognini [33] performed a set of tests in full-scaled RC frames infilled with

brick masonry. The tests were analysed for monotonic OOP loading after application of cyclic IP loading to introduce prior damage on the walls. The used systems were bare frame, unreinforced infills, horizontally reinforced, and reinforced with meshes. The authors concluded that the OOP behaviour was strongly improved by the reinforcement material.

Later, Lunn and Rizkalla [96] performed an experimental campaign comprising 14 full-scale specimens, four as-built specimens (reference specimens) and 10 strengthened specimens. The main aim of this study was to assess the efficiency of different strengthening strategies to improve the OOP behaviour. Varela-Rivera et al. [97] tested six confined walls made with vertical hollow concrete blocks to assess the effect of the boundary conditions in which the authors found that the panels with four and three supports reached similar maximum strength. Pereira et al. [51] carried out a testing campaign of scaled infill panels subjected to uniform OOP loadings applied by airbags to assess the effect of plaster and bed joint reinforcement. From the results, the authors concluded that the bed joint reinforcement provided higher strength and deformation capacity to the panel; however, it is not relevant when subjected to IP loading demands. Guidi et al. [98] developed an experimental campaign comprised of six panels with different thicknesses (large and thick) and tested with textile-reinforced mortar technique to assess the improvement of the OOP behaviour. Hak et al. [82] studied the OOP behaviour of strong infill panels in the context of the modern construction in the southern European countries. da Porto et al. [83] tested the efficiency of strengthening mortars to improve the seismic behaviour of infill panels subjected to IP and OOP loading sequence. Moreno-Herrera et al. [99] tested the influence of the masonry unit and aspect ratio on the OOP capacity of confined infill walls, from which it was concluded that (1) the maximum OOP displacements were larger for walls built with solid bricks; (2) the OOP strength depends highly on the masonry compressive strength; and (3) the OOP capacity decreases with the increase of the panel aspect ratio.

Recently, Akhoundi et al. [100] tested three scaled infill panels made with hollow clay horizontal bricks to study the effect of the workmanship and the effect of a central opening (window). From the results, the authors pointed out a variation of about 30% related to the workmanship and a reduction of the panel OOP strength and deformation capacity due to the opening.

Furtado et al. [84] studied the effect of the gravity load and the previous damage due to prior IP test and concluded that the gravity load modifies the cracking pattern and the previous damage (0.5% IP drift) reduced the OOP strength capacity of about 70% and the panel behaved as a rigid body. Later, the authors [101] studied the effect of the panel width support condition in which it was observed a reduction of the panel OOP strength capacity of about 60%.

Di Domenico et al. [14] carried out an experimental campaign comprised of three infill panels made with hollow clay bricks, with the same geometrical properties, construction materials, and workmanship. The major goal was to assess the effect of adopting different boundary conditions

to the confining RC frames; namely, it was tested a panel bounded along all edges to the surrounding frame (specimen OOP_4E), a panel detached from the confining frame at the upper edge (specimen OOP_3E), and a panel bounded to the confining frame only along the upper and lower edges (specimen OOP_2E). The authors concluded that the panel OOP_2E exhibited brittle failure and the remaining ones some displacement capacity for arching mechanism. Concerning the maximum strength, the panel with all edges bounded (OOP_4E) reached 1.6 times higher strength and the specimen OOP_3E reached 1.3 times higher strength than the value obtained by the panel OOP_2E.

Ricci et al. [12] performed OOP tests in scaled infill panels previously damaged due to quasistatic IP tests. Three different levels of prior IP drift were adopted, namely, 0.16% (IP + OOP_L), 0.37% (IP + OOP_M), and 0.58% (IP + OOP_H). Additionally, the results were compared with the one reference specimen OOP_4E (with no prior damage) that was tested by Di Domenico et al. [14] and described in the previous paragraph. The authors concluded that all the specimens reached an almost bilinear response behaviour with a pseudolinear response up to peak load and a softening branch after the maximum load. As expected, the specimens with medium-high in-plane damage exhibited lower strength capacity and lower stiffness. In fact, larger IP drift demands caused higher reduction of the panel OOP capacity.

Later, Ricci et al. [102] investigated the influence of the panel slenderness ratio and of the in-plane/out-of-plane interaction on the out-of-plane strength. To this aim, the authors tested three specimens with the slenderness ratio of 22.9 and compared with the results obtained by panels with the lower slenderness ratio of 15.2, tested in a previous testing campaign [12, 14]. From the results, the panels with the slenderness ratio of 22.9 reached larger peak loads (twice the results of the panels with slenderness ratio of 15.2). This result indicates that panels with larger slenderness ratio potentiate the development of arching mechanism, which can increase the panel OOP strength capacity. However, further experimental investigations must be developed to reinforce the conclusions and results obtained in this testing campaign. Finally, it was again observed the reduction of the OOP strength capacity with larger IP drift demands.

Lastly, De Risi et al. [71] carried out an experimental campaign on square infill walls in RC frames to investigate about the OOP behaviour of the masonry infills and about the IP/OOP interaction. Overall, four specimens were tested under OOP monotonic load. Three of them were firstly damaged due to cyclic IP actions, with different levels of demand. The remaining one was only subjected to OOP loading and thus was considered as reference specimen. The main purpose of the testing campaign was to assess the influence of the infill panel aspect ratio on the IP/OOP interaction through the comparison between the tests performed in this campaign and tests performed in the campaigns carried out by Ricci [12, 14] with nominally identical infills except that for the aspect ratio of the specimens. The authors concluded that, from the comparison between the square panels and the rectangular ones, it was observed that,

at roughly same drift demand, square and rectangular infills exhibit very different damage states, namely, the rectangular specimens reached higher levels of damage than the square ones. Obviously, at the same time, it was observed that, for the same IP drift, the square panels exhibited a strength reduction of 24% while the rectangular panel exhibited larger degradation of about 58%. A complete list of these campaigns can be found in Table 2 containing the variables under study, number of tests, loading approach, and masonry unit.

Recently, Butenweg et al. [103] carried out an experimental campaign of combined IP-OOP tests in full-scale RC frames filled with high thermal insulating clay brick. The main novelty of this experimental investigation is the simultaneous application of the IP and OOP loadings. From the testing campaign, the authors pointed out that boundary condition in the connection area between the infill panel and the frame is a crucial point for earthquake damage of the infill walls.

3.3. Retrofit and Strengthening Techniques. The retrofit and improvement of infill walls seismic behaviour is a complex subject, since it cannot be disconnected from their effect on the overall building response. It is paramount to take this coupled behaviour into consideration. In this context, two main approaches can be considered, as described below: (i) disconnection of infills from the structural system and (ii) effective integration in the superstructure and strengthening of the panel.

3.3.1. Disconnection of the Panel from the Structural System. Concerning this first assumption, three different strategies can be adopted: the use of sliding devices, energy dissipation devices, and assuming a disconnection using gap. From the literature, it is possible to find out that some authors tested the use of sliding devices to reach a good seismic performance of the panel. For example, Mohammadi et al. [104] carried out an experimental campaign to achieve engineered infilled frames in two stages. One of the techniques used on Stage 1 was the use of an infill “fuse,” in which some sliding layers were provided in the infill. In these techniques, some elements such as small parts of the columns or horizontal layers in infills (called “fuses”) are supposed to yield or slide before infill cracking. Two 2/3 scaled, 3 m-long and 2 m-high single-story single-bay infilled steel frames having an IPE-140 standard shape were tested under cyclic lateral in-plane loading. The specimens were used to check the efficiency of the mentioned technique in increasing ductility. The authors found in a previous experimental work that multilayer infill panels, composed of layers of masonry and concrete materials, are acceptable to be used in engineered infilled frames, as they have a better ductility in comparison with the single-layer ones, and their strength can be adjusted by changing the layer thickness and material [105]. The author concluded that supplying the infills with sliding fuses had the following advantages: (1) increasing the deformation capacity and consequently the ductility of the infilled frame; (2) avoid necking in cyclic load-displacement behaviour for

nonfused specimens; (3) preventing the panel from the occurrence of damage/cracking during seismic actions; and (4) high efficiency of the sliding fuse in increasing ductility of the infilled frames. Despite the advantages of the sliding fuse, simple configuration of the applied sliding fuse had two main shortcomings: (1) increasing the vulnerability of shear failure in some column zones and (2) creating a potential surface for OOP movement of the wall in the fuse area.

Two further testing campaigns were performed by Preti et al. [106] focused on the development of a similar engineered solution with sliding joints to reduce the infill-frame interaction and ensure OOP stability. The authors validated the potential of horizontal partition joints (embedded in few masonry mortar beds and acting as sliding joints) to ensure a ductile mechanism for the infill under IP loading; during the tests, it was prevented the development of the typical diagonal strut mechanism. Two additional works developed by Morandi et al. [107] and Verlatto et al. [108] can be found in the literature.

Some authors proposed solutions composed of energy dissipation devices that consist of the disconnection between the panel and the frame structure. Goodno et al. [109] proposed design criteria formulated in terms of energy, which provide optimal balance of stiffness and energy dissipation to the structure through appropriate cladding connection. Aliaari and Memari [110] tested a seismic IM wall isolator from the main envelope structure (SIWIS). The solution consisted in using subframes to be attached to the structural frame, and the infill wall then was constructed within the subframe. The OOP stability of the panel was provided through the top subframe member. The authors stated that the location of SIWIS elements showed that due to the fact of being located at the top of the wall, the frame will first contact the panel at that point under lateral drift and will tend to close the gap if there were no SIWIS elements. Later, Aliaari and Memari [111] carried out an IP test of a two-bay three-story steel frame with three different configurations: (i) bare frame, (ii) infilled braced frame, and (iii) pinned frame equipped with the proposed SIWIS device. The authors also tested a series of components on three different designs for the fuse element. From the tests, the authors pointed out that the response of the frame with SIWIS elements was significantly affected by the stiffness and strength properties of the SIWIS elements.

Finally, seismically active countries such as New Zealand, Japan, and some states in the USA adopted the practice of separating the infill walls from their frames by including a gap. This strategy was based on the poor seismic performance of the infill panels in past events. Additionally, the seismic design codes required that nonstructural elements are not damaged during earthquakes with low magnitude and do not affect the structural performance of the main structure in events with large magnitude. Due to that, the separation between the panel and the frame became the most common practice [112]. Separation gaps allow the frame to deflect freely without mobilizing the wall. However, this approach can result in serious consequences when the panel is subjected to some OOP loadings. Some approaches have been presented by different authors aiming to be effective for both IP and OOP loadings [107, 108, 113, 114].

TABLE 2: Literature review of OOP experimental tests of masonry infill walls.

Author	Number of tests	Loading approach	Masonry unit	Variables under study
Dawe and Seah [76]	8	Airbags	VHCB	Horizontal connections with reinforcement Slenderness Openings Boundary conditions
Frederiksen [95]	15	Airbags	HCHB SCB	Boundary conditions
Angel et al. [13]	13	Airbags	HCHB VHCB	Masonry unit IP + OOP IP + OOP
Calvi and Bolognini [33]	9	Airbags	HCHB	Bed joint reinforcement Meshes
Lunn and Rizkalla [96]	14	Airbags	CSB	Strengthening strategies
Varela-Rivera et al. [97]	6	Airbags	VHCB	Boundary condition
Pereira et al. [51]	7	Airbags	HCHB	Bed joint reinforcement Plaster
Guidi et al. [98]	6	4 points load	HCHB	Slenderness Strengthening strategies
Hak et al. [82]	5	4 points load	VCHB	Strong infills
da Porto et al. [83]	8	4 points load	HCHB VHCB	Strengthening mortars
Moreno-Herrera et al. [99]	8	Airbags	SCB VCHB	Masonry unit Aspect ratio
Akhoundi et al. [100]	3	Airbags	HCHB	Workmanship Opening
Furtado et al. [84]	3	Airbags	HCHB	Gravity load IP-OOP
Furtado et al. [101]	2	Airbags	HCHB	Panel width support Gravity load
Di Domenico et al. [14]	3	4 points load	HCHB	Boundary conditions
Ricci et al. [12]	3	4 points load	HCHB	IP-OOP
Ricci et al. [102]	3	4 points load	HCHB	IP-OOP Slenderness
De Risi et al. [71]	4	4 points load	HCHB	Aspect ratio
Butenweg et al. [103]	4	Airbag	VHCB	IP-OOP

VHCB: vertical hollow concrete block; SB: solid brick; CSB: concrete solid brick; HCHB: hollow clay horizontal brick.

3.3.2. Effective Strengthening of the Panel. The integration of the infill panels on the substructure and respective behaviour improvement and reduction of the OOP vulnerability can be achieved by using different strengthening techniques such as fiber-reinforced polymers (FRP) [115], engineered cementitious composites (ECC) [116], textile-reinforced mortars (TRM) [33], and bed joint reinforcement [33].

The knowledge and techniques to improve the way infilled RC buildings respond to earthquakes have been the object of several studies and tests. However, in parallel to these advances in the last years, and due to the concerns with thermal comfort, new bricks and new techniques have also been developed for buildings' façade walls with the main goal of reducing the cooling and heating losses. As a result of the innovation, new types of masonry units and construction technologies have been developed, being pushed by the market competition. The masonry industry improved the thermal properties of masonry units and developed new, faster, and cheaper technologies of construction [117]. The use of external thermal insulation composite systems (ETICS) is now common in the external walls with energy saving purposes. Distinct types of ties, generally from steel or

plastic and having different shapes and geometry (very dependent on the wall system), are usually adopted [118]. However, it cannot be found over the literature any study regarding the effect of the ETICS in the infilled RC frame seismic performance.

Backing to the FRP technique, Carney and Myers [119] tested two series of IM walls made with concrete blocks to be subjected to OOP loadings. A total of twelve walls with different strengthening schemes using FRP composite materials were tested. Two FRP strengthening techniques were adopted with anchorages for both techniques. The first method was composed by the application of externally bonded glass FRP laminates. This strategy includes a primer and a glass fiber sheet to form the composite material. The authors stated that glass fiber sheets are more economical and provide more compatible strength than the carbon fibers. The second method consisted in the application of near-surface-mounted (NSM) glass FRP rods. These rods were attached to the wall using an epoxy-based grout. The specimens strengthened with anchorage produced a system capable of carrying a load of approximately twice that of the reference one. Later, Hamid et al. [120] carried out an

experimental investigation to study the IP behaviour of face shell mortar bedded IM wall assemblages retrofitted with FRP laminates. Tests including specimens loaded in compression with different bed joint orientations, diagonal tension specimens, and specimens loaded under joint shear were carried out. The FRP laminate was selected according to an equivalent-stiffness-based approach, from which the laminate required was equated to the minimum steel reinforcement ratio of 0.2% (based on the gross cross-sectional area of the panel) according to the requirement of the Masonry Standards Joint Committee [121]. Lastly, Lunn and Rizkalla [96] carried out an extensive experimental campaign composed by 14 full-scale infilled RC frame specimens, which included four unstrengthened specimens and 10 strengthened specimens. Solid clay bricks were used to build the IM wall specimens. The strengthened specimens were reinforced with externally bonded glass fiber-reinforced polymer sheets applied in the exterior tension face of the external leaf of the panel. Different coverage ratios were adopted by the authors considering only unidirectional (vertical or horizontal) directions. Three different anchorage systems were used. From the testing campaign, the authors concluded that the externally bonded solution was effective if proper anchorage of the FRP laminate is guaranteed. Overlapping the FRP reinforcement onto the RC frame revealed to be very effective for double-wythe specimens, but less for single-wythe specimens. This strengthening technique requires the following steps to be applied: (1) application of primer; (2) smoothing of the surface with a layer of putty; (3) application of a first layer of epoxy resin; (4) positioning of the fibers; and (5) use of a small paint roller (FRP) to press the strip or a palette-knife (SRP), to allow proper impregnation of strands.

Moving to the ECC technique, in 2015, Kesner and Billington [122] studied the application of ductile fiber-reinforced mortar material referred to as engineered cementitious composites. The study was about the use of ECC to retrofit precast panels in lieu of a traditional reinforced concrete or masonry. From the testing campaign, it was observed that different levels of strength and stiffness increment can be achieved by varying the mix design of the ECC material and the amount of reinforcement in the panels. Kyriakides and Billington [44] studied the impact of a thin layer of ECC in IM wallets, made with solid clay bricks, subjected to flexure strength tests. The variables studied were the use of wall anchors to improve the ECC-masonry bond and alternate steel reinforcement ratios within the ECC layer in the form of welded wire fabric. From the tests, it was observed that the ECC retrofit increased the strength and stiffness by 45 and 53%, respectively. Billington et al. [123] proposed a thin layer of sprayable ECC applicable to retrofit an infilled RC frame subjected to IP loadings. From the 2/3-scale tests, the authors concluded that the ECC enhanced the performance of the infill walls in terms of both strength and deformation capacity. The authors also pointed out that the retrofit details need special attention to bond the ECC layer to the infill panel and to connect the ECC to the frame. Barros [124] carried out a testing campaign of

masonry wallets subjected to flexural strength tests parallel and perpendicular to the bed joints using hollow clay horizontal bricks. The objective of the experimental campaign was to assess the efficiency of the ECC strengthening technique to improve the OOP capacity and to evaluate the effect of different ECC thicknesses. For that, 30 specimens were built with geometric dimensions 600×600 mm made with 150 mm thick hollow clay horizontal bricks. For each type of tests were tested 5 as-built specimens (Group R), 5 retrofitted with 10 mm ECC thick (Group A), and 5 retrofitted with 20 mm ECC thick (Group B). From the flexural tests parallel to the horizontal bed joints, it was observed that the failure mode of the as-built specimens (Figure 6(a)) was characterized by the detachment of the first row of bricks from the adjacent row which according to the author was controlled by the mortar-brick adhesion. Regarding the retrofitted specimens, similar damages were observed in both groups, shear failure occurred most of the times due to the geometry of the panel (small distance between the OOP loading application and OOP restrains), and the remaining failures were characterized by the crushing of the bricks combined with one or two major horizontal cracks. It was observed that Group A and Group B specimens reached an average flexural strength of 0.43 MPa and 0.46 MPa, respectively. Therefore, it can be concluded that the double thickness of the ECC layer did not provide any significant effect in terms of strength (increase of around 6%). The authors pointed out that, due to the fragility of this type of masonry units, the ECC layer was too strong and the damages concentrated in the masonry. Regarding the comparison between the as-built specimens and the retrofitted ones, it was obtained an increase of the flexural strength of about 5.38 times and 5.75 times for the Group A and Group B specimens, respectively. The authors compared also the OOP displacement corresponding to the occurrence of the maximum OOP loading ($d_{f,oop,max}$). The $d_{f,oop,max}$ of the Group A and Group B specimens was around 1.86 times and 2.04 times higher than that of the as-built specimens. The double thickness of the Group B specimens contributed for a $d_{f,oop,max}$ 9% larger.

Finally, some studies were performed to study the efficiency of using textile-reinforced mortars (TRMs) to improve the OOP seismic behaviour of infill panels. Since 1980, the use of textile-reinforced mortar technique (TRM) started to be adopted. The most basic application is the fiber-reinforced mortar, which consists in a mixture of mortar with a percentage of fibers randomly distributed within its composition. It is generally used as shotcrete, which became widespread for tunnel reinforcements. Some of the factors that affect the effectiveness of this solution are fiber slenderness and length as well as the size of aggregates in the mortar matrix since they define the bonding properties and thus the capacity to behave as a composite [125]. More complex solutions using the same kind of material imply defining a direction for the reinforcement, according to the material requirements of the design of the structure; in this way, the fibers can develop their maximum capacity. The constructive solutions are unidirectional and bidirectional reinforcement meshes.

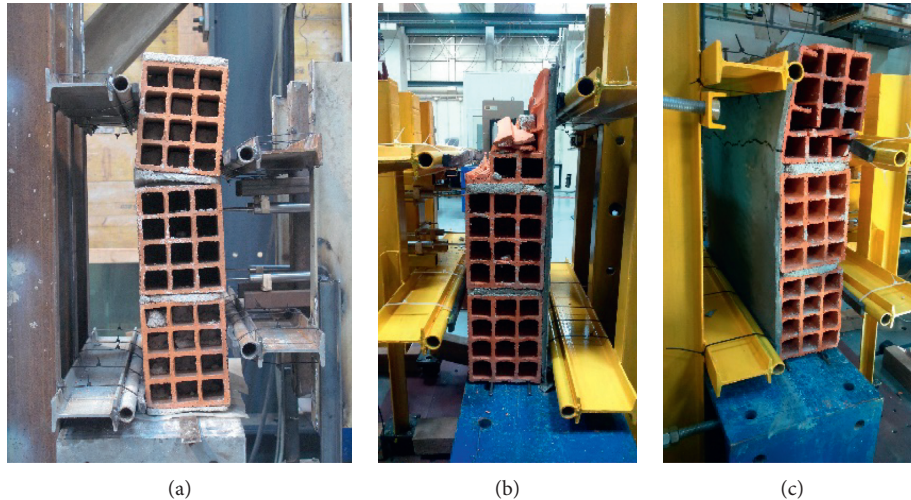


FIGURE 6: Test results obtained by Barros [124]: damages observed after the flexural strength tests parallel to the horizontal bed joints. (a) As-built specimens, (b) Group A, and (c) Group B.

The first investigations were related to the tensile properties of fiber-reinforced mortar and its application to retrofit RC structures that made it suitable for reinforcing beams (for both bending and shear) or jacketing and confining columns. The application as a method of retrofitting IM walls is a relatively new concept still under investigation, with many parameters still to be defined. Among the parameters that affect the performance of the reinforcement, there are some remarkable ones, namely: (1) density of the mesh, depending on quantity of fibers in each thread (defined by mass of textile-reinforced mortar) and the separation among them; and (2) mortar and textile surfaces properties, affecting the bond between the element and the reinforcement. Calvi and Bolognini [33] tested two different retrofit strategies, namely, bed joints steel reinforcement and external steel reinforcement combined with bed joint reinforcement. The external reinforcement was composed by mortar layer reinforcement. The design methodology was not provided by the authors. From the testing campaign, the authors observed that the presence of little reinforcement improved significantly the panel response, namely, by increasing the deformation capacity and by modifying the damage limit states for higher drift levels. Guidi et al. [98] carried out combined IP-OOP tests with the aim of characterizing the OOP behaviour of IM walls made with different types of masonry units, with and without reinforcement. Two specimens were unreinforced, and other two were made of reinforced masonry, having both horizontal and vertical bed joint reinforcement. The remaining two specimens were built with thin (120 mm) clay units with plaster layer, one of them was strengthened by means of a special quadriaxial net made with hybrid glass fibers that was casted in an extra fiber-reinforced plaster layer. From the test results, it was observed that the thick masonry systems tested (both reinforced and unreinforced) presented higher OOP strength, due to the development of an arch mechanism, even for higher values of previous IP drift. The thinner specimens, even when

strengthened, developed bending OOP failure that somehow limited the panel strength. The OOP strength of reinforced infill walls was higher than that of unreinforced walls, for higher IP prior drift. Strength decreased due to the increase of in-plane drift (or damage) was smaller in reinforced masonry (-6%) than in unreinforced masonry (-23%). Lastly, Koutas et al. [126] studied the development and performance of new textile-based anchors used to transfer tensile forces in models made of IM wallets and reinforced concrete prisms, to simulate the connection between infill walls and RC frames using TRM. None of these strengthening techniques has been tested under simultaneous IP-OOP loadings.

4. Numerical Modelling Approaches to Study the Seismic Behaviour of Masonry Infill Walls

In recent years, the study of the influence of infill panels on the seismic response of existing buildings has been deeply investigated. The contribution of the IM walls to the building's seismic performance can be favorable or not, depending on a series of phenomena, detailing aspects, and mechanical properties, such as the relative stiffness and strength between the frames and the masonry walls, and the type of connection between masonry and structures [5–8, 127–129].

For the assessment of infilled RC frame structures, the nonlinear behaviour induced by earthquakes should be considered [3, 70, 130, 131]. Different techniques are available in the literature to simulate the response of infilled frames, from refined micromodels to simplified macromodels [3, 131]. For the nonlinear analysis of complex structures when subjected to earthquakes, in many cases, it is not suitable to adopt refined models. Thus, for the simulation of the response of infilled frame structures, considering the IM walls and their interaction with the surrounding frame elements, the adoption of simplified models is unavoidable.

Different approaches are available in the literature to simulate the infill panels' seismic behaviour, which can be divided into two different groups, namely, micromodelling and simplified macromodelling approaches. The first of them involves models in which the panel is discretized into numerous elements to consider the local effects in detail, and the second includes simplified models based on a physical understanding of the behaviour of the infill panels. In the case of the last group, a small number of struts are used to represent the effect of the infill panels on the structural response of buildings when subjected to lateral loadings.

This section presents a review of the numerical modelling strategies to simulate the seismic behaviour of masonry infill walls. Comparison and discussion among the modelling strategies will be presented.

4.1. Detailed Micromodelling Approaches. The micromodelling is a refined/detailed strategy in which all the elements composing the wall are modelled, masonry units, mortar joints as volumetric elements, and boundary link models simulating the contact and friction conditions between the individual elements and frame. A simplified approach within the micromodelling may consist in reducing the number of elements by combining a brick with the surrounding mortar, which is connected to the rest by link models. These approaches are expensive both on the modelling phase and on computational demands, especially when applied to dynamic and nonlinear analysis. The detailed modelling allows obtaining results that help to understand the behaviour at local level and the panel cracking pattern, which can be very useful for calibration of global models and to perform parametric studies. This is an important advantage of the micromodels when compared with the simplified macromodels. This modelling procedure allows to assess and quantify the influence of each parameter on the seismic response of the infill panel [131].

From the literature, it can be observed that micromodelling was started in 1967 with the work carried out by Mallick and Severn [132], concerning the simulation of the IP behaviour of an infilled RC frame, with particular focus in the frame-panel interface. The authors' strategy was to model the wall by rectangular elastic elements with two degrees of freedom per node. The frame-wall interaction was provided by the consideration of frictional shear forces to simulate slippage.

A different approach was proposed by different authors such as Rots [133], Lofti and Shing [134], and Lourenço [135] with the introduction of the continuous-interface models' concept, which basically can be applied to bed joints by accounting for the interaction between the tangential and normal stress. Lourenço [135] proposed a model in which the Coulomb friction rule, tension cutoff, and compression strength are combined. From this, the obtained damages are concentrated in the IM wall bed joints and in the middle of the masonry units. One of the simplifications proposed is to simulate the IM panel as a three-phase material in which the units/mortar and their interfaces are modelled as continuous and discontinuous elements, respectively. For this purpose,

the assumption made by the author was to use a simplified modelling for two-phase material, where the units are simulated by continuous elements, but the mortar and interfaces were lumped to discontinuous elements.

Finally, a more simplified approach was proposed by assuming one-phase materials, in which units, mortars, and interfaces are combined into a continuum and homogeneous element. Chen and Liu [136] developed a finite element model to simulate the IP behaviour of concrete masonry infills bounded by steel frames with openings. The authors proved that the model had the capability of simulating the experimental tests with high accuracy. Mohyeddin et al. [137] developed a generic three-dimensional discrete-finite-element model that has been constructed for infilled RC frames using a commercial software to assess the in-plane and out-of-plane behaviour interaction. From the results, the authors found some differences between the behaviour predicted by the finite element model and the experimental results. The reasons behind these differences were justified by the authors as the combination of large coefficients of variation of masonry material properties and existence of weaker areas within the infill panel which were attributed to workmanship and that cannot be modelled.

Several other studies and efforts were carried out by other authors [68, 138–148]. Asteris et al. [131] present an extensive and in-depth state-of-the-art review concerning the infill masonry micromodelling approaches.

4.2. Simplified Macromodelling Approaches. The macromodelling with equivalent diagonal struts was originally developed to capacitate numerical analysis models of infilled frames with high shear stiffness. From its evolution with multistrut models, it was possible to integrate shear and tensile stresses within the contact length between wall and frame. Models have started to become more complex, with some considering the reduction of stiffness and strength under dynamic loads, or other equivalent approaches to consider the shear slip at the middle of the infill walls. One of the aspects yet to be developed is the OOP behaviour itself, an even more important issue when combined with the diagonal cracking created by IP demands on the masonry infill walls.

First, Polyakov [149] in 1956 proposed an equivalent strut model to simulate the IM wall behaviour. The proposal was based on experimental observation studies on steel frames with focus on normal and shear stresses on the infill walls, in which it was found that the stresses were only transferred by the compression corners of infill-frame interfaces from the structure to the nonstructural elements. From that work, the authors developed a numerical technique to estimate the load intensity to create diagonal cracking. Holmes [150] improved the previous concept, being the first author to propose a formulation for the diagonal strut. The proposed formula to calculate the equivalent strut width is a simplified approach, calibrated for steel frames with brickwork and concrete infill walls. It triggered several other studies to define the width more accurately. This simplified model considered deformation and ultimate strength of the global infill panel.

From these innovative works, successive authors have proposed improvements for the calculation method and a series of other modelling refinements, replacing the infill walls with additional diagonal struts. For example, El-Dakhakhni et al. [151] proposed a model with three diagonal struts on each direction, one in the diagonal of the panel and the other two nonparallel in off-diagonal. According to the researchers, it was better suited to compute the wall stiffness and describe the development of stresses along the frame elements when compared to other models with less diagonal struts. The frame was modelled with elastic elements with the nonlinearity lumped on the frame joints with springs. This simplified nonlinear model was capable of computing the frame-infill interaction and corner crushing failure mechanism.

Later, Crisafulli and Carr [152] proposed an improved strut model to compute the behaviour of infilled frame systems. For that, it was presented an integration of struts and spring to computing independently two phenomena: (i) diagonal cracking and corner crushing and (ii) shear sliding. The model considers six strut members using hysteresis rules. It consists in two diagonal and parallel struts in each direction, which carry the axial loads on the panel, and another pair to describe shear from the top and bottom of the panel, which are activated in each direction, depending on the activation due to axial compressive loads while the panel is deformed.

Crisafulli [153] compared different one-strut, double-strut, and triple-strut models, concluding that the double-strut model was the most balanced of the strategies, achieving accurate results without too much complexity in terms of calibration and computational efforts. According to the authors, the model finds its limitation on the connection to beam-column joints that avoids accurate development of bending moments and shear forces on the structural elements.

Recently, some advances have emerged regarding the strut models capable of simulating the combined IP and OOP behaviour. Kadyśiewski and Mosalam [154] proposed a model capable of simulating both in-plane and out-of-plane behaviour of the infill walls, with a single diagonal beam-column element with a node at the midspan having a concentrated mass to trigger the OOP inertia forces. A new macroelement model was also proposed by Trapani et al. [155] for the simulation of the IP-OOP response of infilled frames subjected to seismic actions. The model consists of two diagonals plus one horizontal and one vertical struts. Each strut is represented by two fiber-section modelling beam-column elements. The model can capture the arching action of the wall under an OOP load as well as the interaction between the IP and OOP actions.

5. Conclusions and Open Issues

This manuscript aims at presenting an overview regarding the seismic performance of infilled RC structures and with focus on the infill wall damages. A brief revision of the most common damages observed in this type of structures in the last major earthquakes was presented. From that, eleven

typologies of damages were defined concerning the infilled RC structures. From this revision, the main conclusions that can be achieved are that in the assessment of existing buildings and in the design of new buildings:

- Consideration of the masonry infill walls in the structural design (based on simple checking rules/procedures after the structural design) should be enforced

- Attention should be given to the stiffness differences between the 1st storey and the upper storeys (storey height, dimensions and position of openings, and distribution of masonry infill walls)

- Appropriate strengthening of the panel to the OOP loadings should be designed, with adequate connection of the reinforcement material to the RC elements

A state-of-the-art review concerning the testing of infilled RC structures was provided where the major aspects of each testing campaign were discussed. The analysed campaigns have investigated the influence of the infill panel on the lateral response of the whole frame, depending on the brick typology, on the infill-to-frame relative stiffness and strength, and on the presence of openings with different opening ratios and eccentricities, among other investigated parameters. The experimentally observed failure mode has been different depending on the main geometrical and mechanical features of infills and frames. Experimental results indicated that, under in-plane actions, (i) specimens with strong infills can exhibit a better performance than those with weak infills in terms of the observed lateral strength, stiffness, ductility, and energy dissipation capacity; (ii) the presence of the infills—even with openings—can improve the in-plane performance of RC frames; and (iii) a great attention should be paid to the shear load acting on RC members due to their interaction with the infill panel, especially if the infill is strong and the frame is nonconforming to the most updated seismic codes.

The out-of-plane tests of masonry infill walls available in the literature are still scarce, and the large number of variables such as the specimen geometries, masonry unit, loading protocol, among others, makes very difficult to achieve further and more robust conclusions and, thus, makes a step forward towards the reduction of the collapse risk for these panels. From those tests, it can be pointed out that the effect of previous damage caused by prior IP drift demand can highly reduce the OOP strength capacity of the infills and lead to fragile collapses due to the reduction of the probability of arch mechanism development. The slenderness and the reduction of the panel width support reduce the panel OOP capacity as well as the aspect ratio. An open issue is the testing of infill panels with openings (such as doors or windows) which represent mode adequately the buildings facades. The IP + OOP combination requires also higher efforts to reinforce the conclusions achieved until the present. The realization of tests with multiple loadings (IP and OOP) at the same time is one of the open issues for future research studies.

Regarding the strengthening of infill walls, two different approaches, which are commonly adopted in research

studies, have been presented. Looking for the sustainable solutions regarding the strengthening strategies is still an open issue as well as the development of guidelines to the design and application of these strategies. To this aim, many studies and experimental tests are needed, which allow assessing the efficiency of the techniques under both IP loadings and OOP loadings. Special attention should be provided to the connection of the reinforcement material to the surrounding frame. Without proper design and detailing, the retrofitting of the infill panels could result in an inadequate performance when subjected to earthquakes until the collapse.

Finally, simplified macromodels can be used and implemented by structural engineers nowadays with lower computational effort and easy implementation methodologies. Strut-based models with the capability of simulating the infills out-of-plane behaviour need further calibration based on experimental data. However, from the state-of-art review, there is a lack of enough results that covered the innumerable number of variables that are related to these nonstructural elements, which currently produce also the lack of proper code provisions to help practitioners in the design and assessment of infilled RC structures. This gap should be urgently filled.

Conflicts of Interest

The authors declare that they have no conflicts of interest.

Acknowledgments

This work was financially supported by UID/ECI/04708/2019—CONSTRUCT—Instituto de I&D em Estruturas e Construções funded by national funds through the FCT/MCTES (PIDDAC) and specifically through the research project POCI-01-0145-FEDER-016898—ASPASSI—Safety Evaluation and Retrofitting of Infill masonry enclosure Walls for Seismic demands. This work was also supported by AXA Research Fund Post-Doctoral Grant “Advanced non-linear modelling and performance assessment of masonry infills in RC buildings under seismic loads: the way forward to design or retrofitting strategies and reduction of losses.” These supports are gratefully acknowledged.

References

- [1] A. Furtado, H. Rodrigues, A. Arède, and H. Varum, “Out-of-plane behavior of masonry infilled RC frames based on the experimental tests available: a systematic review,” *Construction and Building Materials*, vol. 168, pp. 831–848, 2018.
- [2] P. G. Asteris, L. Cavaleri, F. Di Trapani, and V. Sarhosis, “A macro-modelling approach for the analysis of infilled frame structures considering the effects of openings and vertical loads,” *Structure and Infrastructure Engineering*, vol. 12, no. 5, pp. 551–566, 2016.
- [3] P. G. Asteris, S. T. Antoniou, D. S. Sophianopoulos, and C. Z. Chrysostomou, “Mathematical macromodeling of infilled frames: state of the art,” *Journal of Structural Engineering*, vol. 137, no. 12, pp. 1508–1517, 2011.
- [4] M. T. De Risi, C. Del Gaudio, P. Ricci, and G. M. Verderame, “In-plane behaviour and damage assessment of masonry infills with hollow clay bricks in RC frames,” *Engineering Structures*, vol. 168, pp. 257–275, 2018.
- [5] X. Romão, A. A. Costa, E. Paupério et al., “Field observations and interpretation of the structural performance of constructions after the 11 May 2011 Lorca earthquake,” *Engineering Failure Analysis*, vol. 34, pp. 670–692, 2013.
- [6] L. Hermanns, A. Fraile, E. Alarcón, and R. Á. and n, “Performance of buildings with masonry infill walls during the 2011 Lorca earthquake,” *Bulletin of Earthquake Engineering*, vol. 12, no. 5, pp. 1977–1997, 2014.
- [7] F. De Luca, G. M. Verderame, F. Gómez-Martinez, and A. Pérez-García, “The structural role played by masonry infills on RC buildings performances after the 2011 Lorca, Spain, earthquake,” *Bulletin of Earthquake Engineering*, vol. 12, no. 5, pp. 1999–2026, 2014.
- [8] P. Ricci, F. De Luca, and G. M. Verderame, “6th April 2009 L’Aquila earthquake, Italy: reinforced concrete building performance,” *Bulletin of Earthquake Engineering*, vol. 9, no. 1, pp. 285–305, 2011.
- [9] R. S. Vicente, H. Rodrigues, H. Varum, A. Costa, and J. A. R. Mendes da Silva, “Performance of masonry enclosure walls: lessons learned from recent earthquakes,” *Earthquake Engineering and Engineering Vibration*, vol. 11, no. 1, pp. 23–34, 2012.
- [10] C. Del Gaudio, M. T. De Risi, P. Ricci, and G. M. Verderame, “Empirical drift-fragility functions and loss estimation for infills in reinforced concrete frames under seismic loading,” *Bulletin of Earthquake Engineering*, vol. 17, no. 3, pp. 1285–1330, 2019.
- [11] L. Sousa and R. Monteiro, “Seismic retrofit options for non-structural building partition walls: impact on loss estimation and cost-benefit analysis,” *Engineering Structures*, vol. 161, pp. 8–27, 2018.
- [12] P. Ricci, M. Di Domenico, and G. M. Verderame, “Experimental assessment of the in-plane/out-of-plane interaction in unreinforced masonry infill walls,” *Engineering Structures*, vol. 173, pp. 960–978, 2018.
- [13] R. Angel, D. Abrams, D. Shapiro, J. Uzarski, and M. Webster, *Behavior of Reinforced Concrete Frames, with Masonry Infills*, Civil Engineering Studies, Research Series No. 589, UIU-ENG, University of Illinois, Springfield, IL, USA, 1994.
- [14] M. Di Domenico, P. Ricci, and G. M. Verderame, “Experimental assessment of the influence of boundary conditions on the out-of-plane response of unreinforced masonry infill walls,” *Journal of Earthquake Engineering*, pp. 1–39, 2018.
- [15] H. Varum, A. Furtado, H. Rodrigues, J. Dias-Oliveira, N. Vila-Pouca, and A. Arède, “Seismic performance of the infill masonry walls and ambient vibration tests after the Ghorka 2015, Nepal earthquake,” *Bulletin of Earthquake Engineering*, vol. 15, no. 3, pp. 1185–1212, 2017.
- [16] D. Gautam, H. Rodrigues, K. K. Bhetwal, P. Neupane, and Y. Sanada, “Common structural and construction deficiencies of Nepalese buildings,” *Innovative Infrastructure Solutions*, vol. 1, no. 1, 2016.
- [17] M. T. De Risi, C. Del Gaudio, and G. M. Verderame, “Evaluation of repair costs for masonry infills in RC buildings from observed damage data: the case-study of the 2009 L’Aquila earthquake,” *Buildings*, vol. 9, no. 5, p. 122, 2019.
- [18] European Committee for Standardization, *Design of Structures for Earthquake Resistance-Part 1-1: General Rules, Seismic Actions and Rules for Buildings*, European Committee for Standardization, Brussels, Belgium, 2005.
- [19] H. Varum, R. Dumar, A. Furtado, A. R. Barbosa, D. Gautam, and H. Rodrigues, “Chapter 3—seismic

- performance of buildings in Nepal after the gorkha earthquake,” in *Impacts and Insights of the Gorkha Earthquake*, D. Gautam and H. Rodrigues, Eds., pp. 47–63, Elsevier, Amsterdam, Netherlands, 2018.
- [20] H. Varum, *Seismic assessment, strengthening and repair of existing buildings*, Ph.D. thesis, Universidade de Aveiro, Aveiro, Portugal, 2003.
- [21] A. Furtado, H. Rodrigues, H. Varum, and A. Costa, “Evaluation of different strengthening techniques’ efficiency for a soft storey building,” *European Journal of Environmental and Civil Engineering*, vol. 21, no. 4, pp. 371–388, 2017.
- [22] P. Ricci, M. T. De Risi, G. M. Verderame, and G. Manfredi, “Influence of infill distribution and design typology on seismic performance of low- and mid-rise RC buildings,” *Bulletin of Earthquake Engineering*, vol. 11, no. 5, pp. 1585–1616, 2013.
- [23] H. Sezen, K. Elwood, A. Whittaker, K. Mosalam, J. Wallace, and J. Stanton, *Structural Engineering Reconnaissance of the August 17, 1999, Kocaeli (Izmit), Turkey, Earthquake*, Pacific Earthquake Engineering Research Center, New York, NY, USA, 2000.
- [24] G. Verderame, I. Iervolino, and P. Ricci, “Report on the damages on buildings following the seismic event of 6th of April 2009,” 2009, <http://www.reluis.it>.
- [25] F. Celano, M. Cimmino, O. Coppola, G. Magliulo, and P. Salzano, “Report dei danni registrati a seguito del terremoto del Centro Italia del 24 agosto 2016,” 2016, <http://www.reluis.it>.
- [26] D. J. Kakaletsis and C. G. Karayannis, “Influence of masonry strength and openings on infilled R/C frames under cycling loading,” *Journal of Earthquake Engineering*, vol. 12, no. 2, pp. 197–221, 2008.
- [27] S. Aly and M. A. Mooty, “Cyclic behaviour of masonry infilled RC frames with and without openings,” in *Proceedings of the 26th Conference on Our World in Concretes and Structures*, Singapore, August 2001.
- [28] F. Akhoundi, G. Vasconcelos, P. Lourenço, C. Palha, and L. Silva, “In-plane and out-of plane experimental characterization of RC masonry infilled frames,” in *Proceedings of the M2D-6th International Conference on Mechanics and Materials in Design*, pp. 427–440, Azores, Portugal, 2015.
- [29] G. Al-Chaar, M. Issa, and S. Sweeney, “Behavior of masonry-infilled nonductile reinforced concrete frames,” *Journal of Structural Engineering*, vol. 128, no. 8, pp. 1055–1063, 2002.
- [30] M. Baran and T. Sevil, “Analytical and experimental studies on infilled RC frames,” *International Journal of Physical Science*, vol. 5, no. 13, pp. 1981–1988, 2010.
- [31] S. H. Basha and H. B. Kaushik, “Behavior and failure mechanisms of masonry-infilled RC frames (in low-rise buildings) subject to lateral loading,” *Engineering Structures*, vol. 111, pp. 233–245, 2016.
- [32] A. Bergani and C. Nuti, “Experimental tests and global modeling of masonry infilled frames,” *Earthquake and Structures*, vol. 9, no. 2, pp. 281–303, 2015.
- [33] G. M. Calvi and D. Bolognini, “Seismic response of reinforced concrete frames infilled with weakly reinforced masonry panels,” *Journal of Earthquake Engineering*, vol. 5, no. 2, pp. 153–185, 2001.
- [34] L. Cavaleri and F. Di Trapani, “Cyclic response of masonry infilled RC frames: experimental results and simplified modeling,” *Soil Dynamics and Earthquake Engineering*, vol. 65, pp. 224–242, 2014.
- [35] J. Centeno, C. Ventura, and S. Foo, “Shake table testing of gravity load designed reinforced concrete frames with unreinforced masonry infill walls,” in *Proceedings of the 14th World Conference on Earthquake Engineering*, Beijing, China, October 2008.
- [36] T.-C. Chiou and S.-J. Hwang, “Tests on cyclic behavior of reinforced concrete frames with brick infill,” *Earthquake Engineering & Structural Dynamics*, vol. 44, no. 12, pp. 1939–1958, 2015.
- [37] F. Colangelo, “Pseudo-dynamic seismic response of reinforced concrete frames infilled with non-structural brick masonry,” *Earthquake Engineering & Structural Dynamics*, vol. 34, no. 10, pp. 1219–1241, 2005.
- [38] D. Combesure and P. Pegon, “Application of the local-to-global approach to the study of infilled frame structures under seismic loading,” *Nuclear Engineering and Design*, vol. 196, no. 1, pp. 17–40, 2000.
- [39] G. Gazić and V. Sigmund, “Cyclic testing of single-span weak frames with masonry infill,” *Grđevinar*, vol. 68, no. 8, pp. 617–633, 2016.
- [40] G. Guidi, F. da Porto, N. Verlatto, and C. Modena, *Comportamento Sperimentale nel Piano e Fuori Piano di Tamponamenti in Muratura Armata e Rinforzata. Edile e Ambientale (Padova)*, Dipartimento di Ingegneria Civile, Edile e Ambientale, Padua, Italy, 2013.
- [41] S. Haider, “In-plane cyclic response of reinforced concrete frames with unreinforced masonry infills,” Ph.D. thesis, Rice University, Houston, TX, USA, 1995.
- [42] A. Hashemi and K. M. Mosalam, “Shake-table experiment on reinforced concrete structure containing masonry infill wall,” *Earthquake Engineering & Structural Dynamics*, vol. 35, no. 14, pp. 1827–1852, 2006.
- [43] H. R. Khoshnoud and K. Marsono, “Experimental study of masonry infill reinforced concrete frames with and without corner openings,” *Structural Engineering and Mechanics*, vol. 57, no. 4, pp. 641–656, 2016.
- [44] M. A. Kyriakides and S. L. Billington, “Behavior of unreinforced masonry prisms and beams retrofitted with engineered cementitious composites,” *Materials and Structures*, vol. 47, no. 9, pp. 1573–1587, 2014.
- [45] M. Lafuente and A. Molina, “Seismic resistant behavior of minor reinforced concrete frames with masonry infill walls,” in *Proceedings of the 12th World Conference on Earthquake Engineering*, Auckland, New Zealand, February 2000.
- [46] A. Mansouri, M. S. Marefat, and M. Khanmohammadi, “Experimental evaluation of seismic performance of low-shear strength masonry infills with openings in reinforced concrete frames with deficient seismic details,” *The Structural Design of Tall and Special Buildings*, vol. 23, no. 15, pp. 1190–1210, 2014.
- [47] A. B. Mehrabi, P. Benson Shing, M. P. Schuller, and J. L. Noland, “Experimental evaluation of masonry-infilled RC frames,” *Journal of Structural Engineering*, vol. 122, no. 3, pp. 228–237, 1996.
- [48] M. S. Misir, O. Ozelcik, S. C. Girgin, and U. Yucel, “The behavior of infill walls in RC frames under combined bi-directional loading,” *Journal of Earthquake Engineering*, vol. 20, no. 4, pp. 559–586, 2016.
- [49] P. Morandi, S. Hak, and G. Magenes, “In-plane experimental response of strong masonry infills,” in *Proceedings of the 9th International Masonry Conference 2014*, Guimaraes, Portugal, July 2014.
- [50] A. Parducci and A. Checci, “Contributo delle tamponature di mattoni alla resistenza sismica delle strutture intelaiate,” in *Proceedings of the Sixth International Brick Masonry Conference*, Rome, Italy, May 1982.

- [51] P. Pereira, M. Pereira, J. Ferreira, and P. Lourenço, "Behavior of masonry infill panels in RC frames subjected to in plane and out of plane loads," in *Proceedings of the Presented at the 7th Conference on Analytical Models and New Concepts in Concrete and Masonry Structure*, Cracow, Poland, 2012.
- [52] F. Pires, *Influência das paredes de alvenaria no comportamento de estruturas de betão armado sujeitas a ações horizontais*, LNEC, Lisbon, Portugal, 1990.
- [53] S. Schwarz, A. Hanaor, and D. Z. Yankelevsky, "Experimental response of reinforced concrete frames with AAC masonry infill walls to in-plane cyclic loading," *Structures*, vol. 3, pp. 306–319, 2015.
- [54] V. Sigmund and D. Penava, "Experimental study of masonry infilled R/C frames with opening," in *Proceedings of the 12th World Conference on Earthquake Engineering*, Lisboa, Portugal, 2012.
- [55] P. B. Shing, A. Stavridis, I. Koutromanos et al., "Seismic performance of non-ductile RC frames with brick infill," in *Proceedings of the Improving the Seismic Performance of Existing Buildings and Other Structures*, San Francisco, CA, USA, December 2009.
- [56] K. Stylianidis, "Experimental investigation of masonry infilled R/C frames," *The Open Construction and Building Technology Journal*, vol. 6, no. 1, pp. 194–212, 2012.
- [57] T. Suzuki, H. Choi, Y. Sanada et al., "Experimental evaluation of the in-plane behaviour of masonry wall infilled RC frames," *Bulletin of Earthquake Engineering*, vol. 15, no. 10, pp. 4245–4267, 2017.
- [58] G. Verderame, P. Ricci, M. T. De Risi, and C. Del Gaudio, "Experimental assessment and numerical modelling of conforming and non-conforming RC frames with and without infills," *Journal of Earthquake Engineering*, pp. 1–42, 2019, (In press).
- [59] Waly, "Experimental and analytical work on the seismic performance of different types of masonry infilled reinforced concrete frames under cyclic loading," M.Sc thesis, School of Natural and Applied Sciences of Dokuz Eylül University, İzmir, Turkey, 2010.
- [60] E. Yuksel and P. Teymur, "Earthquake performance improvement of low rise RC buildings using high strength clay brick walls," *Bulletin of Earthquake Engineering*, vol. 9, no. 4, pp. 1157–1181, 2011.
- [61] R. Zarnic and M. Tomažević, "The behaviour of masonry infilled reinforced concrete frames subjected to cyclic lateral loading," in *Proceedings of the 8th World Conference on Earthquake Engineering*, San Francisco, CA, USA, July 1984.
- [62] C. Zhai, J. Kong, X. Wang, and Z. Chen, "Experimental and finite element analytical investigation of seismic behavior of full-scale masonry infilled RC frames," *Journal of Earthquake Engineering*, vol. 20, no. 7, pp. 1171–1198, 2016.
- [63] J. Zovkic, V. Sigmund, and I. Guljas, "Cyclic testing of a single bay reinforced concrete frames with various types of masonry infill," *Earthquake Engineering & Structural Dynamics*, vol. 42, no. 8, pp. 1131–1149, 2013.
- [64] P. Negro and G. Verzeletti, "Effect of infills on the global behaviour of R/C frames: energy considerations from pseudodynamic tests," *Earthquake Engineering & Structural Dynamics*, vol. 25, no. 8, pp. 753–773, 1996.
- [65] T. Kalman Šipoš, V. Sigmund, and M. Hadzima-Nyarko, "Earthquake performance of infilled frames using neural networks and experimental database," *Engineering Structures*, vol. 51, pp. 113–127, 2013.
- [66] G. Blasi, F. De Luca, and M. A. Aiello, "Brittle failure in RC masonry infilled frames: the role of infill overstrength," *Engineering Structures*, vol. 177, pp. 506–518, 2018.
- [67] L. Liberatore, F. Noto, F. Mollaioli, and P. Franchin, "In-plane response of masonry infill walls: comprehensive experimentally-based equivalent strut model for deterministic and probabilistic analysis," *Engineering Structures*, vol. 167, pp. 533–548, 2018.
- [68] A. B. Mehrabi and P. B. Shing, "Finite element modeling of masonry-infilled RC frames," *Journal of Structural Engineering*, vol. 123, no. 5, pp. 604–613, 1997.
- [69] D. Cardone and G. Perrone, "Developing fragility curves and loss functions for masonry infill walls," *Earthquake and Structures*, vol. 9, no. 1, pp. 257–279, 2015.
- [70] M. N. Fardis and T. B. Panagiotakos, "Seismic design and response of bare and masonry-infilled reinforced concrete buildings. Part II: infilled structures," *Journal of Earthquake Engineering*, vol. 1, no. 3, pp. 475–503, 1997.
- [71] M. T. De Risi, M. Di Domenico, P. Ricci, G. M. Verderame, and G. Manfredi, "Experimental investigation on the influence of the aspect ratio on the in-plane/out-of-plane interaction for masonry infills in RC frames," *Engineering Structures*, vol. 189, pp. 523–540, 2019.
- [72] A. V. Tsantilis and T. C. Triantafillou, "Innovative seismic isolation of masonry infills using cellular materials at the interface with the surrounding RC frames," *Engineering Structures*, vol. 155, pp. 279–297, 2018.
- [73] Q. Peng, X. Zhou, and C. Yang, "Influence of connection and constructional details on masonry-infilled RC frames under cyclic loading," *Soil Dynamics and Earthquake Engineering*, vol. 108, pp. 96–110, 2018.
- [74] S. A. A. Shah, J. S. Khan, S. M. Ali, K. Shahzada, W. Ahmad, and J. Shah, "Shake table response of unreinforced masonry and reinforced concrete elements of special moment resisting frame," *Advances in Civil Engineering*, vol. 2019, Article ID 7670813, 17 pages, 2019.
- [75] H. Moghaddam, P. Dowling, and N. Ambraseys, "Shaking table study of brick masonry infilled frames subjected to seismic actions," in *Proceedings of the Presented at the World Conference on Earthquake Engineering—9WCEE*, Tokyo, Japan, 1988.
- [76] J. L. Dawe and C. K. Seah, "Out-of-plane resistance of concrete masonry infilled panels," *Canadian Journal of Civil Engineering*, vol. 16, no. 6, pp. 854–864, 1989.
- [77] M. Beconcini, "Sulla resistenza a forze orizzontali di pareti in elementi forati in laterizio," *Costruire in laterizio*, vol. 55, pp. 60–69, 1997.
- [78] R. D. Flanagan and R. M. Bennett, "Bidirectional behavior of structural clay tile infilled frames," *Journal of Structural Engineering*, vol. 125, no. 3, pp. 236–244, 1999.
- [79] M. Griffith and J. Vaculik, "Out-of-plane flexural strength of unreinforced clay brick masonry walls," *TMS Journal*, vol. 25, no. 1, pp. 53–68, 2007.
- [80] M. C. Griffith, J. Vaculik, N. T. K. Lam, J. Wilson, and E. Lumantarna, "Cyclic testing of unreinforced masonry walls in two-way bending," *Earthquake Engineering & Structural Dynamics*, vol. 36, no. 6, pp. 801–821, 2007.
- [81] J. Varela-Rivera, M. Polanco-May, L. Fernandez-Baqueiro, and E. I. Moreno, "Confined masonry walls subjected to combined axial loads and out-of-plane uniform pressures," *Canadian Journal of Civil Engineering*, vol. 39, no. 4, pp. 439–447, 2012.
- [82] S. Hak, P. Morandi, and G. Magenes, "Out-of-plane experimental response of strong masonry infills," in

- Proceedings of the Presented at the Second European Conference on Earthquake Engineering and Seismology—2ECEES*, Istanbul, Turkey, August 2014.
- [83] F. da Porto, G. Guidi, N. Verlato, and C. Modena, “Effectiveness of plasters and textile reinforced mortars for strengthening clay masonry infill walls subjected to combined in-plane/out-of-plane actions/Wirksamkeit von Putz und textiltbewehrtem Mörtel bei der Verstärkung von Ausfachungswänden aus Ziegel,” *Mauerwerk*, vol. 19, no. 5, pp. 334–354, 2015.
- [84] A. Furtado, H. Rodrigues, A. Arède, and H. Varum, “Experimental evaluation of out-of-plane capacity of masonry infill walls,” *Engineering Structures*, vol. 111, pp. 48–63, 2016.
- [85] M. Mosoarca, C. Petrus, V. Stoian, and A. Anastasiadis, “Behaviour of masonry infills subjected to out of plane seismic actions part 2: experimental testing,” in *Proceedings of the Presented at the International Brick and Block Masonry Conference—IB2MAC*, Padua, Italy, June 2016.
- [86] L. Silva, G. Vasconcelos, P. Lourenço, and F. Akhoundi, “Experimental evaluation of a constructive system for earthquake resisting masonry infill walls,” in *Proceedings of the Presented at the Brick and Block Masonry Conference (IB2MAC)*, Padua, Italy, June 2016.
- [87] T. Liauw and K. Kwan, “Experimental study of shear wall and infilled frame on shake-table,” in *Proceedings of the Presented at the World Conference on Earthquake Engineering - 10WCEE*, Madrid, Spain, July 1992.
- [88] R. Klingner, D. C. Rubiano, V. Singhal, and S. Sweeney, “Evaluation and analytical verification of shaking table data from infilled frames,” in *Proceedings of the Presented at the World Conference on Earthquake Engineering—11WCEE*, Acapulco, Mexico, 1996.
- [89] M. Fardis, S. Bousias, P. B. Franchioni, and T. Panagiotakos, “Shake-table tests of a three-story reinforced concrete frame with masonry infill walls,” *Earthquake Engineering & Structural Dynamics*, vol. 28, no. 6, pp. 173–191, 1999.
- [90] R. Zarnic, S. Gostic, A. Crewe, and A. Taylor, “Shaking table tests of 1:4 reduced scale models of masonry infilled reinforced concrete frame buildings,” *Earthquake Engineering & Structural Dynamics*, vol. 30, pp. 819–834, 2001.
- [91] G. Corte, L. Fiorinho, and F. Mazzolani, “Lateral-loading tests on a real RC building including masonry infill panels with and without FRP strengthening,” *Journal of Materials in Civil Engineering*, vol. 20, no. 6, pp. 419–431, 2008.
- [92] S. Komaraneni, D. Rai, M. Eeri, and V. Singhal, “Seismic behavior of framed masonry panels with prior damage when subjected to out-of-plane loading,” *Earthquake Spectra*, vol. 27, no. 4, pp. 1077–1103, 2011.
- [93] A. Stavridis, I. Koutromanos, and P. Shing, “Shake-table tests of a three-story reinforced concrete frame with masonry walls,” *Earthquake Engineering & Structural Dynamics*, vol. 41, pp. 1089–1108, 2012.
- [94] M. Tondelli, K. Beyer, and M. DeJong, “Influence of boundary conditions on the out-of-plane response brick masonry walls in buildings with RC slabs,” *Earthquake Engineering & Structural Dynamics*, vol. 45, no. 8, pp. 1337–1356, 2016.
- [95] V. Frederiksen, “Membrane effect in laterally loaded masonry walls. A second order phenomenon,” in *Proceedings of the Presented at the 6th Canadian Masonry Symposium*, University of Saskatchewan, Saskatoon, Canada, June 1992.
- [96] D. S. Lunn and S. H. Rizkalla, “Strengthening of infill masonry walls with FRP materials,” *Journal of Composites for Construction*, vol. 15, no. 2, pp. 206–214, 2011.
- [97] J. L. Varela-Rivera, D. Navarrete-Macias, L. E. Arède, and E. I. Moreno, “Out-of-plane behaviour of confined masonry walls,” *Engineering Structures*, vol. 33, no. 5, pp. 1734–1741, 2011.
- [98] G. Guidi, F. da Porto, M. Benetta, N. Verlato, and C. Modena, “Comportamento Sperimentale nel Piano e Fuori Piano di Tamponamenti in Muratura Armata e Rinforzata,” in *Proceedings of the XV Convegno Nazionale ANIDIS—“L’ingegneria Sismica in Italia”*, Padova, Italy, 2013.
- [99] J. Moreno-Herrera, J. Marinković, and L. Salatić, “Out-of-Plane design procedure for confined masonry walls,” *Journal of Structural Engineering*, vol. 142, no. 6, Article ID 04015126, 2016.
- [100] F. Akhoundi, G. Vasconcelos, P. Lourenço, and B. Silva, “Out-of-plane response of masonry infilled RC frames: effect of workmanship and opening,” in *Proceedings of the Presented at the International Brick and Block Masonry Conference—IB2MAC*, Padua, Italy, 2016.
- [101] A. Furtado, H. Rodrigues, A. Arède, and H. Varum, “Effect of the panel width support and columns axial load on the infill masonry walls out-of-plane behavior,” *Journal of Earthquake Engineering*, pp. 1–29, 2018.
- [102] P. Ricci, M. Di Domenico, and G. M. Verderame, “Experimental investigation of the influence of slenderness ratio and of the in-plane/out-of-plane interaction on the out-of-plane strength of URM infill walls,” *Construction and Building Materials*, vol. 191, pp. 507–522, 2018.
- [103] C. Butenweg, R. R. Marinković, and R. Salatić, “Experimental results of reinforced concrete frames with masonry infills under combined quasi-static in-plane and out-of-plane seismic loading,” *Bulletin of Earthquake Engineering*, vol. 17, pp. 3397–3422, 2019.
- [104] M. Mohammadi, V. Akrami, and R. Mohammadi-Ghazi, “Methods to improve infilled frame ductility,” *Journal of Structural Engineering*, vol. 137, no. 6, pp. 646–653, 2011.
- [105] M. Mohammadi, “Stiffness and damping of infilled steel frames,” *Structures & Buildings*, vol. 160, no. 2, pp. 105–118, 2007.
- [106] M. Preti, N. Bettini, and G. Plizzari, “Infill walls with sliding joints to limit infill-frame seismic interaction: large-scale experimental test,” *Journal of Earthquake Engineering*, vol. 16, no. 1, pp. 125–141, 2012.
- [107] P. Morandi, R. Milanesi, and G. Magenes, “Innovative solution for seismic-resistant masonry infills with sliding joints: in-plane experimental performance,” *Engineering Structures*, vol. 176, pp. 719–733, 2018.
- [108] N. Verlato, G. Guidi, F. da Porto, and C. Modena, “Innovative systems for masonry infill walls based on the use of deformable joints: combined in-plane/out-of-plane tests,” in *Proceedings of the 16th IB2MAC—International Brick and Block Masonry Conference*, Padua, Italy, June 2016.
- [109] B. Goodno, J. Pinelli, and J. Craig, “An optimal design approach for passive damping of building structures using architectural cladding,” in *Proceedings of the World Conference on Earthquake Engineering—11WCEE*, Acapulco, Mexico, 1996.
- [110] A. S. Aliaari and A. M. Memari, “Analysis of masonry infilled steel frames with seismic isolator subframes,” *Engineering Structures*, vol. 27, no. 4, pp. 487–500, 2005.

- [111] M. Aliaari and A. M. Memari, "Experimental evaluation of a sacrificial seismic fuse device for masonry infill walls," *Journal of Architectural Engineering*, vol. 13, no. 2, pp. 111–125, 2007.
- [112] A. Charleson, *Seismic Design for Architects*, Elsevier Architectural Press, Amsterdam, Netherlands, 2008.
- [113] M. Marinković and C. Butenweg, "Innovative decoupling system for the seismic protection of masonry infill walls in reinforced concrete frames," *Engineering Structures*, vol. 197, 2019.
- [114] A. Tasligedik, S. Pampanin, and A. Palermo, "Low damage seismic solutions for non-structural drywall partitions," *Bulletin of Earthquake Engineering*, vol. 13, no. 4, pp. 1029–1050, 2015.
- [115] E. Akin, G. Ozcebe, and U. Ersoy, "Strengthening of brick infilled reinforced concrete (RC) frames with carbon fiber reinforced polymers (CFRP) sheets," in *Seismic Risk Assessment and Retrofitting: With Special Emphasis on Existing Low Rise Structures*, pp. 367–386, Springer, Dordrecht, Netherlands, 2009.
- [116] M. A. Kyriakides and S. L. Billington, "Cyclic response of nonductile reinforced concrete frames with unreinforced masonry infills retrofitted with engineered cementitious composites," *Journal of Structural Engineering*, vol. 140, no. 2, Article ID 04013046, 2014.
- [117] M. Tomaževič, M. Lutman, and V. Bosiljkov, "Robustness of hollow clay masonry units and seismic behaviour of masonry walls," *Construction and Building Materials*, vol. 20, no. 10, pp. 1028–1039, 2006.
- [118] A. Collina and G. Lignola, "The external thermal insulation composite system (ETICS) more than comfort and energy saving," in *Proceedings of the Presented at the Third Portuguese Congress on Construction Mortars—3PCCM*, Lisbon, Portugal, March 2010.
- [119] P. Carney and J. J. Myers, "Shear and flexural strengthening of masonry infill walls with FRP for extreme out-of-plane loading," in *Proceedings of the Architectural Engineering Conference (AEI)*, Austin, TX, USA, September 2003.
- [120] A. A. Hamid, W. W. El-Dakhkhni, Z. H. R. Hakam, and M. Elgaaly, "Behavior of composite unreinforced masonry-fiber-reinforced polymer wall assemblages under in-plane loading," *Journal of Composites for Construction*, vol. 9, no. 1, pp. 73–83, 2005.
- [121] MSJC, *Building Code Requirements for Masonry Structures*, MSJC, San Jacinto, CA, USA, 2004.
- [122] K. Kesner and S. L. Billington, "Investigation of infill panels made from engineered cementitious composites for seismic strengthening and retrofit," *Journal of Structural Engineering*, vol. 131, no. 11, pp. 1712–1720, 2005.
- [123] S. Billington, M. Kyriakides, B. Blackard, K. Willam, and A. Stravidis, "Evaluation of a sprayable, ductile cement-based composite for the seismic retrofit of unreinforced masonry infills," in *Proceedings of the 2009 ATC and SEI Conference on Improving the Seismic Performance of Buildings and Other Structures*, San Francisco, CA, USA, December 2009.
- [124] S. Barros, "Caracterização de argamassas com fibras de PVA para reforço de paredes de alvenaria," M.Sc thesis, Faculdade de Engenharia da Universidade do Porto, Porto, Portugal, 2017.
- [125] J. Gómez, "Innovative retrofitting materials for brick masonry infill walls," M.Sc thesis, University of Minho, Guimarães, Portugal, 2012.
- [126] L. Koutas, A. Pitytzogia, T. C. Triantafyllou, and S. N. Bousias, "Strengthening of infilled reinforced concrete frames with TRM: study on the development and testing of textile-based anchors," *Journal of Composites for Construction*, vol. 18, no. 3, 2014.
- [127] M. N. Fardis, "Experimental and numerical investigations on the seismic response of RC infilled frames and recommendations for code provisions ECOEST/PREC 8," Report No. 6, LNEC, Lisbon, Portugal, 1996.
- [128] M. Dolsek and P. Fajfar, "The effect of masonry infills on the seismic response of a four storey reinforced concrete frame—a probabilistic assessment," *Engineering Structures*, vol. 30, no. 11, pp. 3186–3192, 2008.
- [129] P. G. Penna, S. T. Morandi, D. S. Rota, C. Z. Manzini, F. Porto, and G. Magenes, "Performance of masonry buildings during the emilia 2012 earthquakes," *Bulletin of Earthquake Engineering*, vol. 12, no. 5, pp. 2255–2273, 2014.
- [130] M. Dolsek and P. Fajfar, "Simplified non-linear seismic analysis of infilled reinforced concrete frames," *Earthquake Engineering & Structural Dynamics*, vol. 34, no. 1, pp. 49–66, 2005.
- [131] P. Asteris, D. Cotsovos, C. Chrysostomou, A. Mohebbkhan, and G. Al-Chaar, "Mathematical micromodelling of infilled frames: state of the art," *Engineering Structures*, vol. 56, pp. 1905–1921, 2013.
- [132] D. V. Mallick and R. T. Severn, "The behaviour of infilled frames under static loading," *Proceedings of the Institution of Civil Engineers*, vol. 38, pp. 639–656, 1967.
- [133] J. Rots, "Smeared and discrete representations of localized fracture," *International Journal of Fracture*, vol. 51, no. 1, pp. 45–59, 1991.
- [134] H. Lofti and P. Shing, "An appraisal of smeared crack models for masonry shear wall analysis," *Computers and Structures*, vol. 41, no. 3, pp. 413–425, 1991.
- [135] P. Lourenço, *Computational strategies for masonry structures*, Ph.D thesis, Delft University, Delft, Netherlands, 1996.
- [136] X. Chen and Y. Liu, "Numerical study of in-plane behaviour and strength of concrete masonry infills with openings," *Engineering Structures*, vol. 82, pp. 226–235, 2015.
- [137] A. Mohyeddin, H. M. Goldsworthy, and E. F. Gad, "FE modelling of RC frames with masonry infill panels under in-plane and out-of-plane loading," *Engineering Structures*, vol. 51, pp. 73–87, 2013.
- [138] R. Goodman, R. Taylor, and T. Brekke, "A model for the mechanics of jointed rock," *ASCE Journal of the Soil and Mechanics and Foundations Division*, vol. 94, no. 3, pp. 637–659, 1968.
- [139] G. J. W. King and P. C. Pandey, "The analysis of infilled frames using finite elements," *Proceedings of the Institution of Civil Engineers*, vol. 65, no. 4, pp. 749–760, 1978.
- [140] P. B. Shing and A. B. Mehrabi, "Behaviour and analysis of masonry-infilled frames," *Progress in Structural Engineering and Materials*, vol. 4, no. 3, pp. 320–331, 2002.
- [141] G. Kost, W. Weaver, and R. Barber, "Nonlinear dynamic analysis of frames with filler panels," *ASCE Journal of the Structural Division*, vol. 100, no. 4, pp. 743–757, 1974.
- [142] L. Te-Chang and K. Kwok-Hung, "Nonlinear behavior of non-integral infilled frames," *Computer Structures*, vol. 18, no. 3, pp. 551–560, 1984.
- [143] J. L. Dawe and C. K. Seah, "Behaviour of masonry infilled steel frames," *Canadian Journal of Civil Engineering*, vol. 16, no. 6, pp. 865–876, 1989.
- [144] R. R. Yuen, J. S. Kuang, and B. S. M. Ali, "Assessing the effect of bi-directional loading on nonlinear static and dynamic behaviour of masonry-infilled frames with openings," *Bulletin of Earthquake Engineering*, vol. 14, no. 6, pp. 1721–1755, 2016.

- [145] V. Bolis and M. Preti, "Openings in infills with horizontal sliding joints: a parametric study to support the design," *Bulletin of Earthquake Engineering*, vol. 17, no. 9, pp. 5101–5132, 2019.
- [146] A. Stavidris and P. Shing, "Finite-element modelling of nonlinear behavior of masonry-infilled RC frames," *Proceedings of the Institution of Civil Engineers*, vol. 136, no. 1, pp. 285–296, 2010.
- [147] W. W. Kubalski, M. Butenweg, and A. A. Marinković, "Investigation of the seismic behaviour of infill masonry using numerical modelling approaches," in *Proceedings of the 16th World Conference on Earthquake Engineering (16WCEE)*, vol. 2, Santiago, Chile, 2017.
- [148] R. R. Milanese, P. Morandi, and G. Magenes, "Local effects on RC frames induced by AAC masonry infills through FEM simulation of in-plane tests," *Bulletin of Earthquake Engineering*, vol. 16, no. 9, pp. 4053–4080, 2018.
- [149] S. V. Polyakov, *Masonry in Framed Buildings. Gosudalstvennoe'stvo Literature po Straitel' stuv i Arkitecture*, G. L. Cairns, Ed., Building Research Station, Watford, UK, 1956.
- [150] M. Holmes, "Combined loading on infilled frames," *Proceedings of the Institution of Civil Engineers*, vol. 25, no. 1, pp. 31–38, 1963.
- [151] W. W. El-Dakhkhni, M. Elgaaly, and A. A. Hamid, "Three-strut model for concrete masonry-infilled steel frames," *Journal of Structural Engineering*, vol. 129, no. 2, pp. 177–185, 2003.
- [152] F. J. Crisafulli and A. J. Carr, "Proposed macro-model for the analysis of infilled frame structures," *Bulletin of the New Zealand Society for Earthquake Engineering*, vol. 40, no. 2, pp. 69–77, 2007.
- [153] F. Crisafulli, "Seismic behavior of reinforced concrete structures with masonry infills," Ph.D thesis, University of Canterbury, Christchurch, New Zealand, 1997.
- [154] S. Kadysiewski and K. M. Mosalam, *Modeling of Unreinforced Masonry Infill Walls Considering In-Plane and Out-Of-Plane Interaction*, PEER, New York, NY, USA, 2009.
- [155] F. D. Trapani, P. B. Shing, and L. Cavaleri, "Macroelement model for in-plane and out-of-plane responses of masonry infills in frame structures," *Journal of Structural Engineering*, vol. 144, no. 2, Article ID 04017198, 2018.

Research Article

Numerical Investigation on the Influence of In-Plane Damage on the Out-of-Plane Behavior of Masonry Infill Walls

Xiaomin Wang ¹, Weitong Zhao ², Jingchang Kong ^{1,2} and Tiejun Zhao^{3,4}

¹Key Laboratory of Earthquake Engineering and Engineering Vibration, Institute of Engineering Mechanics, China Earthquake Administration, Harbin 150080, China

²School of Civil Engineering, Yantai University, Yantai 264005, China

³School of Civil Engineering, Qingdao University of Technology, Qingdao 266033, China

⁴Cooperative Innovation Center of Engineering Construction and Safety in Shandong Blue Economic Zone, Qingdao 266033, China

Correspondence should be addressed to Jingchang Kong; kjch8811@126.com

Received 4 October 2019; Revised 20 December 2019; Accepted 28 December 2019; Published 21 February 2020

Guest Editor: Maria T. de Risi

Copyright © 2020 Xiaomin Wang et al. This is an open access article distributed under the Creative Commons Attribution License, which permits unrestricted use, distribution, and reproduction in any medium, provided the original work is properly cited.

This study presents a finite element model to investigate the bidirectional seismic behavior of masonry infill walls. The test data are utilized to verify the numerical model. The comparison between the analytical and the experimental results indicates that the finite element model can successfully predict the failure mode, stiffness, and strength of the masonry infill wall. Based on the model, the effects of aspect ratio (height to length), slenderness ratio (height to thickness), and masonry strength on the out-of-plane (OOP) response of infill wall with in-plane (IP) damage are explored. Considering the aspect ratio, slenderness ratio, and masonry strength of infill wall, the OOP behavior of infill wall with and without IP damage is studied. Finally the reduction of the stiffness and strength in the OOP direction, due to the IP damage, is discussed.

1. Introduction

Masonry infill walls are frequently adopted as interior partitions and exterior enclosures in RC frame structures. During an earthquake event, masonry infill walls interact with the bounding frames and contribute to the seismic performances of framed structures, often resulting in severe in-plane (IP) damage, out-of-plane (OOP) failure, or even collapse. A large proportion of researches on seismic performance of masonry-infilled frame structures focus on their IP behavior since the infill walls have changed the primary IP load transferring path, which usually results in significant failure of frame structures. However, infill walls are subjected to IP and OOP loads simultaneously. The IP and OOP response are not independent, which means the damage in one direction may influence the response and capacity in the other direction. Therefore, it is necessary to consider the IP and OOP interaction effects to precisely assess the seismic performance of masonry-infilled frame structures.

In last decades, a certain number of experimental investigations, numerical finite element analyses, and theoretical works have been performed. In 1950's, some experimental investigations begin to focus on the OOP response of infill and masonry walls. Thomas [1] and Mc Dowell et al. [2] found out that the arching resistance mechanism forms in masonry walls under OOP loading, which shows that the OOP capacity is dominated by compressive strength rather than tensile strength. Dawe and Seah [3] tested masonry-infilled steel frames under airbag-imposed OOP loads and proposed an OOP capacity model based on the arching mechanism. Dafnis et al. [4] performed shake table tests of masonry-infilled frames in the OOP direction and pointed out that the boundary condition at the top of infill walls has an important effect on OOP response. Similarly, pure OOP tests for masonry-infilled frames are performed by Tu et al. [5, 6].

Angel et al. [7] firstly tested several masonry-infilled RC frames subject to both IP and OOP loads and stated the OOP

capacity is significantly reduced due to IP displacement demand. Based on the arching mechanism, the authors proposed a simplified strength model to account for the IP and OOP interaction effects. Flanagan and Bennett [8, 9] performed a series of tests on masonry infilled steel frames under pure OOP, different sequential, and combined bidirectional loadings to investigate the interaction effects in two directions and proposed a prediction for the OOP strength. Similar experimental studies were also performed by Calvi and Bolognini [10], Kuang and Yuen [11], Pereira et al. [12], Hak et al. [13], and Ricci et al. [14] to further investigate the IP and OOP interaction in infilled RC frames. These experimental programs have demonstrated that the damage in one direction has a detrimental effect on the response of infilled frames in the other direction, and the detrimental effect increases as the damage in one direction increases. To better understand the IP and OOP interaction, a number of experiments were performed to individuate the significant parameters. Angel et al. [7], Ricci et al. [15], and da Porto et al. [16] tested a series of infilled RC frames with different thickness of infill panels to study the influence of slenderness ratio on IP and OOP interaction effects. de Risi et al. [17] investigated the influence of the aspect ratio on the IP and OOP interaction by conducting some masonry-infilled RC frame experiments.

Furthermore, many numerical researches concerning this topic were also carried out. Rabinovitch and Madah [18] and Zhai et al. [19] proposed finite element models for the pure OOP response of infill masonry walls. Mohyeddin et al. [20] and Yuen and Kuang [21] developed 3D discrete finite element models to represent seismic performance of masonry-infilled RC frames under IP and OOP loading. Mohammadi [22] performed a series of numerical analyses to study the effect of IP damage on OOP strength of unreinforced masonry walls. Verlato et al. [23] developed a numerical model of infill masonry walls to carry out parametric analyses for better understanding the main factors influencing the OOP behavior. A nonlinear finite element model was adopted by Agnihotri et al. [24] to consider the influence of slenderness ratio and aspect ratio on IP and OOP interaction. Based on a series of finite element analyses, Zizzo et al. [25] proposed a formulation for the OOP strength reduction factor.

Kadysiewski and Mosalam [26] and Mosalam and Gunay [27] proposed a discrete fiber model to consider the IP and OOP interaction effects of masonry infill walls. Furtado et al. [28] developed a simplified strut model with four struts and two lumped masses for seismic assessment of masonry-infilled RC frames. Adopting the 3D simplified numerical models, the seismic performance of masonry-infilled RC frame structures is analyzed by Mosalam and Günay [27] and Furtado et al. [29]. Di Trapani et al. [30] proposed a macroelement model for IP and OOP responses of masonry-infilled frame structures. Morandi et al. [31] proposed a simplified design approach for masonry-infilled RC frames by taking into account the relation between IP and OOP damage. Pasca et al. [32] reviewed analytical models for the assessment of OOP response of masonry infill walls and examined their suitability by experimental data.

Based on previous studies, it has widely been recognized that the infill slenderness ratio (height to thickness) has a significant influence on the IP and OOP interaction. For equal IP displacement demand, a larger slenderness ratio of infill wall may induce a more severe damage. Meanwhile, at equal IP displacement demand, a larger slenderness ratio decreases the stability of infill walls in the OOP direction, which increases the strength/stiffness reduction and risk of collapse. In addition, the IP response of infill walls is affected by the infill aspect ratio (width to height) too, which may result in different damage levels for infill walls. Moreover, the vertical stability and horizontal stability of infill walls in the OOP direction may change for different aspect ratios. Therefore, the influence of the infill aspect ratio on IP and OOP interaction effects deserves more attention. However, the investigation on the influence of these parameters on the seismic behavior of masonry-infilled RC frames under IP and OOP loads appears to be relatively limited in the existing literatures. Hence, some systematic parametric studies to enhance the understanding level of IP and OOP interaction effects are still needed.

In this paper, a discrete finite element model for masonry-infilled RC frames is described. Then, the influence of different IP lateral drift levels on OOP capacity is studied by using the calibrated finite element model. Different aspect ratios, slenderness ratios, and masonry strengths are considered in the models to evaluate the dependency of these parameters to IP and OOP interaction effects. The results in terms of OOP strength and stiffness reduction for different IP demands are discussed.

2. Finite Element Model

In this paper, a finite element model with a discrete modeling approach is built in ABAQUS/standard module to precisely simulate the nonlinear behavior of masonry-infilled RC frame structures. In this model, appropriate element types and constitutive relationships are selected to simulate the behavior of concrete, reinforcing bars, and masonry blocks. Particularly, contact pairs are utilized to model the cracking and slipping of mortar joints.

2.1. Finite Element Model for the RC Frame. The RC frame is constructed by modeling the concrete members and reinforcement bars separately. The concrete members in the frame are modeled by using 3-D solid elements (C3D8R) with a damaged plastic model as constitutive relationship.

The compression behavior is composed of initial hardening and the following softening section, while the peak strength is followed only by softening behavior in tension. The degradations of the elastic stiffness in tension and compression are independent. Two independent scalar internal damage variables, D_t and D_c , are introduced in the model to characterize the damage of material under tensile and compressive actions. The stress-strain relations are governed by scalar damaged elasticity as follows:

$$\sigma = (1 - d)D_0^{\text{el}} : (\varepsilon - \varepsilon^{\text{pl}}) = D^{\text{el}} : (\varepsilon - \varepsilon^{\text{pl}}), \quad (1)$$

where D_0^{el} is defined as the undamaged elastic stiffness of the material, $D^{\text{el}} = (1 - d)D_0^{\text{el}}$ is the degraded elastic stiffness, and d is the scalar stiffness degradation variable, which can take the values in the range from 0 to 1.

The yield function represents a surface in effective stress space and accounts for different evolution of strength under tension and compression, which determines the states of failure or damage. The yield function takes the following form:

$$(\bar{\sigma}, \bar{\varepsilon}^{\text{pl}}) = \frac{\bar{q} - 3\alpha\bar{p} + \beta\bar{\varepsilon}^{\text{pl}}\langle\bar{\sigma}_{\text{max}}\rangle - \gamma\langle\bar{\sigma}_{\text{max}}\rangle}{1 - \alpha} - \bar{\sigma}_c \varepsilon_c^{\text{pl}}, \quad (2)$$

where α and β are the dimensionless material constants, which can be calculated by the ratio of the biaxial to uniaxial compressive strengths and uniaxial tensile stress-strain relation. The parameter γ enters the yield function only for stress states of triaxial compression, when $\bar{\sigma}_{\text{max}} < 0$. \bar{p} is the effective hydrostatic pressure, and \bar{q} is the Mises equivalent effective stress. $\bar{\sigma}_{\text{max}}$ is the maximum eigenvalue of effective stress tensor in which the notation $\langle \cdot \rangle$ is the Macaulay bracket. The plastic-damage model assumes nonassociated potential flow, in which the flow potential is the Drucker-Prager hyperbolic function. The uniaxial stress-strain relationship for concrete is defined according to the Chinese code for design of concrete structures (GB50010-2010).

The columns, beams, and slabs are built separately and assembled into an RC frame by using the Tie connect command. Tie connect command is used to realize the binding between different components in ABAQUS, which utilizes "master-slave relation" to define the constraint and prevent the slipping between master and slaver contact surfaces. The reinforcement bars in columns, beams, wall mudsills, and slabs of the frame are all modeled with truss elements (T3D2). A bilinear elastoplastic model with same tensile and compressive capacity is adopted to model the constitutive relationship of reinforcement bars, and the hardening modulus is approximately assumed to be 1.0% of the elastic modulus. The von Mises failure surface with a total stress range of twice the yield stress is assumed for the reinforcing bars. Reinforcement bars are connected to the concrete components by using Embedded command. This connection type has more freedom compared with the Tie command, which allows different components to connect under interferential conditions.

2.2. Finite Element Model for the Infill Wall. To better simulate the cracking and slipping of mortar joints in infill walls, a discrete modeling approach is adopted here, as shown in Figure 1.

In particular, mortar joints between adjacent masonry units are modeled by means of contact pairs, which is realized by defining the contact cohesive behavior, friction behavior, and hard contact to consider the comprehensive behavior of mortar joints. At the initial loading stage, contact cohesive behavior is activated to resist to the tensile and shear forces. Once the strength of contact surface is deteriorated, the stiffness of contact surface is gradually decreasing, and the friction behavior is activated. When

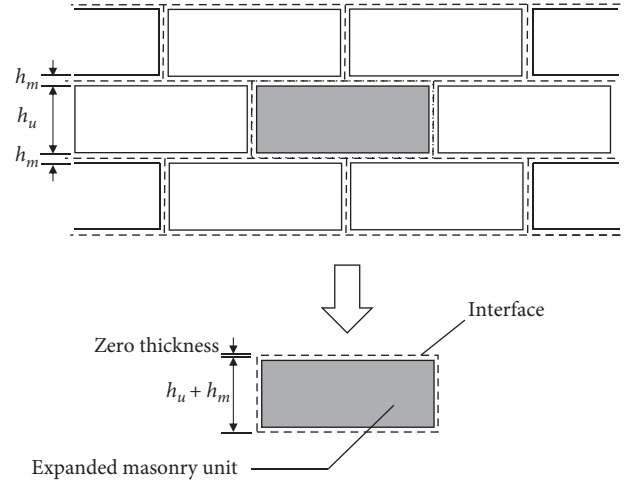


FIGURE 1: Discrete modeling approach.

cohesive behavior has completely deteriorated, the tensile strength of contact surface reduces to zero, and the friction behavior resists to the shear force. The hard contact is adopted to account for the compressive force and prevent the percolation of adjacent masonry blocks. For the joints at the frame-to-infill interface, contact pairs are also utilized to model the cracking and slipping behavior.

An extended version of the classical isotropic Coulomb friction model is adopted, in which friction factor is a connection between the friction force and compressive normal stress. A friction factor of 0.7 is used according to the Chinese code for design of masonry structures (GB50003-2011). The surface-based cohesive model is established by defining three laws as follows. The linear elastic traction-separation law prior to damage is written in terms of an elastic constitutive matrix:

$$t = \begin{Bmatrix} t_n \\ t_s \\ t_t \end{Bmatrix} = \begin{bmatrix} K_{nn} & K_{ns} & K_{nt} \\ K_{sn} & K_{ss} & K_{st} \\ K_{tn} & K_{ts} & K_{tt} \end{bmatrix} \begin{Bmatrix} \delta_n \\ \delta_s \\ \delta_t \end{Bmatrix}, \quad (3)$$

where t is the nominal traction stress vector, consisting of three components, t_n , t_s , and t_t , which represent the normal and the two shear tractions, respectively. δ_n , δ_s , and δ_t are the associated separations. The interface stiffness K is defined as follows [33]:

$$K_{nn} = \frac{E_u E_m}{h_m (E_u - E_m)}, \quad (4)$$

$$K_{ss} = K_{tt} = \frac{G_u G_m}{h_m (G_u - G_m)},$$

where E_u , E_m , G_u , and G_m are the elastic modulus and the shear modulus of the mortar and the masonry block and h_m is the thickness of the mortar. The other terms in K are assumed to be zero.

Damage initiation refers to the beginning of degradation of the cohesive response at a contact point. The damage initiation criterion is defined as the quadratic stress criterion represented as

$$\left\{ \frac{\langle t_n \rangle}{t_n^0} \right\}^2 + \left\{ \frac{t_s}{t_s^0} \right\}^2 + \left\{ \frac{t_t}{t_t^0} \right\}^2 = 1, \quad (5)$$

where t_n^0 , t_s^0 , and t_t^0 represent the peak values of the contact stress when the separation is either purely normal to the interface or purely in the first or the second shear direction, respectively. The damage initiates when the equation is met. The damage evolution law describes the rate at which the cohesive stiffness is degraded once the corresponding initiation criterion is reached. A scalar damage variable, D , represents the overall damage at the contact point, which evolves from 0 to 1. The contact stress components are affected by the damage according to

$$\begin{aligned} t_n &= \begin{cases} (1-D)\bar{t}_n, & \bar{t}_n \geq 0, \\ \bar{t}_n, & \text{no damage to compressive stiffness,} \end{cases} \\ t_s &= (1-D)\bar{t}_s, \\ t_t &= (1-D)\bar{t}_t. \end{aligned} \quad (6)$$

To keep the overall dimension of the infill wall unchanged, each masonry block and surrounding half thickness of mortar joints are treated as a combined masonry block (as shown in Figure 1) since the thickness of mortar joints cannot be represented by contact pairs. Combined masonry blocks are modeled by using solid elements (C3D8R) adopting a damaged plastic model.

The uniaxial stress-strain relation is defined according to the formulation proposed by Angel et al. [7]:

$$\sigma = \frac{27f_m(250\varepsilon_{cr} - 1)}{4\varepsilon_{cr}^3} \varepsilon^3 + \frac{27f_m(1 - 333\varepsilon_{cr})}{4\varepsilon_{cr}^2} \varepsilon^2 + 750f_m\varepsilon, \quad (7)$$

where ε_{cr} is the crushing strain of the masonry wall and f_m is the compressive strength, ε_{cr} is determined as $\varepsilon_{cr} = 1.6\varepsilon_{max}$. The relation is developed by Liu [34], and ε_{max} is the strain at peak strength.

2.3. Verification of the Finite Element Model. In this section, a specimen referred as specimen 2 in the test [7] is utilized to verify the proposed finite element model for simulating the behavior of masonry-infilled RC frames. The specimen is subjected to the combined loading in both IP and OOP directions. The slenderness ratio (height to thickness) of the infill wall is 34, and the detailed geometry and reinforcement information is shown in Figure 2. The material properties for the concrete, masonry blocks, and reinforcement bars are given in Table 1.

The loading mode of numerical analyses is the same as that in the test, and four analysis steps are successively applied. At the first analysis step, self-weight of the specimen is applied and is kept constant during the analysis. At the second analysis step, the vertical load of 241.15 kPa is applied on columns of the RC frame and is kept constant during the analysis. At the third analysis step, the lateral load in the IP direction is applied at the end of beam and with a displacement-controlled procedure. The load is incrementally

applied until the interstory displacement ratio (IDR) reaches 0.3% and then the force returns to zero. At the fourth analysis step, the uniform incremental load in the OOP direction is applied on the surface of the infill panel to simulate the airbag loading until the OOP failure has occurred.

The comparison of damage patterns for OOP loading between numerical and experimental results is reported in Figure 3. The damage pattern at the final state of the experiment is shown in Figure 3(a), and it indicates that the crack distribution under IP loading is mainly located at the extremities of the two columns and the beam, whereas stair-stepped diagonal cracks are observed in the infill panel under OOP loading, and an arching mechanism is formed. Figure 3(b) shows the equivalent plastic strain nephogram obtained from finite element analysis, and it illustrates that the damage in the frame has occurred at beam-column joints and bottom of columns. The damage of the infill panel at the OOP direction is characterized by stair-stepped diagonal cracks. In general, a good agreement in terms of damage patterns between finite element analysis and experimental result is achieved.

The IP lateral load-displacement curve obtained from finite element analysis is compared with the corresponding curve from the experimental result, as shown in Figure 4(a). It is illustrated that the initial IP stiffness of the experimental result is slightly larger than that of the analysis result. As the load increases, however, brittle fracture in mortar joints of the infill panel is observed in the experiment, and only compressive stress and friction act, which results in an abrupt reduction of the IP stiffness. In the finite element analysis, the cohesive stress between masonry units is set to gradually decrease as the load increases. Therefore, a smooth load-displacement curve is obtained and no abrupt reduction in the IP stiffness is observed. In general, a good agreement in terms of overall trend, especially at a later stage, is achieved. Figure 4(b) gives the OOP load-displacement curves, and it shows that the initial stiffness and ultimate load from the analysis have a good match with that of the experimental result, while the yielding stiffness from the analysis is slightly larger than that of the experimental results.

The values of initial stiffness and ultimate load in both the IP and the OOP directions obtained from finite element analysis and experimental result are listed in Table 2. The IP secant stiffness at the cracking load of the infill panel is chosen as the initial IP stiffness, and the OOP secant stiffness at 20% of ultimate load is chosen as the initial OOP stiffness. As the OOP load is conducted by only controlling the amplitude of the OOP pressure of the wall, the descending branch of the load-displacement curves cannot be captured. Thus the ultimate load in this paper is corresponding to the load at the OOP displacement of 50 mm.

The error of initial IP stiffness between finite element analysis and the experimental result is 3.7%, whereas the error of ultimate load is only 0.6%. In the OOP direction, the error in initial stiffness estimate is 5.0%, and the ultimate

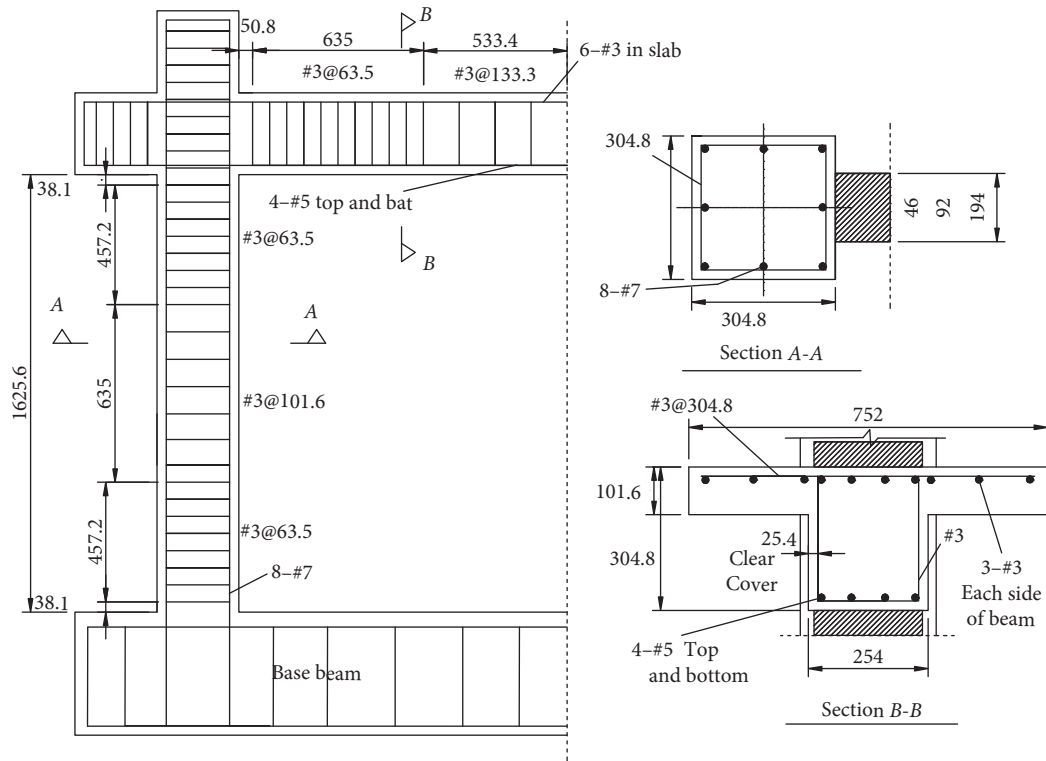


FIGURE 2: Geometry and reinforcement information (mm).

TABLE 1: Material properties.

Material	Compressive strength (MPa)	Elastic modulus (MPa)	Tensile strength (MPa)	Reinforcement bars	Yielding strength (MPa)	Ultimate strength (MPa)
Concrete in frame	55	2.8×10^4	2.05	#3	452	731
Concrete in wall mudsills	27.5	2.0×10^4	2.05	#5	488	760
Masonry	10.9	8.2×10^3	0.3	#7	457	700

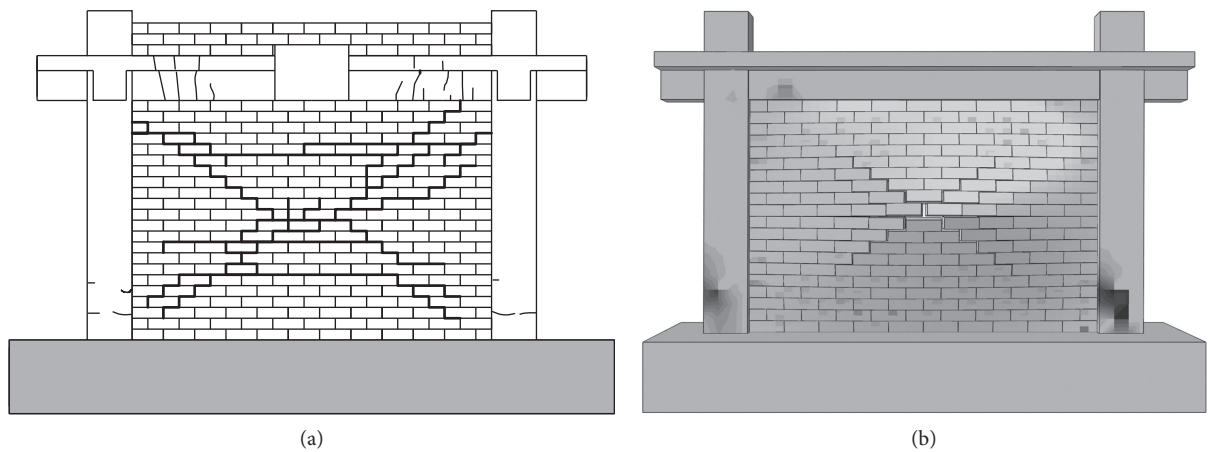


FIGURE 3: Damage patterns for (a) experimental and (b) numerical results.

load for the analysis is equal to that of the experimental result. Based on the above comparison, it can be concluded that the finite element model with discrete modeling

approach can be used to accurately simulate the nonlinear behavior of masonry-infilled RC frame structures under both IP and OOP loads.

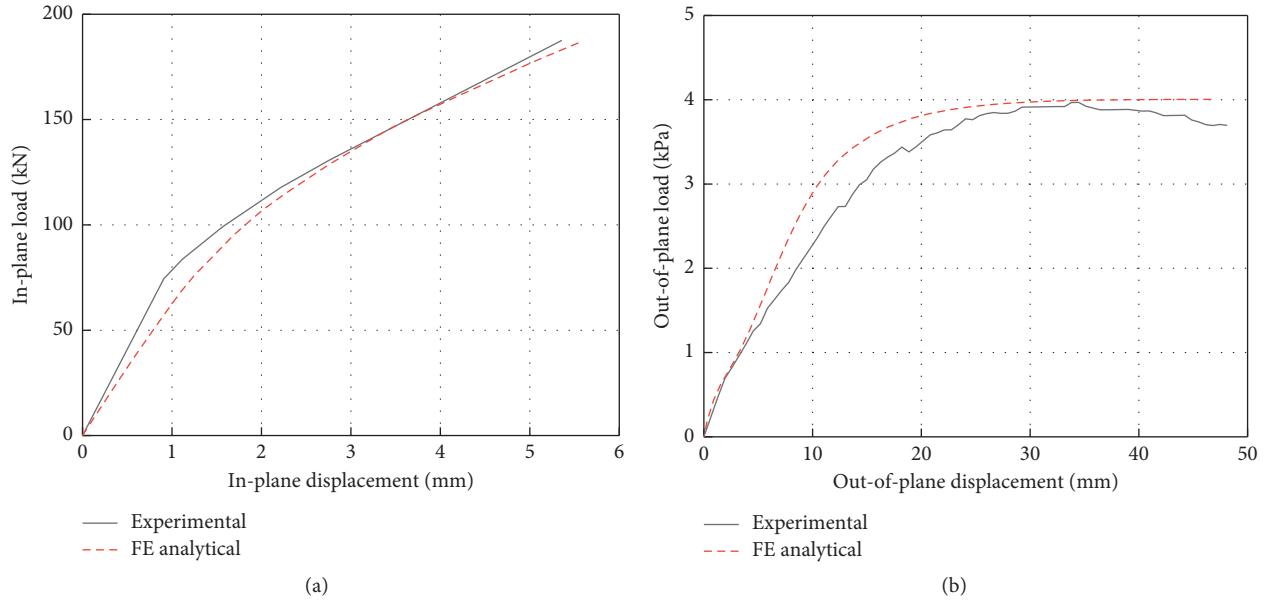


FIGURE 4: Load-displacement curves in (a) IP and (b) OOP directions.

TABLE 2: Comparison of numerical and experimental results.

	Initial stiffness (kN/mm)	Ultimate load (kN)	
IP	Analysis	33.7	187.6
	Experiment	35.0	186.4
Error (%)		3.7	0.6
OOP	Analysis	319.2	4.0
	Experiment	336.0	4.0
Error (%)		5.0	0

2.4. Sensitivity Analysis for the Finite Element Model. A sensitivity analysis has been conducted to investigate the stability of the numerical results to the modeling parameters used to describe the behavior of the masonry-infilled RC frames. The purpose of the analysis is to identify the most influential parameters and assess the reliability of nonlinear finite element modeling in view of the expected uncertainties in the modeling parameters.

This study considers the modeling parameters used for describing the behavior of the infill walls and cannot be easily obtained from the material tests. The selected parameters are varied, one at a time, to a lower and a higher value, and the range of variation reflects the level of uncertainty associated with the value of the respective parameter. The parameters considered in the study and their bounds of variation are summarized in Table 3 and Figure 5(a). The verified numerical model for specimen 2 is used as the baseline.

To quantify the influence of these parameters on the structural response, the ultimate load and initial stiffness are adopted as the structural response quantities. The percentage change of a response quantity (Q) with respect to the baseline value (Q_B) when the value of a parameter (P) is increased or decreased is used to represent the variation amplitude, which can be described as

$$C_{Q,P} = \pm \max \frac{Q - Q_B}{Q_B} \times 100\%. \quad (8)$$

In addition, the sensitivity of a response quantity to each parameter is obtained from the following formula:

$$S_{Q,P} = \max \left| \frac{Q - Q_B}{Q_B} \frac{P_B}{P - P_B} \right|. \quad (9)$$

Figures 5 and 6 show the percentage change and sensitivity of the structural response quantities, respectively. As shown in Figures 5(b) and 6(a), the percentage change and sensitivity of the ultimate load are not significant for the parameter values considered, except for the variation of the mortar interface shear stiffness perpendicular to the infill panel. In Figures 5(c) and 6(b), the percentage change and sensitivity of the initial stiffness for the variations of parameters considered are presented. The initial stiffness is most sensitive to the interface shear stiffness in two directions. Therefore, the values of these two parameters are not expected to vary considerably. In the modeling, these two parameters are set to the same value and to match the behavior of shear tests.

3. Parametric Analysis

In this section, the influence of IP damage on the OOP seismic performance of infill walls, with different aspect ratios and slenderness ratios, is investigated, using the calibrated numerical model as a reference. The effects of the aspect ratio and slenderness ratio on the OOP behavior of infill walls with IP damage are analyzed.

3.1. Effect of the Aspect Ratio. Infill walls with three different aspect ratios (height to width, H/L) of 0.44, 0.66, and 1.33 are analyzed, respectively, obtained by altering

TABLE 3: Variation of values for modeling parameters.

Parameter type	K_{nn} (N/m)	K_{ss} (N/m)	K_{tt} (N/m)	Friction factor μ	Fracture energy G^I (N·m)	Shear fracture energy G_s^{II} (N·m)	Shear fracture energy G_t^{II} (N·m)
Variation of parameter	$1e7$	$1.5e7$	$1.5e7$	0.5	7.5	75	75
	$1e8$	$1.5e8$	$1.5e8$	0.7	15	150	150
	$1e9$	$1.5e9$	$1.5e9$	0.9	30	300	300

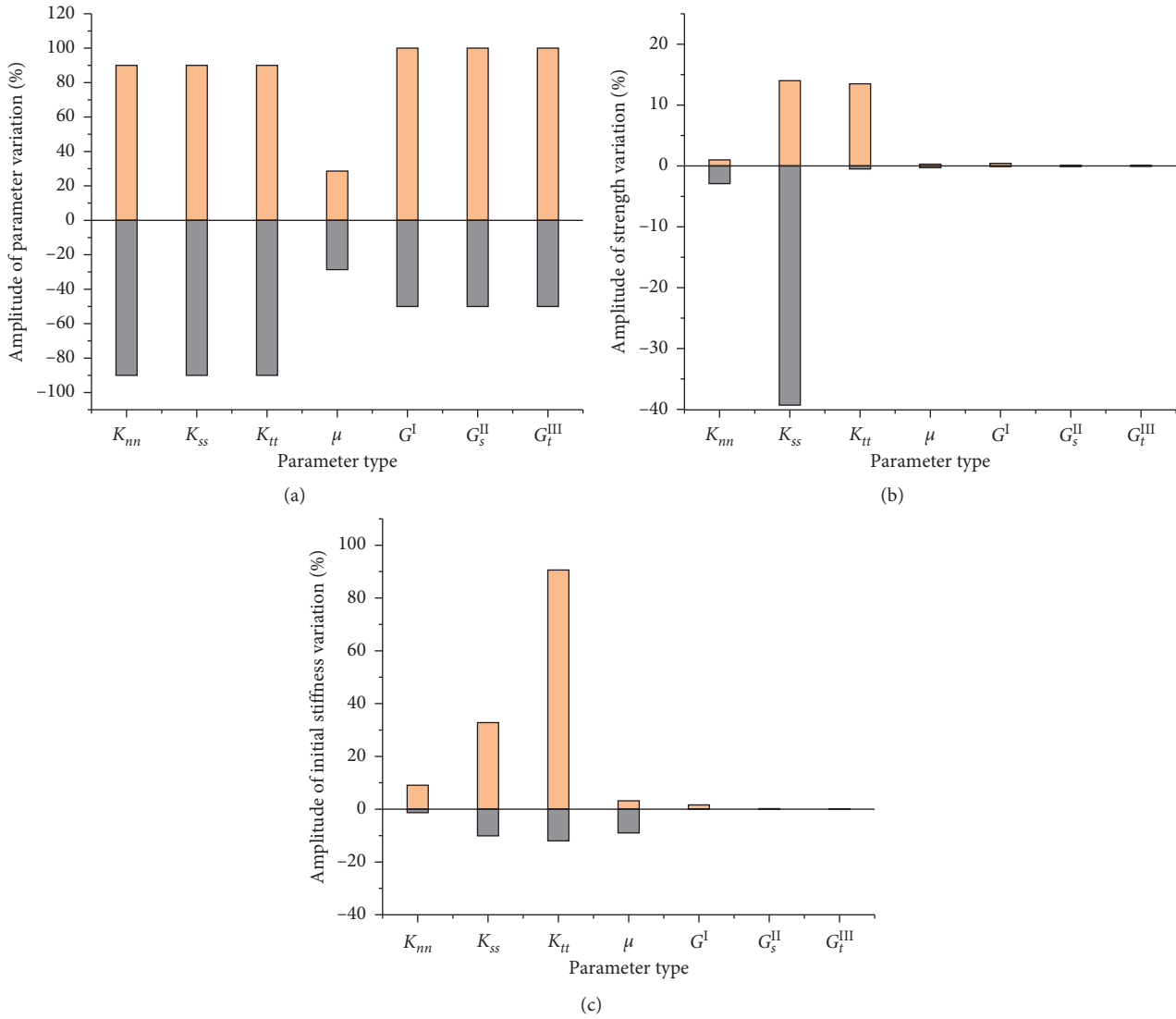


FIGURE 5: Percentage change of modeling parameters and structural response. (a) Parameter variation. (b) Ultimate load. (c) Initial stiffness.

the width of the infill wall. The height and thickness of all infill walls are 1625 mm and 58 mm, respectively. Detailed information for each analysis model is listed in Table 4. For each aspect ratio, three analyses with different IP damage levels are conducted. It should be stated that the damage level in this study is defined as the maximum IDR. The first is loaded in the OOP direction without any IP damage. The other two correspond to OOP loading, with the IP-IDRs of 0.3% and 0.7% have been first reached, respectively. Thus, nine analyses are conducted.

The ultimate load is corresponding to the load at OOP displacement of 50 mm. The stiffness is computed at the point corresponding to 20% of the ultimate load. The obtained stiffness and ultimate load are listed in Table 4. The OOP load-displacement curves for each analyzed infilled model are described in Figure 7.

3.2. *Effect of the Slenderness Ratio.* Infill walls with three different slenderness ratios (height to thickness, H/T) of 17, 26, and 34, are analyzed, respectively, obtained by altering

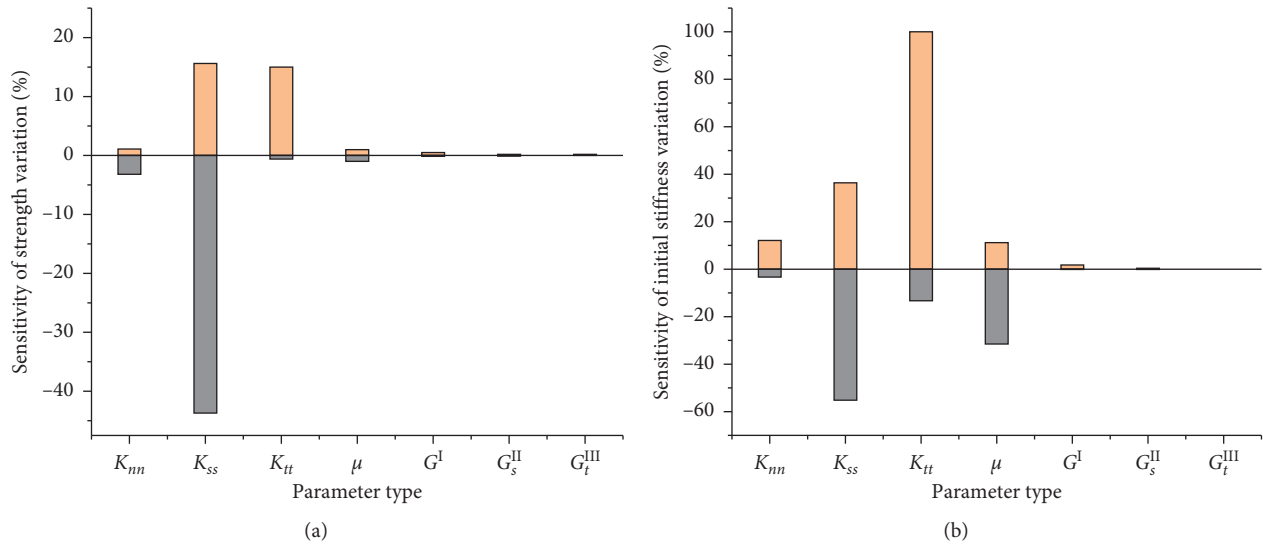


FIGURE 6: Sensitivity of structural response to modeling parameters. (a) Ultimate load. (b) Initial stiffness.

TABLE 4: The information and analysis results of infill walls with different aspect ratios.

Aspect ratio (H/L)	0.44			0.67			1.33		
Width (mm)	3658			2438			1220		
IP-IDR (%)	0	0.3	0.7	0	0.3	0.7	0	0.3	0.7
Stiffness ($\text{kN/mm} \times 10^3$)	0.08	0.02	0.01	1.23	0.31	0.15	4.23	2.28	2.07
Ultimate load (kPa)	1.4	1.1	1.0	5.3	4.0	3.1	30.6	22.9	22.6

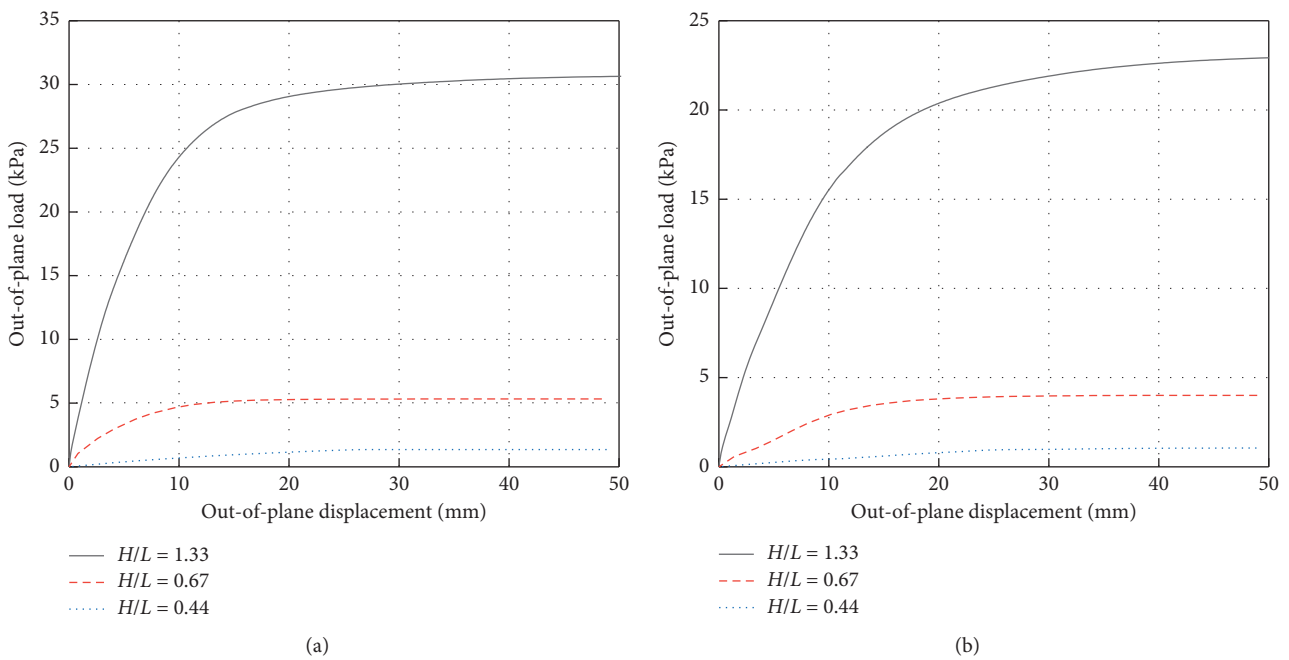


FIGURE 7: Continued.

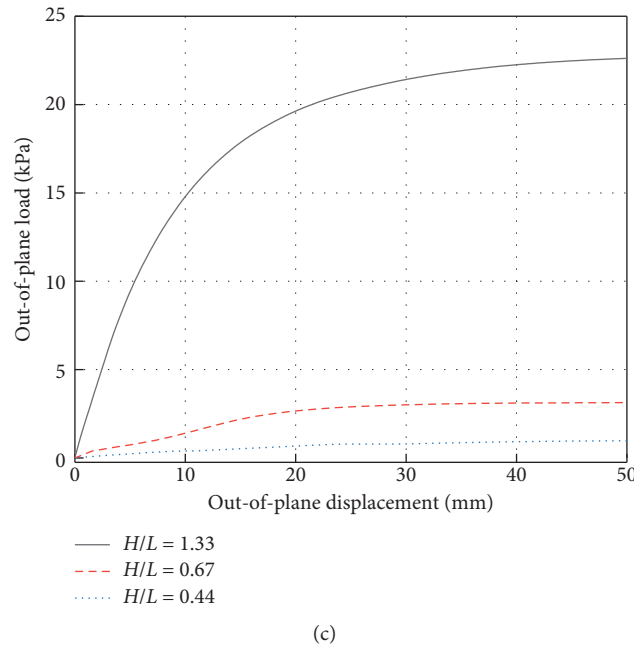


FIGURE 7: OOP load-displacement curves of infill walls with different aspect ratios. (a) Without IP damage. (b) With IP damage (IDR = 0.3%). (c) With IP damage (IDR = 0.7%).

the thickness of the infill wall. The height and width of all infill walls are 1625 mm and 2438 mm. Detailed information for different models is listed in Table 5. For each slenderness ratio, three analyses are conducted. The first is loaded in the OOP direction without IP damage. The other two correspond to OOP loading, with the IP-IDRs of 0.3% and 0.7% have been first reached, respectively. Similarly, nine analyses are conducted.

The stiffness and the ultimate load are obtained by using the same method as described above. The obtained stiffness and ultimate load are given in Table 5. The OOP load-displacement curves for each analyzed infilled model are described in Figure 8.

3.3. Effect of the Masonry Strength. In this part, infill walls with three different masonry strengths are analyzed, respectively. The values of masonry strength for analysis models are described in Table 6.

For each masonry strength, similar analyses with three different IP damage levels (without IP damage and IP-IDRs of 0.3% and 0.7%) are conducted. The obtained stiffness and ultimate load are listed in Table 6. Figure 9 shows the OOP load-displacement curves for analysis of infilled models with different IP damage levels.

4. Discussion of the Results

The relationship between the OOP ultimate load and stiffness with respect to the aspect ratio of infill walls with and without IP damage is presented in Figures 10(a) and 11(a), respectively. It is clear that the aspect ratio significantly influences the OOP performance of infilled

frames. For the infill walls with a larger aspect ratio of 1.33 (the equal height and less span), the values of OOP ultimate load for different IDRs of 0, 0.3%, and 0.7% increase 577%, 573%, and 729%, compared with that of the infill wall with the aspect ratio of 0.67, and the values of stiffness increase 344%, 735%, and 1380%. The great increase of the ultimate load and stiffness should be attributed to the effect of the arching action that can play a larger role for smaller spans.

The ratio of the ultimate load and stiffness obtained for the IP damaged wall to the value obtained for the IP undamaged wall (i.e., R_f and R_K) is computed and reported with IP-IDR in Figures 10(b) and 11(b), respectively. It can be seen that the OOP performance is significantly affected by the IP damage level. As the IP damage increases, the OOP ultimate load and stiffness rapidly decrease. In addition, the aspect ratio also has the influence on the reduction of the OOP performance. At a given IP-IDR, the ultimate load and stiffness reduction are quite lower for the infills with smaller aspect ratio (with larger span).

The relationship between the OOP ultimate load and stiffness with respect to the slenderness ratio of infill walls with and without damage is presented in Figures 12(a) and 13(a), respectively. It can reflect the influence of the slenderness ratio on the OOP performances of infill walls. In particular, for larger slenderness ratio, the ultimate load and stiffness are reduced. To be specific, the values of ultimate load for different IDRs of 0%, 0.3%, and 0.7% increase 719%, 850%, and 1042%, and the values of stiffness increase 271%, 574%, and 627%, when the results of the infill wall with the slenderness ratio of 17 are compared to that with the slenderness ratio of 34. This can be attributed to the OOP arching action that thinner infill

TABLE 5: The information and analysis results of infill walls with different slenderness ratios.

Slenderness ratio (H/T)	17			26			34		
Thickness (mm)	96			63			58		
IP-IDR (%)	0	0.3	0.7	0	0.3	0.7	0	0.3	0.7
Stiffness ($\text{kN/mm} \times 10^3$)	3.33	1.78	0.94	1.79	0.55	0.27	1.23	0.31	0.15
Ultimate load (kN)	38.1	34.0	32.3	10.6	7.8	7.2	5.3	4	3.1

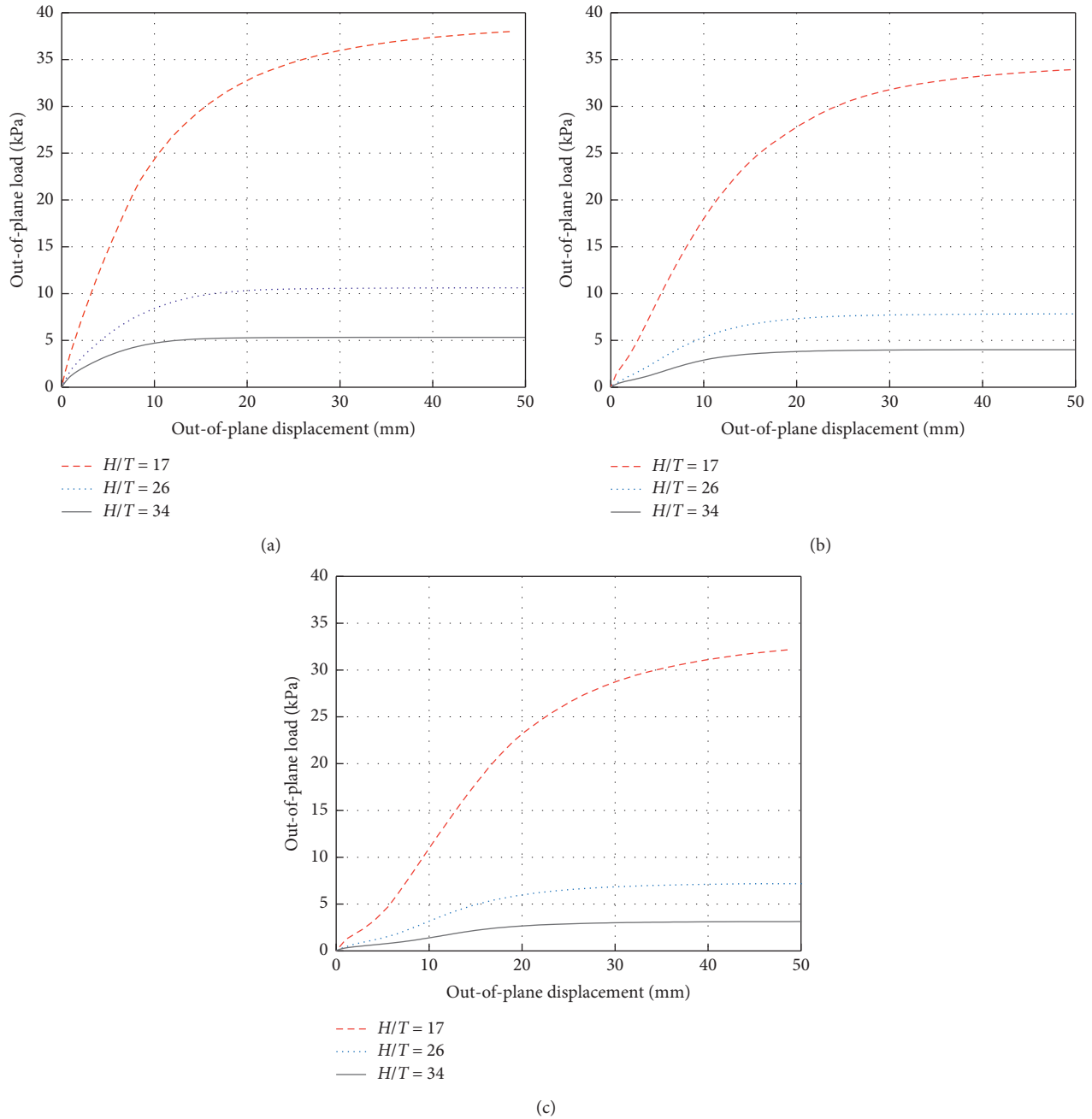


FIGURE 8: OOP load-displacement curves of infill walls with different slenderness ratios. (a) Without IP damage. (b) With IP damage (IDR = 0.3%). (c) With IP damage (IDR = 0.7%).

TABLE 6: The information and analysis results of infill walls with different masonry strengths.

Compressive strength of masonry (MPa)	4.9			10.9			16.9		
Tensile strength of masonry (MPa)	0.14			0.30			0.47		
Elastic modulus of masonry (GPa)	3.7			8.2			12.7		
IP-IDR (%)	0	0.3	0.7	0	0.3	0.7	0	0.3	0.7
Stiffness ($\text{kN/mm} \times 10^3$)	0.88	0.23	0.14	1.23	0.31	0.15	1.34	0.35	0.17
Ultimate load (kN)	2.95	2.19	1.73	5.33	4.00	3.13	6.52	5.07	4.07

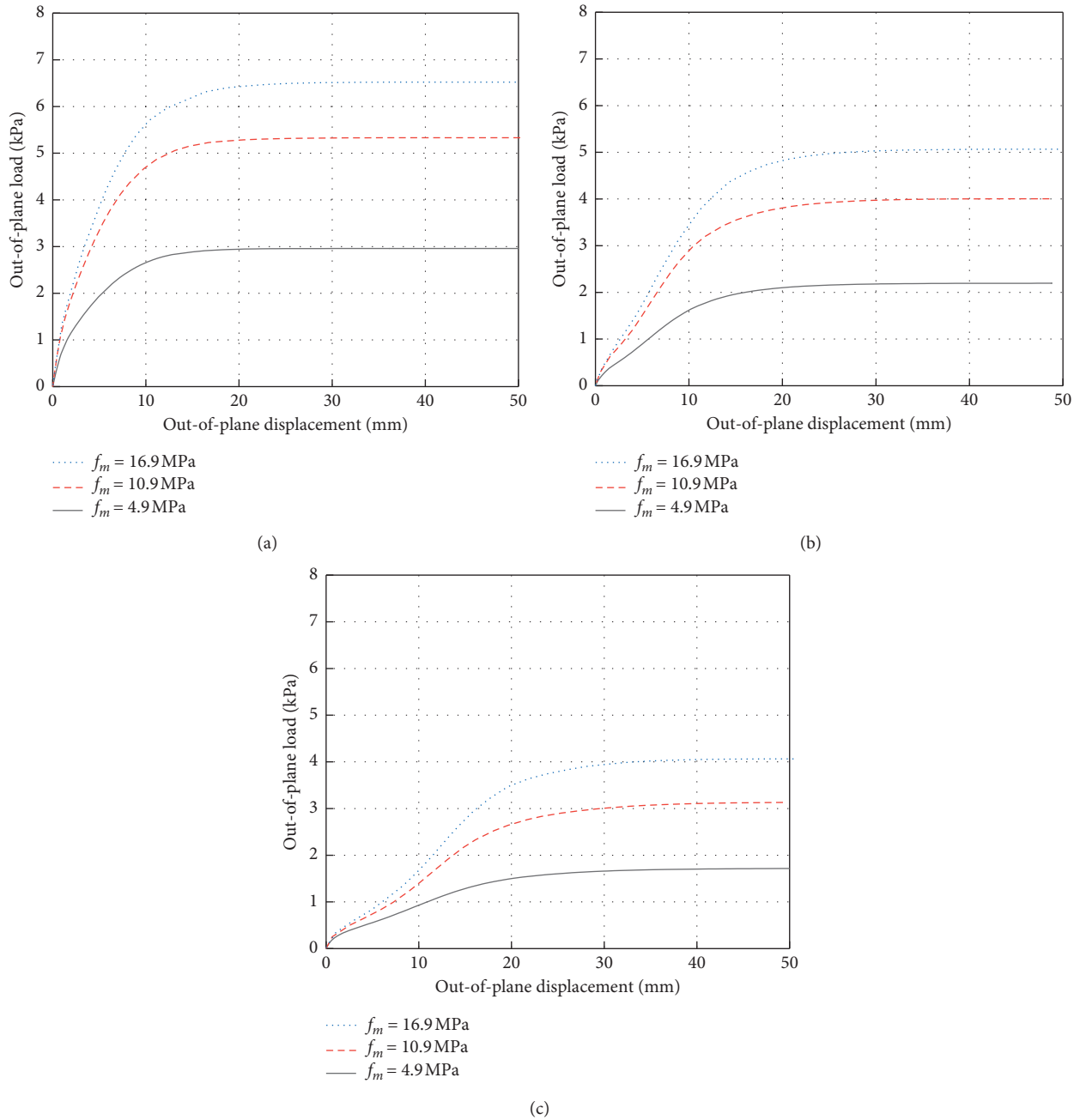


FIGURE 9: OOP load-displacement curves of infill walls with different masonry strengths. (a) Without IP damage. (b) With IP damage (IDR = 0.3%). (c) With IP damage (IDR = 0.7%).

wall is formed less obviously and the strength of masonry material is not fully utilized to resist loads. For the thicker infill wall, the contact between the wall and columns is larger and can provide more sufficient constrain to the OOP deformation of the infill wall. The ratio of the ultimate load and stiffness obtained for the IP damaged wall to the value obtained for the IP undamaged wall (i.e., R_f and R_K) is computed and reported with IP-IDR in Figures 12(b) and 13(b), respectively. It can be seen that the slenderness ratio significantly influences the IP and OOP interaction. At a given IP-IDR, the ultimate load and

stiffness are significantly reduced for the infill walls with larger slenderness ratio (with thinner infill wall). Furthermore, it shows that the values of R_f and R_K for infill walls with slenderness ratios of 26 and 34 follow a similar trend, while a significant difference is observed for the values of the infill wall with a slenderness ratio of 17. The observation is consistent with the finding in the studies of Angel et al. [7] and Ricci et al. [14].

In Figures 14(a) and 15(a), the relationship between the OOP ultimate load and stiffness with respect to the masonry strength of infill walls with and without damage is presented.

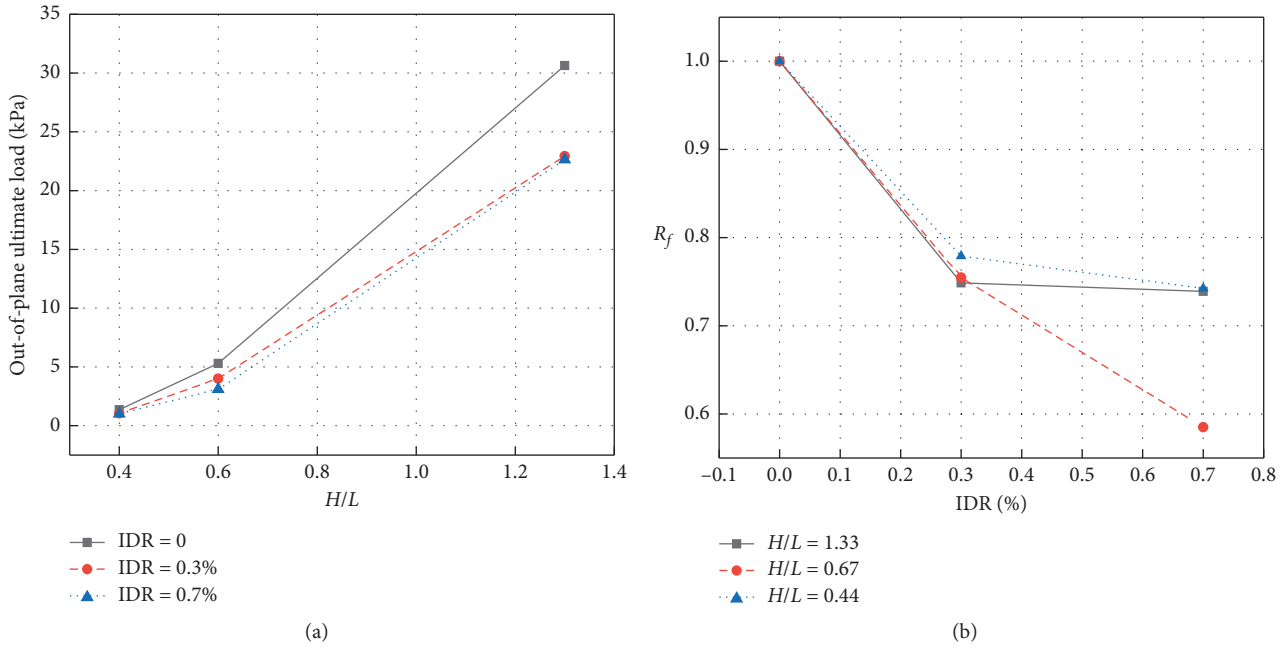


FIGURE 10: The effect (a) aspect ratio and (b) IP damage on the OOP strength of the infill wall.

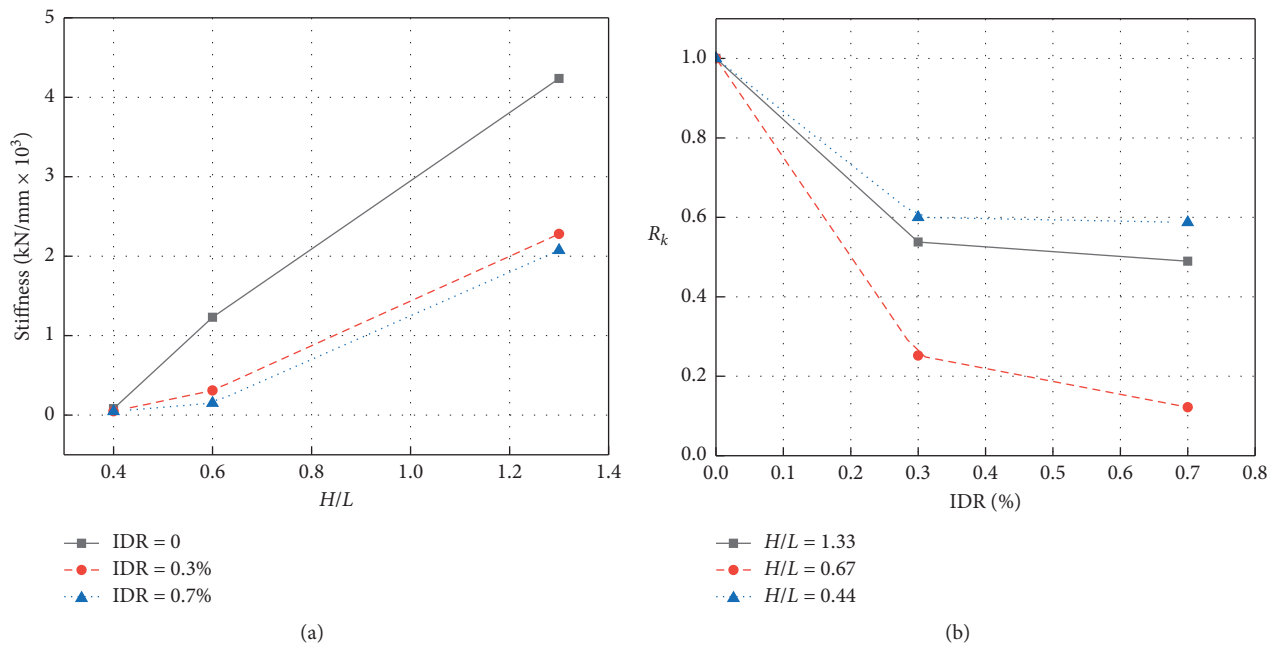


FIGURE 11: The effect of (a) aspect ratio and (b) IP damage on the OOP stiffness of the infill wall.

The ratio of the ultimate load and stiffness obtained for the IP damaged wall to the value obtained for the IP undamaged wall (i.e., R_f and R_k) is computed and reported with IP-IDR in Figures 14(b) and 15(b), respectively. It can be concluded that the masonry strength has a great influence on the OOP performance of infilled frames with and without IP damages. The increase of the masonry strength leads to the increase of both the ultimate load and stiffness. However, the influence of the masonry strength on the OOP ultimate load and stiffness reduction is not significant.

The analytical results are compared with value provided in the New Zealand code [35] and the prediction developed by Angel et al. [7], Ricci et al. [14], and Zizzo et al. [25] in Figure 16. The slenderness ratio plays a most important role on the interaction of IP and OOP performance of the infill wall. However, the influence of masonry strength and aspect ratio is not that obvious. The reduction factors of the infill wall with different slenderness ratios tend to approximate the value in the New Zealand code [35] with IDR increasing. In other words, the value provided by the New Zealand code

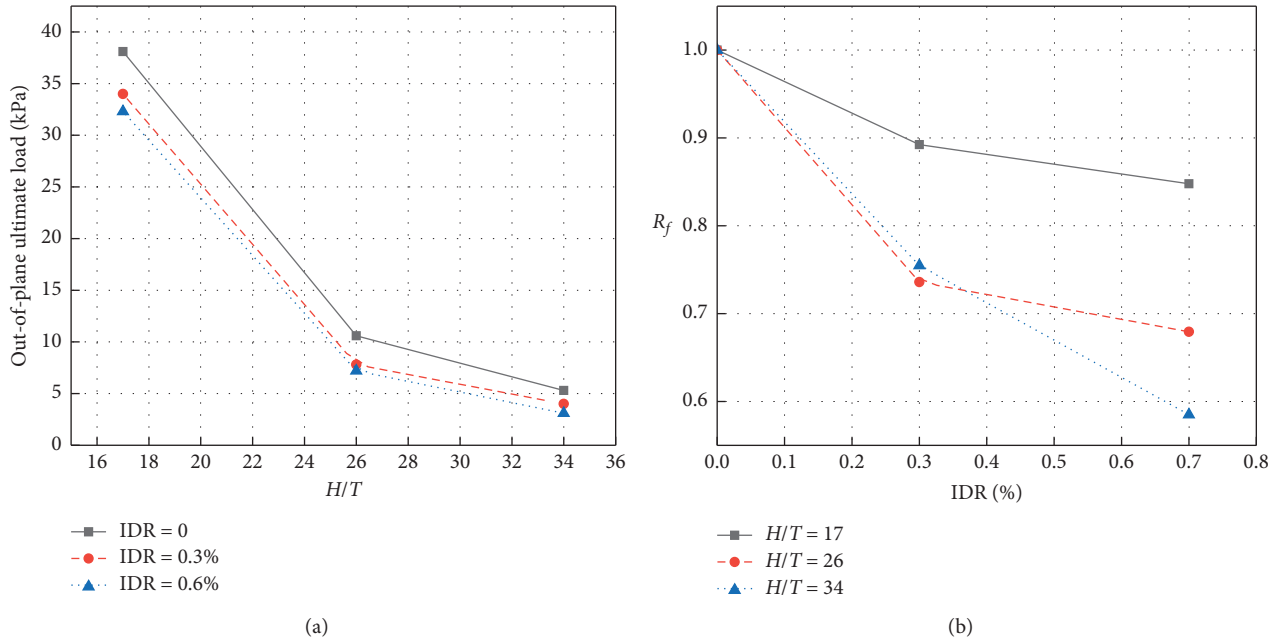


FIGURE 12: The effect of (a) slenderness ratio and (b) IP damage on the OOP strength of the infill wall.

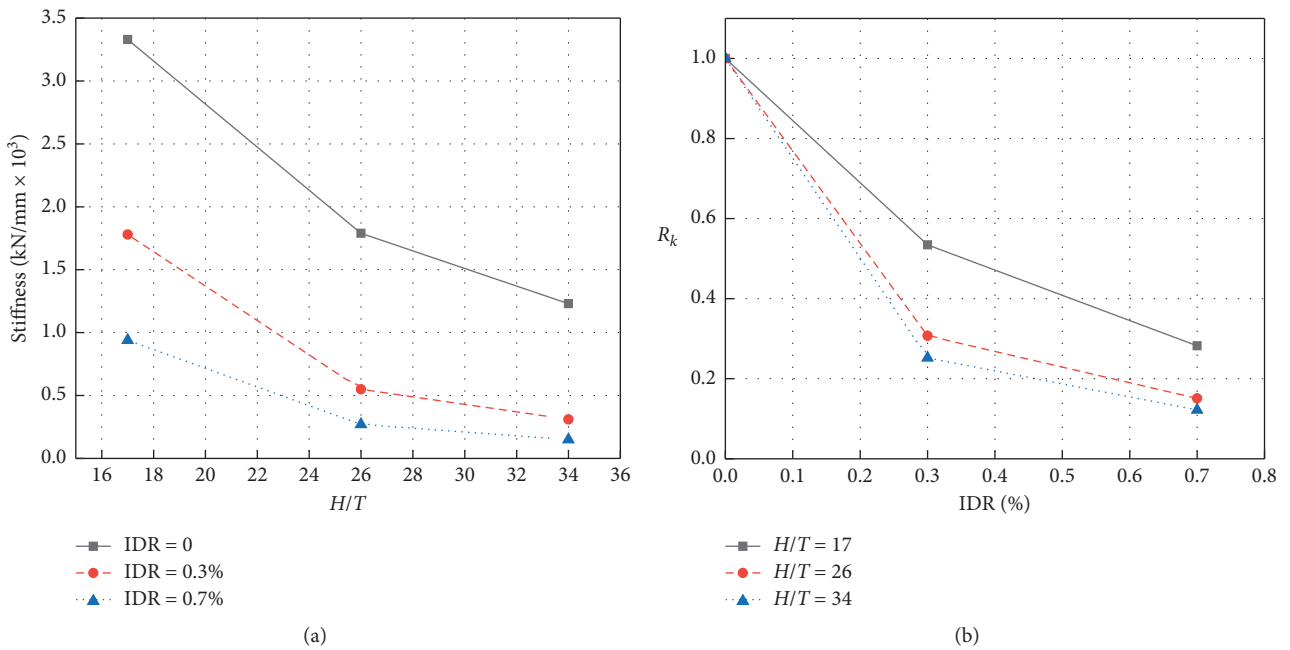


FIGURE 13: The effect (a) slenderness ratio and (b) IP damage on the OOP stiffness of the infill wall.

[35] is similar to the lower bound in this paper. However, the predictions in literatures [7, 14, 25] are quite different with the analytical result in this paper. This can be attributed to the experimental fact that the specimen without IP damage in the study of Angel et al. [7] is different from that with IP damage. The performance of the mortar in the specimen without IP damage is better comparing with that in the specimen with IP damage, which results in a higher ultimate load for the specimen without IP damage and a lower

reduction ratio. However, the analytical models in this paper are exactly the same to each other. So the ultimate load without IP damage in this numerical investigation is lower than the experimental one, and the reduction ratio seems to be higher. Furthermore, the infill walls in literature [14, 25] are quite weak, and the masonry block will be damaged severely with relatively small IDR. However, the OOP behavior is influenced significantly by the IP masonry block damage. So, with a small IDR, the ultimate OOP load

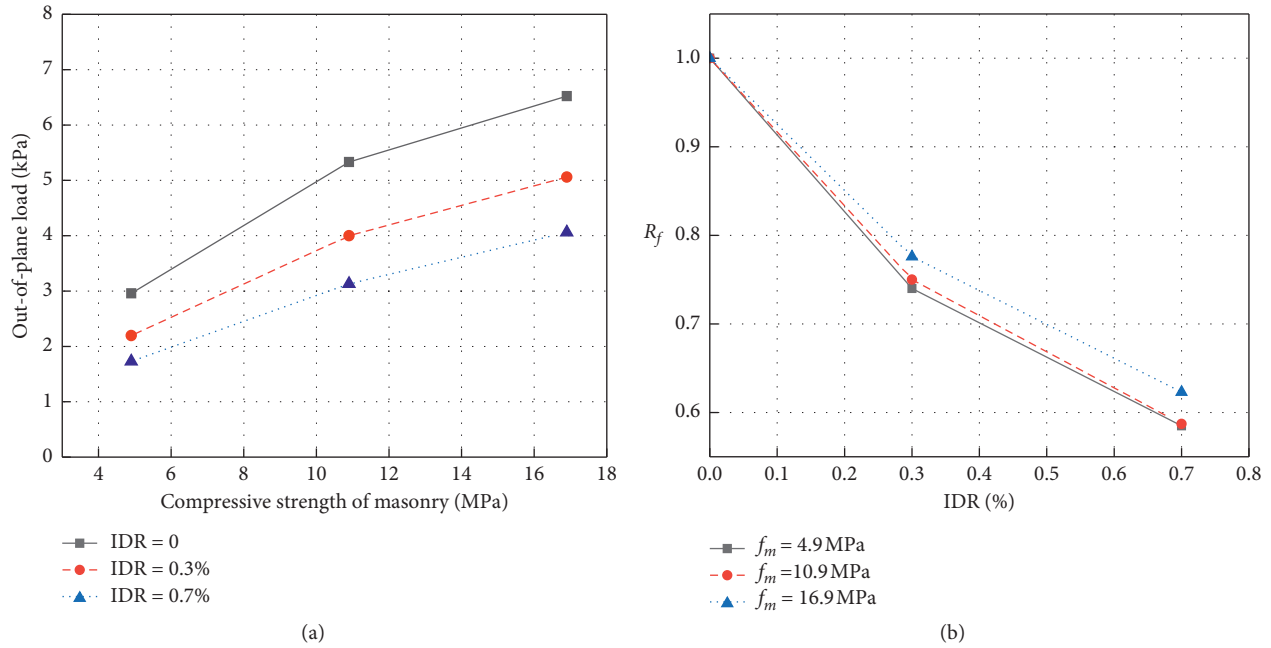


FIGURE 14: The effect (a) masonry strength and (b) IP damage on the OOP strength of the infill wall.

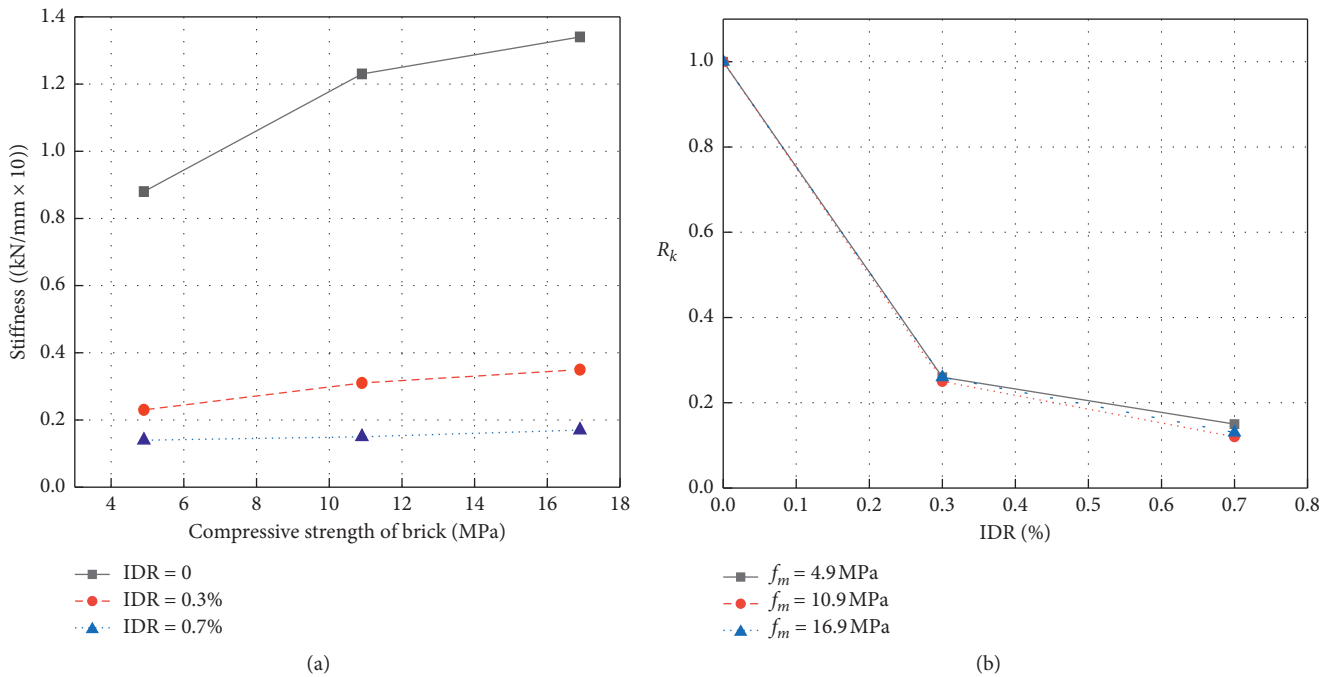


FIGURE 15: The effect (a) masonry strength and (b) IP damage on the OOP stiffness of the infill wall.

decreased obviously due to the severe IP damage, which results in a much lower reduction ratio.

5. Conclusions

This manuscript presents a 3D finite element modeling strategy to investigate OOP seismic behavior of masonry infill walls considering the existed IP damage. A numerical

model for an experiment in the literature is established and calibrated. Then using the calibrated model as a reference, the effect of aspect ratio, slenderness ratio, and masonry strength on the IP and OOP interaction of infill walls is studied. Finally, the strength and stiffness reduction by the IP-IDR, considering the effect of aspect ratio, slenderness ratio, and masonry strength, is discussed. The following conclusions are drawn from this study:

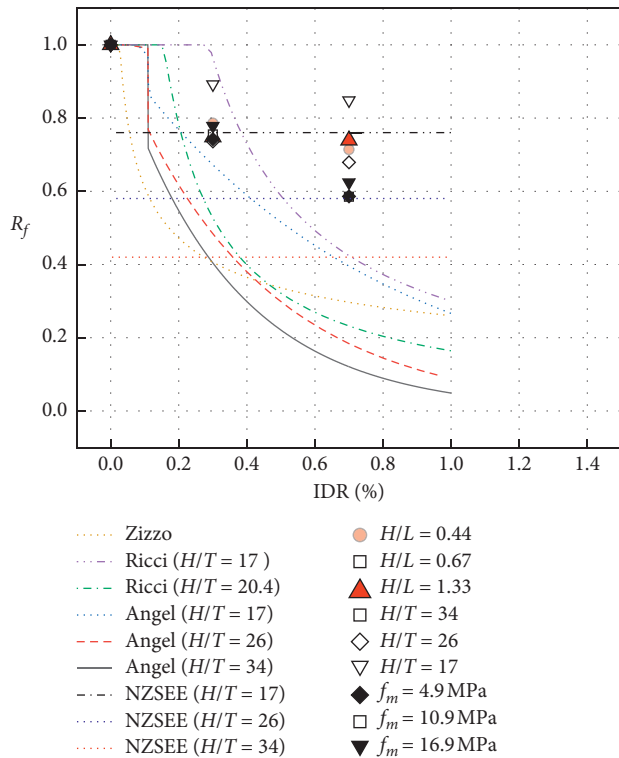


FIGURE 16: Comparison of the strength reduction factor of infill walls.

- (1) The IP damage of the infill wall influences the OOP seismic performance significantly, including the OOP stiffness and ultimate load. The ultimate load will be decreased to less than 60% of the capacity of that only OOP loaded, as the result of the IP damage.
- (2) The OOP load capacity and stiffness will be reduced due to the decrease of aspect ratio since the OOP arch action will get weak in the wider infill wall. The aspect ratio influences the reducing effect of the IP damage to the OOP seismic performance. So the aspect ratio should be considered in the evaluation of the effect of the IP damage in the future work.
- (3) The OOP load capacity and stiffness will be reduced as there is increase in the slenderness ratio since the arching action does not form that well as the thicker infill wall. The effect of IP damage on the OOP seismic performance is more obvious due to the increase of the slenderness ratio.
- (4) The masonry strength has a great influence on the OOP performance of infilled frames with and without IP damages. The increase of the masonry strength leads to the increase of both the ultimate load and stiffness. However, the influence of the masonry strength on the OOP ultimate load and stiffness reduction is not significant.

The work in this paper is the preliminary research. Since the OOP test is loading controlled, descending of load capacity cannot be obtained. Thus, the finite element model should be improved in the future. In addition, a simplified

modeling technology should be proposed, which can simultaneously consider the IP and OOP seismic performance of infill walls. Thus, the behavior of infill walls in the earthquake event could be considered reasonably in the seismic analysis of RC frames.

Data Availability

The data of numerical results used to support the findings of this study can be obtained by contacting the corresponding author mailto: via email.

Conflicts of Interest

The authors declare that there are no conflicts of interest regarding the publication of this paper.

Acknowledgments

This investigation was supported by Scientific Research Fund of Institute of Engineering Mechanics, China Earthquake Administration (Grant Nos. 2018D15 and 2019D09), the National Nature Science Foundation of China (Nos. 51808478 and 51908484), and the Natural Science Foundation of Shandong (Nos. ZR2019QEE033 and ZR2019BEE039). These supports are greatly appreciated.

References

- [1] F. G. Thomas, "The strength of brickwork," *Structural Engineering*, vol. 31, no. 2, pp. 35–46, 1953.
- [2] E. L. Mc Dowell, K. E. Mc Kee, and E. Sevin, "Arching action theory of masonry walls," *Journal of the Structural Division*, vol. 82, no. 2, pp. 1–8, 1956.
- [3] J. L. Dawe and C. K. Seah, "Out-of-plane resistance of concrete masonry infilled panels," *Canadian Journal of Civil Engineering*, vol. 16, no. 6, pp. 854–864, 1989.
- [4] A. Dafnis, H. Kolsch, and H.-G. Reimerdes, "Arching in masonry walls subjected to earthquake motions," *Journal of Structural Engineering*, vol. 128, no. 2, pp. 153–159, 2002.
- [5] Y. H. Tu, P. M. Liu, and H. P. Lin, "OOP seismic behavior of unreinforced masonry in-filled walls," in *Proceedings of the Structures Congress: New Horizons and Better Practices*, pp. 1–10, Long Beach, CA, USA, May 2007.
- [6] Y.-H. Tu, T.-H. Chuang, P.-M. Liu, and Y.-S. Yang, "Out-of-plane shaking table tests on unreinforced masonry panels in RC frames," *Engineering Structures*, vol. 32, no. 12, pp. 3925–3935, 2010.
- [7] R. Angel, D. P. Abrams, D. Shapiro, J. Uzarski, and M. Webster, "Behavior of reinforced concrete frames with masonry infills," Technical Report, University of Illinois Engineering Experiment Station. College of Engineering. University of Illinois at Urbana-Champaign., Urbana, Ill, USA, 1994.
- [8] R. D. Flanagan and R. M. Bennett, "Bidirectional behavior of structural clay tile infilled frames," *Journal of Structural Engineering*, vol. 125, no. 3, pp. 236–244, 1999.
- [9] R. D. Flanagan and R. M. Bennett, "Arching of masonry infilled frames: comparison of analytical methods," *Practice Periodical on Structural Design and Construction*, vol. 4, no. 3, pp. 105–110, 1999.
- [10] G. M. Calvi and D. Bolognini, "Seismic response of reinforced concrete frames infilled with weakly reinforced masonry

- panels,” *Journal of Earthquake Engineering*, vol. 5, no. 2, pp. 153–185, 2001.
- [11] J. S. Kuang and Y. P. Yuen, “Effect of OOP loading on IP behavior of unreinforced infilled RC frames,” in *Proceedings of the International Conference on Computing in Civil and Building Engineering*, Nottingham, UK, June 2010.
 - [12] M. F. P. Pereira, M. F. N. Pereira, J. E. D. Ferreira, and P. B. Lourenco, “Behavior of masonry infill panels in RC frames subjected to in plane and out of plane loads,” in *Proceedings of the 7th International Conference on Analytical Models and New Concepts in Concrete and Masonry Structures*, Krakow, Poland, June 2011.
 - [13] S. Hak, P. Morandi, and G. Magenes, “OOP experimental response of strong masonry infills,” in *Proceedings of the European Conference on Earthquake Engineering and Seismology*, pp. 139–144, Istanbul, Turkey, June 2014.
 - [14] P. Ricci, M. Di Domenico, and G. M. Verderame, “Empirical-based out-of-plane URM infill wall model accounting for the interaction with in-plane demand,” *Earthquake Engineering & Structural Dynamics*, vol. 47, no. 3, pp. 802–827, 2018.
 - [15] P. Ricci, M. Di Domenico, and G. M. Verderame, “Experimental investigation of the influence of slenderness ratio and of the in-plane/out-of-plane interaction on the out-of-plane strength of URM infill walls,” *Construction and Building Materials*, vol. 191, no. 12, pp. 507–522, 2018.
 - [16] F. da Porto, G. Guidi, M. Dalla Benetta, and N. Verlato, “Combined IP/OOP experimental behaviour of reinforced and strengthened infill masonry walls,” in *Proceedings of the 12th Canadian Masonry Symposium*, Vancouver, Canada, June 2013.
 - [17] M. T. de Risi, M. Di Domenico, P. Ricci, G. M. Verderame, and G. Manfredi, “Experimental investigation on the influence of the aspect ratio on the in-plane/out-of-plane interaction for masonry infills in RC frames,” *Engineering Structures*, vol. 189, no. 6, pp. 523–540, 2019.
 - [18] O. Rabinovitch and H. Madah, “Finite element modeling and shake-table testing of unidirectional infill masonry walls under out-of-plane dynamic loads,” *Engineering Structures*, vol. 33, no. 9, pp. 2683–2696, 2011.
 - [19] C.-H. Zhai, J.-C. Kong, X.-M. Wang, and X.-H. Wang, “Finite-element analysis of out-of-plane behaviour of masonry infill walls,” *Proceedings of the Institution of Civil Engineers—Structures and Buildings*, vol. 171, no. 3, pp. 203–215, 2018.
 - [20] A. Mohyeddin, H. M. Goldsworthy, and E. F. Gad, “FE modelling of RC frames with masonry infill panels under in-plane and out-of-plane loading,” *Engineering Structures*, vol. 51, pp. 73–87, 2013.
 - [21] Y. P. Yuen and J. S. Kuang, “Masonry-infilled rc frames subjected to combined in-plane and out-of-plane loading,” *International Journal of Structural Stability and Dynamics*, vol. 14, no. 02, p. 1350066, 2014.
 - [22] G. M. Mohammadi, “Out of plane strength of infill panels,” in *Proceedings of the 14th World Conference on Earthquake Engineering*, Beijing, China, October 2008.
 - [23] N. Verlato, G. Guidi, and F. da Porto, “Experimental testing and numerical modelling of infill masonry walls subjected to IP damage,” in *Proceedings of the Second European Conference on Earthquake Engineering and Seismology*, pp. 25–29, Istanbul, Turkey, August 2014.
 - [24] P. Agnihotri, V. Singhal, and D. C. Rai, “Effect of in-plane damage on out-of-plane strength of unreinforced masonry walls,” *Engineering Structures*, vol. 57, pp. 1–11, 2013.
 - [25] M. Zizzo, L. Cavaleri, and F. Di Trapani, “Out of plane capacity of infills after in plane loading: a prediction analytical model,” in *Proceedings of the COMPDYN 2019 7th ECCOMAS Thematic Conference on Computational Methods in Structural Dynamics and Earthquake Engineering*, Crete, Greece, June 2019.
 - [26] S. Kadsiewski and K. M. Mosalam, “Modeling of Unreinforced Masonry Infill Walls Considering IP and OOP interaction,” in *Proceedings of the 11th Canadian Masonry Symposium*, Toronto, Ontario, June 2009.
 - [27] K. M. Mosalam and S. Günay, “Progressive collapse analysis of reinforced concrete frames with unreinforced masonry infill walls considering in-plane/out-of-plane interaction,” *Earthquake Spectra*, vol. 31, no. 2, pp. 921–943, 2015.
 - [28] A. Furtado, H. Rodrigues, A. Arède, and H. Varum, “Simplified macro-model for infill masonry walls considering the out-of-plane behaviour,” *Earthquake Engineering & Structural Dynamics*, vol. 45, no. 4, pp. 507–524, 2016.
 - [29] A. Furtado, H. Rodrigues, A. Arède, and H. Varum, “Influence of the in plane and out-of-plane masonry infill walls’ interaction in the structural response of RC buildings,” *Procedia Engineering*, vol. 114, pp. 722–729, 2015.
 - [30] F. Di Trapani, P. B. Shing, and L. Cavaleri, “Macroelement model for IP and OOP responses of masonry infills in frame structures,” *Journal of Structural Engineering*, vol. 144, no. 2, Article ID 04017198, 2018.
 - [31] P. Morandi, S. Hak, and G. Magenes, “Simplified OOP resistance verification for slender clay masonry infills in RC frames,” in *Proceedings of the XV ANIDIS, L’Ingegneria Sismica in Italia*, Padua, Italy, July 2013.
 - [32] M. Pasca, L. Liberatore, and R. Masiani, “Reliability of analytical models for the prediction of OOP capacity of masonry infills,” *Structural Engineering and Mechanics*, vol. 64, no. 6, pp. 765–781, 2017.
 - [33] P. B. Lourenço and J. G. Rots, “Multisurface interface model for analysis of masonry structures,” *Journal of Engineering Mechanics*, vol. 123, no. 7, pp. 660–668, 1997.
 - [34] G. Q. Liu, *The Research on the Basic Mechanical Behavior of Masonry structure*, Hunan University, Changsha, China, 2005, in Chinese.
 - [35] NZSEE 2017. New Zealand Society for Earthquake Engineering (NZSEE), Structural Engineering Society New Zealand Inc. (SESOC), New Zealand geotechnical society inc., Ministry of business, innovation and employment, earthquake commission. The Seismic Assessment of Existing Buildings (The Guidelines), Part C – Detailed Seismic Assessment, 2017.

Research Article

Seismic Performance Evaluation of Modern Bare and Masonry-Infilled RC SMRF Structures

M. E. Ahmad, N. Ahmad , S. Pervez, A. Iqbal, A. Z. Khan, M. E. Rahim, W. Hassan, K. Umer, and K. Khan

Department of Civil Engineering, UET Peshawar, Peshawar, KP, Pakistan

Correspondence should be addressed to N. Ahmad; naveed.ahmad@uetpeshawar.edu.pk

Received 30 July 2019; Revised 12 August 2019; Accepted 30 August 2019; Published 30 October 2019

Guest Editor: André Furtado

Copyright © 2019 M. E. Ahmad et al. This is an open access article distributed under the Creative Commons Attribution License, which permits unrestricted use, distribution, and reproduction in any medium, provided the original work is properly cited.

Improper execution of modern code-designed structures in many developing countries have resulted in significant deficient building stock; low strength of concrete, reduced reinforcement, inappropriate detailing of beam-column members, and lack of lateral ties in joint panels. Observations based on earthquake-induced damages and experimental studies conducted on such buildings have revealed significant vulnerability of beam-column joints of bare moment-resisting frame structures. Shake table tests were conducted on selected three 1:4 reduced-scale three-story reinforced concrete (RC) moment-resisting frames, including one bare RC frame and two masonry-infilled RC frames, having relatively lower bay width-to-height ratio. The models were tested under multilevels of seismic excitations using natural acceleration time history of 1994 Northridge and also free vibration tests, to acquire the models' dynamic characteristics, i.e., frequencies and elastic viscous damping, and seismic response parameters, i.e., roof displacement, interstory drift and interstory shear, and seismic response curves, in order to understand the role of masonry infill in the selected frames under moderate seismic actions. The inclusion of masonry infill avoided joint shear hinging of the frame. Additionally, the infill provided energy dissipation to the structure through masonry sliding over multiple cracks. This enabled the structure to control seismic displacement demand and resist relatively higher ground motions, yet limiting structural damages.

1. Introduction

The damaged buildings and the resulting casualties observed in majority of the past earthquakes have provided ample evidence that the existing deficient reinforced concrete buildings, those nonconforming to modern seismic codes, are vulnerable against earthquake-imposed actions [1–6]. These observations have revealed that substandard materials (low-strength concrete, reduced size, and low-quality re-bars), reduced reinforcement and improper detailing, inadequate anchorage of beam reinforcement in joints, and joints lacking confining ties are major factors causing damage and early collapse of buildings under seismic excitations. Despite the modern nature of reinforced concrete constructions, execution of specified designs in the field still remains a challenge in many developing countries. This has resulted in significant construction deficiencies in the

existing building stock. Such vulnerable building stock constitutes a life-safety risk that must be reduced for future earthquakes to avoid socioeconomic disruption. It is worth mentioning that a significant fraction of these structures do not have to be completely replaced; instead, cost-effective rehabilitation techniques can be utilized for seismic upgradation of existing structures [7–19].

Earthquakes always cause damage to deficient RC frame structures in a more complex manner, unlike the more desirable plastic mechanisms observed in code-conforming structures. Most of the time, computation of dynamic properties of deficient structures using simplified analytical procedures is not very accurate, although sufficiently accurate for code-conforming models. The purpose of this research is to understand the seismic behavior of deficient RC special moment-resisting frame (SMRF) structures subjected to seismic excitations, obtain elastic dynamic

properties of considered structures through free vibration tests, and comprehend the role of masonry infill in limiting structural damages in deficient moment-resisting frame structures.

Shake table tests were conducted on a three-story RC bare frame having weaker beam-column joints, which is representative of modern frame structures found in developing countries, and two three-story masonry-infilled RC frames, with the aim to study the effect of masonry infill in improving the seismic behavior of RC moment-resisting frame structures and, further, to obtain the models' seismic response parameters.

2. Experimental Program

2.1. Description of Test Models. Three-story one-bay by one-bay frame structures were considered for investigation, including an RC bare frame and two masonry-infilled RC frames (Figure 1). A frame with relatively lower bay width-to-height aspect ratio was considered. The beams have a cross section of 24 inch \times 15 inch (610 mm \times 381 mm) and clear length of 9.50 feet (289.56 cm) and 13.50 feet (411.48 cm) in the N-S and E-W directions, respectively. The columns have a cross section of 15 inch \times 15 inch (381 mm \times 381 mm) and an interstory height of 9.0 feet (274.32 cm). The frame also included infills of solid brick masonry having thickness of 9 inch (228.60 mm). The structural frame was analyzed using the lateral static force procedure given in the BCP-SP [20] for highest seismic hazard zones, which refers to seismic Zone 4 (PGA = 0.40 g), and designed to the ACI-318 [21] recommendations for SMRF structure. The structure design was carried out in the finite element-based software ETABS CSI [22], considering all the load combinations for dead, live, and earthquake loads given in the BCP-SP [20] for commercial and public buildings. Concrete with a compressive strength of 3000 psi (21 MPa) and steel rebars with an yield strength of 60,000 psi (414 MPa) were considered in the design.

In the test model construction, lateral ties were not provided in the beam-column joints, which is a common construction deficiency observed in recent SMRF structures in most of the developing countries [23]. Additionally, concrete with a compressive strength of 2500 psi (17.24 MPa) was used, and longitudinal reinforcement ratio of beam was reduced by 25%. Furthermore, due to the introduction of confined masonry construction technique in the region, the construction sequence of masonry-infilled RC frames has been modified. The present research considered the conventional masonry-infilled RC frame that involved the construction of bare frame, which was then provided with masonry infill. Additionally, a *hybrid* masonry-infilled RC frame was considered, which involved the construction of RC columns, followed by the construction of masonry infill. In the later construction, beams and slabs were casted simultaneously after the masonry infill construction is completed. The beams in this construction are directly placed on the top of masonry infill. Masonry panels in the latter acts like a loadbearing walls since it is carrying both gravity and lateral loads.

2.2. Testing of Masonry-Infill Constituent Materials and Subassemblies. Basic tests were conducted on masonry constituent materials for the estimation of mechanical properties of masonry infill. Figure 2 shows the reduced scale masonry brick unit and wallettes prepared for basic testing. These included tests on brick units, mortar, masonry prisms, and masonry wallettes. Mechanical properties such as compressive strength, in-plane shear, and diagonal tensile strength were determined. The tests were performed according to the standard testing procedures, given as follows: ASTM C-67-06 for testing of masonry units, ASTM C109/C109M-08 for testing of mortar cubes, ASTM C-1314-07 for testing of masonry prisms, and E-519-02 and RILUM LUM B6 for testing of masonry wallettes. Table 1 reports the basic mechanical properties of masonry used for infill in test structures.

2.3. Shake Table Testing of 1 : 4 Reduced-Scale Models

2.3.1. Construction of 1 : 4 Reduced-Scale Test Models. Simple model idealization was adopted to construct 1 : 4 reduced-scale test models. The models' linear dimensions were reduced by a scale factor $S_L = 4.0$. However, the mechanical properties of constituent materials (i.e., rebars, concrete, and masonry) remained the same. Concrete for the 1 : 4 reduced-scale model was prepared with a mix proportion of cement, sand, and 3/8 inch (9 mm) down coarse aggregate. This takes into account the aggregate scaling requirements, and also, achieves the desired concrete strength of 2500 psi (17.24 MPa). A supplemental mass of 400 kg per floor was added to cause significant nonlinearity in the bare frame model subjected to seismic excitations. Tables 2 and 3 report various properties of the designed prototype models and its corresponding reduced scale model. Concrete strength and number of rebars in beam-column members were reduced in the test models in order to take into account the construction deficiencies as observed in the field. The model-to-prototype conversion factors are also listed, which are essential to convert the measured quantities of the reduced-scale model to the corresponding prototype model.

2.3.2. Input Excitations and Test Model Instrumentation Plan. The models were tested using natural acceleration time history for base excitation and free vibration tests. A natural acceleration time history of 1994 Northridge earthquake, particularly the horizontal component recorded at 090 CDMG Station 24278, was extracted from the PEER strong motions database (Figure 3). This record was selected after careful analysis of the number of accelerograms for earthquakes generated by reverse faulting. This record has a maximum acceleration of 0.57 g, maximum velocity of 518 mm/sec, and maximum displacement of 90 mm. The accelerogram time step was reduced by a scale factor of $\sqrt{4}$, shrinking the time duration required for model excitation. The input acceleration of the model was linearly scaled using scaling factors from 0.05 to 2.5 times in order to scale the amplitude of input acceleration to multilevels. The input acceleration amplitude multiplied by a scale factor of 1.0 and 2.50 are referred as NR1 and NR2, respectively.

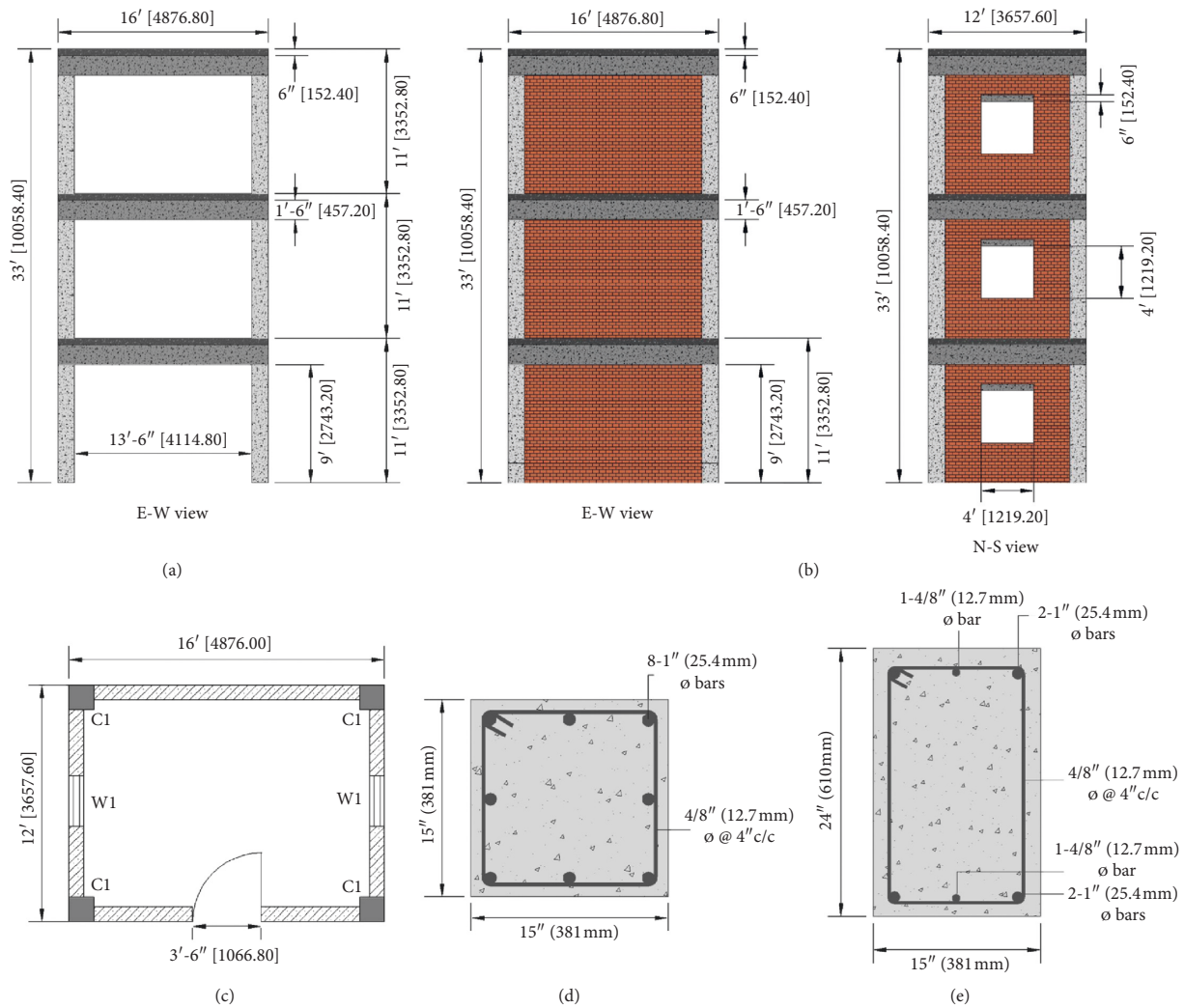


FIGURE 1: Geometric and reinforcement details of the prototype frames. The dimensions in brackets are given in mm. (a) RC bare frame (b) Masonry-infilled RC frame. (c) Plane view. (d) Column X-section. (e) Beam X-section.



FIGURE 2: Brick masonry unit and wallettes used for basic testing of masonry constituents. (a) Masonry wallettes. (b) Brick unit.

The test models were instrumented with accelerometers and displacement transducers at the base and floor levels, in order to record the actual input acceleration time history at the base of the model and floors' acceleration and displacement response (Figure 4).

2.4. Observed Seismic Behavior of Tested Models. Typically, frames conforming to seismic codes have been observed with beam-sway mechanism, i.e., experience flexure yielding

at the beam ends and slight flexure cracking at the bottom end of columns at the ground story under input excitation representative of design basis earthquake [24]. Unlike the code-conforming structures, deficient models have been observed with flexure cracking also in columns and severe damages in joint panels under input excitation well below the design-basis earthquake [7, 24]. The use of low-strength concrete and the lack of lateral ties in joint panels, along with improper reinforcement and detailing, have resulted in the

TABLE 1: Mechanical properties of masonry used for infills in 1 : 4 reduced-scale models.

S. no.	Test	Samples	Properties	Mean value	Std. dev.
1	Compression tests on mortar cubes as per ASTM C-109	6	$f_{m,m}$ (MPa)	12.35	0.45
2	Initial rate of absorption tests on brick masonry units as per ASTM C-67	6	IRA (gm/min/30 in ²)	34.50	7.35
3	Water absorption tests on brick masonry units as per ASTM C-67	6	WA (%)	10.42	1.27
4	Compression tests on brick masonry units as per ASTM C-67	6	$f_{m,b}$ (MPa)	9.87	1.33
5	Compression tests on masonry column prisms as per ASTM C-1314	4	f_m (MPa)	4.22	0.85
6	Compression tests on masonry prisms (305 mm × 305 mm) as per ASTM C-1314	4	f_m (MPa)	4.05	0.17
7(a)	Direct in-plane shear tests on masonry wallettes (305 mm × 305 mm) as per the RILEM specifications	4	T_0 (MPa)	0.36	0.04
7(b)	Direct in-plane shear tests on masonry wallettes (305 mm × 305 mm) as per the RILEM specification	4	f_{tu} (MPa)	0.26	0.03

TABLE 2: Properties of test models.

Structural properties	
Prototype frame	Test models (scale 1 : 4)
Beams	
15 in × 18 in (381 mm × 457 mm)	3.75 in × 4.5 in (96 mm × 114 mm)
Columns	
15 in × 15 in (381 mm × 381 mm)	3.75 in × 3.75 in (96 mm × 96 mm)
Slab	
6 in (153 mm)	1.5 in (40 mm)
Concrete strength	
3000 psi (21 MPa)	2500 psi (17.24 MPa)
Aggregate size: 1 in	Aggregate size: 3/8 in
Steel strength	
60000 psi (414 MPa)	60000 psi (414 MPa)
#8 rebar (25.40 mm)	#2 rebar (6.35 mm)
#4 rebar (12.70 mm)	#1 rebar (3.18 mm)

TABLE 3: Model-to-prototype quantity conversion factors.

Simple model similitude requirement		
Physical quantity	Relationship	Scale factor
Length	$S_L = L_p/L_m$	4
Stress	$S_f = f_p/f_m$	1
Strain	$S_\varepsilon = \varepsilon_p/\varepsilon_m$	1
Specific mass	$S_\rho = \rho_p/\rho_m$	1
Displacement	$S_d = d_p/d_m = S_L$	4
Force	$S_F = F_p/F_m = S_L^2 S_f$	16
Time	$S_t = t_p/t_m = S_L \sqrt{S_\varepsilon S_\rho / S_f}$	$\sqrt{4}$
Frequency	$S_\Omega = \Omega_p/\Omega_m = 1/S_t$	1/ $\sqrt{4}$
Velocity	$S_v = v_p/v_m = \sqrt{S_\varepsilon S_\rho / S_f}$	1
Acceleration	$S_a = a_p/a_m = S_f/S_L S_\rho$	1/4

concrete cover spalling and core crushing of joint panels under seismic excitations. The seismic behavior of considered bare and masonry-infilled RC frames is described as follows.

2.4.1. *Model 1: Bare RC SMRF Structure.* For input excitation of NR1 (i.e., acceleration amplitude 100% of

Northridge), the model was observed with few hairline flexure cracks in the columns at the ground and first story. Slight vertical cracks were observed at the ends of the beams of in-plane frames on the first floor. Very few hairline cracks were observed in the joint panels on the first floor. For input excitation of NR2 (i.e., acceleration amplitude 250% of Northridge), further slight-to-moderate cracks appeared in the structure, particularly in the joint panels (Figure 5). Few

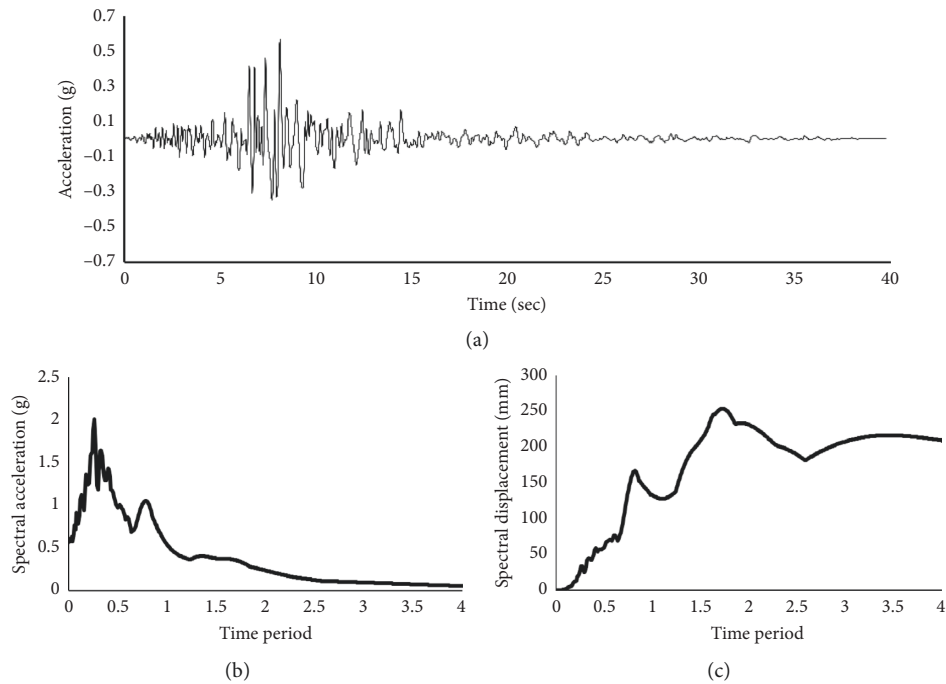


FIGURE 3: Selected earthquake record for shake table tests. (a) Northridge 1994 acceleration time history. (b) 5% damped acceleration response spectra. (c) 5% damped displacement response spectra.

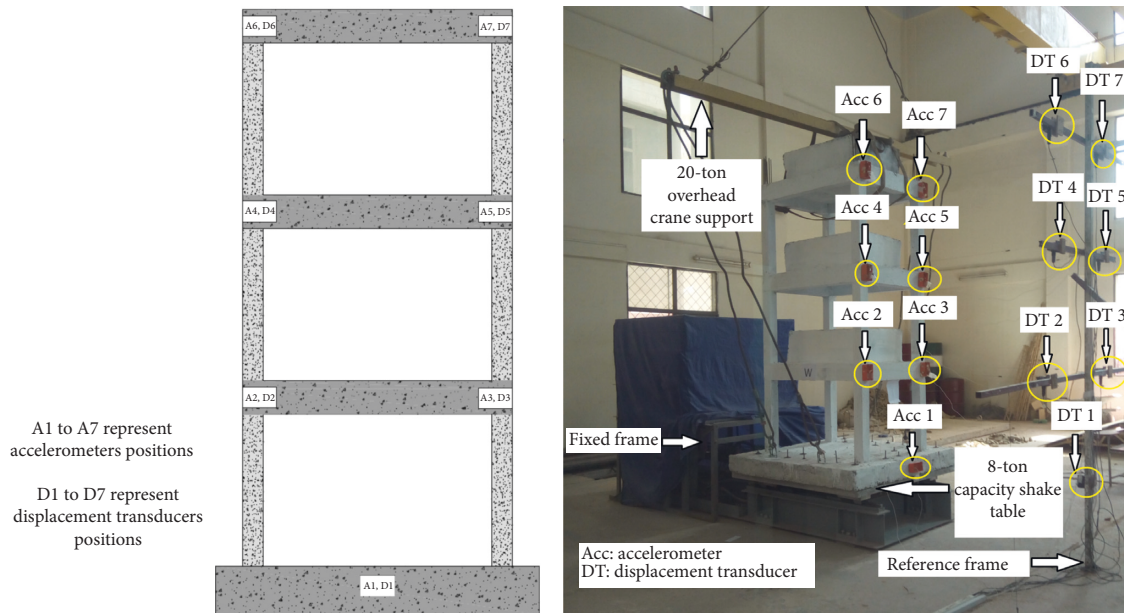


FIGURE 4: Test model instrumentation plan.

slight cracks also occurred in the joint panels on the second floor. The number and severity of cracks were primarily higher in the joint panels on the first floor, which is due to the fact that the bending and rotation demand are usually higher in beam-column connection at first floor. Flexure cracks at the top and bottom ends of first-story columns aggravated further. Slight flexure cracks were also observed at the base of columns on the second story. On ground story, slight flexure cracks were observed at the top ends, and very

few hairline cracks appeared on the ground-story columns at distance from the bottom ends. The severity of damage in the joint panels is due to the lack of lateral ties in the panels, resulting in joint shear strength lower than the excitation-induced joint shear demand. Following the localized shear damages in joint panels upon the exceedance of principal tensile strength of concrete in joints, global instability and abrupt story mechanism are very likely to result in the catastrophic collapse of the structure [25, 26, 27].



FIGURE 5: Damages observed in the frame structure under 200% earthquake motions. (a) In-plane loaded frame. (b) Face-loaded frame. (c) Damage to joints on first floor. (d) Damages observed in beams and joints at the second floor. (e) Damage pattern at corners.

The relatively lower damage in beams is suggesting the contribution of slab to the stiffness and strength of beams, thereby forcing columns to undergo inelastic actions. This can be contrasted with the mechanism developed in the counterpart portal frame for the same structure, when the slab contribution is neglected. It is worth to mention that the exterior column depth is 15 times the diameter of longitudinal rebars in beams, indicating the ACI 318 requirements for column depth are not sufficient to avoid flexure inelastic actions in columns and shear damages in joint panels.

2.4.2. Model 2 and Model 3: Masonry-Infilled RC SMRF Structures. For input excitation of NR1, the model was observed with hairline through cracks in in-plane masonry infills having opening for doors. This comprised primarily

horizontal cracks at the masonry bed joints. These cracks were observed on all the three stories; however, the severity of cracks was high on ground story, which is due to the higher interstory drift demand at the ground story. Solid in-plane parallel masonry wall panels were observed with horizontal and vertical cracks at the masonry and frame interfaces, causing separation of masonry infill. This was observed only on the ground story. Out-of-plane wall panels having opening for windows were also observed with minor through cracks, propagating from the windows corners. Such damages were observed on all the three stories.

For input excitations of NR2, the existing cracks further aggravated and few additional cracks were also observed (Figure 6). Masonry infill separation has been also observed at the ground story in the in-plane walls having opening for door. Vertical and horizontal cracks also appeared in the parallel in-plane solid masonry infill on both the second and

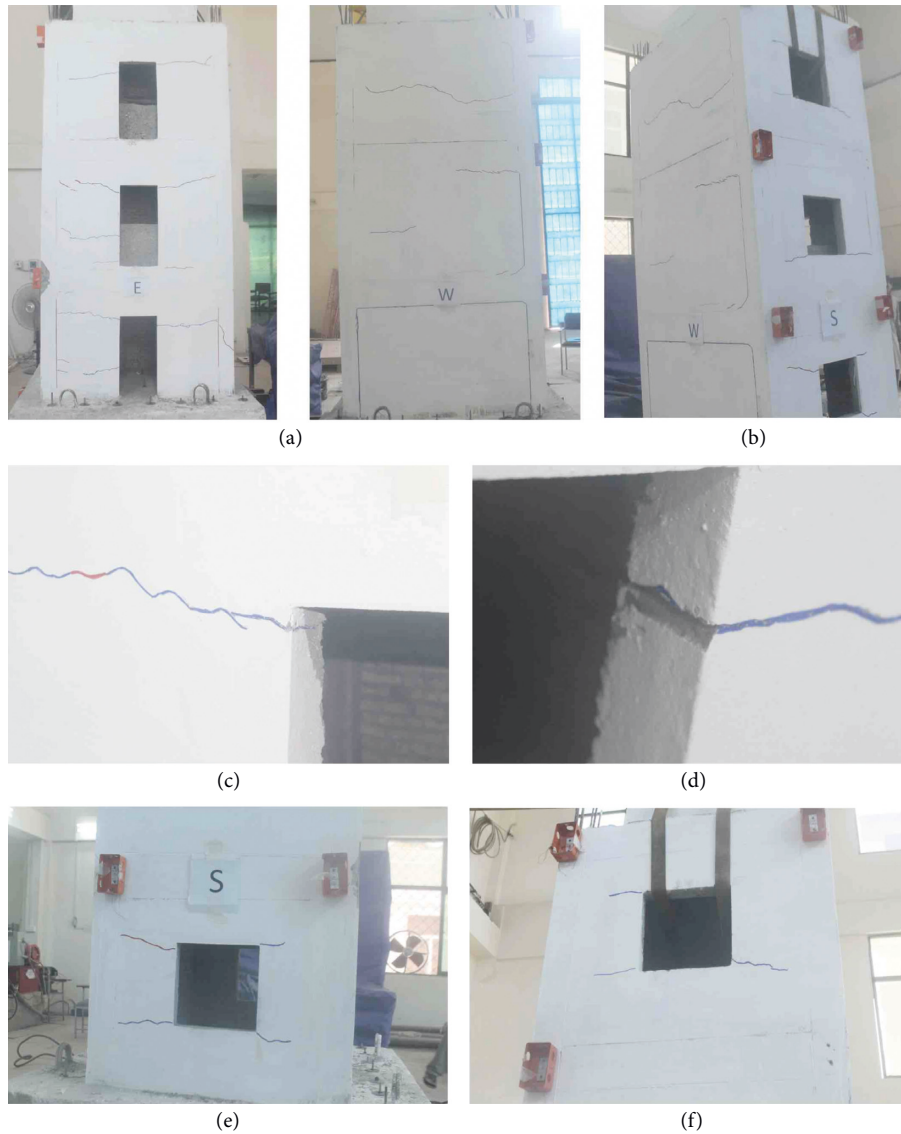


FIGURE 6: Damages observed in the hybrid masonry-infilled frame structure under 200% earthquake motions. (a) In-plane loaded frame. (b) Face-loaded frame. (c) Through horizontal cracks in masonry panel. (d) Horizontal sliding at the masonry bed joint. (e) Damage to out-of-plane panel on ground story. (f) Damage to out-of-plane panel on third story.

third stories. The third-story masonry solid wall panel was observed with horizontal cracks. Flexure damages in beams and columns and shear cracks in beam-column joint panels were not observed. It is due to the fact that under later loads, the masonry infill develops diagonal compression strut bearing against the beam and column at distance from the joint panels. Localized opposing shear force is developed in beams and columns at the strut contact at distance from the joint panel. This reduces shear demand on joint panels, due to which the joint panels are not subjected to large shear deformation.

Both the masonry-infilled frames, conventional and hybrid, behaved very much similar. However, the conventional masonry-infilled RC frame was observed with relatively more distributed cracks and panel separation of in-plane walls over all the three stories. No cracking or damage was observed in beams, columns, and joint-panel regions;

this shows effectiveness of masonry infill in avoiding joint-panel damage of the bare frame.

3. Elastic Dynamic Properties of Test Structures

3.1. Fundamental Frequency/Time Period. Structural modal frequencies were computed through low-amplitude tests performed on structures through shake table impact (jerk loading) before the actual tests. Roof acceleration response of the model was obtained and analyzed to derive floor acceleration response spectra, in frequency domain, to identify the structural predominant frequency. Figure 7 shows floor spectra developed for bare frame structure under the free-vibration test. The lowest predominant frequency was identified for each model: 3.271 Hz (0.305 sec) for bare frame, 3.418 Hz (0.293 sec) for hybrid masonry-infilled frame, and 3.369 Hz (0.297 sec) for masonry-infilled

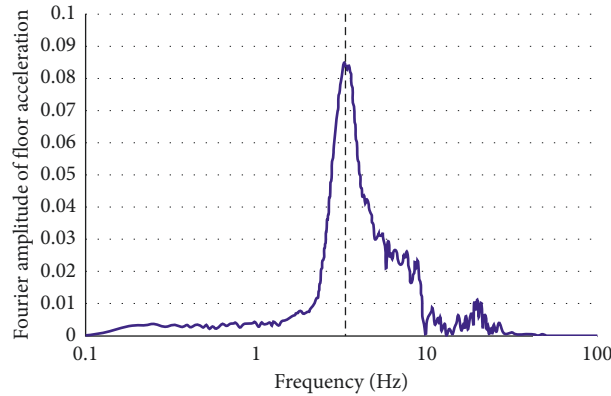


FIGURE 7: Fourier spectra of floor acceleration response at roof level for free vibration of undamaged bare frame structure. The values are those for the reduced scale test model.

frame reduced scale test models. This corresponds to the prototype time period of 0.61 sec for bare frame, 0.59 sec for hybrid masonry-infilled frame, and 0.59 sec for masonry-infilled frame. As expected, the elastic period of masonry-infilled structure is relatively lower than the bare frame structures. Further, the time period of hybrid masonry-infilled structure is also less than that of the counterpart conventional masonry-infilled structure. It is worth to mention that structural stiffness of masonry-infilled frames increased due to inclusion of masonry infill. However, this also increased the structural mass, and the period variation in bare to masonry-infilled structure is not very significant. It is due to the fact that the frame itself is significantly stiffer, and also, due to the relatively lower bay width-to-height ratio of frame, the frame is mainly governed by the global flexure/rocking frame behavior. For these reasons, the infill does not contribute significantly to the frame stiffness.

The present Building Code of Pakistan [20] has proposed structural height-based equation to calculate the structure period of RC frame:

$$T_a = 0.03h^{3/4}, \quad (1)$$

where T is the fundamental period of structure and h is the total height of structure in feet. The above equation provides an estimate of fundamental period of 0.41 sec for prototype of bare frame, which is about 50% lower than the measured structural period. Similar discrepancy between calculated and observed time period of reinforced concrete structures has been observed in many other studies [28, 29]. The code also allows a 30% increase in the time period of structure calculated using equation (1), as the actual model analysis of structure may give higher value for time period. Considering this increase, the time period will increase to 0.54 sec for bare frame. Therefore, the discrepancy in calculated and measured time period reduces to about 12%. Furthermore, the fact that simplified formulation provided by codes provides underestimating estimates of the vibration period of structures is somehow expected, given that such underestimation is usually conservative within a force-based approach to seismic design.

3.2. Elastic Viscous Damping. The decay function for the time history response as proposed by Chopra [30] was used to calculate the test model damping:

$$\zeta = \frac{1}{2n\pi} \ln\left(\frac{A_1}{A_n}\right), \quad (2)$$

where ζ represents the elastic damping coefficient; A_1 represents the peak amplitude of response displacement at reference point 1; A_n represents the peak amplitude of response displacement at reference point after n cycles; and n represents the number of cycles between the peaks. The model damping was calculated from the free vibration tests conducted on models, carried out by means of shake table jerk loading. The structure displacement response at the top was considered and analyzed for calculating the decay in the displacement history (Figure 8). The damping was calculated from logarithmic decay of the last two cycles. The structural damping measured herein is 10.57% for bare frame, 13.36% for hybrid masonry-infilled frame, and 13.73% for masonry-infilled frame. The measured elastic damping can be contrasted with the normally proposed 5% elastic damping.

4. Observed Seismic Response of Test Structures

4.1. Acceleration-Displacement Response Spectrum of Input Excitations. To analytically compute the acceleration and displacement demands on the hypothetical elastic structure, acceleration-displacement response spectrum (ADRS) were developed for each tests by taking recorded accelerations time history at the base of the models. The elastic peak acceleration and displacement demand on hypothetical structure may be read at the intersection on the ADRS drawing a radial line whose slope is equal to the square of the circular frequency of the structure for the first mode vibration period (see Figure 9). As typical for the elastic response analysis, 5% viscous damping is normally considered for the elastic analysis of structures. Although the acceleration time history of 1994 Northridge earthquake has been used for all the three models, the actual recorded input excitations of all the test models differ to some extent. It is worth mentioning that the input to the shake table controller was the same in all cases; however, the controller develops

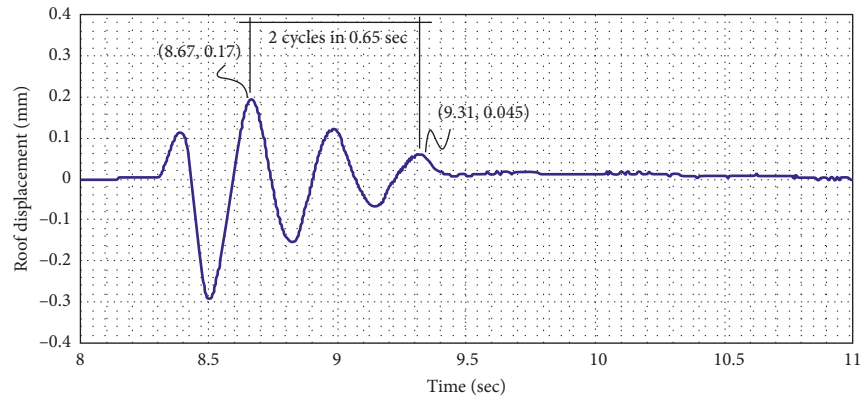


FIGURE 8: Top-floor displacement response of undamaged bare frame structure for the free vibration test. The values are those for the reduced scale test model.

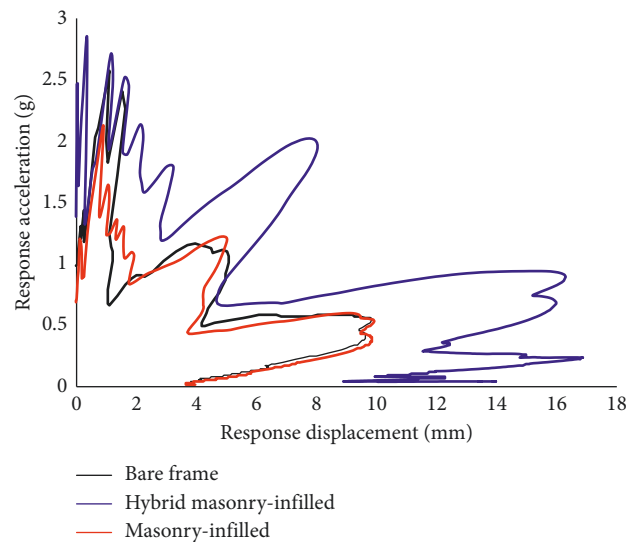


FIGURE 9: Acceleration-displacement response spectrum for recorded input excitation at the base of test models under 100% (NR1) of earthquake motions.

different auto transfer function in all structure cases. Although this depends on the test model stiffness and masses, uncertainties may be encountered due to the automatic control system of controller and the differences the controller face in the current hydraulic pressure and temperature. The latter cannot be maintained exactly the same in all cases.

4.2. Interstory Drift, Lateral Displacement, and Interstory Shear Demands. Floor response acceleration and response displacements recorded for each tests were analyzed to obtain the interstory drift profile (Figure 10), lateral floor displacement peak response envelope (Figure 11), and interstory shear (Figure 12). The story shear was calculated based on the equilibrium consideration and by summing the floor inertial forces. The inertial forces at floor levels were the total inertial forces calculated by multiplying the floor absolute acceleration with the lumped mass. The absolute acceleration was measured through 1-DOF accelerometers.

Under NR1, the bare frame has experienced interstory drift demand of about 0.89%, which has been reduced by 77% and 80% for the hybrid and conventional masonry-infilled frame, respectively. Similarly, under NR2, the bare frame has experienced interstory drift demand of about 1.63%, which has been reduced by about 74% for the hybrid and conventional masonry-infilled structures, respectively. The infilled structures have controlled the seismic drift demand, largely, because of their relatively high structural stiffness, and also, because of structural energy dissipation capability.

The later can be explained by realizing the occurrence of higher number of cracks experienced in conventional masonry-infilled structures, thereby providing sources for energy dissipation through friction sliding. The masonry panels separation in conventional masonry-infilled structure at all floors allowed the structure to linearly distribute lateral seismic displacement demand on structure, as evidenced from the linear deflected shape of masonry-infilled structure (Figure 10). On the contrary, relatively high stiffness of masonry-infilled RC structures attracted higher

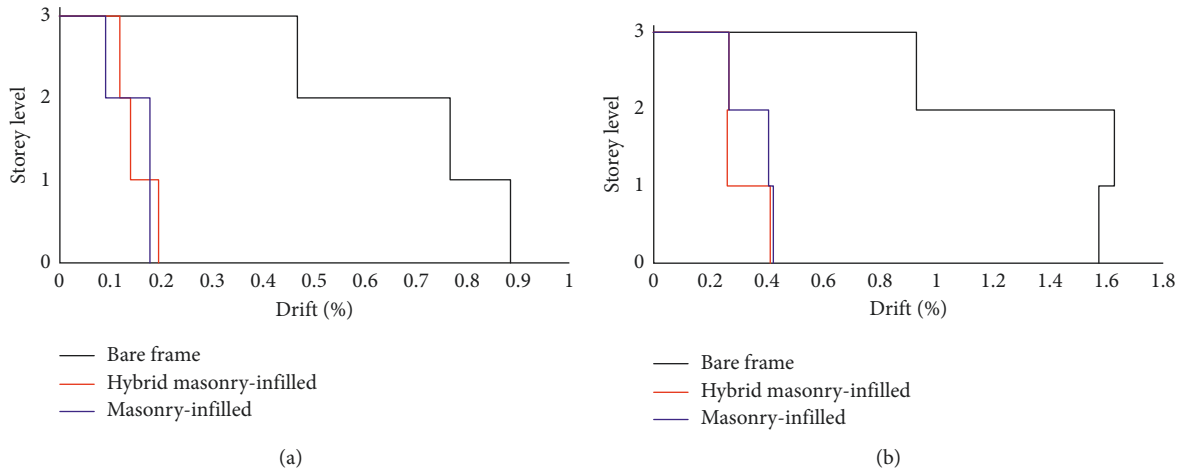


FIGURE 10: Maximum interstory drift envelope of test models for increasing input excitation. (a) Interstory drift demand under NR1. (b) Interstory drift demand under NR2.

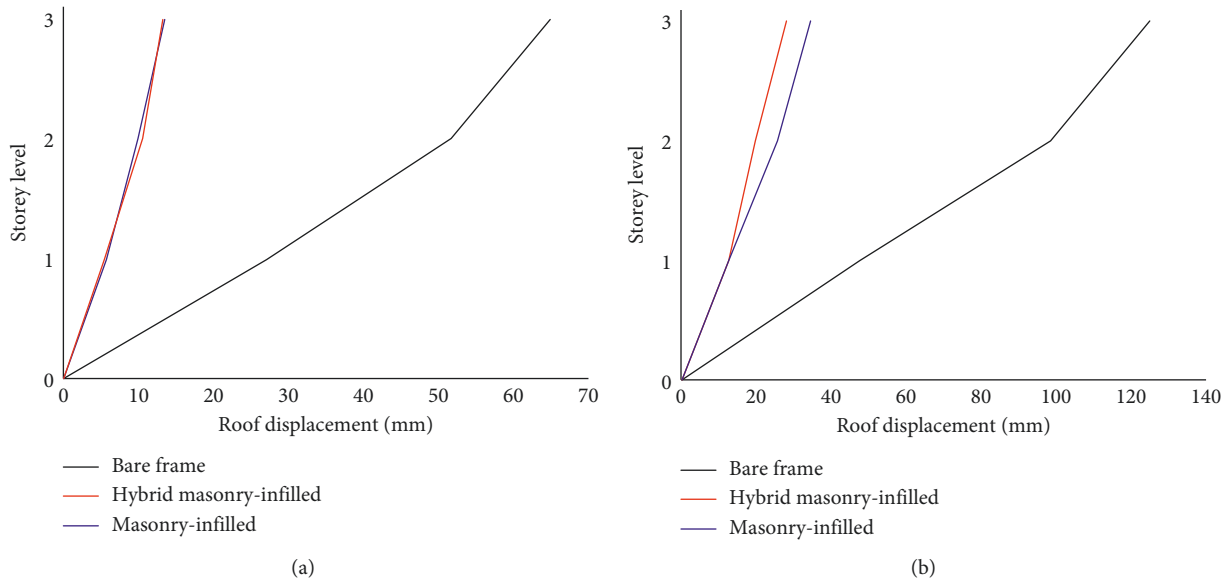


FIGURE 11: Maximum lateral displacement envelope of test models for increasing input excitation. Displacements were converted to the corresponding prototype values. (a) Lateral displacement under NR1. (b) Lateral displacement under NR2.

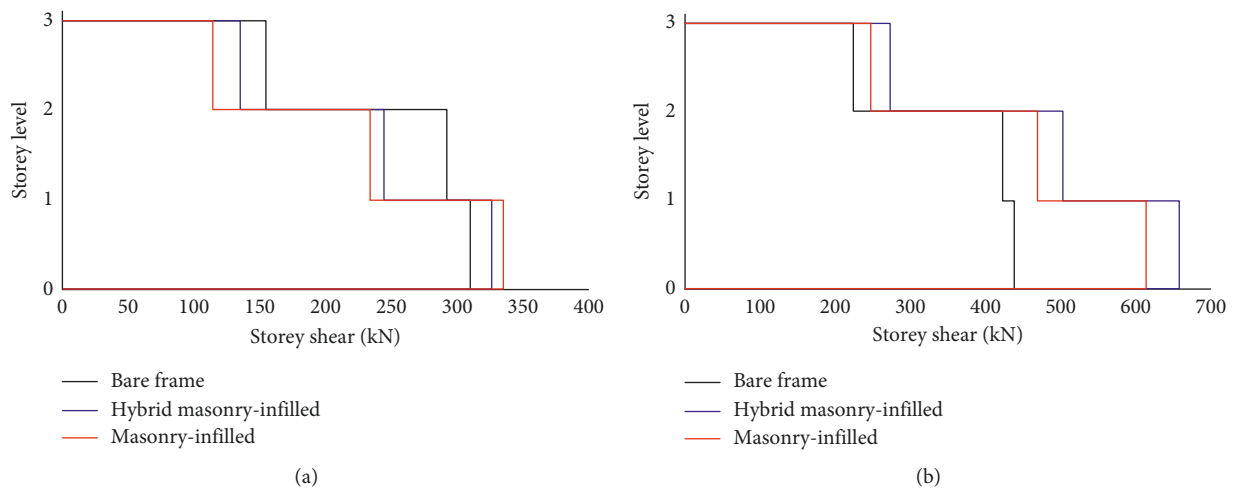


FIGURE 12: Maximum interstory shear envelope of test structures for increasing input excitation. Story shears were converted to the corresponding prototype values. (a) Interstory shear under NR1. (b) Interstory shear under NR2.

base shear force. Under NR1, both the masonry-infilled structures attracted similar base shear force with marginal difference, which increases under higher input excitation.

4.3. Floor Acceleration Amplification. The model amplification was measured dividing the structural peak response acceleration at the top floor over the peak input acceleration at the base of the model:

$$\text{Amp} = \left(\frac{\max A_{\text{roof}}}{\max A_{\text{base}}} \right), \quad (3)$$

where Amp represents the top floor acceleration amplification factor; $\max A_{\text{roof}}$ represents the peak acceleration observed at the roof level; and $\max A_{\text{base}}$ represents the peak acceleration of earthquake motions observed at the base of the model.

The measured amplification initially increased with increasing intensity that suggests a direct correlation between the intensity and the acceleration amplification (Figure 13). However, the amplification started decreasing with further increase in input base excitation that highlights the onset of cracking/damage in structures. This is also evident from the hysteretic response and cumulative energy dissipation of test models (Figures 14 and 15). The occurrence of cracking and damage provided energy dissipation capacity; due to this, the structures' peak response accelerations were reduced. The maximum acceleration amplification observed in the bare frame is 3.10, which is reduced to 2.60 and 2.47 in case of hybrid masonry-infilled and masonry-infilled structures, respectively. As expected, the floor acceleration amplification was reduced in case of masonry-infilled structures, which was due to the relatively higher structural damping available in these structures, provided by masonry panel-frame interaction (vertical and horizontal cracks at infill-frame interfaces) and masonry friction sliding observed at the masonry bed joint in cracked/damaged infill.

4.4. Seismic Response Curves. The peak-observed input accelerations, expressed as PGA, were correlated with the roof displacement demand to derive seismic response curves for test models (Figure 16). These curves show the structural lateral deformation against the input excitations. As can be seen, initially, the curves behave linearly but deviate due to onset of structural damages and tend to flatten for extreme level shaking (e.g., in case of bare frame).

The later corresponds to the development of non-linearity in the structural system due to cracking/damage. A minor deviation in the response curve of masonry-infilled frames is due to the cracking/damages observed in masonry infill. On the other hand, a large deviation has been observed in the response curve for bare frame, which was due to the shear damages observed in joint panels. These joint panel damages allowed the structure to deform to larger lateral displacement under relatively lower input excitations. It can be observed that both the masonry-infilled structures increased the structural resistance against the input excitation, thereby making the structure

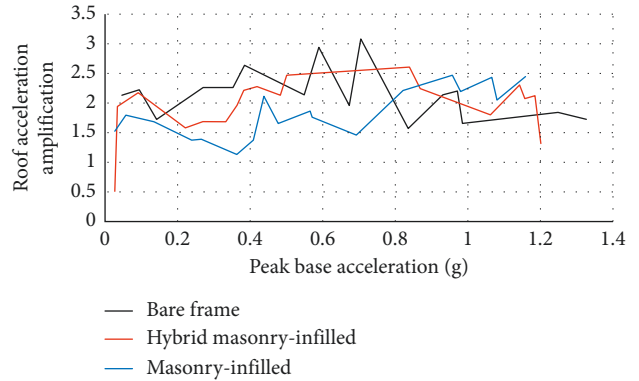


FIGURE 13: Acceleration amplification of structures correlated with input excitation peak acceleration. The values are those for the reduced scale test model.

able to resist higher peak input acceleration. Furthermore, the inclusion of masonry infill enabled the structure to control lateral deformation under earthquake ground motions, which was primarily due to the relatively high stiffness of the masonry-infilled structures, and by larger part, it was due to the characteristics of the damaged masonry-infills that provided energy dissipation through masonry sliding over multiple cracks.

5. Seismic Performance Assessment of Test Models

5.1. Seismic Analysis of Test Models Using Static Force Procedure

5.1.1. Measured Mode Shapes and Participation Factors. The estimation of elastic base shear requires the identification of deflected shape of structure and participation factor for the first mode of vibration, which is inferred from the measured lateral floor displacement of the tested models. A structural node can have 6 degrees-of-freedom for deformation; however, lateral horizontal translation of floors is the predominant deformation of frame structures for structural vibration under seismic excitation. Thus, a simple three-degrees-of-freedom system with lumped masses at the floor was used to express the lateral response of the tested models. The lumped weights associated with each of the three floors of test models were equal to, from third to first story, [0.625 0.655 0.655] and [0.725 0.855 0.855] for the bare frame and masonry-infill model, respectively. Since structural displacements during lateral vibration are generally larger at the first mode, the coordinates of deflected shape were determined by normalizing measured lateral floor displacements of the structure at times of peak response with respect to the roof floor. First-mode participation factors were determined from the modal coordinates and floor weights in accordance with equation (4), which are given in Table 4:

$$\Gamma_1 = \frac{\sum_{i=1}^m w_i \phi_{1i}}{\sum_{i=1}^m w_i \phi_{1i}^2}, \quad (4)$$

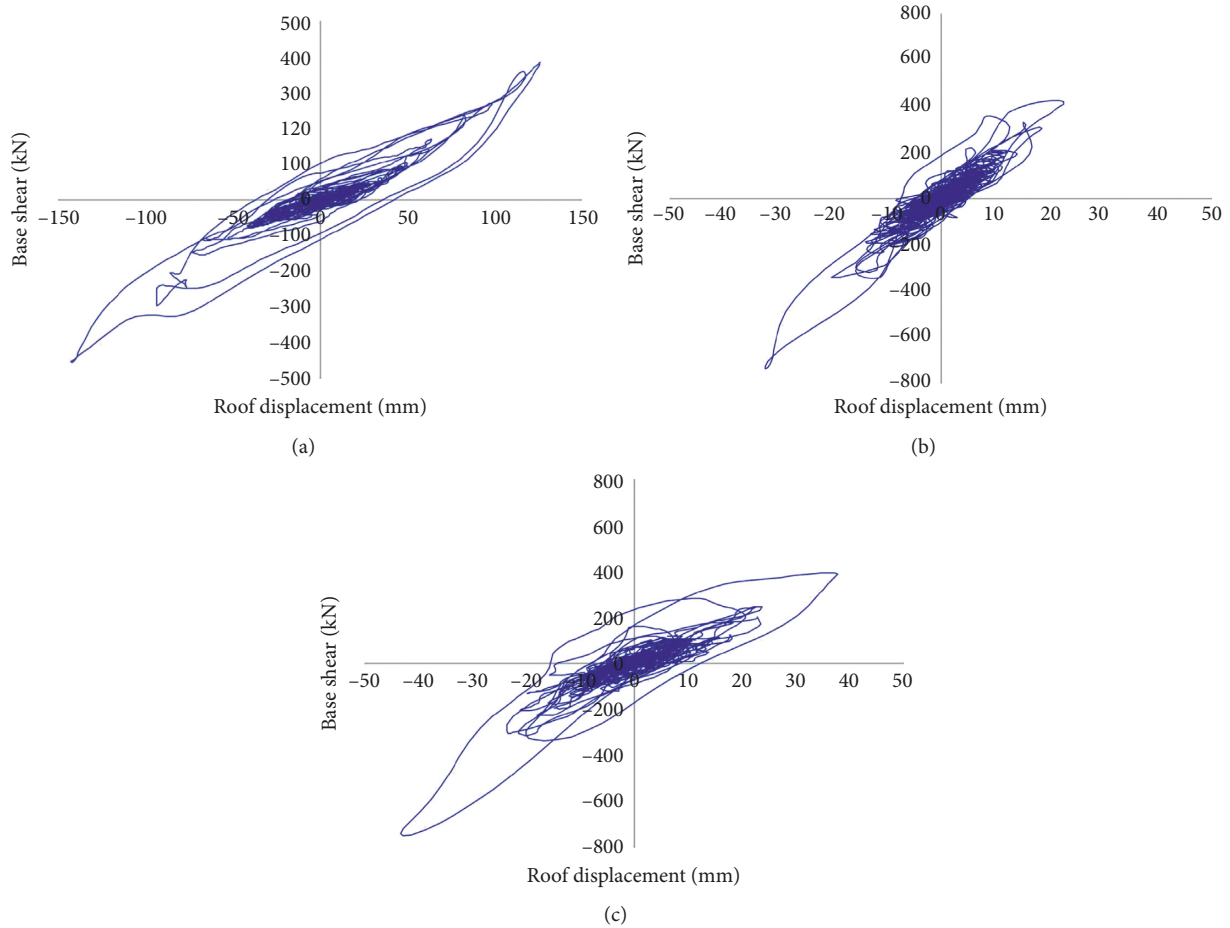


FIGURE 14: Measured force-displacement hysteretic response of the prototype of test models for NR2. (a) Bare frame. (b) Hybrid masonry-infilled. (c) Masonry-infilled.

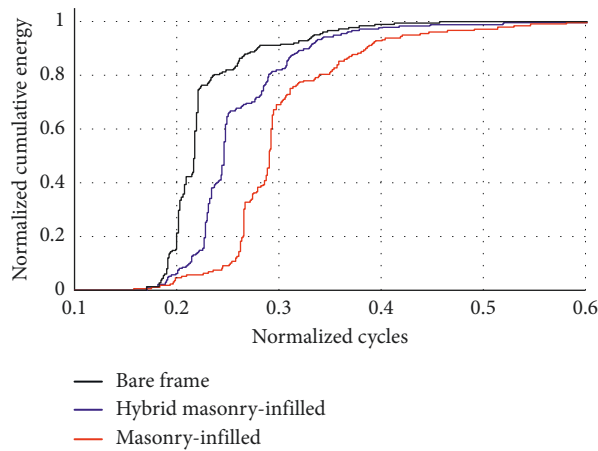


FIGURE 15: Normalized cumulative energy dissipation of test structures under NR2. A curve with more flatness signifies higher energy dissipation.

where w_i is the floor weight, ϕ_1 represents the coordinates of mode shape, and i is the floor level. The calculated participation factor was used to determine the percentage

of the total weight effective in the first mode of the structure, in accordance with equation (5), and is given in Table 4.

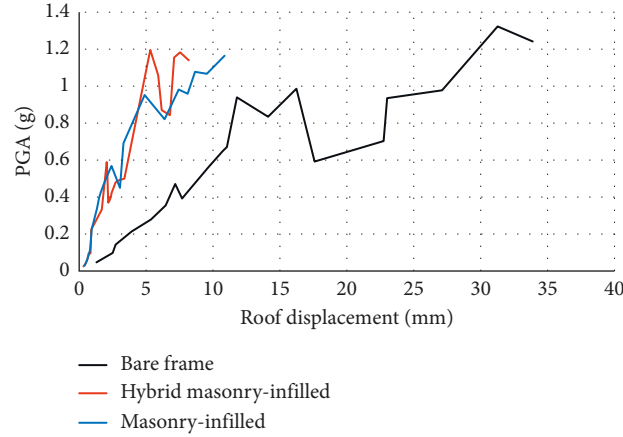


FIGURE 16: Seismic response curves developed for the prototype of test models.

TABLE 4: Base shear force demands for models calculated from the 5% damped elastic acceleration spectrum generated for input acceleration.

Model	Test run	Frequency (Hz)	S_a (g)	Γ_1	$W_{\text{effective}}$ (%)	V_{b1} (kN)*	Diff. (%)
Bare frame	BF_NR1	3.08	0.91	1.23	90.19	249	-19.68
	BF_NR2	2.73	1.94	1.22	89.69	528	20.27
Hybrid masonry infill	HM_NR1	3.37	0.71	1.28	90.69	246	-24.54
	HM_NR2	3.32	1.36	1.31	89.22	464	-29.48
Masonry infill	CM_NR1	3.32	0.85	1.25	89.72	291	-13.13
	CM_NR2	3.13	1.23	1.25	88.85	418	-31.81

*The values were converted to the corresponding prototype structures using the applicable scaling factors.

$$W_{\text{effective}} (\%) = \frac{\Gamma_1 \sum_{i=1}^m w_i \phi_{1i}}{W} \times 100. \quad (5)$$

The percentage of the total weight of structure that is effective in the first mode ranged from about 88.85% to 90.69% and is higher for the first test runs. This is because, for the first test runs, the deflected shape was more linear, and thus, lateral floor displacements were higher.

5.1.2. Base Shear Force. The elastic base shear demand for a specified mode is related to the spectral acceleration S_a , which is calculated in accordance with the following equation:

$$V_{b1} = \Gamma_1 \frac{S_{a1}}{g} \sum_{i=1}^m w_i \phi_{1i}, \quad (6)$$

where V_{b1} is the elastic base shear demand for first mode and S_{a1} is the spectral acceleration demand on the hypothetical elastic model, obtained from the elastic acceleration spectrum at the fundamental time period of the test models obtained through free vibration tests. Thus, base shear demand of a hypothetical linearly behaving system was deduced, which is given in Table 4. Table 4 also reports the difference observed between the analytically predicted and experimentally observed base shear force. The negative value indicates underprediction, and the positive value indicates overprediction. The difference between the actual and analytically computed base shear is relatively less in case of

NR1 but increased in case of NR2. It is due to the fact that under higher seismic excitations, the onset of structural nonlinearity makes the analytical prediction less accurate. The base shear force calculated analytically is less in all cases, which seems to be due to the approximations made, i.e., considering only Mode 1 for computation and idealizing model vibration period based on the free vibration tests. The base shear force calculated analytically for bare frame in case of NR2 is higher than the actually observed. It is due to the fact that under NR2 the bare frame was subjected to significant nonlinearity, whereby the static procedure that assumes linear behavior becomes less accurate and overpredicts base shear force.

5.2. Seismic Fragility Functions. Seismic fragility functions are a set of mathematical cumulative distribution functions that describe structural damages probabilistically in terms of the performance level exceedance of structure, given the input excitation. It is derived using standard normal cumulative distribution functions, as formulated [31]:

$$P_{LS} = \Phi \left(\frac{1}{\beta} \ln \left(\frac{\text{PGA}}{\text{pga}_{LS}} \right) \right), \quad (7)$$

where P_{LS} is the probability of exceedance of a given limit state, Φ is the standard normal cumulative distribution mathematical function, PGA is the specified peak ground acceleration demand, pga_{LS} is the peak ground acceleration corresponding to ground motions capable of exceeding the structure specified drift level by 50%, and β is the logarithmic

TABLE 5: PGA_{LS} derived for roof drift of 0.30%.

Performance levels	Mean values of PGA, pga_{LS}	Log. standard deviation β
Bare frame	0.45	0.60
Hybrid masonry-infill	1.16	0.60
Masonry-infill	1.05	0.60

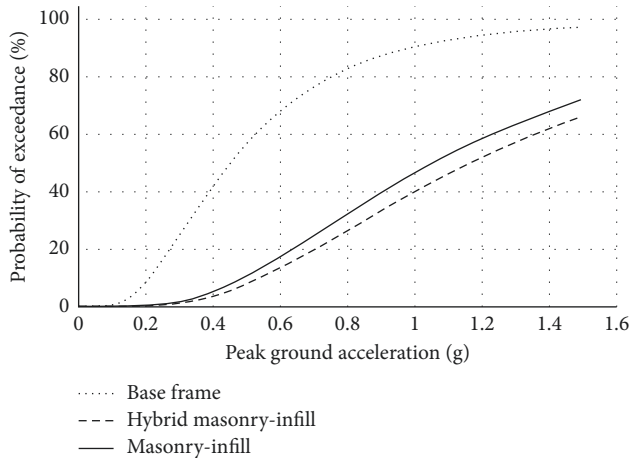


FIGURE 17: Seismic fragility functions derived for probabilistic assessment of test models. The functions are derived for a roof drift of 0.30%.

standard deviation that defines total uncertainties. Derivation of fragility functions for a structure requires pga_{LS} and β for each limit state. The value of β varies from 0.40 to 0.60 [32, 33], $\beta=0.60$ was taken in the present case. For the present building, pga_{LS} was obtained from the seismic response curves (Figure 16). Since, the masonry-infill structure were laterally displaced to only 0.30% roof drift, roof drift of 0.30% was taken as the reference roof drift for which the corresponding PGAs were obtained through second-order polynomial interpolation. These values were considered as the mean estimate of pga_{LS} and listed in Table 5. Fragility functions derived using equation (7) are reported in Figure 17. Considering the 10% probability of exceedance for the specified roof drift of 0.30%, the bare frame will resist 0.21 g, hybrid masonry-infill frame will resist 0.54 g, and conventional masonry-infill will resist 0.50 g. The use of masonry infill (i.e., hybrid and conventional) increased the seismic resistance of the bare frame by 157% and 133%, respectively. Both the hybrid and conventional masonry-infill frames resulted in similar fragility functions; however, the hybrid masonry-infill frame has relatively more resistance in comparison to conventional masonry infill.

The indicated input excitation has 50% probability to exceed the specified roof drift of 0.30%.

6. Conclusions

Shake table tests were performed on three 1 : 4 reduced-scale three-story reinforced concrete frames, with and without masonry infill, representative of modern frame structures found in most of the developing countries, possessing construction deficiencies like lack of ties in joint panels and

concrete having low strength. The models were tested using natural acceleration time history of 1994 Northridge, with multilevel excitations. Additionally, free vibration shake table impact (jerk) tests were conducted. Seismic behavior of the test models was observed, and fundamental dynamic properties and seismic response parameters were obtained. The seismic response of bare frame and masonry-infill frames were critically compared. The seismic performance of test models was assessed using static force procedure and probabilistic fragility functions.

The lack of lateral ties in beam-column joint panels in SMRF structures resulted in the local shear damage of joint panels. The SMRF structure, with structural members detailed as per the ACI-318-05 but lacking confining ties in the joint panel region, has revealed significant damages in joint panel regions of bare frames under earthquake motions. These damages, if experienced under moderate ground motions, create challenges in routine repairing. The inclusion of masonry infill, either through a conventional masonry-infilled construction or hybrid masonry-infill construction, has avoided damages in the joint panel region by altering lateral load path and controlling lateral displacement demands on structures through energy dissipation offered by masonry sliding observed at multiple cracks. Through the infill-frame interaction, conventional masonry-infill RC structure offered more energy dissipation as compared to hybrid masonry-infilled RC structures. The same has been manifested in the probabilistic fragility functions developed for the test models for a target roof drift, which has revealed that the masonry infill has enhanced the seismic resistance of structures by 133% to 157% using conventional and hybrid masonry infill, respectively.

Data Availability

The related dataset can be provided by contact at naveed.ahmad@uetpeshawar.edu.pk.

Disclosure

The research work presented herein is based on the final year projects of senior undergraduate students in the Department of Civil Engineering of UET Peshawar.

Conflicts of Interest

The authors declare that they have no conflicts of interest.

References

- [1] M. H. Arslan and H. H. Korkmaz, "What is to be learned from damage and failure of reinforced concrete structures during

- recent earthquakes in Turkey?," *Engineering Failure Analysis*, vol. 14, no. 1, pp. 1–22, 2007.
- [2] S. Ates, V. Kahya, M. Yurdakul, and S. Adanur, "Damages on reinforced concrete buildings due to consecutive earthquakes in Van," *Soil Dynamics and Earthquake Engineering*, vol. 53, pp. 109–118, 2013.
 - [3] J. K. Bothara and K. M. O. Hicyilmaz, "General observations of building behavior during the 8th october 2005 Pakistan earthquake," *Bulletin of the New Zealand Society for Earthquake Engineering*, vol. 41, no. 4, pp. 209–233, 2008.
 - [4] B. Erdil, "Why RC buildings failed in the 2011 Van, Turkey, earthquakes: construction versus design practices," *Journal of Performance of Constructed Facilities*, vol. 31, no. 3, Article ID 04016110, 2016.
 - [5] T. Rossetto and N. Peiris, "Observations of damage due to the Kashmir earthquake of october 8, 2005 and study of current seismic provisions for buildings in Pakistan," *Bulletin of Earthquake Engineering*, vol. 7, no. 3, pp. 681–699, 2009.
 - [6] J. G. Ruiz-Pinilla, J. M. Adam, R. Pérez-Cárcel, J. Yuste, and J. J. Moragues, "Learning from RC building structures damaged by the earthquake in Lorca, Spain, in 2011," *Engineering Failure Analysis*, vol. 68, pp. 76–86, 2016.
 - [7] N. Ahmad, A. Shahzad, M. Rizwan et al., "Seismic performance assessment of non-compliant SMRF-reinforced concrete frame: shake-table test study," *Journal of Earthquake Engineering*, vol. 23, no. 3, pp. 444–462, 2019.
 - [8] N. Ahmad, J. Akbar, M. Rizwan, B. Alam, A. N. Khan, and A. Lateef, "Haunch retrofitting technique for seismic upgrading deficient RC frames," *Bulletin of Earthquake Engineering*, vol. 17, no. 7, pp. 3895–3932, 2019.
 - [9] J. Akbar, N. Ahmad, and B. Alam, "Seismic strengthening of deficient RC frames using reinforced concrete haunch," *ACI Structural Journal*, vol. 166, no. 1, pp. 225–235, 2019.
 - [10] J. Akbar, N. Ahmad, and B. Alam, "Seismic performance of RC frames retrofitted with haunch technique," *Structural Engineering and Mechanics*, vol. 67, no. 1, pp. 1–8, 2018.
 - [11] M. Banazadeh, M. Gholhaki, and H. Parvini Sani, "Cost-benefit analysis of seismic-isolated structures with viscous damper based on loss estimation," *Structure and Infrastructure Engineering*, vol. 13, no. 8, pp. 1045–1055, 2017.
 - [12] A. Benavent-Climent, L. Morillas, and D. Escolano-Margarit, "Seismic performance and damage evaluation of a reinforced concrete frame with hysteretic dampers through shake-table tests," *Earthquake Engineering & Structural Dynamics*, vol. 43, no. 15, pp. 2399–2417, 2014.
 - [13] F. Bencardion, A. Condello, and F. Castiglione, "An innovative solution for the structural consolidation of RC modern cultural heritage," *International Journal of Architectural Heritage*, vol. 11, no. 6, pp. 829–842, 2017.
 - [14] M. Dolce, D. Cardone, F. C. Ponzo, and C. Valente, "Shaking table tests on reinforced concrete frames without and with passive control systems," *Earthquake Engineering & Structural Dynamics*, vol. 34, no. 14, pp. 1687–1717, 2005.
 - [15] R. Marques, P. Lamego, P. B. Lourenci, and M. L. Sousa, "Efficiency and cost-benefit analysis of seismic strengthening techniques for old residential buildings in Lisbon," *Journal of Earthquake Engineering*, vol. 22, no. 9, 2018.
 - [16] E. Oliver-Saiz and A. Benavent-Climent, "Shake-table test of a reinforced concrete frame retrofitted with hysteretic damper connected using an improved joint structure," in *Proceedings of the Second European Conference on Earthquake Engineering and Seismology*, Istanbul, Turkey, August 2014.
 - [17] S. I. Pardalopoulos, S. J. Pantazopoulou, and G. E. Thermou, "Seismic rehabilitation of substandard RC buildings with masonry infills," *Journal of Earthquake Engineering*, pp. 1–30, 2018.
 - [18] A. Sharma, G. R. Reddy, R. Eligehausen, G. Genesio, and S. Pampanin, "Seismic response of reinforced concrete frames with haunch retrofit solution," *ACI Structural Journal*, vol. 111, no. 3, pp. 673–684, 2014.
 - [19] A. Sharma, G. R. Reddy, and K. K. Vaze, "Shake table tests on a non-seismically detailed RC frame structure," *Structural Engineering and Mechanics*, vol. 41, no. 1, pp. 1–24, 2012.
 - [20] BCP, *Building Code of Pakistan: Seismic Provisions-2007*, Technical Report, Ministry of Housing and Works, Islamabad, Pakistan, 2007.
 - [21] ACI-318, *Building Code Requirements for Structural Concrete-ACI 318-05*, American Concrete Institute, Farmington Hills, MI, USA, 2005.
 - [22] ETABS, *Structural Software for Building Analysis and Design—ETABS*, Computer and Structures Inc. (CSI), Walnut Creek, CA, USA, 2009.
 - [23] Y. I. Badrashi, Q. Ali, M. Ashraf, and M. Rashid, "Seismic design characterization of RC special moment resisting frames in Pakistan—field survey to laboratory experiments," *Journal of Engineering and Applied Sciences*, vol. 35, no. 2, pp. 25–32, 2016.
 - [24] M. Rizwan, N. Ahmad, and A. N. Khan, "Seismic performance of compliant and noncompliant special moment-resisting reinforced concrete frames," *ACI Structural Journal*, vol. 115, no. 4, pp. 1063–1073, 2018.
 - [25] G. M. Calvi, G. Magenes, and S. Pampanin, "Experimental test on a three story RC frame designed for gravity only," in *Proceedings of the 12th European Conference on Earthquake Engineering*, London, UK, September 2002.
 - [26] R. Park, "A summary of results of simulated seismic load tests on reinforced concrete beam-column joints, beam and columns with substandard reinforcing details," *Journal of Earthquake Engineering*, vol. 6, no. 2, pp. 147–174, 2001.
 - [27] M. J. N. Priestley, "Displacement-based seismic assessment of reinforced concrete buildings," *Journal of Earthquake Engineering*, vol. 1, no. 1, pp. 157–192, 1997.
 - [28] H. Crowley and R. Pinho, "Period-height relationship for existing European reinforced concrete buildings," *Journal of Earthquake Engineering*, vol. 8, no. 1, pp. 93–119, 2004.
 - [29] A. Shing and M. Vona, "Experimental and numerical evaluation of the fundamental period of undamaged and damaged RC framed buildings," *Bulletin of Earthquake Engineering*, vol. 8, no. 3, pp. 643–656, 2010.
 - [30] A. K. Chopra, *Dynamics of Structures: Theory and Applications to Earthquake Engineering*, Prentice-Hall, Upper Saddle River, NJ, USA, 3rd edition, 2003.
 - [31] C. A. Kircher, A. A. Nassar, O. Kustu, and W. T. Holmes, "Development of building damage functions for earthquake loss estimation," *Earthquake Spectra*, vol. 13, no. 4, pp. 663–682, 1997.
 - [32] J. K. Bothara, R. P. Dhakal, and J. B. Mander, "Seismic performance of an unreinforced masonry building: an experimental investigation," *Earthquake Engineering and Structural Dynamics*, vol. 39, no. 1, pp. 45–68, 2009.
 - [33] FEMA, *Multi-hazard Loss Estimation Methodology, Earthquake Model, HAZUS-MH 2.1: Technical Manual*, Federal Emergency Management Agency (FEMA), Washington, DC, USA, 2003.

Research Article

Shaking Table Test Study on Seismic Performance of Hollow Rectangular Piers

Yanli Shen  and Bo Wei

Hebei University of Engineering, Handan 056038, China

Correspondence should be addressed to Yanli Shen; shenyanli@hebeu.edu.cn

Received 9 June 2019; Accepted 28 July 2019; Published 22 August 2019

Guest Editor: André Furtado

Copyright © 2019 Yanli Shen and Bo Wei. This is an open access article distributed under the Creative Commons Attribution License, which permits unrestricted use, distribution, and reproduction in any medium, provided the original work is properly cited.

To study the seismic performance of hollow reinforced concrete piers under dynamic loads, nine hollow pier specimens with different stirrup ratios, reinforcement ratios, and axial compression ratios are designed and manufactured. The El Centro wave, Taft wave, and artificial Lanzhou wave are selected as seismic excitation for the shaking table test. The effects of the reinforcement ratio, stirrup ratio, and axial compression ratio on the failure mode, period, damping, acceleration and displacement response, dynamic magnification factor, ductility, and energy dissipation of specimens under different working conditions are studied. The results show that all the nine reinforced concrete piers have good seismic performance. Subjected to ground motion excitation, horizontal through cracks appeared on the pier surface. With the increase of ground motion excitation, the period of piers increases but the maximum period does not exceed 0.62 s, and the damping ratio increases as well and ranges from 0.02 to 0.064. With the increase of the ground motion excitation, the acceleration response of pier specimens increases, the dynamic magnification factor decreases, the displacement ductility coefficient decreases, and the energy dissipation of the specimens increases. The reinforcement ratio, stirrup ratio, and axial compression ratio have different effects on the above parameters. The test results can provide reference for seismic design of hollow rectangular piers and have certain engineering significance and value.

1. Introduction

Hollow section is the ideal section form of piers. Hollow section can bring maximum benefit to the structure, and it will also reduce the influence of pier self-weight on bridge seismic response [1]. Therefore, hollow piers are widely used in engineering, so it is important to strengthen the research of hollow piers.

However, most shaking table tests have been carried out for solid piers. Matthew [2], according to the American seismic design code, designed and manufactured a full-scale circular solid section reinforced concrete pier, eliminating the influence of size effect, and studied the whole process of pier failure. Sakai and Unjoh [3] carried out multidimensional seismic simulation shaking table tests on circular solid piers and analysed the failure mechanism of piers. Calvi et al. [4] focused on some relevant aspects of the damage development and collapse modes of hollow piers, such as absence of confinement, inadequate shear strength, shifting

of the critical section, and insufficient length of lap splices. Mo et al. [5–8] and Pinto et al. [9] studied the seismic performance of hollow rectangular section RC piers and gave the corresponding prediction models of seismic response of these piers according to the design codes of the authors' country. Cassese et al. [10, 11] designed and realized four concrete bridge piers with a hollow rectangular section with different shear span-to-section depth ratios to test the seismic performance of existing piers. Si and Ai [12, 13] carried out the pseudostatic test and shaking table test on reinforced concrete pier specimens. The experimental results verified that the reinforced concrete pier based on the displacement design method can meet the expected ductility seismic requirements. Wang [14] and Zhou [15], respectively, input unidirectional and bidirectional ground motion excitations to conduct shaking table tests on round-end solid piers of high-speed railways and studied the influence of the reinforcement ratio and shear span ratio on solid piers of railways. Most of the studies on hollow

rectangular piers are based on pseudostatic tests at home and abroad. Shaking table tests on hollow piers are rare. Shen and Gu [16] designed and manufactured two hollow high pier with different stirrup ratios. Shaking table tests were carried out to study the seismic response of piers under different earthquake excitations. Du et al. [17] made five large-scale hollow reinforced concrete pier specimens and carried out cyclic load tests to evaluate their seismic performance. Jiang et al. [18, 19] carried out cyclic load tests and shaking table tests on large-scale hollow pier specimens and discussed the influence of pier height, axial compression ratio, and other factors on pier ductility. Han et al. [20] designed and manufactured 12 hollow rectangular RC piers, carried out cyclic load tests, and established a fiber model. The tests showed that the ductility coefficient and the equivalent viscous damping ratio of the specimens meet the requirements of seismic design and all the specimens had good seismic performance. However, the actual earthquake motion process is a complex vibration process. The pseudostatic loading test ignores the influence of loading rate on the structural strength and stiffness characteristics and fails to reflect the seismic performance of components in actual vibration. Therefore, the pseudostatic loading test has great limitations [21]. Therefore, it is necessary to carry out shaking table tests for hollow rectangular piers to study the failure mechanism of the pier structure, analyse its failure mode, and evaluate its seismic performance.

To study the seismic performance of hollow piers under dynamic loading, nine hollow rectangular reinforced concrete piers with different stirrup ratios, reinforcement ratios, and axial compression ratios were designed and manufactured. Shaking table tests were carried out to study the failure mode, dynamic characteristics, acceleration and displacement response, dynamic magnification factor, ductility, and energy dissipation of hollow rectangular piers. This paper focuses on the failure mode and response analysis of shaking table tests on hollow piers. It can provide reference for performance-based seismic design of hollow piers.

2. Shaking Table Test Design

2.1. Similarity Constants. In this study, the prototype of pier was a hollow pier in engineering. The height of the prototype pier was 11.5 m. Considering the loading capacity of the shaking table in the laboratory and the limitation of test conditions, the length similarity constant was 1 : 8. Other similarity constant were deduced and calculated according to the general similitude law [22]. The specific values are shown in Table 1.

2.2. Model Design and Construction. Nine hollow piers were designed and manufactured in this test. The pier numbers were M1, M2, M3, M4, M5, M6, M7, M8, and M9, and their geometric dimensions were identical. According to the length similarity constant, the pier height of the tested specimens was 1.44 m. The cross section of the specimens was 180 × 250 mm, the inner hollow part was 60 × 130 mm, and the wall thickness was 60 mm. Three views of the pier are shown in Figure 1. Concrete strength grade of the pier model was C20. The

TABLE 1: Similarity constants.

Parameter	Similarity relation	Similarity ratio
Length	l_r	0.125
Elastic modulus	E_r	0.78
Density	$\bar{\rho}_r = m_m + m_a + m_{om}/l_r^3 (m_p + m_{op})$	6.22
Stress	$\sigma_r = E_r$	0.78
Strain	$r_r = l_r$	0.125
Time	$t_r = \sqrt{l_r^2 \bar{\rho}_r / E_r}$	0.353
Velocity	$v_r = \sqrt{E_r / \bar{\rho}_r}$	0.354
Acceleration	$a_r = E_r / l_r \bar{\rho}_r$	1
Frequency	$\omega_r = \sqrt{E_r / l_r^2 \bar{\rho}_r}$	2.83

diameter of the longitudinal reinforcement was 6 mm and 8 mm, and the strength grade of the longitudinal reinforcement was HRB335. A galvanized iron wire with diameters of 3 mm and 4 mm was used for stirrups. Details of model specimens are shown in Figure 1. The mechanical properties of concrete and steel bars are listed in Tables 2 and 3, respectively. The physical parameters of each specimen are shown in Table 4. And the picture of the specimen is shown in Figure 2.

2.3. Counterweight Design. In this experiment, iron blocks were used to simulate the artificial mass, and the counterweight box was made to hold iron blocks and fixed on the top of the pier model. The counterweight box was welded with a Q235 steel plate of 5 mm thickness. The size of the counterweight box was 1.0 m × 1.0 m × 0.7 m. In order to achieve a fixed connection with the top of the model specimen, a rectangular sleeve with a cross section of 0.3 × 0.25 m and a height of 0.3 m was welded inside the counterweight box. The bolt holes were reserved at the top of the rectangular sleeve, and the bolts were reserved at the top of the model specimen through the nuts. The counterweight box weighed 200 kg. The object of the counterweight box is shown in Figure 3.

2.4. Test Content and Layout of Test Points. Acceleration sensors and velocity sensors were arranged on the pier top and bottom of hollow pier specimens to record the acceleration and velocity responses of the pier top and bottom. An acceleration sensor was arranged on the platform to record the ground motion of the platform; five concrete strain gauges were arranged on the two sides of the vertical loading direction (transverse bridge direction) of the pier specimens. There were 10 concrete strain gauges, numbered H1–H5 and H6–H10, respectively, from bottom to top; three steel strain gauges were arranged on the bottom of the pier with longitudinal reinforcement at each corner. There were 12 steel strain gauges. The layout of specific measuring points is shown in Figure 4.

2.5. Ground Motion Waves and Loading Conditions. Three kinds of ground motion waves, El Centro wave, Taft wave, and artificial Lanzhou wave, were used as excitation in this experiment. Loading conditions are listed in Table 5.

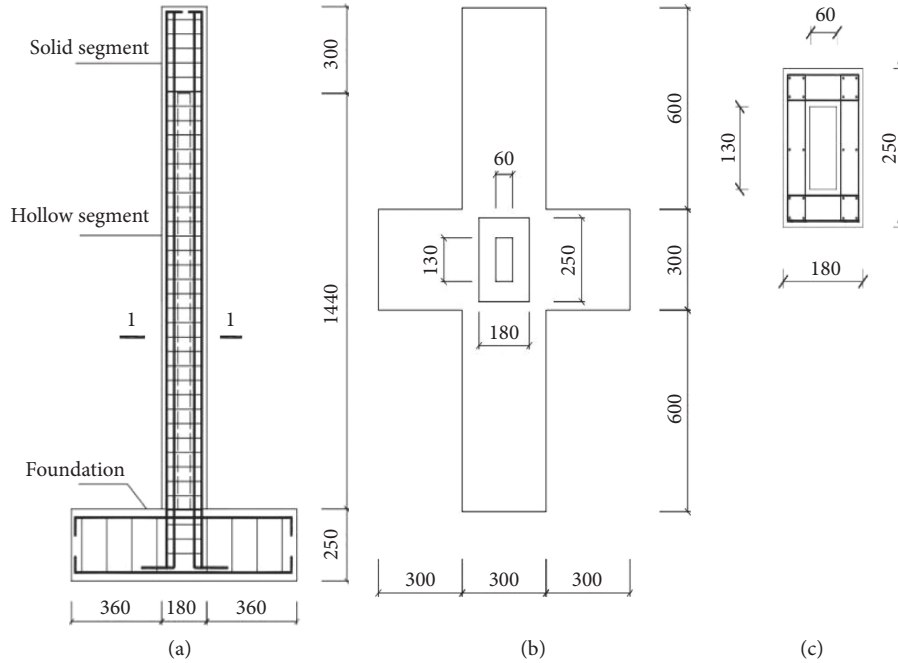


FIGURE 1: Details of the model specimen. (a) Front view. (b) Top view. (c) 1-1 cross sections.

TABLE 2: Mechanical properties of concrete.

Strength grade	Compressive strength (MPa)	Elastic modulus (MPa)
C20	13.4	18560
C30	20.1	20000

TABLE 3: Mechanical properties of steel bars.

Diameter (mm)	Yield strength (MPa)	Tensile strength (MPa)	Elongation (%)	Elastic modulus (MPa)
8	389.1	614.4	8.1	194550
6	385.3	613.8	8.5	192650
4	383.4	601.4	9.1	191700
3	383.2	577.2	8.8	191600

TABLE 4: Detailed physical parameters of the specimen.

Specimen	Pier height (mm)	Axial compression ratio	Longitudinal reinforcement		Transverse reinforcement		
			Diameter (mm)	Reinforcement ratio (%)	Diameter (mm)	Distance (mm)	Stirrup ratio (%)
M1	1440	0.1	8	2.7	4	50 (double)	4.0
M2	1440	0.1	8	2.7	4	50	2.0
M3	1440	0.1	8	2.7	3	70	0.81
M4	1440	0.1	8	2.7	3	130	0.44
M5	1440	0.1	6	1.5	3	130	0.44
M6	1440	0.05	8	2.7	3	70	0.81
M7	1440	0.05	8	2.7	3	130	0.44
M8	1440	0.05	6	1.5	3	130	0.44
M9	1440	0.05	6	1.5	3	70	0.81

3. Results and Discussion

3.1. Reappearance of Ground Motion Waves. Taking three waves in 0.75 g condition as an example, the theoretical value of the acceleration-time history curve and the measured

value of the acceleration-time history curve of the platform were compared, as shown in Figure 5. It can be seen that the curve shapes of measured values and theoretical values are in good agreement, which shows that the performance of the shaking table is good.



FIGURE 2: Picture of the pier specimen.



FIGURE 3: Counterweight box.

3.2. Failure Mode. All specimens began to crack at the bottom of the pier. With the increase of the peak acceleration of ground motion, cracks continued to extend upward, and the original cracks became wider and deeper. All pier specimens showed horizontal through cracks, and bridge piers were all bending failure. The specific failure modes of each specimen are shown in Table 6. The distribution of post-earthquake cracks of pier specimens is shown in Figure 6.

3.3. Natural Vibration Period of Piers. The pier model of this experiment can be regarded as a single-degree-of-freedom system. When the input ground motion stops, the pier specimen will generate free vibration. The vibration period of the pier can be obtained by fast Fourier transform of the acceleration- or displacement-time history curve of the pier top at this stage. The period after each stage is shown in Figure 7.

From Figure 7, it can be seen that, with the increase of the input ground motion, the vibration period of each specimen increased, which indicated that the specimens were damaged under the effect of ground motion, and the stiffness of the specimens reduced. Comparing M1 and M2, M6 and M7, and M8 and M9, it was found that the vibration

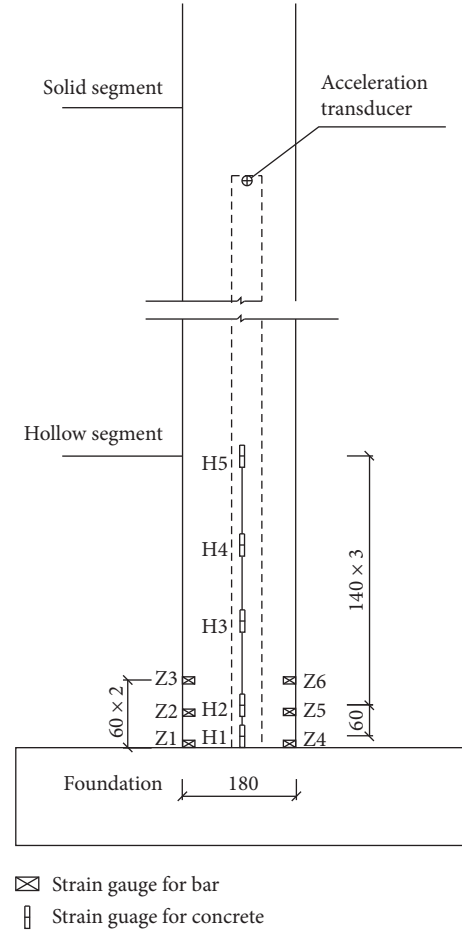


FIGURE 4: Layout of measuring points.

periods of each group of specimens were similar. This showed that the stirrup ratio has a relatively small impact on the specimen period. Comparing M4 and M5, M6 and M9, and M7 and M8, it can be seen that the reinforcement ratio has a significant impact on the period of the specimen. The higher the reinforcement ratio is, the higher the stiffness of the specimen is and the smaller the natural vibration period is. The higher the axial compression ratio is, the higher the vibration period is. In addition, it can be seen from the figure that the period of the M5 specimen was the largest after 1.2 g, which indicated that the stiffness of the M5 specimen decreased most obviously and the damage was more serious. The results showed that high axial compression ratio, low reinforcement ratio, and low stirrup ratio have adverse effects on the period of specimens.

3.4. Damping Ratio of Specimen. Damping mainly affects the decay rate of structural free vibration. The higher the damping ratio is, the higher the decay rate of the structure is. The damping ratio of pier specimens can be obtained by analysing the peak displacement point at the pier top when free vibration occurs. It can be computed as follows:

$$\xi = \frac{1}{2\pi j} \ln \frac{u_i}{u_{i+j}}, \quad (1)$$

TABLE 5: Loading conditions.

Condition number	Peak value of input ground motion wave (g)	Input ground motion wave
1	0.035	White noise
2	0.25	El Centro wave
3		Taft wave
4		Artificial Lanzhou wave
5	0.035	White noise
6	0.5	El Centro wave
7		Taft wave
8		Artificial Lanzhou wave
9	0.035	White noise
10	0.75	El Centro wave
11		Taft wave
12		Artificial Lanzhou wave
13	0.035	White noise
14	1.0	El Centro wave
15		Taft wave
16		Artificial Lanzhou wave
17	0.035	White noise
18	1.2	El Centro wave
19		Taft wave
20		Artificial Lanzhou wave
21	0.035	White noise

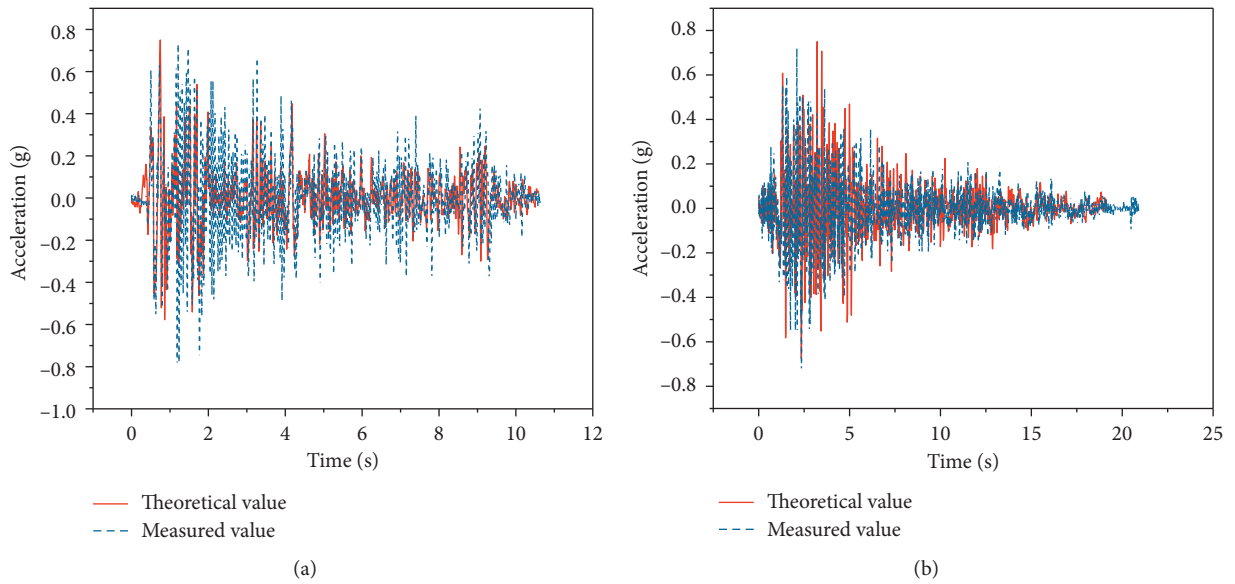


FIGURE 5: Continued.

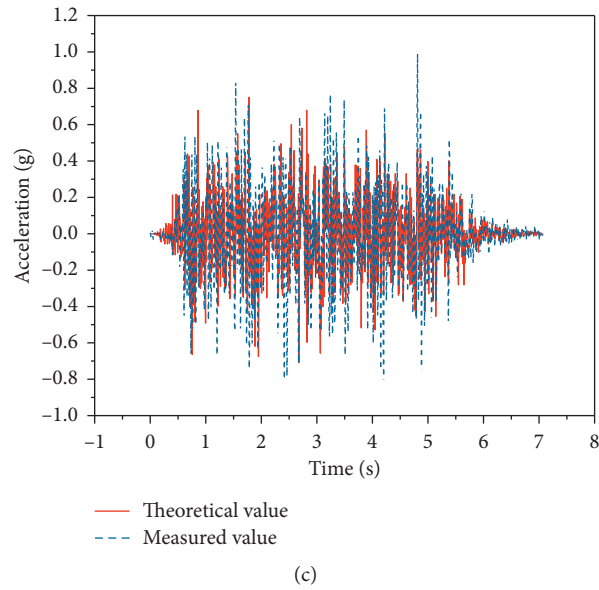


FIGURE 5: Acceleration-time history curves. (a) El Centro wave. (b) Taft wave. (c) Artificial Lanzhou wave.

TABLE 6: Failure modes.

Loading conditions (g)	Failure modes
0.25	The specimens had slight vibration, and no visible cracks appeared.
0.5	The vibration of the specimens was obvious, and there were slight cracks at the four bottom corners of the specimens. M7 produced penetrating cracks. There were some horizontal cracks in the middle and lower parts of M5, M8, and M9. Wider cracks occurred at the connection between the bottom of the column and the base of the specimen.
0.75	Shaking of the specimen became increasingly severe, and the specimen was pulled out from the base. Previous cracks on M3 and M4 continued to extend, their widths increased, and new cracks occurred. New penetrating cracks appeared on the M7 specimen.
1.0	The previous crack continued to extend. M3, M4, M5, and M6 had penetrating cracks, the column was pulled out from the base obviously, the new cracks continued to extend upward, and the cover concrete at the root of the pier column began to spall.
1.2	Shaking of the specimen became increasingly severe. All the nine pier specimens had penetrating cracks, the number of cracks increased, and the width of cracks widened. M7 produced four through cracks when the input ground motion was 0.5 g and 0.75 g. With the increase of the peak acceleration of input ground motion, the width of cracks continued to increase, but new cracks did not occur. The cracks of other specimens continued to extend to the upper part of the pier, and the number of cracks increased obviously, but all the specimens had vertical bearing capacity.

where ξ = damping ratio, u_i = the i th peak displacement, and u_{i+j} = the first $(i+j)$ th peak displacement.

Figure 8 shows the damping ratios of piers. It can be seen from the figure that, with the increase of the peak acceleration

of the input ground motion excitation, the damping ratio of the specimens increased and ranged from 0.02 to 0.064 overall. The damping ratio was little different among the specimens. Comparing groups, it was found that the damping ratio of M4



(a)



(b)



(c)



(d)



(e)



(f)

FIGURE 6: Continued.



FIGURE 6: Distribution of postearthquake cracks of each pier: (a) M1; (b) M2; (c) M3; (d) M4; (e) M5; (f) M6; (g) M7; (h) M8; (i) M9.

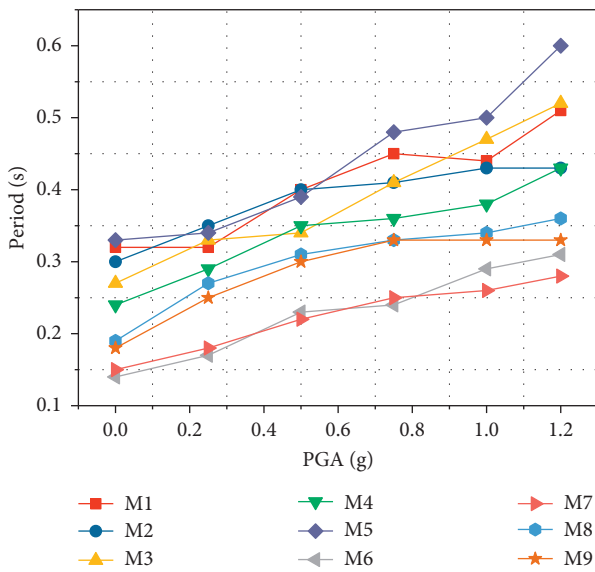


FIGURE 7: Natural vibration period of piers.

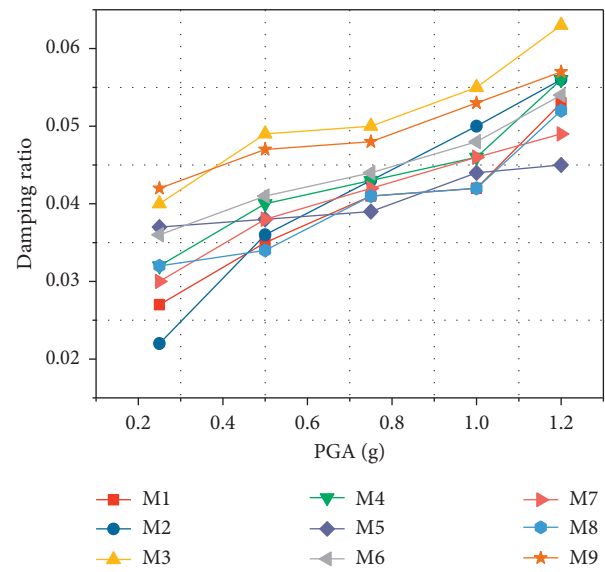


FIGURE 8: Damping ratio.

was higher than that of M5 and the damping ratio of M6 was higher than that of M9. It showed that when the axial compression ratio and stirrup ratio remain unchanged, the higher the reinforcement ratio is, the smaller the damping ratio is. Comparing M3 and M6, M4 and M7, and M5 and M8, it can be judged that, with the increase of the axial compression ratio, the damping ratio increased. Comparing M3 and M4, M6 and M7, and M8 and M9, it was found that the higher the stirrup ratio is, the higher the damping ratio of the specimen is. It indicated that the decay rate of the specimen is faster.

3.5. Acceleration Response of Piers. The acceleration of the pier top under three kinds of waves is shown in Figure 9.

With the increase of the input ground motion excitation, the maximum acceleration of the pier top increased. The acceleration-time history curves of M6 specimens under working conditions 10 (El Centro 0.75 g), 11 (Taft 0.75 g), and 12 (Taft 0.75 g) are listed, as shown in Figure 10.

Comparing M4 and M5, M6 and M9, and M7 and M8, it was shown that the pier top extreme acceleration of the former was bigger than that of the latter, which showed that when the axial compression ratio and stirrup ratio are the same, the higher the longitudinal reinforcement ratio is, the bigger the pier top extreme acceleration is. Taking the Taft wave as an example, when the PGA was 0.25 g, with the decrease of the longitudinal reinforcement ratio, the three extreme accelerations declined by 30%, 44%, and 21%,

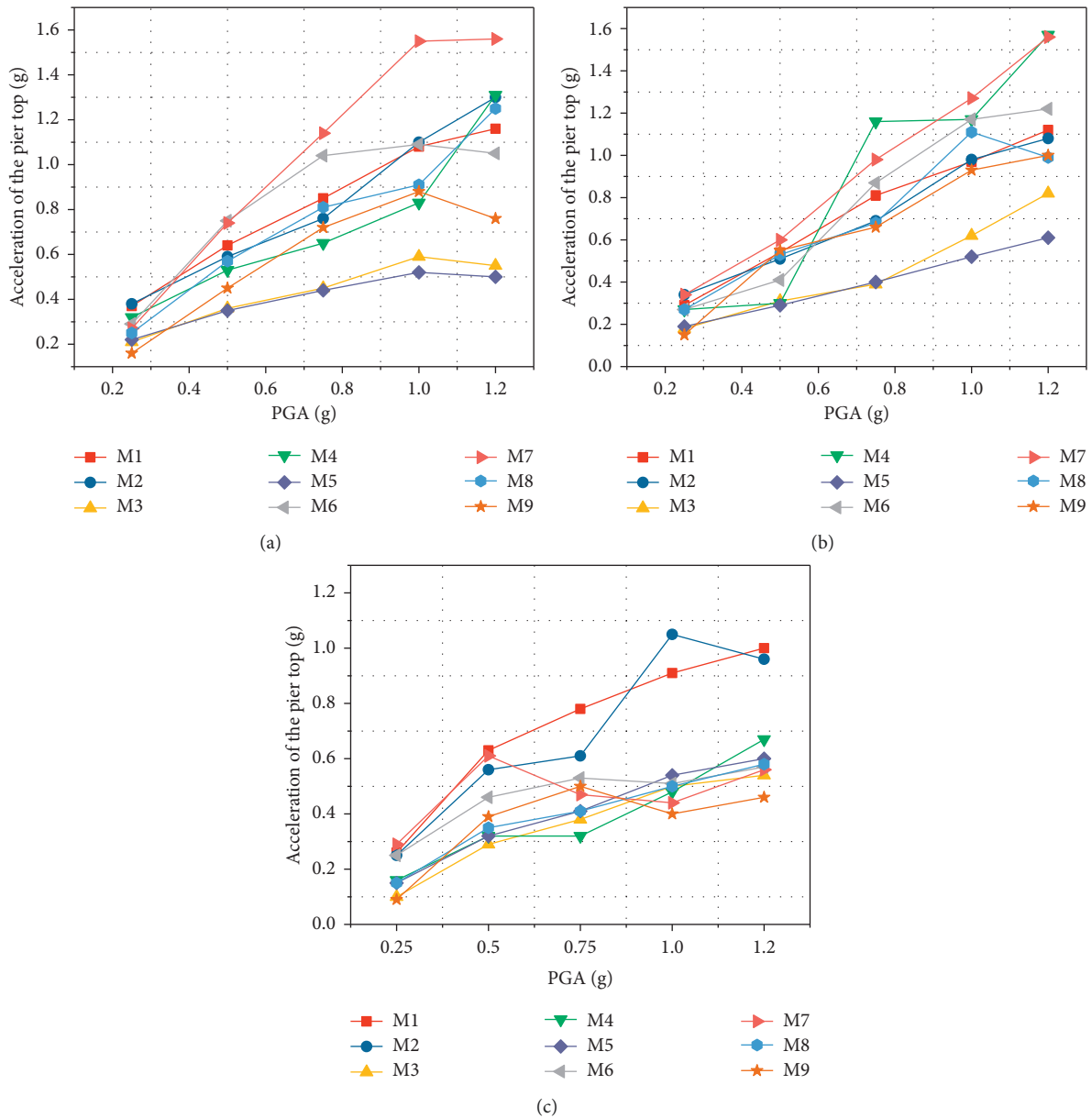


FIGURE 9: Acceleration response on the pier top under different ground motion waves. (a) El Centro wave. (b) Taft wave. (c) Artificial Lanzhou wave.

respectively; when the PGA was 0.75 g, the three extreme accelerations declined by 66%, 24%, and 31%, respectively; when the PGA was 1.0g, the three extreme accelerations declined by 56%, 21%, and 13%, respectively. It showed that, under the action of high axial compression ratio, the extreme acceleration of the pier top decreased sharply when the reinforcement ratio decreased, which indicated that the longitudinal reinforcement ratio has a more obvious effect on pier top extreme acceleration at high axial compression ratio, while the stirrup ratio has little effect on the pier top extreme acceleration.

Comparing M3 and M6, M4 and M7, and M5 and M8, it can be seen that the former was smaller than the latter, indicating that the maximum acceleration of the pier top increased with the decrease of the axial compression ratio.

This is because the upper mass decreased, the period of the specimen decreased, and the acceleration response of the pier top increased.

Comparing M3 and M4, M6 and M7, and M8 and M9, it can be seen that, with the increase of the stirrup ratio, the peak acceleration of the pier top decreased. This tendency is obvious under El Centro waves and Taft waves, but the effect of stirrups under artificial Lanzhou waves is not obvious. The effect of stirrups is more obvious at high axial compression ratio.

3.6. Displacement Response of Pier Top. The extreme displacement of the pier top of each specimen is shown in Figure 11. Figure 12 shows the pier top displacement-time

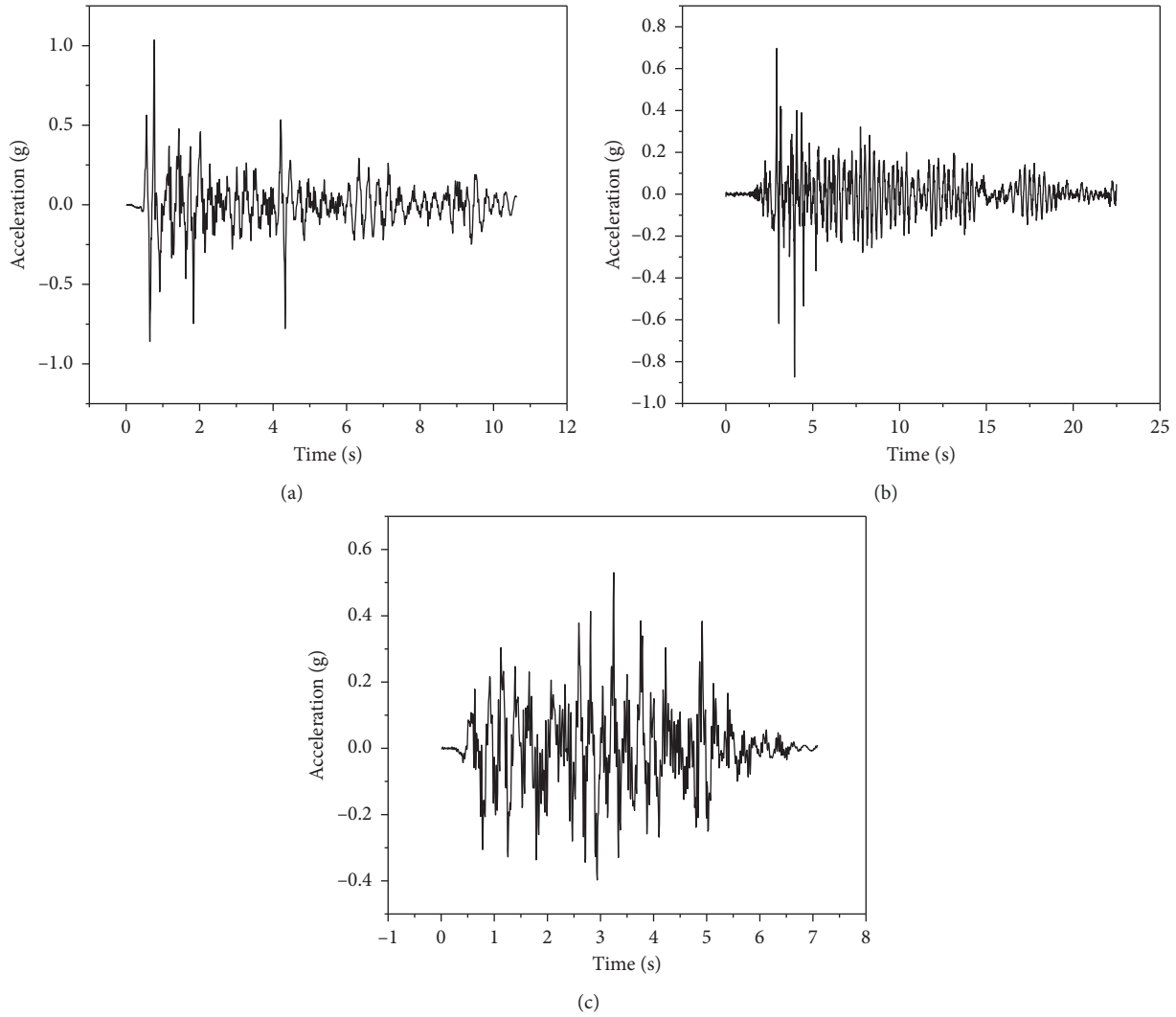


FIGURE 10: Acceleration-time history curve of the pier top. (a) El Centro wave. (b) Taft wave. (c) Artificial Lanzhou wave.

history curve of the M6 specimen at 0.75 g. It can be seen that the displacement of the pier top increased with the increase of the PGA. Increasing reinforcement ratios can reduce displacement of the pier top. The higher the axial compression ratio, the bigger the displacement response of the pier top, and the increase of the displacement of the pier top was at least 20%. The higher the stirrup ratio is, the bigger the extreme displacement of the pier top is.

3.7. Dynamic Magnification Factor. Dynamic magnification factor is the ratio of the maximum absolute acceleration response of the specimen to the maximum input ground motion acceleration. The dynamic magnification factor after each stage is shown in Figure 13. With the increase of the input ground motion excitation, the damage of pier specimens accumulated and the period increased, so the dynamic magnification factor decreased. It can be seen from Figure 13 that the bigger the reinforcement ratio is, the bigger the stiffness of the specimen is and the bigger the dynamic magnification factor is. With the increase of the axial

compression ratio, the upper mass increased, the period increased, and the dynamic magnification factor decreased. Increasing stirrup ratios can slow down the decreasing trend of dynamic magnification factor. The trend of dynamic magnification factor is consistent with the trend of acceleration response.

3.8. Displacement Ductility Factor. It is an important index to evaluate the seismic performance of bridges. In this paper, Shigeki's method was used to approximate the displacement ductility factor of the specimens [23]. The method assumes that the lateral displacement restoring force model of the pier top is an ideal elastic-plastic model. It can be calculated as follows:

$$\mu = \frac{\delta_i}{\delta_y} = \frac{T_i^2}{T_0^2}, \quad (2)$$

where μ = displacement ductility factor, δ_i = maximum displacement response under seismic loading of a certain intensity, δ_y = yield displacement, T_i = natural vibration

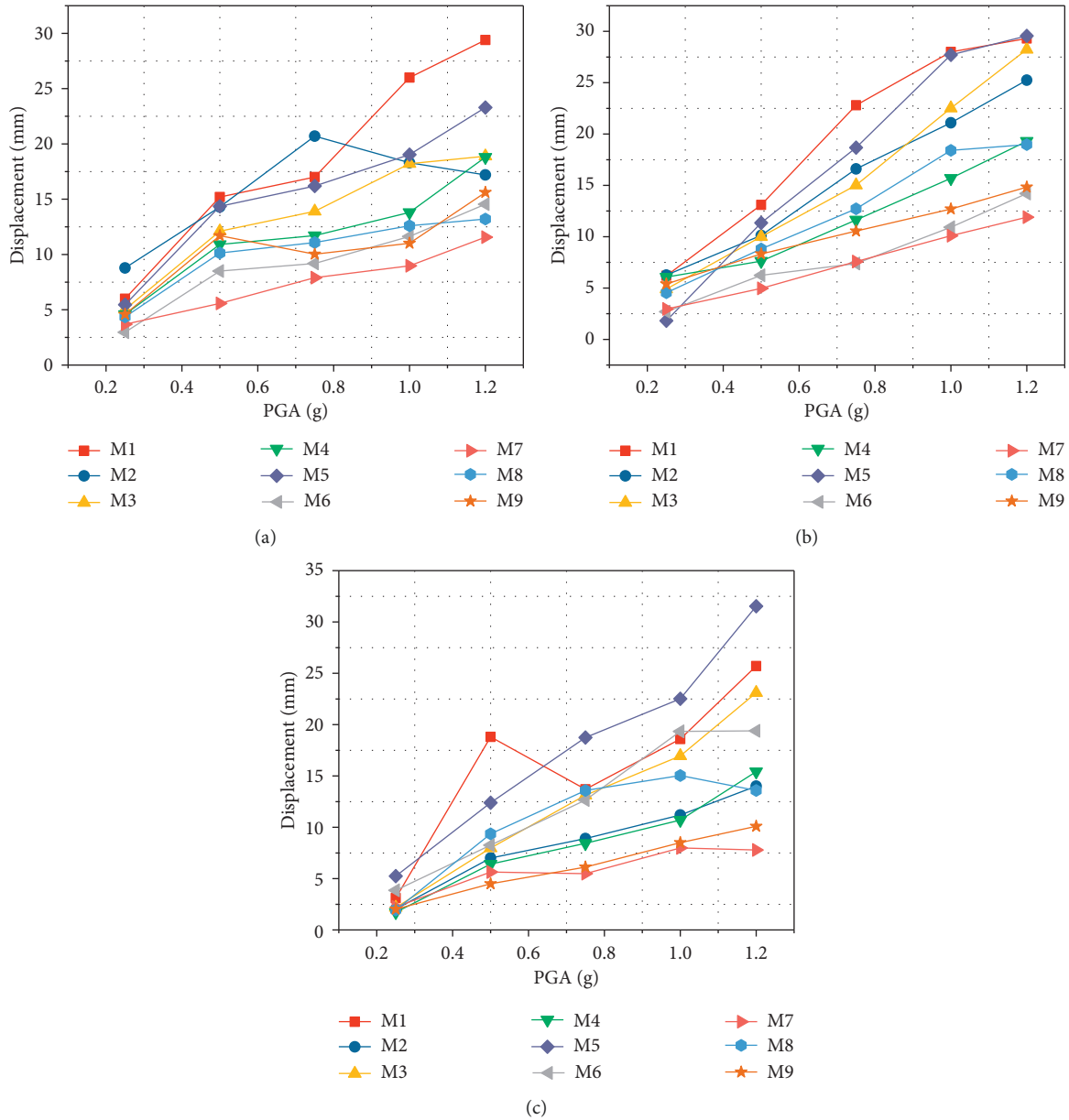


FIGURE 11: Displacement response on the pier top under different ground motion waves. (a) El Centro wave. (b) Taft wave. (c) Artificial Lanzhou wave.

period after certain working conditions, and T_0 = natural vibration period before loading.

The displacement ductility factor obtained is shown in Figure 14.

It can be seen that the displacement ductility factor increased with the increase of the PGA. The displacement ductility coefficients of all pier specimens were between 1.0 and 5.0. Increasing reinforcement ratios and stirrup ratios can increase the displacement ductility factor of pier specimens, and increasing axial compression ratios can reduce the displacement ductility factor.

3.9. Energy Dissipation of Specimens. The energy dissipation capacity of piers is an important parameter to measure the seismic performance of piers. The better the

energy dissipation capacity is, the better the seismic performance of piers is. In this test, the piers can be calculated according to the SDOF system. The energy balance equation of the nonlinear SDOF system is as follows:

$$\int_0^t m\ddot{u}(t)\dot{u}(t)dt + \int_0^t c\dot{u}(t)\dot{u}(t)dt + \int_0^t k\dot{u}(t)\dot{u}(t)dt = - \int_0^t m\ddot{u}_g(t)\dot{u}(t)dt. \quad (3)$$

Simplifying formula (3) yields the following formula:

$$E_k(t) + E_D(t) + E_s(t) + E_H(t) = E_1(t). \quad (4)$$

Formula (4) corresponds to formula (3), where $E_k(t)$ = kinetic energy of the SDOF system, $E_D(t)$ = structural

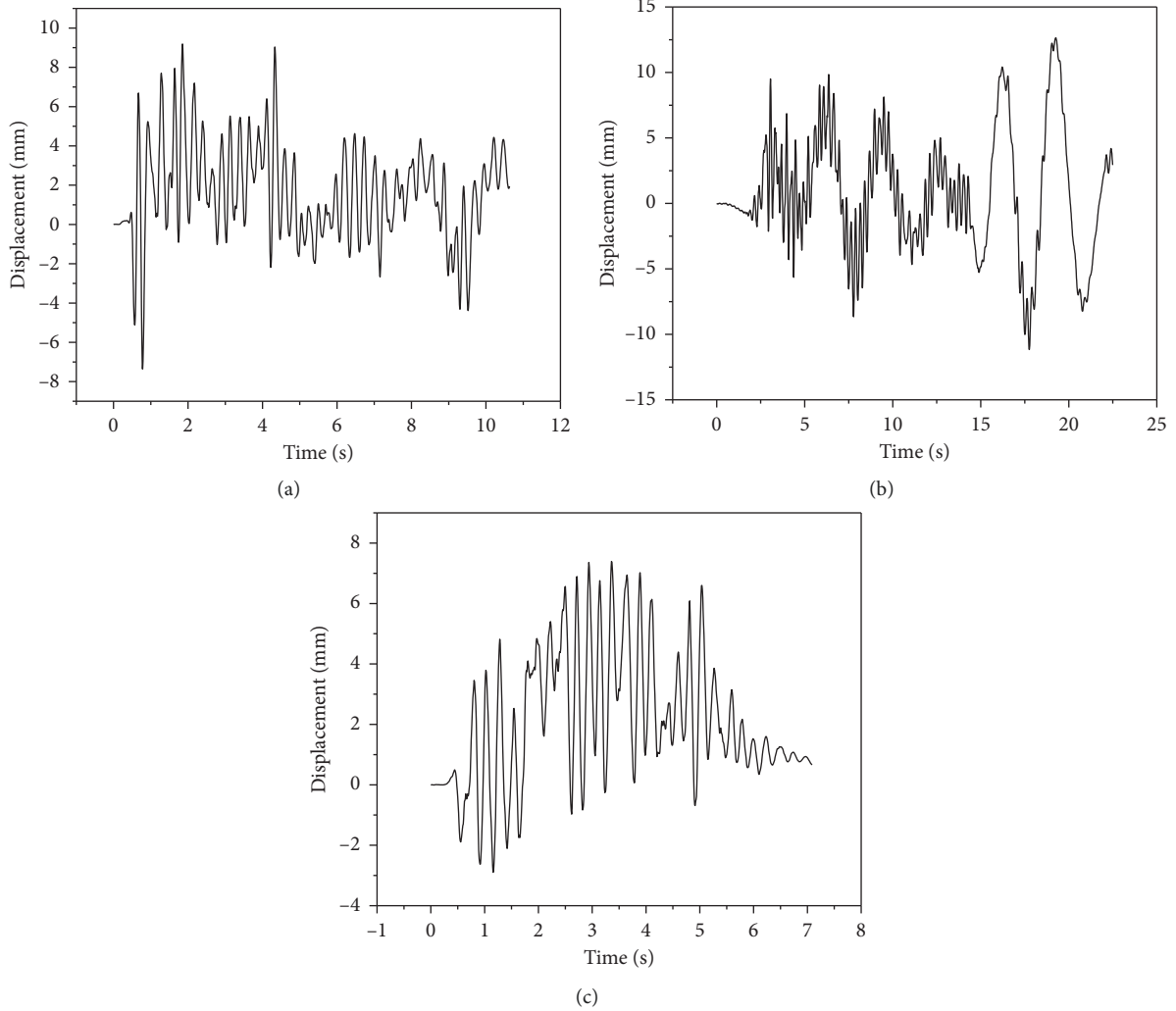


FIGURE 12: Displacement-time history curve of the pier top. (a) El Centro wave. (b) Taft wave. (c) Artificial Lanzhou wave.

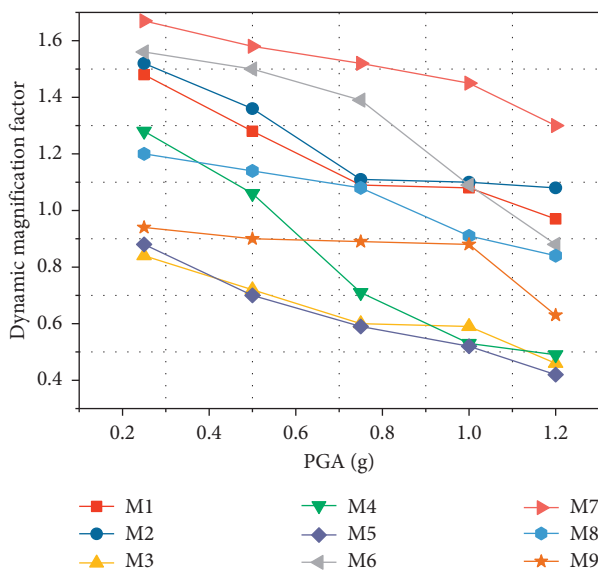


FIGURE 13: Dynamic magnification factor.

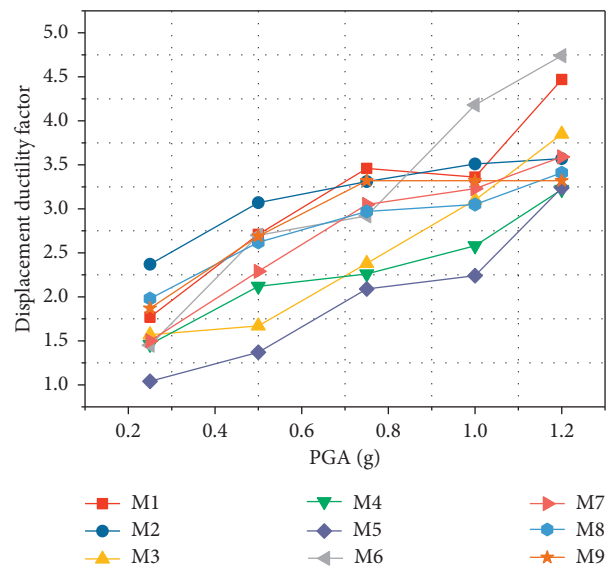


FIGURE 14: Displacement ductility factor.

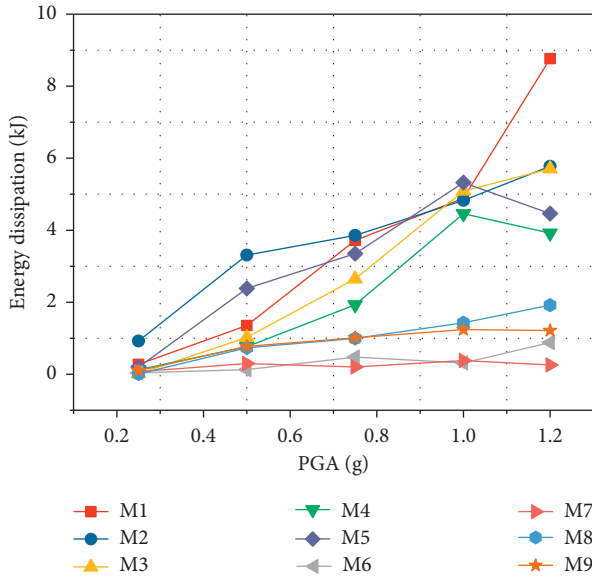


FIGURE 15: Energy dissipation of each pier specimen.

damping energy dissipation, $E_s(t)$ = elastic deformation energy, $E_H(t)$ = hysteretic energy, and $E_I(t)$ = total input seismic energy. When the earthquake excitation ends, $E_k(t) = 0$ and $E_s(t) = 0$, so formula (4) is transformed as follows:

$$E_D(t_e) + E_H(t_e) = E_I(t_e). \quad (5)$$

Therefore, the total input seismic energy is the total energy dissipation of pier specimens. Energy dissipation of each pier specimen is shown in Figure 15. It can be seen that the energy dissipation of each specimen increased with the increase of the PGA. The energy dissipation of M1–M5 piers was higher than that of M6–M9, which indicated that increasing the axial compression ratio can increase the energy dissipation of piers, especially when the input ground motion excitation is stronger, and the energy dissipation of the specimen increased significantly with the increase of the axial compression ratio.

Comparing M1, M2, M3, and M4, it was found that the stirrup ratio of the four specimens decreased in turn, and the energy dissipation of the specimens decreased. It can be seen that the energy dissipation of the specimens increased with the increase of the stirrup ratio. Under the action of high axial compression ratio, the effect of stirrups on energy dissipation of specimens is more obvious.

It can also be seen that the energy dissipation of M5, M9, and M8 was bigger than that of M4, M6, and M9, respectively. The results showed that the higher the reinforcement ratio is, the smaller the total seismic input energy is and the smaller the energy dissipation of the specimen is.

4. Conclusions

In this paper, nine hollow rectangular reinforced concrete pier columns with a geometric similarity ratio of 1/8 were designed and fabricated. The El Centro wave, Taft wave, and artificial Lanzhou wave were selected as seismic

excitation for the shaking table test to study the influence of different parameters on the seismic performance of hollow piers. The following conclusions are drawn from this study:

- (1) With the increase of the PGA, cracks continued to develop and gradually became deeper and wider. Horizontal cracks were dominant under the action of ground motion excitation, in accordance with the bending failure mode. The period of piers increased continuously. The period of all specimens did not exceed 0.62 s, and the damping ratio ranged from 0.02 to 0.064.
- (2) The dynamic amplification factor of the pier specimen decreased with the increase of the PGA and increased with the increase of the reinforcement ratio.
- (3) The pier top acceleration response increased with the increase of the reinforcement ratio and decreased with the increase of the axial compression ratio and stirrup ratio, but the stirrup ratio had a relatively small impact on pier top acceleration response. The reinforcement ratio had a more obvious influence on pier performance at high axial compression ratio.
- (4) The displacement of the pier top increased with the increase of the PGA, decreased with the increase of the reinforcement ratio, and increased with the increase of the axial compression ratio and stirrup ratio.
- (5) With the increase of the PGA, the displacement ductility factor of pier specimens increased. The energy consumption of pier specimens increased with the increase of the stirrup ratio and axial compression ratio and decreased with the increase of the reinforcement ratio.
- (6) The axial compression ratio, reinforcement ratio, and stirrup ratio have evident effects on the ductility of the pier columns. Therefore, it is suggested that the axial compression ratio should be limited and the reinforcement ratio and stirrup ratio should be properly increased in the design of hollow rectangular piers in the future.

Data Availability

The data used to support the findings of this study are available from the corresponding author upon request.

Conflicts of Interest

The authors declare that there are no conflicts of interest regarding the publication of this paper.

Acknowledgments

This research was funded by the National Natural Science Fund of China (NSFC) (grant no. 51378169) and Natural Science Foundation of Hebei Province in China (E2013402072).

References

- [1] X. Du and Q. Han, "Research progress on seismic design of bridges," *Earthquake Engineering and Engineering Vibration*, vol. 34, no. 4, pp. 1–14, 2014.
- [2] J. S. Matthew, *A Full-Scale, Single-Column Bridge Bent Tested by Shake-Table Excitation*, PEER, Berkeley, CA, USA, 2015.
- [3] J. Sakai and S. Unjoh, "Shake table experiment on circular reinforced concrete bridge column under multidirectional seismic excitation," in *Proceedings of the Research Frontiers at Structures Congress*, vol. 5, no. 249, pp. 1–12, Long Beach, CA, USA, May 2007.
- [4] G. M. Calvi, A. Pavese, A. Rasulo, and D. Bolognini, "Experimental and numerical studies on the seismic response of R.C. hollow bridge piers," *Bulletin of Earthquake Engineering*, vol. 3, no. 3, pp. 267–297, 2005.
- [5] Y. L. Mo and I. C. Nien, "Seismic performance of hollow high-strength concrete bridge columns," *Journal of Bridge Engineering*, vol. 7, no. 6, pp. 338–349, 2002.
- [6] Y.-K. Yeh, Y. L. Mo, and C. Y. Yang, "Seismic performance of rectangular hollow bridge columns," *Journal of Structural Engineering*, vol. 128, no. 1, pp. 60–68, 2002.
- [7] Y. K. Yeh, Y. L. Mo, and C. Y. Yang, "Seismic performance of hollow circular bridge piers," *ACI Structure Journal*, vol. 98, no. 6, pp. 862–871, 2001.
- [8] Y.-K. Yeh, Y. L. Mo, and C. Y. Yang, "Full-scale tests on rectangular hollow bridge piers," *Materials and Structures*, vol. 35, no. 2, pp. 117–125, 2002.
- [9] A. V. Pinto, J. Molina, and G. Tsionis, "Cyclic tests on large-scale models of existing bridge piers with rectangular hollow cross-section," *Earthquake Engineering & Structural Dynamics*, vol. 32, no. 13, pp. 1995–2012, 2003.
- [10] P. Cassese, P. Ricci, and G. M. Verderame, "Experimental study on the seismic performance of existing reinforced concrete bridge piers with hollow rectangular section," *Engineering Structures*, vol. 144, pp. 88–106, 2017.
- [11] P. Cassese, M. T. De Risi, and G. M. Verderame, "Seismic assessment of existing hollow circular reinforced concrete bridge piers," *Journal of Earthquake Engineering*, vol. 6, pp. 1–36, 2018.
- [12] B. Si, H. Li, D. Wang et al., "Experimental evaluation of the seismic performance of reinforced concrete bridge piers designed on the basis of displacement (I): quasi-static test," *Earthquake Engineering and Engineering Vibration*, vol. 28, no. 1, pp. 123–129, 2008.
- [13] Q. Ai, H. Li, D. Wang et al., "Experimental evaluation of seismic performance of reinforced concrete bridge piers designed on the basis of displacement (II): shaking table test," *Earthquake Engineering and Engineering Vibration*, vol. 28, no. 3, pp. 39–46, 2008.
- [14] H. Wang, "Influence of reinforcement ratio on seismic response of round-ended bridge pier in high speed railway," School of Civil Engineering, Central South University, Changsha, China, Master dissertation, 2014.
- [15] Z. Zhou, "The influence of shear-span ration on the seismic response of round-ended solid piers in high speed rail," School of Civil Engineering, Central South University, Changsha, China, Master dissertation, 2014.
- [16] Y. Shen and S. Gu, "Shake table test for reinforced concrete hollow rectangular pier," *Journal of Architecture and Civil Engineering*, vol. 35, no. 5, pp. 128–133, 2018.
- [17] X. Du, M. Chen, and Q. Han, "Experimental evaluation of seismic performance of reinforced concrete hollow bridge columns," *Journal of Vibration and Shock*, vol. 30, no. 11, pp. 254–259, 2011.
- [18] L. Jiang, G. Shao, J. Jiang et al., "Experimental study on seismic performance of solid piers with round ended cross-section in high-speed railway," *China Civil Engineering Journal*, vol. 46, no. 3, pp. 86–95, 2013.
- [19] L. Jiang, G. Shao, and H. Wang, "Experimental study on seismic performance of hollow piers with rounded rectangular cross section in high-speed railways," *Engineering Mechanics*, vol. 31, no. 3, pp. 72–82, 2014, in Chinese.
- [20] Q. Han, Y. Zhou, and X. Du, "Seismic performance of reinforced concrete rectangular hollow bridge columns," *Engineering Mechanics*, vol. 32, no. 3, pp. 28–40, 2015, in Chinese.
- [21] J. Li, *Introduction to Earthquake Engineering*, Seismological Press, Beijing, China, 1992.
- [22] M. Zhang, "Study on similitude laws for shaking table tests," *Earthquake Engineering and Engineering Vibration*, vol. 17, no. 2, pp. 52–58, 1997, in Chinese.
- [23] S. Unjoh and H. Kobayashi, "Development of an earthquake damage detection system for bridge structures," in *Proceedings of North American Euro Pacific Workshop for Sensing Issues in Civil Structural Health Monitoring*, pp. 165–174, Honolulu, HI, USA, January 2005.

Research Article

Shake Table Response of Unreinforced Masonry and Reinforced Concrete Elements of Special Moment Resisting Frame

Syed Azmat Ali Shah, Junaid Shah Khan , Syed Muhammad Ali, Khan Shahzada, Waqar Ahmad, and Junaid Shah

Department of Civil Engineering, University of Engineering & Technology Peshawar, Peshawar, Pakistan

Correspondence should be addressed to Junaid Shah Khan; junaidshah@uetpeshawar.edu.pk

Received 21 March 2019; Revised 30 April 2019; Accepted 15 May 2019; Published 7 July 2019

Guest Editor: Maria T. de Risi

Copyright © 2019 Syed Azmat Ali Shah et al. This is an open access article distributed under the Creative Commons Attribution License, which permits unrestricted use, distribution, and reproduction in any medium, provided the original work is properly cited.

Half-scaled reinforced concrete frame of two storeys and two bays with unreinforced masonry (URM) infill walls was subjected to base excitation on a shake table for seismic performance evaluation. Considering the high seismic hazard Zone IV of Pakistan, reinforcement detailing in the RC frame is provided according to special moment resisting frames (SMFRs) requirement of Building Code of Pakistan Seismic-Provisions (BCP SP-2007). The reinforced concrete frame was infilled with in-plane solid masonry walls in its interior frame, in-plane masonry walls with door and window openings in the exterior frame, out-of-plane solid masonry wall, and masonry wall with door and window openings in its interior frame. For seismic capacity qualification test, the structure was subjected to three runs of unidirectional base excitation with increasing intensity. For system identification, ambient-free vibration tests were performed at different stages of experiment. Seismic performance of brick masonry infill walls in reinforced concrete frame structures was evaluated. During the shake table test, performance of URM infill walls was satisfactory until design ground acceleration was 0.40g with a global drift of 0.23%. The test was continued till 1.24g of base acceleration. This paper presents key findings from the shake table tests, including the qualitative damage observations and quantitative force-displacement, and hysteretic response of the test specimen at different levels of excitation. Experimental results of this test will serve as a benchmark for validation of numerical and analytical models.

1. Introduction

Constructions such as Reinforced Concrete (RC) frame with unreinforced brick masonry (URM) are commonly observed all over the world particularly in the seismically active regions [1, 2]. In Pakistan, the low-rise URM building is commonly practiced. Due to population growth (207 million, according to 6th Population and Housing Census-2017) and suburbanization, construction trend has been changing from URM buildings to multistorey RC frame infilled with URM walls [3]. URM is considered as nonstructural element, and on regular basis it is ignored in the structural analysis and design [4]. However, the presence of the URM wall can significantly alter the lateral load resisting mechanism and complete dynamic behavior by interaction of the infill wall with bounding RC frame under seismic loading [5]. Frame infill interaction may produce desirable (increase

in lateral stiffness, lateral-load capacity, damping, ductility, and energy dissipation capacity) and undesirable effects (soft story mechanism, short column effect, and torsional action) on the global structural performance of the building [6]. Performance of the infilled RC frame has been studied with simplified analytical models (equivalent diagonal strut models by Stafford Smith [7]); Madan et al. [8] detailed finite element analysis (FEA) [9–12] and also with experiments, i.e., quasi-static, pseudodynamic, and shake table tests [13–17]. Many researchers claimed that even though extensive research has been done on masonry infilled RC frames over the decades, the behavior and seismic performance evaluation of such structures is not fully understood [17]. Some design guidelines developed by FEMA 356 [18], ASCE/SEI-7-06 [19], ASCE/SEI Standard 41-06 [20], and ATC-43 [21] for the seismic performance evaluation of masonry infilled RC frame is still considered as unreliable

and inadequate [22]. The existence of complexities is due to insufficient experimental data on large-scale models of multistory and multibays under dynamic loadings [17].

Different failure modes of masonry infilled structures have been witnessed by the past earthquakes and experimental studies. Severe damage has been demonstrated to these types of structures by previous earthquakes (including 1999 Kocaeli, Turkey earthquake [6]; the 2008 Sichuan, China earthquake; and the 1999 Chi-Chi, Taiwan Earthquake). The damage mechanism comprises of partial or full masonry panel failure, shear failure of columns, plastic hinges at columns ends, soft-storey mechanism, and short column effect [23, 24]. Mehrabi et al. [25] experimentally investigated fourteen half-scale masonry infilled RC frame test specimens and categorized 24 distinct failure modes. Later on Stavridis [22] narrowed down these mechanisms into three main failure modes which includes diagonal cracking (occurs in nonductile frames with strong infill), horizontal shear sliding (occurs in weak frames and weak infill), and corner crushing (occurs in strong frames and strong infill) as shown in Figure 1.

For the reason of damage evaluation of masonry infilled buildings, FEMA 306 [26] characterizes opening within infill as one of the most critical parameters affecting both the global and local seismic behaviors of structure. Doors and windows are the most commonly used types of opening within the infill panels. Opening within the infill panels are perfectly considered as assemblies of subcomponents of the appropriate material which can interact with a surrounding frame and can alter the dynamic behavior of structure. Interaction of strong columns and strong piers of infill panels can cause shear failure in the beams. However, interaction of strong spandrel component with frame can reduce the ductility by inducing short column effects and infill panel causing tensile yielding in the column. Experimental investigations have been made by many researchers [27–30] to study the effect of infill openings.

Limited experimental data are available on the dynamic behavior of RC frame infilled with URM since few shake table studies have been conducted on large scale [31, 32]. The typical construction of Pakistan is deficient in terms of workmanship, quality of materials, and arrangement of infill regarding the URM infill wall position and size of opening [33]; material properties of local brick masonry such as initial rate of absorption and compressive strength of the mortar are different from those normally used across the world, which results in low compressive and tensile strength and weak bond between bricks and mortar [33, 34]. Experimental assessment of RC frame infilled with URM typically constructed according to local construction practices of Pakistan is unavailable on large scale having multistorey, multibays under real dynamic loading which is necessary for the calibration and verification of analytical model, providing foundation in defining new strategies of design as recommended by ACI (American Concrete Institute). Therefore, a shake table study of three-dimensional, two-storey, two-bay, solid brick masonry infilled frame is conducted on large six degrees of freedom (6 D.O.F) shake table at Earthquake

Engineering Center (EEC), University of Engineering and Technology (UET), Peshawar. The specimen was half-scaled symmetric RC frame model constructed according to special moment-resisting frame (SMRF) requirements of Building Code of Pakistan Seismic-Provisions (BCP SP-2007). The RC frame was infilled with URM walls having door and window openings at different locations according to local construction practices of Pakistan. Different arrangements of door and window openings, holdfasts for anchorage of masonry wall to column, and construction with local labors make this structure unique. The test specimen was instrumented with accelerometers and displacement transducers and was subjected to six dynamic tests, including ambient free vibration and sinusoidal base motions of increasing intensity. The specimen was tested until the nonstructural URM walls were severely damaged. Experimental programs, including designing, construction, and testing of the specimen as well as the qualitative and quantitative experimental results are reported in this paper. The main original aspect of this research is to explore the damage mechanism of URM infill and RC frame and its ultimate seismic resistance in terms of maximum base shear force and ultimate drift capacity of SMRFs structures infilled with URM infill walls. The results will be further utilized in developing numerical and analytical models, which will provide foundation for the development of seismic design guidelines of infilled RC frame structures.

2. Experimental Program

2.1. Description of Test Specimen. The test specimen selected was RC frame having two storeys and two bays infilled with URM infill walls, which is commonly practiced for low-rise commercial and residential buildings. The test specimen was constructed on the 6 D.O.F shake table at EEC, UET, Peshawar. The three-dimensional, plan and elevation view of the test specimen are shown in Figures 2 and 3, respectively. Extensive experimental investigation through the shake table was carried out to evaluate the performance of brick masonry infilled RC frame structure constructed with indigenous material and labor. The RC frame was designed and constructed according to SMRFs requirement (BCP SP-2007). URM walls were constructed by splitting full-scale brick of $9 \times 4.5 \times 3$ in. ($22.8 \times 11.4 \times 7.6$ cm) into half-scale brick of $4.5 \times 2 \times 1.5$ in. ($11.4 \times 5.0 \times 3.8$ cm) discussed in Section 2.2. URM walls of thickness 4.5 in. (11.4 cm) were constructed with the brickwork of English bond. For bonding of bricks, mortar layer of thickness 1/8 in. (3.17 mm) and compounding ratio of one cement and five sand was used. The reinforced concrete frame was infilled with in-plane solid masonry walls in its interior frame, in-plane masonry walls with door and window openings in exterior frame, out-of-plane solid masonry wall, and masonry wall with door and window openings in its interior frame. To support the dead load of wall above openings, various reinforced concrete lintel beams were provided over the openings. The weight of the test specimen was approximately 16.20 metric tons (16,200 kg).

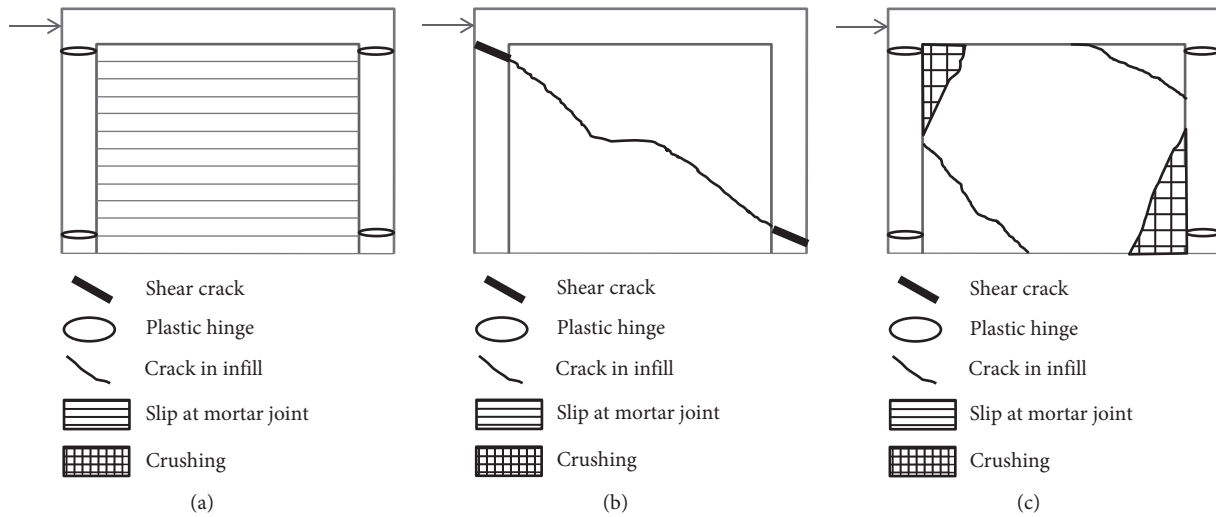


FIGURE 1: Three distinct failure mechanisms of masonry infills. (a) Horizontal sliding. (b) Diagonal cracking. (c) Panel or corner crushing.

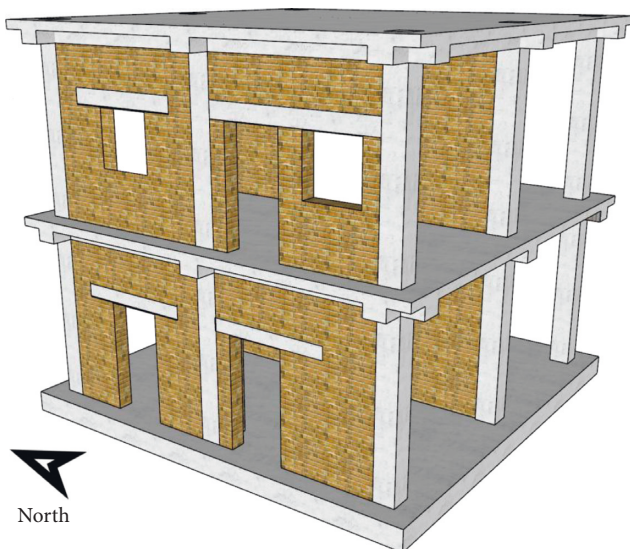


FIGURE 2: Three-dimensional view of prototype.

2.2. Scaling and Designing of RC Frame with URM.

Linear geometric dimensions of the structural element beams, columns, and slabs were reduced by a scale factor of 2. Material in the test specimen such as maximum size of aggregates, reinforcement bars, masonry bricks, and vertical and horizontal thickness of mortar layer were also reduced by half scale. Scaling factors for the fundamental quantities are summarized in Table 1 [35].

The construction process includes preparation of the foundation pad which was constructed directly on the shake table anchored with 36 bolts. Followed by the construction of first-storey columns and floor, similarly second-storey columns and floor were constructed. After the construction of RC frame, URM infilled walls were constructed. Reduced live load according to the lateral static force-based method of UBC 97 was used; therefore only 2560 lb. (1,200 kg) load were applied on the slab of first story.

The RC frame was designed with the lateral static force-based method of seismic design procedures which is based on Uniform Building Code (UBC) 97 and detailed as per SMRF requirements of American Concrete Institute (ACI) Committee 318 Building Code Requirement for Structural Concrete. Beams, columns, and beam-column joints in SMRFs structure is detailed such that it can resist axial, flexural, and shearing actions produced by structure during strong earthquake motion. High seismic hazard region is specified by Zone IV where PGA is greater than 0.32g (BCP SP-2007). Seismic hazard of Zone IV with a design PGA of 0.40g and soil type B was considered. Loads on structure includes the self-weight for structural beam-column elements and slabs, while superimposed dead load for partition URM infill walls, floor finishing, and live load of 40 psf (Pounds per square foot) (0.0019 MPa) was assigned to the structure. The concrete compressive strength of 3,000 psi (Pounds per square inch) (21 MPa) and reinforcing steel of 50,000 psi (344 MPa) which is typically used was considered in the design. The dimensions of the RC frame and reinforcement bars layout are given in Figure 4. Using 6-inch square of beams and columns, two types of reinforcement were provided at different locations as shown in Figure 5. In section 1-1 of beam, the longitudinal reinforcement of 6 #3 (9.52 mm) diameter bars and transverse reinforcement of #2 (6.35 mm) diameter bars at 2 inches (50.8 mm) center-to-center were provided. Section 2-2 of beam is having longitudinal reinforcement of 5 #3 (9.52 mm) bars and transverse reinforcement of #2 (6.35 mm) bars at 3 inches (76.2 mm) center-to-center.

Longitudinal reinforcement provided in the column section 3-3 is 8 #3 (9.52 mm) bars and transverse reinforcement of #2 (6.35 mm) bars at 2 inches (50.8 mm) center-to-center. Column cross section 4-4 is having 8 #3 (9.52 mm) bars of longitudinal reinforcement and #2 (6.35 mm) bars at 1.5 inches (38.1 mm) center-to-center. The transverse reinforcement in the beam and column was provided with 135° hook. The reinforcements in the slabs of

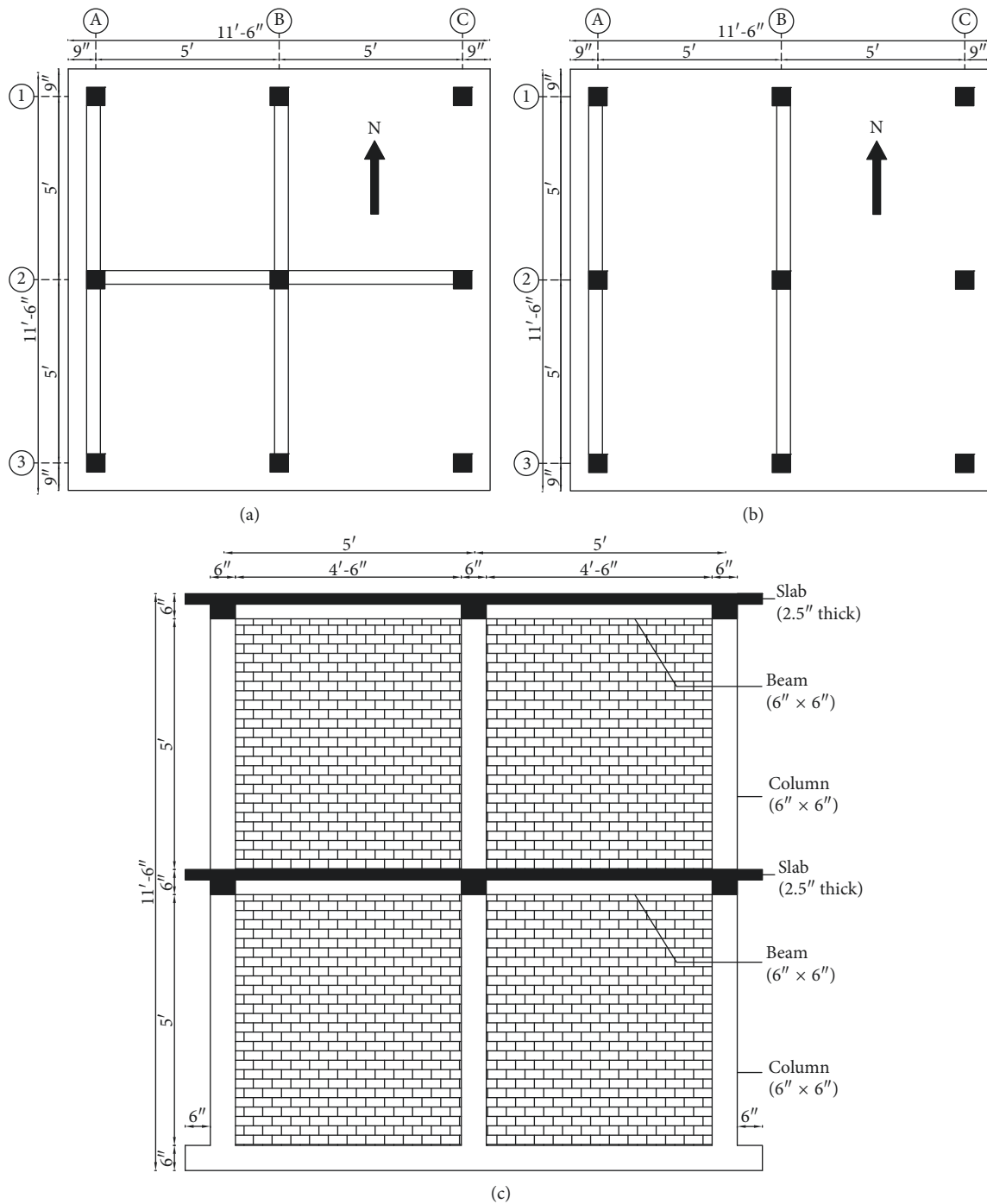


FIGURE 3: Plan and elevation view of the test specimen. (a) First-storey wall layout plan. (b) Second-storey wall layout plan. (c) Elevation view of the interior frame.

both the storeys were same, and the steel reinforcement detail of slabs is shown in Figure 6.

2.3. Material Properties. Various tests were conducted to identify the material properties of the test specimen. Tensile strength tests of #2 (6.35 mm) and #3 (9.52 mm) Grade-50 reinforcing steel bars were conducted as per ASTM A-615. For compressive strength, tests on concrete cylinders

6 × 12 in. (15.2 × 30.4 cm) as per ASTM C873, mortar cubes 2 × 2 in. (5.0 × 5.0 cm) as per ASTM C109, and masonry prism of 9 × 8 × 4.5 in. (22.8 × 20.3 × 11.4 cm) as per ASTM C1314 were carried out as shown in Figure 7(a). For shear strength, the diagonal masonry prism of 24 × 24 × 4.5 in. (60.9 × 60.9 × 11.4 cm) as per ASTM E 519 samples was made during the construction of the test specimen as shown in Figure 7(b). Samples of the concrete cylinder were collected at different stages of concrete casting. During construction

TABLE 1: Scale factors.

Item	General case	Scale factor
Length, l	$\lambda_l = l_p/l_m$	2.00
Area, A	$\lambda_A = A_p/A_m = l_p^2/l_m^2 = \lambda_l^2$	4.00
Volume, V	$\lambda_V = V_p/V_m = l_p^3/l_m^3 = \lambda_l^3$	8.00
Moment of inertia, I	$\lambda_I = I_p/I_m = \lambda_l^4$	16.00
Linear displacement, D	$\lambda_D = l_p/l_m = \lambda_l$	2.00
Angular displacement, Θ	$\lambda_\Theta = 1$	1.00
Curvature, k	$\lambda_k = 1/\lambda_l$	0.50
Modulus of elasticity, E	$\lambda_E = E_p/E_m = 1$	1.00
Stress, σ	$\lambda_\sigma = \sigma_p/\sigma_m = \lambda_E [\sigma = E]$	1.00
Strain, ϵ	$\lambda_\epsilon = 1$	1.00
Mass, S_m	$\lambda_m = \lambda_Q/\lambda_a$	4.00
Concentrated load, Q	$\lambda_Q = \lambda_E * \lambda_l^2$	4.00
Shear force, V	$\lambda_Q = \lambda_E * \lambda_l^2$	4.00
Moment, M	$\lambda_Q = \lambda_E * \lambda_l^3$	8.00
Acceleration, a	$\lambda_a = 1$	1.00

of URM walls, three samples of a masonry prism for compressive strength and three samples of a diagonal prism for tensile strength were constructed and tested after 28 days. Results of material properties are summarized in Table 2.

2.4. Testing Protocols and Input Ground Motions. The structure was subjected to series of sinusoidal base motions with increasing intensity through large 6 D.O.F shake table at EEC, UET, Peshawar. The operating shake table for particular time history requires a self-check test for the development of transfer function, which is dependent on the mass and stiffness of the model. During the validation stage of the shake table with dead weight, development of transfer function with self-check test leads to uncontrollable shaking [36]. Also in the previous studies, problems were encountered by researchers in the form of damage in the model before actual testing [37]. In some of the studies [33, 34, 38], behavior of masonry structures has been extracted through sinusoidal ground motion. Therefore, the structure was subjected to the range of sinusoidal frequencies (0.5–8.00 Hz) and time histories as shown in Table 3. The dynamic characteristics of the test specimen such as period and damping were identified using ambient free vibration test before and after shake table test runs in both directions. The destructive and nondestructive test sequences are shown in Table 3.

Sinusoidal input motions were provided at the base of the test specimen in the North–South direction through a signal generator. The amplitude of vibration was kept constant, while the frequency was increased gradually through the signal generator after each 25 seconds. Three types of structural responses: elastic, inelastic, and collapse of nonstructural URM walls, were recorded. The intensity of shaking was increased from test to test; the PGA was increased from 0.05 to 0.15g with frequency ranges from 0.50–3.00 Hz during Test Run-1 given in Figure 8 which was intended to capture response of the structure in elastic range. To cause a moderate level of damage, it was planned to obtain the dynamic response of structure at resonance. Therefore, the base excitation was increased from 0.05 to

0.60g with frequency between 0.50 and 7.50 Hz at the second stage of experiment shown in Figure 9. In order to observe response of structure at resonance and to cause major collapse in the nonstructural URM walls, the test specimen was subjected to a strong sinusoidal base excitation of PGA 0.05 to 1.24g with frequency varying between 0.50 and 8.00 Hz as shown in Figure 10. It was decided to conclude the base excitation after the collapse of nonstructural URM walls as the masonry walls of the specimen will be strengthened and retrofitted in the future.

2.5. Instrumentation. To measure the displacement and acceleration response histories, the test specimen was instrumented with a total sum of thirteen displacement transducers (DT's) and thirteen uniaxial accelerometers. Prior to the instrumentation, two steel frames were fixed along North and West face of the test specimen. Four accelerometers and four displacement transducers were installed at each floor level and at the base to record the response history in both directions. Instrumentation detail of North and West face is given in Table 4 and Figure 11. All the sensors were calibrated before installation of sensors on steel reference frame and test specimen. The sensors were cross checked to see if all connections are whether functional or not.

The sampling rate was selected to be 200 Hz; to monitor damage in the structure during the shake table test, fifteen video cameras were installed outside and inside the test specimen.

3. System Identification Tests

Ambient-free vibration tests were performed at different stages of experiment to determine the natural frequency and damping ratio of the structural system. These tests were conducted to determine dynamic characteristics of structure in both in-plane North–South direction and out-of-plane East–West direction. The test setup for the ambient-free vibration test is shown in Figure 12. A triaxial accelerometer and weak motion seismometer is connected to data acquisition system of a 24-bit recorder (DR-4,000) and facing toward North. The sampling rate was kept 200 Hz, and sample of free vibration-time history recorded after Test Run-3 is given in Figure 13.

3.1. Time Period and Damping. Period of a structure is primarily dependent on the mass and stiffness. Previous studies [39, 40] showed that RC frame without infill has considerably longer period and lower damping ratio compared to RC frame with infill. To have the values of time period and damping of structure, the specimen was suddenly disturbed and the free vibration response was recorded for around 15–30 seconds in both North–South and East–West directions. Period and damping of the structure were estimated from the acceleration-time history and was determined (Chopra, Dynamics of Structures) as follows:

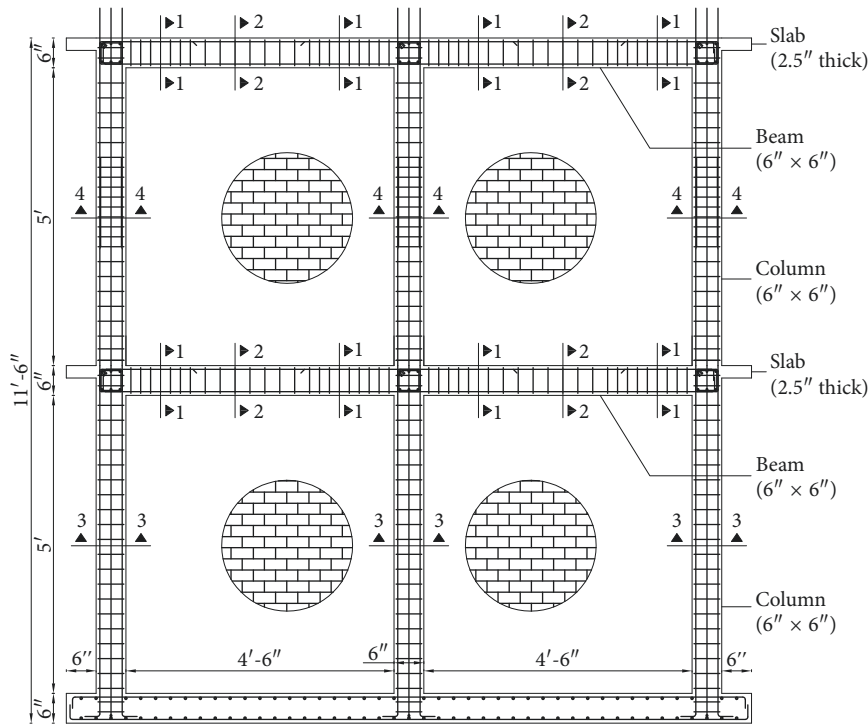


FIGURE 4: Design of the two-storey specimen (dimensions in inches).

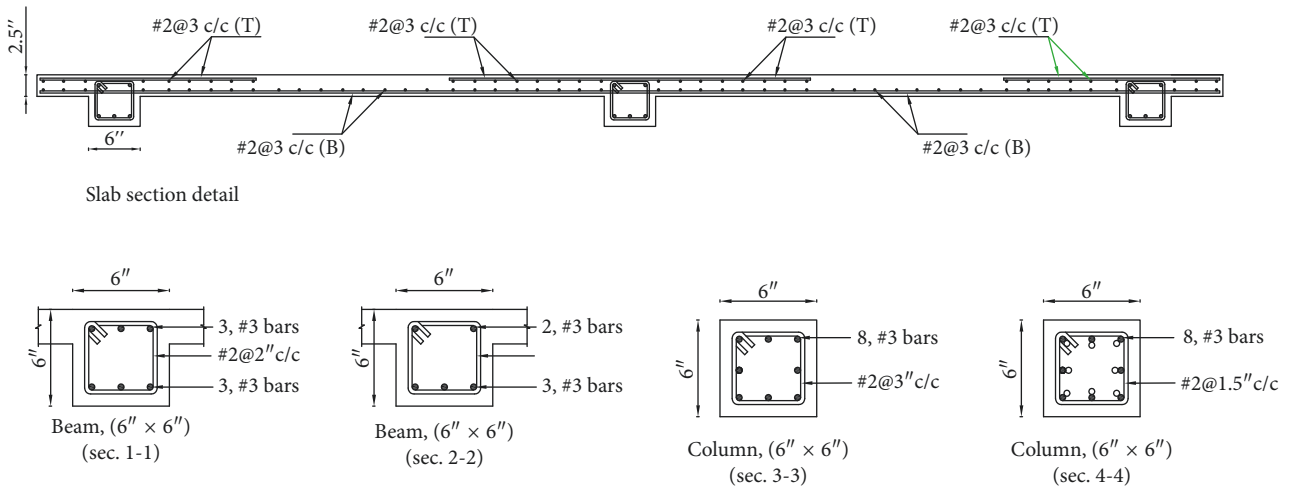


FIGURE 5: Cross-sectional detail of the RC frame (dimensions in inches).

$$\zeta = \frac{1}{2\pi j} \ln \frac{a_i}{a_{i+j}} \quad (1)$$

where ζ is the damping ratio, a_i is the acceleration response at i^{th} peak, and a_{i+j} is the acceleration response at the latter peak. The test results are summarized in Table 5 and discussed in Section 4.

4. Results and Discussion

4.1. Qualitative Test Results

4.1.1. Test Run-1. Prior to the Test Run-1, the dynamic characteristics of test specimen such as natural frequency

and damping were quantified using the ambient-free vibration test. Natural frequency and damping ratio of 6.45 Hz and 2.92% were obtained in the North-South in-plane loading direction of the specimen, while in the East-West out-of-plane loading direction, the natural frequency and damping ratio were found to be 3.48 Hz and 3.90%, respectively. During the shake table Test Run-1, the specimen was subjected to sinusoidal ground excitation with frequency between 0.50 and 3.12 Hz and base acceleration between 0.05 and 0.15g. The frequency of vibration at the base was far away from the fundamental natural frequency (6.45 Hz) of the specimen. However, no visible damage was induced in the structure.

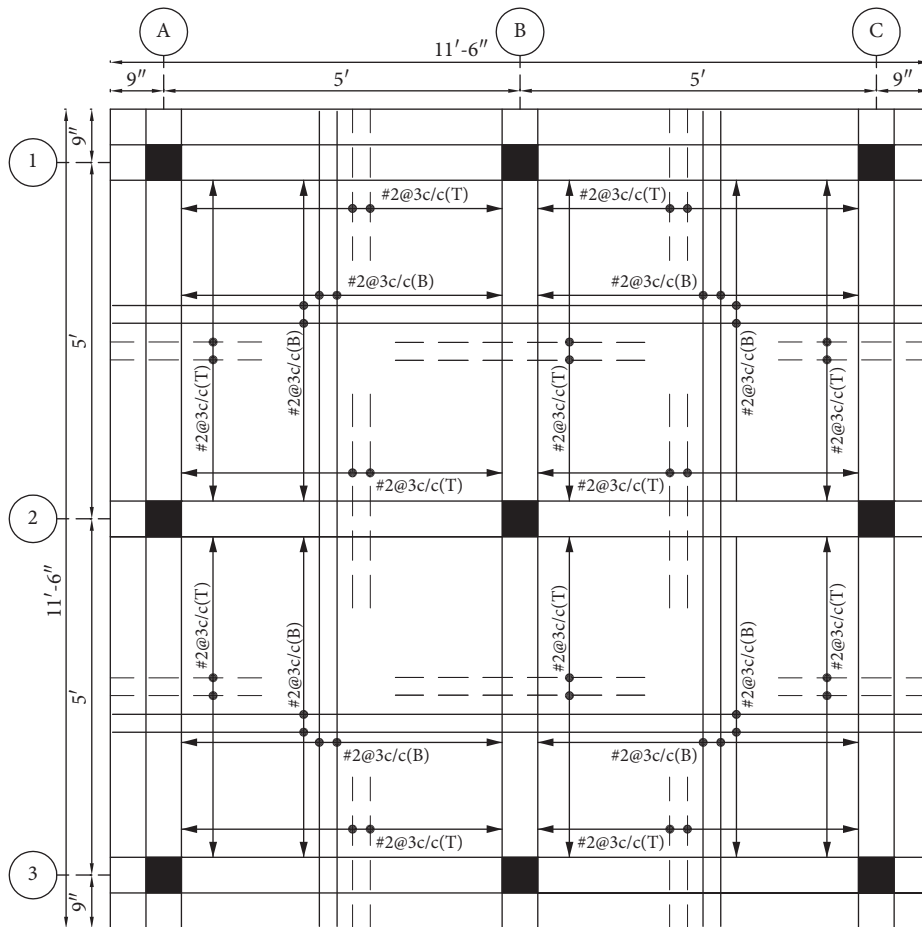


FIGURE 6: Plan view of first- and second-storey specimens with slab reinforcement details.

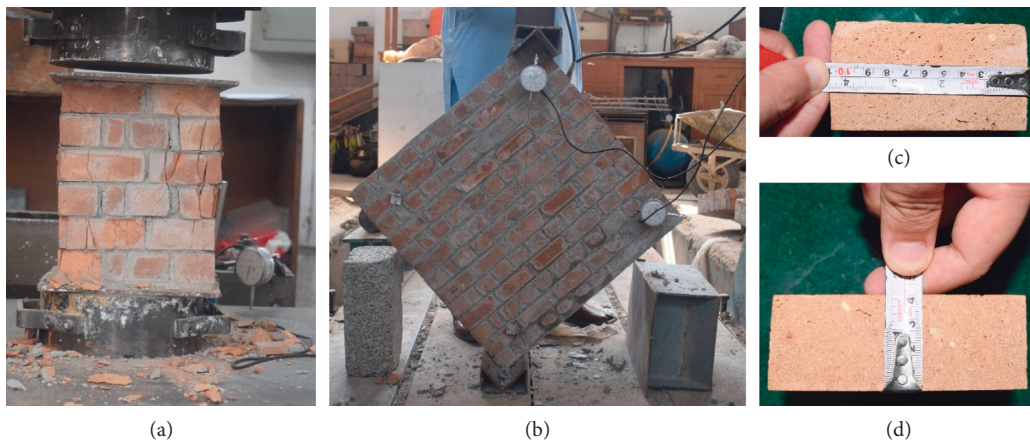


FIGURE 7: (a) Compressive and (b) diagonal tests of brick prism and (c) length and (d) width of brick specimens.

4.1.2. *Test Run-2.* Intensity of the base excitation in Test Run-2 was increased with acceleration between 0.05 and 0.60g. Sinusoidal base motion with frequency 0.50–7.60 Hz was applied, and the fundamental natural frequency of 6.45 Hz was estimated before Test Run-1. However, the structure resonated at the frequency of 5.16 Hz. The decrease in the fundamental frequency is due to microcrack initiation during Test Run-1 and Run-2. Moderate level of damage in

nonstructural URM infill walls and hairline cracks in RC frame was observed.

The PGA reached 0.42g at the resonating frequency 5.16 Hz, which corresponds to design base acceleration of RC frame. Shear cracks originated and extended horizontally along the mortar layers of in-plane URM infill walls towards the bounding RC frame. Vertical shear cracking of mortar layer and separation of URM infill walls from bounding

TABLE 2: Average material properties.

Material	Test type	Test result	
Concrete	Storey level 1		
	Columns	Compressive	3.741 ksi (25.79 MPa)
	Beams and slab	Compressive	3.943 ksi (27.18 MPa)
	Storey level 2		
	Columns	Compressive	4.073 ksi (28.08 MPa)
	Beams and slab	Compressive	4.193 ksi (28.90 MPa)
Reinforcing steel bar	#2	Tensile	
		Yield stress	59.42 ksi (409.68 MPa)
		Yield strain	2.20%
		Peak stress	96.34 ksi (664.24 MPa)
	#3	Peak strain	24.37%
		Tensile	
		Yield stress	49.7 ksi (342.66 MPa)
		Yield strain	1.53%
Brick unit	Peak stress	85.52 ksi (589.63 MPa)	
	Peak strain	21.60%	
	Compressive	5.189 ksi (35.77 MPa)	
	Compressive	1.348 ksi (9.29 MPa)	
Masonry prism	Diagonal	Compressive	0.742 ksi (5.119 MPa)
		Young's modulus	82.56 ksi (569.23 MPa)
		Strain at peak stress	0.013
		Shear strength	0.035 ksi (0.241 MPa)
		Shear modulus	35.01 ksi (241.38 MPa)
		Shear strain	0.0004

TABLE 3: Actual input motion simulated in different phases of experiment.

Testing phase	Frequencies (Hz)	Duration of each frequency (sec)	Amplitude (mm)
Test Run-1	0.50, 1.00, 1.52, 2.08, 2.60, 3.12,	25	3.00
Test Run-2	0.5, 1.00, 1.52, 2.08, 3.12, 4.12, 5.16, 6.25, 7.20, 7.60	25	3.00
Test Run-3	0.44, 1.04, 1.32, 1.58, 1.82, 2.08, 2.40, 2.65, 2.87, 3.16, 3.43, 3.69, 4.00, 4.16, 4.21, 4.52, 4.72, 4.95, 5.18, 5.45, 5.77, 6.00, 6.22, 6.52, 6.80, 7.00, 7.25, 7.52, 7.80, 7.96, 4.20, 4.27, 5.23	25	4.00

frame were clearly observed. First-storey exterior URM walls (Figure 14(a)) on both north and south side panels went through vertical frame infill separation, and horizontal shear cracking particularly at the interface of beam infill. Excessive damage (relative to the remaining infill panels) occurred in infill panels of exterior second storey (Figure 14(b)), and the top course of the masonry panels collapsed due to

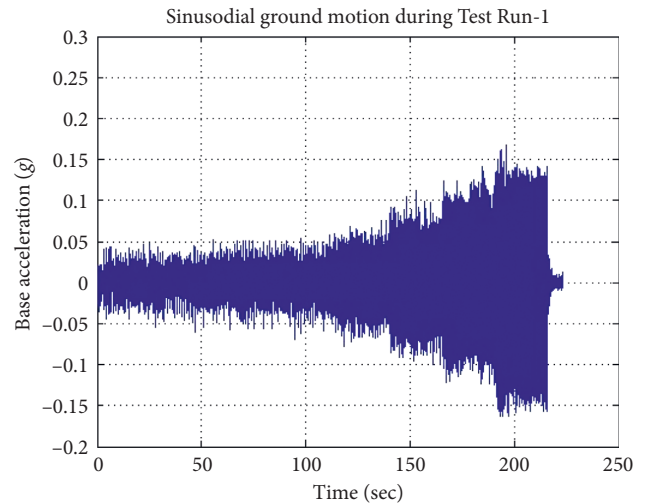


FIGURE 8: Acceleration recorded at the base during Test Run-1.

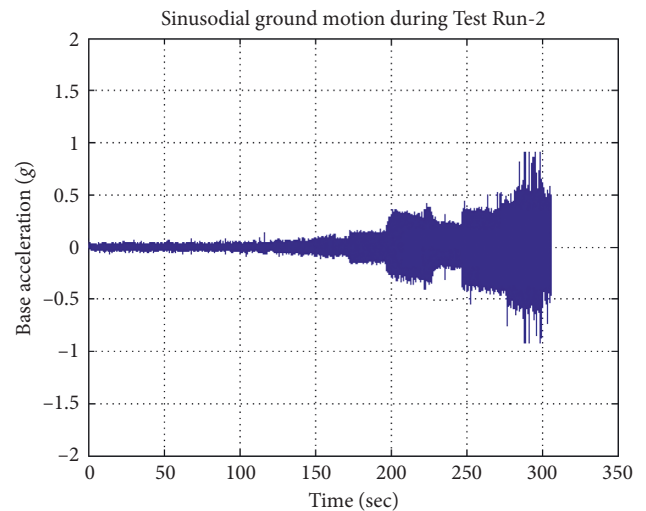


FIGURE 9: Acceleration recorded at the base during Test Run-2.

inadequate binding of panels with beam, while infill walls of exterior second storey (Figure 14(b)) started separating from the bounding RC frame and a clear horizontal shear crack was observed at the 5th row of infill wall with window opening. Similarly, the frame infill separation at the top interface followed by corner crushing behavior was observed in the interior first-storey (Figure 14(c)) URM walls. At the location of holdfast (mild steel plates for anchorage of masonry wall with adjacent columns), horizontal shear cracks along mortar layer extended throughout the interior masonry panels. Second-storey interior (Figure 14(d)) URM walls received horizontal and vertical separation and cracking and corner crushing. Few bricks in the top course slid outward in the solid out-of-plane (Figure 14(e)) wall.

The frequency of vibration at the base was further increased, and the PGA reached 0.60g at the frequency between 6.25 and 7.60 Hz beyond resonating frequency. The global response (drift and base shear) of the structure reduced with further increase in frequency after resonance. The existing damages in URM walls were further enhanced,

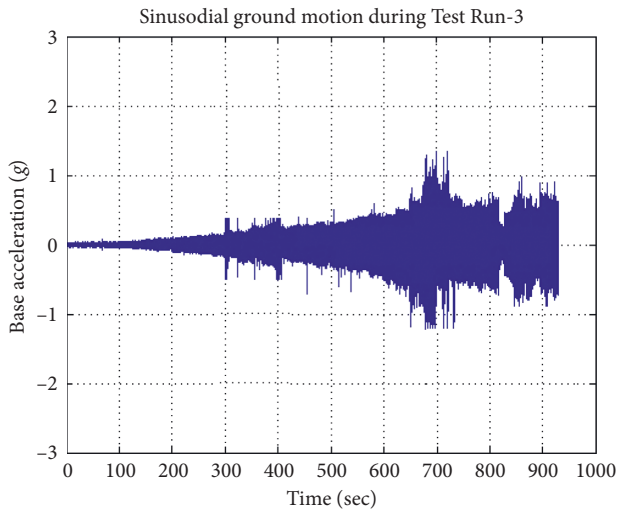


FIGURE 10: Acceleration recorded at the base during Test Run-3.

TABLE 4: Sequence of test.

Test no.	Test type
1	Ambient-free vibration system identification test
2	Shake table test with sinusoidal base motion (0.50–7.50 Hz)
3	Shake table test with sinusoidal base motion (0.50–7.50 Hz)
4	Ambient-free vibration system identification test
5	Shake table test with sinusoidal base motion (0.50–8.00 Hz)
6	Ambient-free vibration system identification test

cracks propagated, and damaged bricks collapsed when the frequency of vibration increased from natural frequency. Due to the low level of vertical stress in unreinforced masonry, URM wall collapsed in shear sliding and flexural (rocking) failure mode. Already cracked portion of URM infill wall with window opening slid outward in shear sliding, and also diagonal tensile cracking was observed in the wall beneath the lintel beam.

The RC frame was investigated with a crack detector after shake table run, determining that RC frame is only damaged at the column ends and crack width was between 8×10^{-4} to 1.5×10^{-3} in. (0.02–0.04 mm.). An ambient-free vibration test was performed after Test Run-2, natural frequency in North–South loading direction decreased to 4.21 Hz, while the damping ratio increased to 5.63%. Natural frequency in the out-of-plane direction decreased from 3.48 to 2.98 Hz, and negligible decrease in the damping ratio from 3.90 to 3.83% was observed.

4.1.3. Test Run-3. Sinusoidal base excitation with frequency between 0.44 and 7.96 Hz and ground acceleration ranging from 0.05–1.24g was recorded at the base during the final stage of this experiment. The structural peak base shear and lateral drift were recorded at this stage of experiment. Nonstructural URM walls were severely damaged, hairline cracks developed in the second-storey columns, and minor

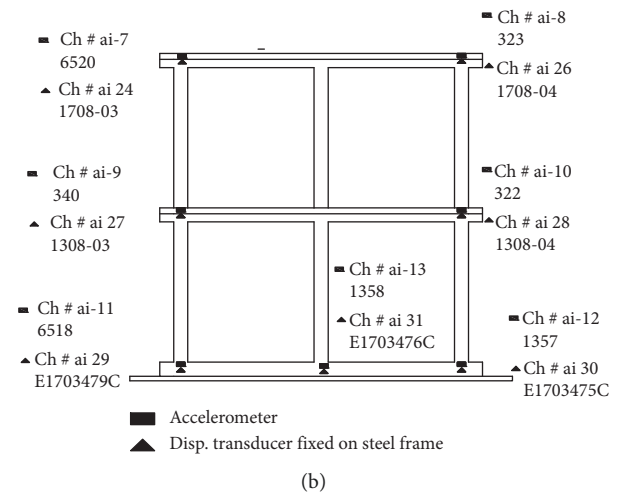
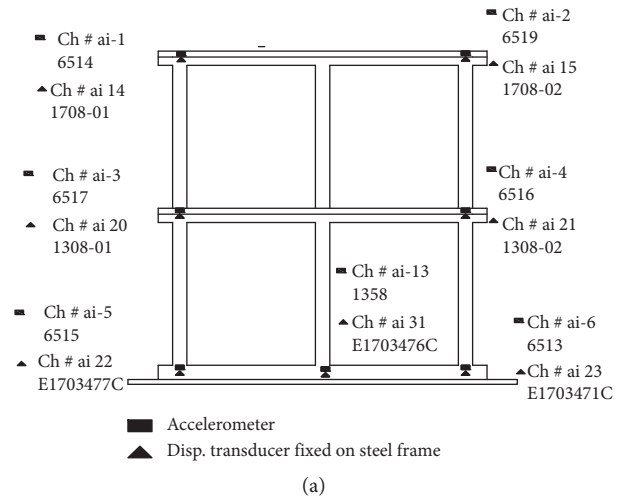


FIGURE 11: Instrumentation setup. (a) North face instrumentation. (b) West face instrumentation.

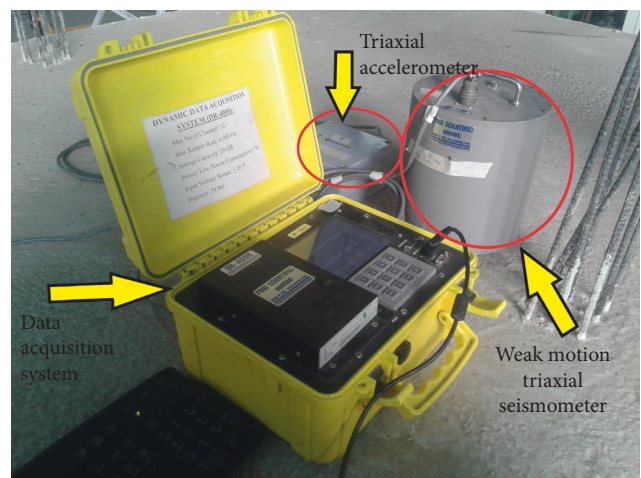


FIGURE 12: Test setup for the free vibration test.

level of damage occurred in the first-storey columns. During excitation at frequency between 0.44 and 4.00 Hz, the base acceleration was within the range of 0.05–0.40g.

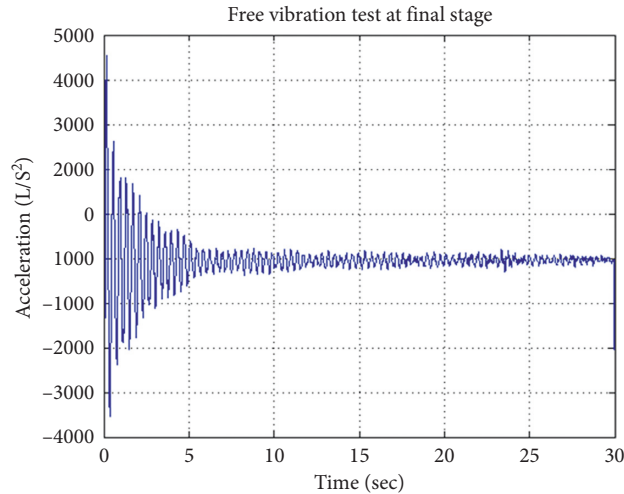


FIGURE 13: Sample of free vibration-time history recorded with the triaxial accelerometer after Test Run-3.

TABLE 5: Detail summary of instrumentation.

Channel no	Serial no of sensor	Sensitivity	Type	Range	Location	Remarks
<i>North face</i>						
ai1	6514	492.2 (mv/g)	Accelerometer	±675 mm	2LNA	
ai14	1708-01	8.5305 (mv/mm)	Displacement transducer		2LND	
ai2	6519	502 (mv/g)	Accelerometer	±675 mm	2RNA	
ai15	1708-02	8.5332 (mv/mm)	Displacement transducer		2RND	
ai3	6517	508.9 (mv/g)	Accelerometer	±312 mm	1LNA	
ai20	1308-01	138.2 (mv/mm)	Displacement transducer		1LND	
ai4	6516	510.1 (mv/g)	Accelerometer	±312 mm	1RNA	
ai21	1308-02	138.1 (mv/mm)	Displacement transducer		1RND	
ai5	6515	501.1 (mv/g)	Accelerometer	±250 mm	0LNA	
ai22	E1703477C	39.81 (mv/mm)	Displacement transducer		0LND	
ai6	6513	499.9 (mv/g)	Accelerometer	±250 mm	0RNA	
ai23	E1703471C	39.90 (mv/mm)	Displacement transducer		0RND	
<i>West face</i>						
ai7	6520	508.5 (mv/g)	Accelerometer	±675 mm	2LWA	
ai24	1708-03	68.632 (mv/mm)	Displacement transducer		2LWD	
ai8	323	509 (mv/g)	Accelerometer	±675 mm	2RWA	
ai26	1708-04	68.654 (mv/mm)	Displacement transducer		2RWD	
ai9	340	510.1 (mv/g)	Accelerometer	±312 mm	1LWA	
ai27	1308-03	137.98 (mv/mm)	Displacement transducer		1LWD	
ai10	322	496.2 (mv/g)	Accelerometer	±312 mm	1RWA	
ai28	1308-04	170.6 (mv/mm)	Displacement transducer		1RWD	
ai11	6518	490.1 (mv/g)	Accelerometer	±250 mm	0LWA	
ai29	E1703479C	39.85 (mv/mm)	Displacement transducer		0LWD	
ai12	1357	5404 (mv/g)	Accelerometer	±250 mm	0RWA	Large accelerometer
ai30	E1703475C	39.75 (mv/mm)	Displacement transducer		0RWD	
ai13	1358	5272 (mv/g)	Accelerometer	±250 mm	0VCA	Large accelerometer
ai31	E1703476C	40.01 (mv/mm)	Displacement transducer		0VCD	

Note. 2: second floor, 1: first floor, 0: bottom, L: left side of the frame, R: right side of the frame, N: north face, W: west face, V: vertical direction, C: center, A: accelerometer, D: displacement transducer.

Exterior URM wall of second storey with window opening only, which was already separated from the RC frame up to window height during Test Run-2 (Figure 15(b)), dropped in shear sliding on the table when frequency reached to 3.16 Hz. Also, few rows of interior solid URM walls of both storeys collapsed in shear sliding when frequency was 3.69 Hz.

The PGA reached 1.24g at resonating frequency of 4.16 Hz, and bricks in the top few rows of first-storey exterior URM wall with door and window openings collapsed. Also, exterior URM infill wall of second storey with window and door openings separated up to lintel beam height and slid outward horizontally. Out-of-plane URM infill wall of first storey collapsed by initiation of horizontal shear cracks



FIGURE 14: Damage observations of URM walls after Test Run-2. (a) Exterior infilled frame of first storey. (b) Exterior infilled frame of second storey. (c) Interior infilled frame of first storey. (d) Interior infilled frame of second storey. (e) Out-of-plane solid infilled frame. (f) Out-of-plane with openings infilled frame.

followed by shear sliding and dropping of brick masonry units from upper rows.

Base excitation was increased from 4.21–7.96 Hz, the dynamic response of structure decreased as the frequency of vibration increased above the natural frequency of structure. The vertical and horizontal mortar layers between RC and URM infill walls started crushing and separated more. The test specimen did not experience further visible damage at this phase of the test run.

In order to cause severe damage to the URM infill wall, the structure was excited with a strong sine wave (high amplitude sinusoidal) of frequency between 4.00 and 5.50 Hz with PGA up to 0.90g through a signal generator. The exterior and interior URM infill walls of second storey along south side and exterior infilled walls of first storey collapsed. Diagonal cracking of URM walls was observed

beneath the lintel beam of exterior URM walls. Out-of-plane infilled wall up to lintel beam height slid horizontally outwards. The performance of the out-of-plane URM wall with window and door opening was significantly better than the out-of-plane solid masonry wall due to horizontal stiffener provided in the form lintel beam throughout the masonry panel. Damage observations in URM walls after Test Run-3 are shown in Figure 15.

RC frame was visually investigated after Test Run-3, a minor level of damage occurred in the RC frame, and some shear and flexural cracking occurred in the first storey top and bottom of columns. Crack width was investigated with crack detector, and cracks of 2×10^{-3} to 1.5×10^{-2} in. (0.05–0.4 mm) was observed at column ends of first storey. On the contrary, the level of damage in second storey was comparatively less than that in first storey, crack width of

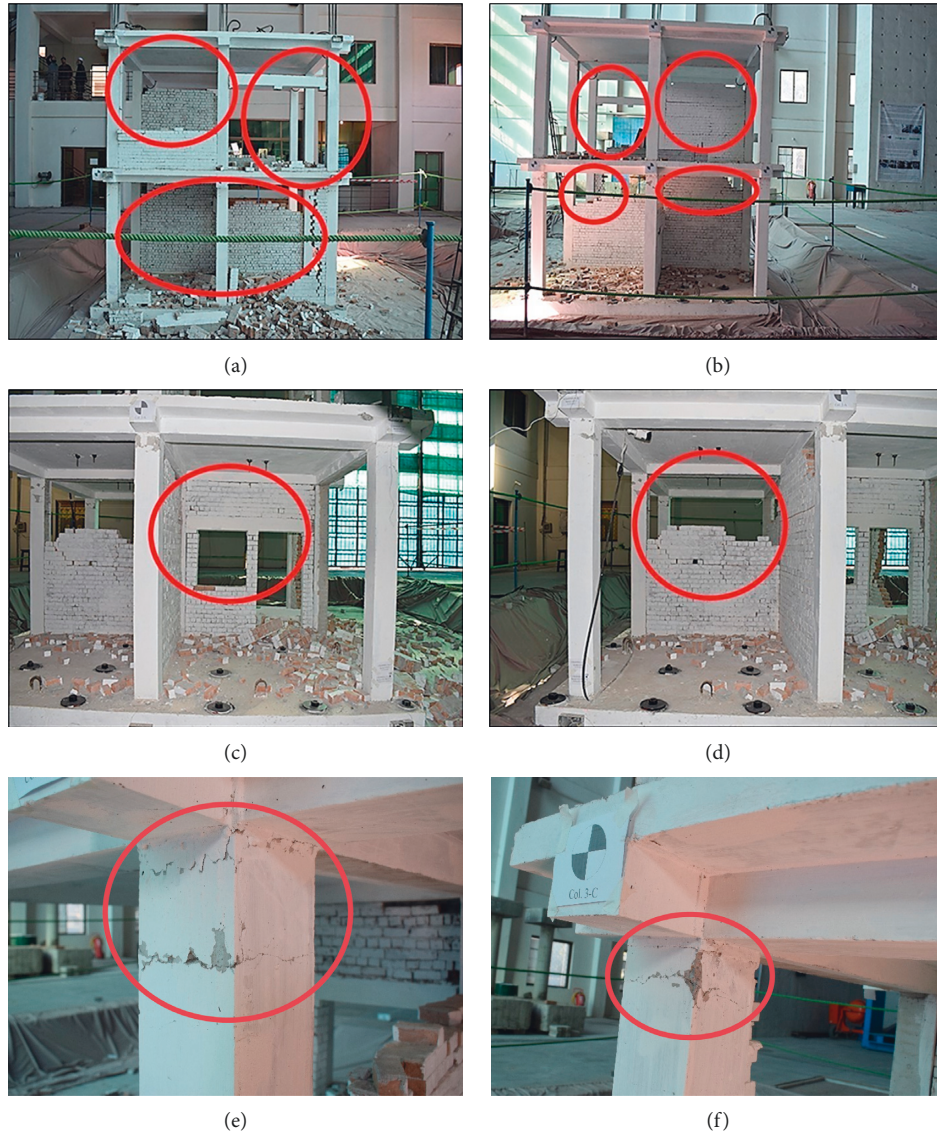


FIGURE 15: Damage observations of URM walls after Test Run-3. (a) West face of the test specimen. (b) East face of the test specimen. (c) South face west-side infilled frame. (d) South face east-side infilled frame. (e) Crack at the top of the exterior column. (f) Crack at the top of the exterior column.

8×10^{-4} to 1.5×10^{-3} in. (0.02–0.04 mm.). The damages observed in RC frame after Test Run-3 is shown in Figure 16. A free vibration test was conducted after Test Run-3, natural frequency in loading direction drops down to 2.67 Hz, and the damping ratio decreases to 4.01%, while in the out-of-plane East–West direction, the natural frequency decreases to 1.93 Hz and damping ratio to 2.19%. The decrease in natural frequency is the indication of damage in the structure, while loss of URM walls causes drop of damping ratio.

4.2. Quantitative Test Results

4.2.1. Force-Displacement. According to Beyer et al. base shear can be calculated by three different methods during shake table test.

Method 1. In this method base shear can be calculated from the force applied by the actuator minus the inertia force of the model foundation and table of the shake table. Inertial force of the model foundation and table can be found through the accelerometer installed on it and from their masses:

$$V_{b,act} = F_{act} - [\text{Acc.} \{M_{\text{Found}} + M_{\text{Shake table}}\}], \quad (2)$$

where $V_{b,act}$ = base shear calculated from accuator, Acc = acceleration recod of accelerometer, M_{Found} = mass of the foundation, $M_{\text{Shake table}}$ = mass of the shaketable.

Method 2. In this method, base shear can be calculated by summing the inertial forces of the two stories. Inertial forces can be calculated by acceleration recorded by accelerometers installed on each floor and from mass of the story.

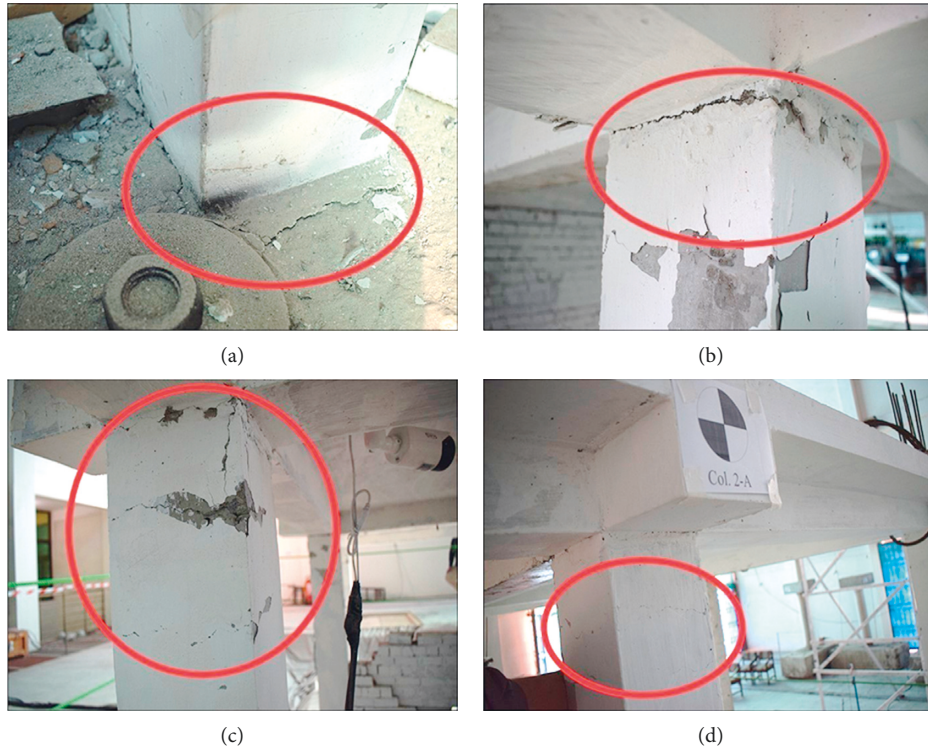


FIGURE 16: Damage observations of URM walls after Test Run-3. (a) Pulling out of column from foundation. (b) Flexural cracking at top end of first storey. (c) Level of cracking and spalling (1st storey). (d) Level of cracking (2nd storey).

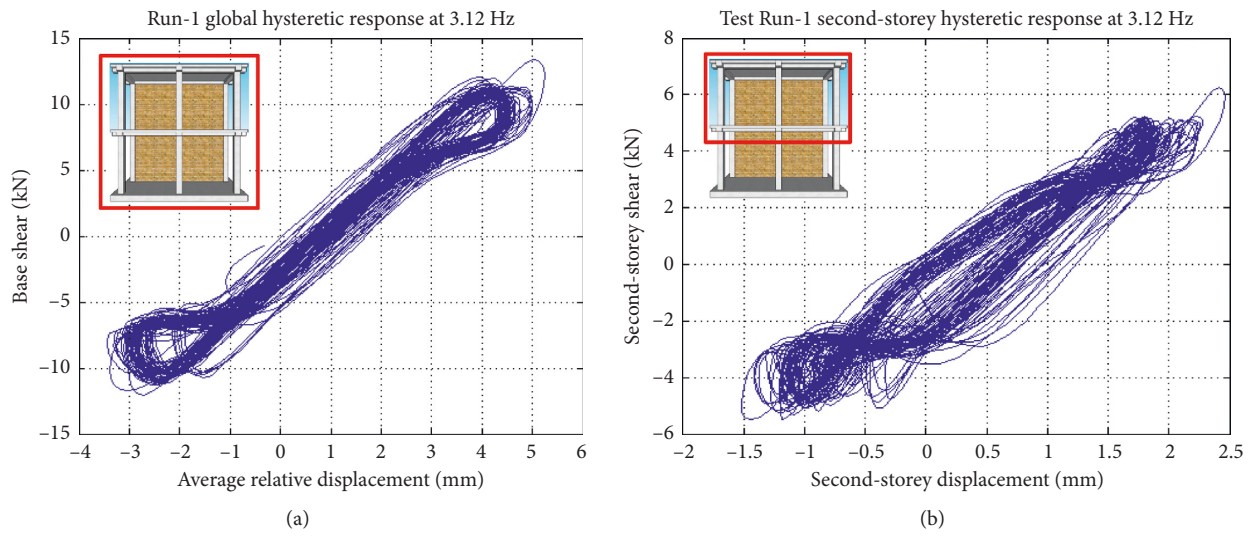
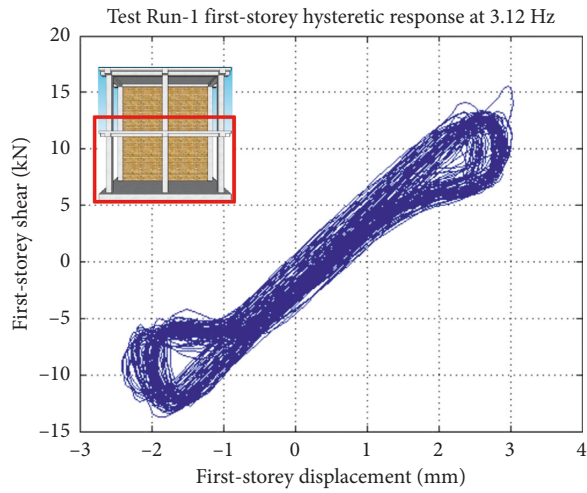
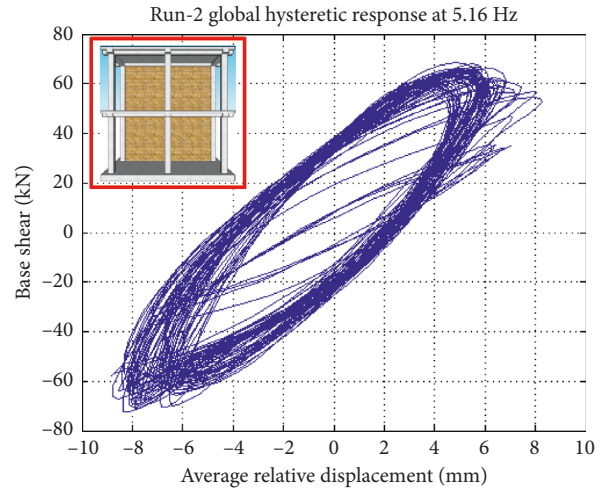


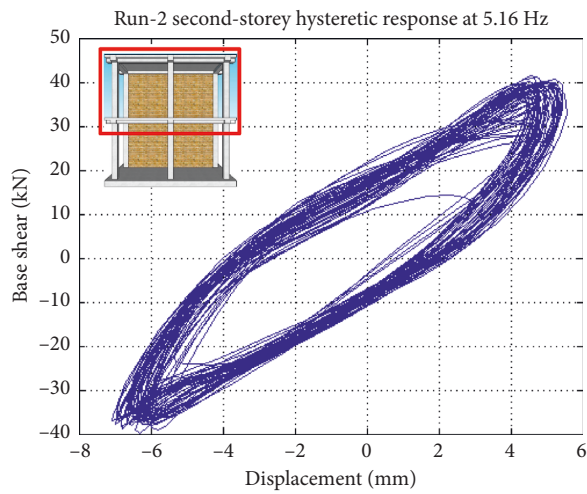
FIGURE 17: Continued.



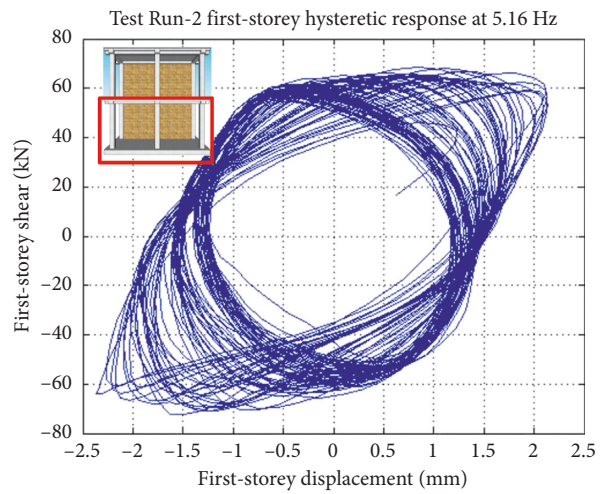
(c)



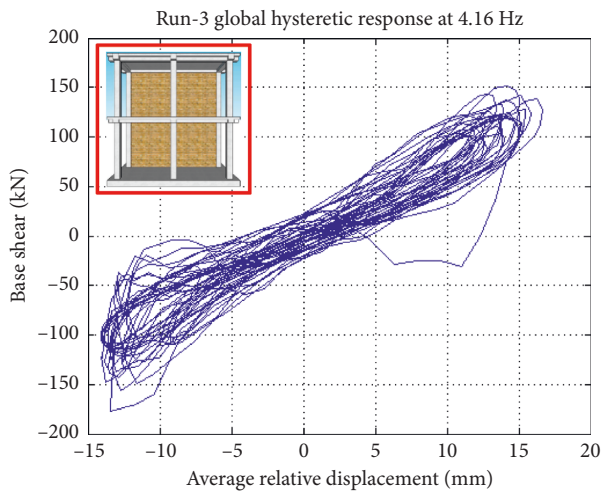
(d)



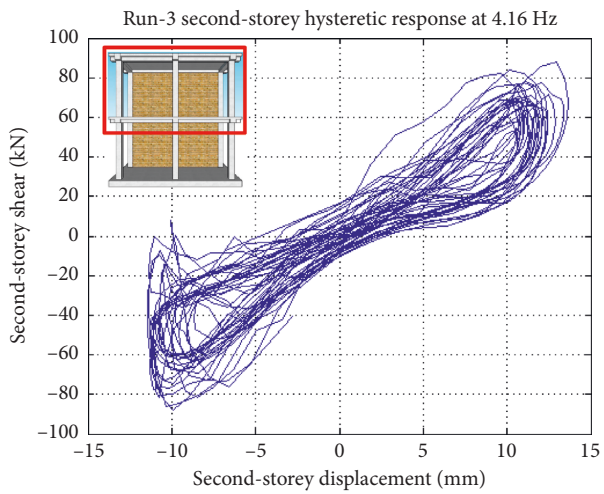
(e)



(f)



(g)



(h)

FIGURE 17: Continued.

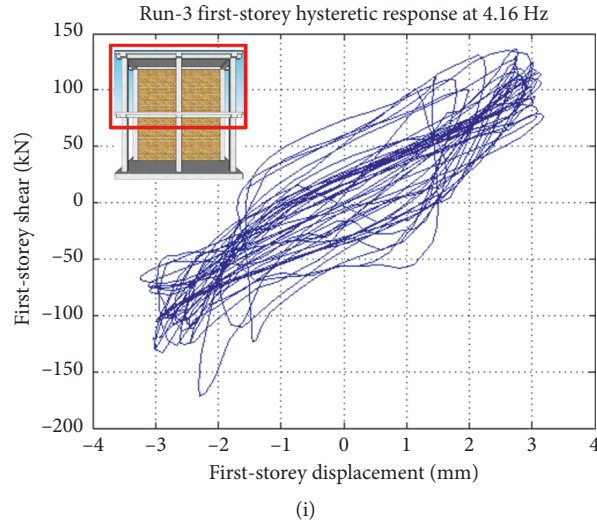


FIGURE 17: Hysteretic behavior of structure at each test run. (a) Run-1 global hysteretic response at 3.12 Hz. (b) Test Run-1 second-storey hysteretic response at 3.12 Hz. (c) Test Run-1 first-storey hysteretic response at 3.12 Hz. (d) Global hysteretic response at 5.16 Hz. (e) Run-2 second-storey hysteretic response at 5.16 Hz. (f) Test Run-2 first-storey hysteretic response at 5.16 Hz. (g) Run-3 Global hysteretic response at 4.16 Hz. (h) Run-3 second-storey hysteretic response at 4.16 Hz. (i) Test Run-3 first-storey hysteretic response at 4.16 Hz.

TABLE 6: Summary of dynamic identification tests.

Testing phase	North-South direction		Damping ratio ζ (%)	East-West direction		Damping ratio ζ (%)
	Period (sec)	Frequency (Hz)		Period (sec)	Frequency (Hz)	
Before Test Run-1	0.15	6.45	2.92	0.28	3.48	3.9
After Test Run-2	0.23	4.21	5.63	0.33	2.98	3.83
After Test Run-3	0.37	2.67	4.01	0.51	1.93	2.19

TABLE 7: Summary of structure response.

Test	Fundamental time period before test (s)	Average acceleration		Global drift (%)	Global base shear coefficient	Damage level	
		Base	Roof			RC frame	URM
Run-1	0.16	0.13	0.18	0.17	0.14	None	None
Run-2	0.24	0.59	1.07	0.24	0.66	Minor	Mild
Run-3	0.37	1.24	2.42	0.54	1.48	Minor	Collapse

Shake table response of unreinforced masonry and reinforced concrete elements of special moment resisting frame.

$$V_{b,acc} = I_{1,acc} + I_{2,acc} \quad (3)$$

Method 3. In this method, base shear can be calculated by the visual measurements of the markers on the slab and foundation.

$$V_{b,mark} = I_{1,mark} + I_{2,mark} \quad (4)$$

Method 2 was adopted for estimation of base shear in this study. Each storey was instrumented with two accelerometers and two displacement transducers in each direction already discussed in instrumentation Section 2.5, and storey acceleration and displacement was estimated by taking the mean values of acceleration and displacement-time histories, respectively. Inertial storey force was estimated by multiplying average acceleration-time history

with approximated storey mass (including self-weight of beams, slabs and half weight of columns below/above + additional mass). The first-storey shear force is the sum of inertial forces of first and second storeys which is equal to base shear, while the second-storey shear is the inertial force of that storey. Relative displacement of the structure was estimated by subtracting average top displacement from the average base displacement. Interstorey displacement was obtained from the average lateral displacement of floor above relative to the average floor displacement below.

The hysteretic behavior of structure is obtained at global and first and second-storey levels as shown in Figure 17. For global hysteretic behavior, the base shear is plotted with average relative displacement. In order to know whether the distribution of displacement over the RC frame is uniform or concentrated in one of the storey, hysteretic

curves are plotted for individual storey: first-storey hysteretic curves are obtained by plotting first-storey drift (displacement at first storey top relative to base) with first-storey shear. second-storey shear is plotted with second-storey drift (roof displacement relative to the top of the first-storey displacement). The hysteretic curve reported here are only for selected frequencies (peak response) of shake table test runs. The peak response takes place at 3.12, 5.16, and 4.16 Hz during Test Run-1, Run-2, and Run-3. The test specimen response at different levels of excitation is summarized in Table 6.

5. Conclusions

This paper discusses the shake table study conducted on half-scale model of RC frame infilled with URM walls constructed on the multiaxis shake table of EEC, UET, Peshawar. The RC frame was designed for high seismic hazard (Zone IV, with PGA 0.40g, and soil type B) according to the SMRFs requirement [41]. URM infill walls were constructed with brickwork in English bond with 1 part cement and 5 parts sand. The structure was subjected to ambient-free vibrations and shake table tests. To study the test qualification of SMRFs structure infilled with different arrangement of URM for local and global response to earthquakes, sinusoidal base motion with predominant frequencies of near-field earthquakes has been used to extract behavior. A sequence of three runs of base excitation with increasing intensity was applied. Masonry infills collapsed mainly in shear sliding and pretty much in flexural rocking when PGA reaches 0.42g, while complete collapse of URM panels takes place when PGA reaches 1.24g. Weak connections of frame infills particularly at the top layer were the primary cause of damage. URM walls with lintel beam do not provided throughout the masonry panel was much more vulnerable to in-plane and out-of-plane damages. The damping ratio increased after Test Run-2 and then decreased after Test Run-3 due to loss of in-plane and out-of-plane URM walls. RC frame maintains its stability and does not attract any serious damage even at PGA of 1.24g. However, the damage mechanism of beam-sway ensured by SMRFs was altered by the column-sway mechanism. Masonry walls within RC frame altered the load path and lateral force distribution (predominant frame action into predominant truss action) among different members of the test structure by amplifying demand force on the adjacent member, causing plastic hinges at columns end. Experimental test results also revealed that the RC frame infilled with different arrangement of URM which is typical of the construction in Pakistan is more vulnerable to seismic actions compared to the other parts of the world. Peak values and damage level at different stages of excitation are summarized in Table 7.

Data Availability

Supporting data will be provided.

Conflicts of Interest

The authors declare that they have no conflicts of interest.

Acknowledgments

The authors are grateful to the Higher Education Commission, Pakistan, for financially supporting the experimental work presented here and Earthquake Engineering Center, University of Engineering and Technology, for providing testing facilities.

References

- [1] H. Alwashali, Y. Torihata, K. Jin, and M. Maeda, "Experimental observations on the in-plane behaviour of masonry wall infilled RC frames; focusing on deformation limits and backbone curve," *Bulletin of Earthquake Engineering*, vol. 16, no. 3, pp. 1373–1397, 2018.
- [2] O. Bolea, "The seismic behaviour of reinforced concrete frame structures with infill masonry in the Bucharest area," *Energy Procedia*, vol. 85, pp. 60–76, 2016.
- [3] Y. I. Badrashi, *Response modification factors*, Ph.D. thesis, Department of Civil Engineering, University of Engineering & Technology Peshawar, Peshawar, Pakistan, 2006.
- [4] H. Al-Washali, Y. Suzuki, and M. Maeda, "Seismic evaluation of reinforced concrete buildings with masonry infill wall," in *Proceedings of the 16th World Conference of Earthquake Engineering, Chile*, At Santiago, Chile, January 2017.
- [5] H. B. Kaushik, D. C. Rai, and S. K. Jain, "Code approaches to seismic design of masonry-infilled reinforced concrete frames: a state-of-the-art review," *Earthquake Spectra*, vol. 22, no. 4, pp. 961–983, 2006.
- [6] EERI 2000, *1999 Kocaeli, Turkey, Earthquake Reconnaissance Report*, vol. 16, EERI, Oakland, CA, USA, 2000.
- [7] B. S. Smith, "Lateral stiffness of infilled frames," *Journal of Structural Division, ASCE*, vol. 88, no. 6, pp. 183–199, 1962.
- [8] A. Madan, A. M. Reinhorn, J. B. Mander, and R. Valles, "Modeling of masonry infill panels for structural analysis," *Journal of Structural Engineering*, vol. 123, no. 10, pp. 1295–1302, 1997.
- [9] G. Al-Chaar, "Evaluating strength and stiffness of unreinforced masonry infill structures," ERDC/CERL TR-02-01, U.S. Army Corps of Engineers, Construction Engineering Research Laboratories, Washington, DC, USA, 2002.
- [10] G. Al-Chaar, A. B. Mehrabi, and T. Manzouri, "Finite element interface modeling and experimental verification of masonry-infilled R/C frames," *Masonry Society Journal*, vol. 26, no. 1–47, 2008.
- [11] H. R. Lotfi and P. B. Shing, "An appraisal of smeared crack models for masonry shear wall analysis," *Computers & Structures*, vol. 41, no. 3, pp. 413–425, 1991.
- [12] T. Manzuri, "Nonlinear finite element analysis and experimental evaluation of retrofitting techniques for unreinforced masonry structures," Dissertation, University of Colorado at Boulder, Boulder, CO, USA, 1995.
- [13] K. Beyer, M. Tondelli, S. Petry, and S. Peloso, "Dynamic testing of a four-storey building with reinforced concrete and unreinforced masonry walls: prediction, test results and data set," *Bulletin of Earthquake Engineering*, vol. 13, no. 10, pp. 3015–3064, 2015.
- [14] M. N. Fardis, S. N. Bousias, G. Franchioni, and T. B. Panagiotakos, "Seismic response and design of RC structures with plan-eccentric masonry infills," *Earthquake*

- Engineering & Structural Dynamics*, vol. 28, no. 2, pp. 171–191, 1999.
- [15] A. Hashemi and K. M. Mosalam, “Seismic evaluation of reinforced concrete buildings including effects of masonry infill walls,” PEER Report 2007/100, University of California, Berkeley, CA, USA, 2007.
- [16] J. Leite and P. B. Lourenço, “Solutions for infilled masonry buildings: shaking table tests,” in *Proceedings of the 15th International Brick and Block Masonry Conference*, Florianópolis, Brazil, June 2012.
- [17] A. Stavridis, I. Koutromanos, and P. B. Shing, “Shake-table tests of a three-story reinforced concrete frame with masonry infill walls,” *Earthquake Engineering & Structural Dynamics*, vol. 41, no. 6, pp. 1089–1108, 2012.
- [18] FEMA 356, *Global Topics Report on the Pre-Standard and Commentary for the Seismic Rehabilitation of Buildings*, American Society of Civil Engineers, Reston, Virginia for Federal Emergency Management Agency, Washington, DC, USA, 2000.
- [19] ASCE/SEI-7-06, *Minimum Design Loads for Buildings and Other Structures*, American Society of Civil Engineers, Reston, VA, USA, 2006.
- [20] ASCE/SEI Standard 41-06, *Seismic Rehabilitation of Existing Buildings*, American Society of Civil Engineers, Reston, VA, USA, 2006.
- [21] ATC-43, *FEMA 306: Evaluation of Earthquake Damaged Concrete and Masonry Wall Buildings*, Federal Emergency Management Agency, Washington, DC, USA, 1998.
- [22] A. Stavridis, *Analytical and experimental study of seismic performance of reinforced concrete frames infilled with masonry walls*, Ph.D. dissertation, University of California, San Diego, CA, USA, 2009.
- [23] V. Li, “Engineered cementitious composite (ECC): material, structural, and durability performance,” in *Concrete Construction Engineering Handbook*, E. Nawy, Ed., pp. 24–46, CRC Press, Boca Raton, FL, USA, Second edition, 2008.
- [24] H. Sezen, A. S. Whittaker, K. J. Elwood, and K. M. Mosalam, “Performance of reinforced concrete buildings during the August 17, 1999 Kocaeli, Turkey earthquake, and seismic design and construction practise in Turkey,” *Engineering Structures*, vol. 25, no. 1, pp. 103–114, 2003.
- [25] A. B. Mehrabi, P. B. Shing, M. P. Schuller, and J. L. Noland, “Performance of masonry-infilled R/C frames under in-plane lateral loads,” Report CU/SR-94/6, Department of Civil, Environmental & Architectural Engineering, University of Colorado Boulder, Boulder, CO, USA, 1994.
- [26] FEMA-306, “Evaluation of earthquake damaged concrete and masonry wall buildings basic procedures manual,” FEMA-306, pp. 183–213, Applied Technology Council, Redwood City, CA, USA, 1999.
- [27] J. R. Benjamin and H. A. Williams, “The behavior of one-story shear walls,” *Proceedings of ASCE*, vol. 4, no. 1723, pp. 1–30, 1958.
- [28] D. Mallick and R. Garg, “Effect of openings on the lateral stiffness of infilled frames,” *Proceedings of the Institution of Civil Engineers*, vol. 49, no. 2, pp. 193–209, 1971.
- [29] T. C. Liauw, “Tests on multistorey infilled frames subjected to dynamic lateral loading,” *ACI Journal Proceedings*, vol. 76, no. 4, pp. 551–564, 1979.
- [30] J. L. Dawe and T. C. Young, “An investigation of factors influencing the behavior of masonry infill in steel frames subjected to in-plane shear,” in *Proceedings of the 7th International Brick Masonry Conference*, Melbourne, Australia, February 1985.
- [31] A. Hashemi and K. M. Mosalam, “Shake-table experiment on reinforced concrete structure containing masonry infill wall,” *Earthquake Engineering & Structural Dynamics*, vol. 35, no. 14, pp. 1827–1852, 2006.
- [32] P. B. Shing and I. Koutromanos, “Seismic performance of masonry infilled RC frames with and without retrofit,” *Journal of Earthquake and Tsunami*, vol. 7, no. 3, article 1350023, 2013.
- [33] K. Shahzada, A. Naeem Khan, A. S. Elnashai, A. Naseer, M. Javed, and M. Ashraf, “Shake table test of confined brick masonry building,” *Advanced Materials Research*, vol. 255–260, pp. 689–693, 2011.
- [34] M. Ashraf, *Development of cost-effective and efficient retrofitting technique for masonry buildings in Pakistan*, Ph.D. thesis, Department of Civil Engineering, University of Engineering & Technology, Peshawar, Pakistan, 2010.
- [35] H. G. Harris and G. M. Sabnis, *Structural Modeling and Experimental Techniques*, CRC Press, Boca Raton, FL, USA, 1999.
- [36] J. Shah, “Validation of 6 DOF shake table for testing of half scaled reinforced concrete model,” *International Journal of Advance Engineering and Research Development*, vol. 5, no. 10, pp. 106–111, 2018.
- [37] M. Rizwan, N. Ahmad, and A. N. Khan, “Seismic performance of SMRF compliant and non-compliant RC frames,” *ACI Structural Journal*, 2017.
- [38] R. Zarnic, S. Gosti, A. J. Crewe, and C. A. Taylor, “Shaking table tests of 1: 4 reduced-scale models of masonry infilled reinforced concrete frame buildings,” *Earthquake Engineering and Structural Dynamics*, vol. 30, no. 6, pp. 819–834, 2001.
- [39] V. Bertero and S. Brokken, “Infills in seismic resistant building,” *Journal of Structural Engineering*, vol. 109, no. 6, pp. 1337–1361, 1983.
- [40] K. M. Amanat and E. Hoque, “A rationale for determining the natural period of RC building frames having infill,” *Engineering Structures*, vol. 28, no. 4, pp. 495–502, 2006.
- [41] BCP-SP, *Building Code of Pakistan Seismic Provisions*, Islamabad: Ministry of Housing, Government of Pakistan, Islamabad, Pakistan, 2007.

Research Article

Building Earthquake Damage Analysis Using Terrestrial Laser Scanning Data

Qisong Jiao , Hongbo Jiang, and Qiang Li

Institute of Crustal Dynamics, China Earthquake Administration, Beijing 100085, China

Correspondence should be addressed to Qisong Jiao; 1985jqs@163.com

Received 26 March 2019; Accepted 21 April 2019; Published 23 May 2019

Guest Editor: Tanja K. Šipos̃

Copyright © 2019 Qisong Jiao et al. This is an open access article distributed under the Creative Commons Attribution License, which permits unrestricted use, distribution, and reproduction in any medium, provided the original work is properly cited.

Terrestrial laser scanners (TLSs) can acquire high-precision three-dimensional point cloud data for earthquake-damaged buildings. In this study, we collected TLS data in the Wenchuan earthquake zone and developed the TLS-BSAM (terrestrial laser scanning-based building shape analysis model) to carry out a building earthquake damage analysis. This model involves equidistance polygon array extraction, shape dispersion parameter calculations, irregular building clustering segmentation, and damage analysis. We chose 21 buildings as samples for the experiments. The results show that when using an equidistance polygon array to depict a three-dimensional building, 0.5 m is a reasonable sampling interval for building earthquake damage analysis. Using certain characteristic parameters to carry out *K*-means clustering, one can efficiently divide irregular buildings into regular blocks. Then, by weighted averages, the shape dispersion parameters can be calculated to express the damage extent to buildings. Among the shape dispersion parameters, at least the weighted average standard deviations of the tilt direction, rectangularity, compactness, and center point are suitable to reflect the damage extent. Higher values reflect more serious damage. On the basis of existing data, the weighted average standard deviations of the tilt direction and center point can be used to establish discriminant functions that can effectively distinguish the damage extent.

1. Introduction

With the diversification of remote sensing data and technical progress in data processing, remote sensing technology can now be used to carry out earthquake damage investigations, which has recently become a topic of sustained interest. Compared with traditional field surveys of earthquake damage, earthquake damage assessments based on remote sensing data are faster, more efficient, and safer. A wide range of earthquake-induced building damage information can be quickly acquired and assessed with new remote sensing technologies. Under the guidance of mathematical statistics, object-oriented methods, and fractal theory, different types of remote sensing data such as optical images, synthetic aperture radar (SAR) imagery, and airborne LiDAR data have been used in building damage assessments. Saito et al. [1] used optical images with 1 m ground resolution

taken by IKONOS before and after the Gujarat earthquake of January 26, 2001, to extract the information about collapsed buildings. Stramondo et al. [2] analyzed the capability of satellite radar and optical remote sensing for earthquake damage detection in urban areas and explored the combined use of radar (SAR) and optical satellite data. Balz and Liao [3] used postseismic high-resolution SAR satellite data for building damage detection caused by the Wenchuan earthquake. Based on airborne LiDAR data, Lin et al. [4] proposed a multiple-primitive-based TIN progressive densification point cloud filtering method to distinguish the ground points and nonground points. He et al. [5] used an original three-dimensional shape descriptor to detect roofs with surface damage and roofs exhibiting structural damage by identifying spatial patterns of compact and regular contours for intact roofs. Li et al. [6] used LiDAR data and high-resolution optical images to detect damages on the scale of a building's

rooftop area and realized a quantitative estimation of the degree of building damage. These studies have important significance for facilitating rapid responses during earthquake relief and postearthquake reconstruction work.

Various remote sensing technologies were employed after the Wenchuan earthquake [7–9], and these data are valuable for damage assessment. However, as the aforementioned studies illustrate, earthquake damage assessment based on remote sensing data also has some disadvantages. Specifically, only information about the top surface and part of a building's sides can be recorded by optical remote sensing data. In addition, earthquake damage assessments based on remote sensing data have been generally aimed at large areas containing many buildings and not a single building. Based on earthquake emergency work of recent years in China, we found that optical remote sensing data cannot identify specific building structures that have been destroyed but have top surfaces that are basically intact. Thus, the accuracy of remote sensing-based damage assessment technology is relatively low and field survey data are still needed to carry out earthquake relief and reconstruction work.

As an alternative data collection method, terrestrial laser scanners (TLSs) can be employed from remote locations. A TLS is a fully automated instrument capable of acquiring high-precision three-dimensional scanning data. It emits a high-speed laser that performs noncontact scanning measurements, and three-dimensional coordinates of the target stored in point cloud format are obtained [10]. This technology is especially useful for carrying out measurements in complex and high-risk environments. Furthermore, TLS technology is advantageous because of its ease of operation with high degrees of automation compared with airborne LiDAR. Point cloud data combined with computer-aided design software can quickly be used to rebuild the target's shape and obtain its three-dimensional digital model. To date, TLS technology has been shown to be a powerful tool in studies involving vegetation mapping, geological hazard control, historic preservation, etc. [11–14]. With regard to earthquake damage assessments, TLSs can provide high-precision three-dimensional information about damaged building structures. Although some scholars have employed TLSs in field survey work after earthquakes and tsunamis and have acquired point cloud data for damaged buildings and secondary disaster areas [15, 16], studies on the quantitative extraction and analysis of building damage information from point cloud data are insufficient.

To solve this problem, we carried out measurements using a TLS in the Wenchuan earthquake zone and proposed the use of the TLS-BSAM (terrestrial laser scanning-based building shape analysis model), which is based on the theory of shape analysis, to carry out quantitative extraction and analysis of building damage information. This model fully considers building irregularities after earthquake damage, and this study represents a useful attempt to provide important basic data for building damage pattern analysis and simulation.

2. Methods

2.1. Shape Analysis. Shape analysis involves storing the shape feature information extracted from images in a particular data structure to carry out identification, comparison, retrieval, and classification procedures [17, 18]. The main steps of shape analysis are computer-driven and include data preprocessing, feature extraction, and shape classification. Data preprocessing is the basis of shape analysis. The purpose of this step is to obtain the outline or surface structure of the object's shape. These data have a great influence on the performance of the shape feature extraction algorithm. Shape feature extraction is the key of shape analysis. Its purpose is to find an accurate and feasible shape representation. Shape classification involves comparing and statistically computing the similarity of object characteristic factors and then identifying unknown samples according to existing examples. The national standard (classification of earthquake damage to buildings and special structures (GBT 24335-2009)) points out that the classification principles for earthquake-damaged buildings are mainly based on load-bearing components with some consideration of non-load-bearing components. In addition, the degrees of difficulty of repair and function loss are also taken into account. In earthquake field surveys, technicians evaluate the damage level based on a building's cracks and assess the degree of dislocation, deformation of walls, integrity of roofs, structural poles, etc. This is a shape analysis process, which provides us with a theoretical basis to use TLS point cloud data while carrying out earthquake damage extraction and analysis.

2.2. Building Dimension Reduction from Three to Two Dimensions. Unlike plane data, point cloud data record different types of building damage in a three-dimensional space. The existing edge detection algorithm for a plane cannot yet effectively build functions to describe a building's three-dimensional contour or area. To simplify and effectively express the shape of a three-dimensional building by means of "dimension reduction," as shown in Figure 1, we used a set of evenly spaced parallel sections to cut the building's point cloud data and acquire intersecting lines that reflect the shape changes at different heights. This transforms the three-dimensional surface recognition into two-dimensional polygon shape (hereafter called the "equidistance polygon array" or EPA) recognition features.

The extraction of EPA data is an important part of data preprocessing in the TLS-BSAM, and the main procedure involves extracting the point cloud contour lines. The edge detection and extraction algorithms for two-dimensional images are quite mature, but they are not suitable for a discrete point cloud. We thus used the convex hull algorithm to solve this problem. The convex hull algorithm can find the minimum convex polygon that meets the condition that all points are inside the polygon or on the edge [19, 20].

Buildings are built in accordance with designs and structural plans, and they are orderly entities, not randomly self-organizing systems. Thus, an intact building with a

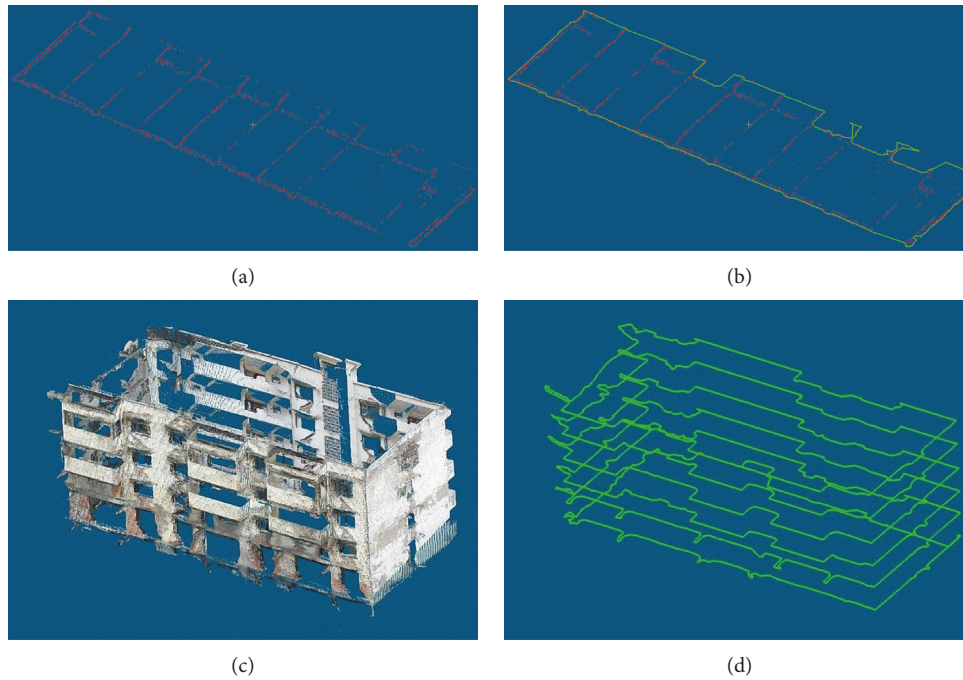


FIGURE 1: Sketch of a building's "dimension reduction." (a) One layer of the building's point cloud; (b) the layer's convex hull polygon; (c) the building's real point cloud; (d) the building's equidistance polygon array at 2 m intervals.

regular shape has a very high similarity EPA and the dispersion of shape characteristic parameters is small. In areas with earthquake-damaged buildings, these orderly systems are destroyed. Consequently, equidistance polygons at different heights will show different degrees of deformation, which ultimately results in a dispersion increase for the shape characteristic parameters. In this study, the analysis of building earthquake damage is based on the degree of shape characteristic parameters dispersion in the EPA. Specifically, building damage is proportional to the degree of shape characteristic parameters dispersion, which means that higher dispersion degrees are associated with greater extents of damage. The standard deviation was used to describe the dispersion degree. Here, larger values of standard deviation are associated with higher dispersion degrees and greater extents of damage.

2.3. Shape Characteristic Parameters Selection. The EPA is made up of the shape polygons, so we chose the shape characteristic parameters based on contour lines to describe its shape, as shown in Table 1.

In practice, the shape characteristic parameters selection does not adhere to "the more the better" principle. Circumference and area are not prominent when describing the shape in some situations. Thus, we chose the aspect ratio r , tilt direction θ , rectangularity R , and compactness C as the main shape characteristic parameters. The compactness C reflects the border regularity, and larger C values are associated with more complex shapes. Meanwhile, we noticed during earthquake field surveys that, although buildings were almost intact, they were already tilted. Therefore, we used the polygon central point (x, y) as another shape

characteristic parameter. If the central point deviation is large, building damage should not be ignored even if the degree of dispersion for the other shape characteristic parameters is small.

2.4. Irregular Building Clustering Segmentation. A building's three-dimensional shape is sometimes irregular, as shown in Figure 2. For such buildings, the standard deviation σ of shape characteristic parameters is often large even if the buildings are intact. To solve this problem, we used the K -means clustering algorithm to divide irregular buildings into several regular parts, which involved dividing the EPA into several regular polygon sequences.

When clustering is completed, the polygon number of different parts is the weight in the earthquake building damage analysis, and larger numbers are associated with higher weights. The building shape dispersion parameters are their weighted average standard deviations.

It should be pointed out that m is the clustering number of the EPA and is identified by the investigator according to the building situation uncovered during the field investigation. When the buildings up-down structures are identical or completely collapsed, the m value is equal to one.

2.5. Earthquake Damage Analysis for Buildings. The Chinese seismic intensity scale (GBT 17742-2008) divides earthquake-damaged buildings into five grades, namely, those that are completely destroyed, seriously damaged, moderately (medium) damaged, slightly damaged, and basically undamaged. In this standard, the main difference

TABLE 1: Common shape characteristic parameters.

Name	Expression	Description
Area	A	Polygon area
Circumference	P	Polygon circumference
Length	l	Length of the minimum enclosing rectangle (MER)
Width	w	Width of the MER
Aspect ratio	$r = l/w$	Length and width ratio of the MER
Tilt direction	θ	Included angle for long and polar axes of the MER
Rectangularity	$R = A/A_{MER}$	Area ratio of the polygon and its MER
Compactness	$C = P^2/A$	Circumference square and area ratio of the polygon

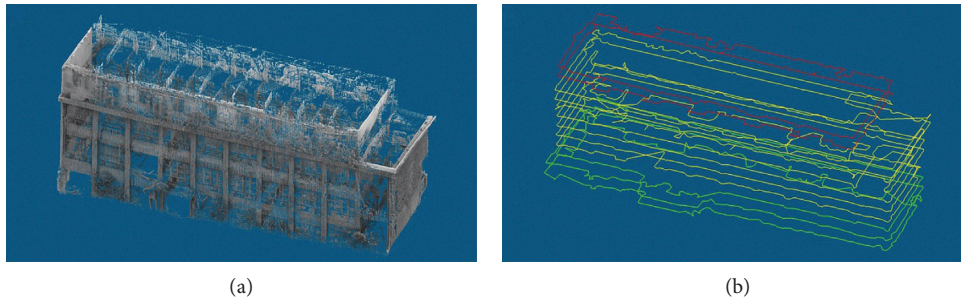


FIGURE 2: A building's point cloud and its EPA map. (a) Building with three different blocks; (b) the building's corresponding EPA in three colors.

between essentially undamaged and slightly damaged buildings is the fracture scale of load-bearing components. This is an endpoint that even experienced investigators often have trouble assessing correctly. Here, we merged these two grades into the slightly damaged grade. In view of the existing technology based on remote sensing data, we are able to easily identify completely destroyed buildings, and thus, we are no longer using point cloud data to analyze them. According to the Earthquake Disaster Standards of the People's Republic of China (DB/T75-2018) "Earthquake Disaster Remote Sensing Assessment Part 3: Building damage," the damage grades of single building are divided into three types including collapse, partial collapse, and no collapse. Among them, the partial collapse is defined as the collapse of part of the building, or the partial destruction of the roof, or the destruction of the surrounding wall. The collapse is defined as the roof completely collapses, or more than 50% of the main structure collapses, twists, deforms, or tilts. Here, we refer to this standard and the serious damage corresponds to collapse and medium damage corresponds to partial collapse.

In this study, the core of the seismic damage analysis is based on a set of known samples with specific characteristic parameters correlated with the earthquake damage; these relationships then serve as a guide for the earthquake damage assessments of unknown buildings. Discriminant analysis is a good technique to accomplish this task. We took the building shape dispersion parameters as the discriminant factors and used Fisher's discriminant method to calculate the linear discrimination functions that were applied to identify the earthquake damage.

Based on the above procedures, we developed the TLS-BSAM to carry out the building earthquake damage analysis. The main workflow of the model is shown in Figure 3.

3. Experiment

The Wenchuan Ms8.0 earthquake occurred on May 12, 2008, and was the most destructive earthquake recorded since the establishment of the People's Republic of China. The epicenter was located at 31.01°N, 103.42°E. The earthquake affected most of China including Gansu, Qinghai, Ningxia, Shanxi, Shanxi, Shandong, Henan, Hunan, Hubei, and Chongqing with an area over 100,000 km². The causative fault was the Longmen mountain fault zone on the eastern margin of the Tibetan Plateau with a focal depth of 14 km. Due to the rapid uplift of the Tibetan Plateau and the influence of gravity, the eastern margin of the Tibetan Plateau gradually subducted along the Longmen mountains and was meanwhile blocked by the Sichuan Basin, resulting in long-term accumulation of tectonic stress. The final stress was suddenly released in the Beichuan to Yingxiu area of Longmen Mountain, triggering a right-lateral thrust earthquake. The epicenter intensity of the Wenchuan earthquake was as high as 11 and the destructiveness was huge. In 2013, Beichuan and Hanwang, which are located in close proximity to the epicenter, were protected as earthquake sites. Buildings were seriously damaged in both of these areas. We selected these two sites as the study area and used a Riegl VZ-1000 laser scanning system equipped with the Riscan Pro software (Figure 4) to acquire and process the building point cloud data.

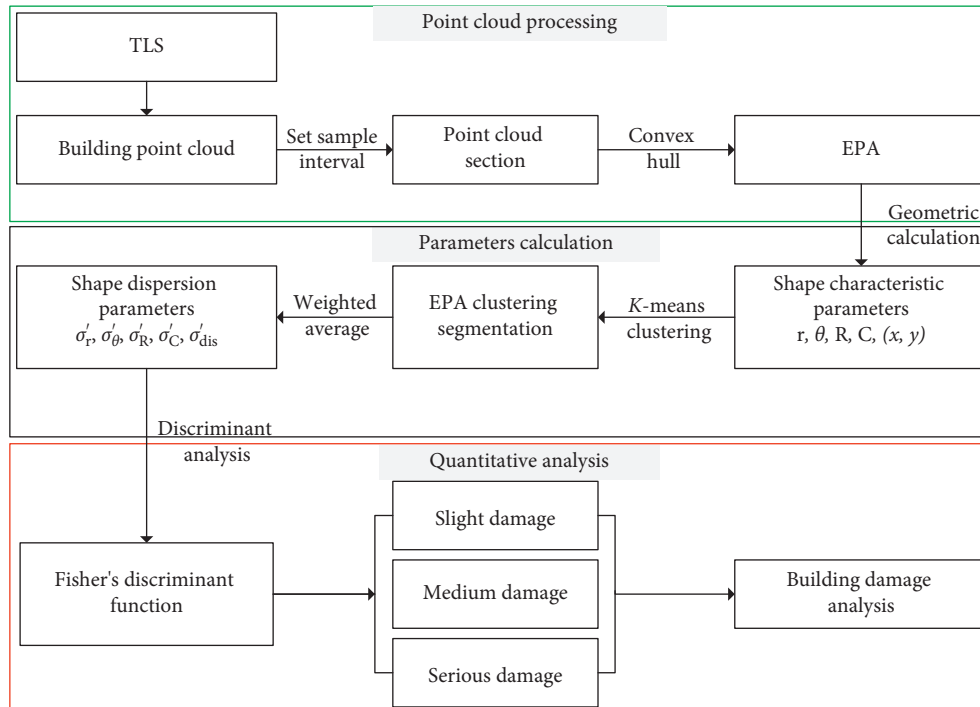


FIGURE 3: Flow chart of the TLS-BSAM.



FIGURE 4: Riegl VZ-1000 laser scanning system.

Prior to the start of the scanning work, a field reconnaissance survey must be conducted to confirm the main objects in the scanning area based on the buildings' original layout. The buildings' locations, areas, and shapes are all taken into consideration when determining the scanning station sites. In addition, to meet the requirements of data registration, each station must have a certain amount of overlap. The accuracy of the scanner is 8 mm at 100 m, and all scans in this study were performed at a close range (<40 m from the target), which helps to improve accuracy. During data registration, the registration error between adjacent scans was less than 2 mm. After all scans were aligned using the Riscan Pro software, the root mean square (RMS) error was less than 7 mm. Following the measurement, building samples were picked from these datasets and each building

was isolated to eliminate noise. The station distribution and the data processing results are shown in Figure 5.

4. Results and Discussion

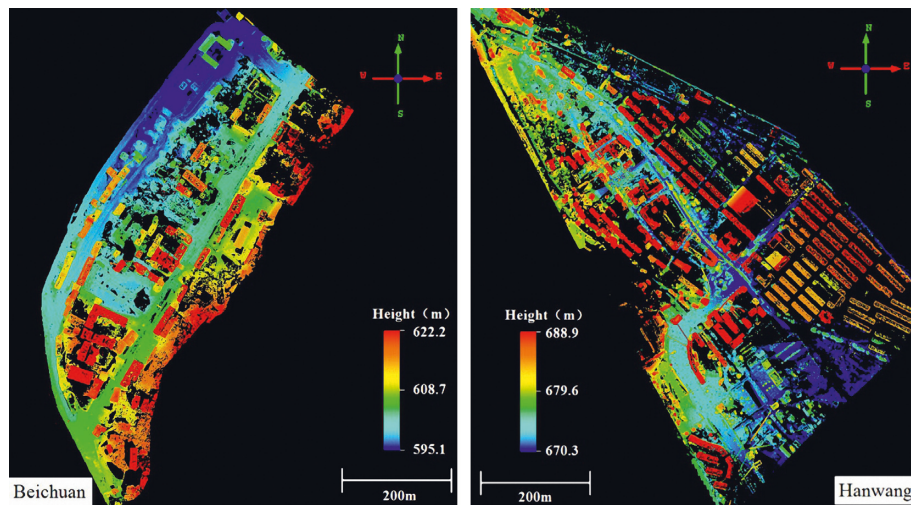
We selected 21 buildings to build the sample dataset, and these structures included 13 damaged buildings in Beichuan and 6 in Hanwang. In order to compare baseline data with the damaged buildings, we also scanned two intact buildings in Dujiangyan and Beijing. The building sample information from the field survey is shown in Table 2. On the basis of the TLS-BSAM, we calculated the σ'_r , σ'_θ , σ'_R , σ'_C , and σ'_{dis} for these 21 buildings and analyzed them with regard to the four aspects discussed in the following sections.

4.1. Influence of Different Sample Intervals on Shape Dispersion Parameters. In order to identify the influence of different sample intervals on shape dispersion parameters, we evaluated six different sample intervals set at 0.25 m, 0.5 m, 1 m, 1.5 m, 2 m, and 2.5 m. With these increases in the sampling intervals, the shape dispersion parameters changed showing a similar behavior. Taking buildings B12, B14, H2, and H3 as examples (Figure 6), the extent of change for σ'_θ was relatively small for sampling intervals of 0.25 to 1.0 m and σ'_C was also relatively small within this range.

This result indicates that when the sample interval is too large, not enough of the EPA can be extracted to reflect building damage features smaller than the sample interval. In addition, not enough samples are collected for clustering, which leads to increases in the error of the shape dispersion parameters. When the sample interval is greater than 2 m, it is close to the height of most buildings and thus not suitable



(a)

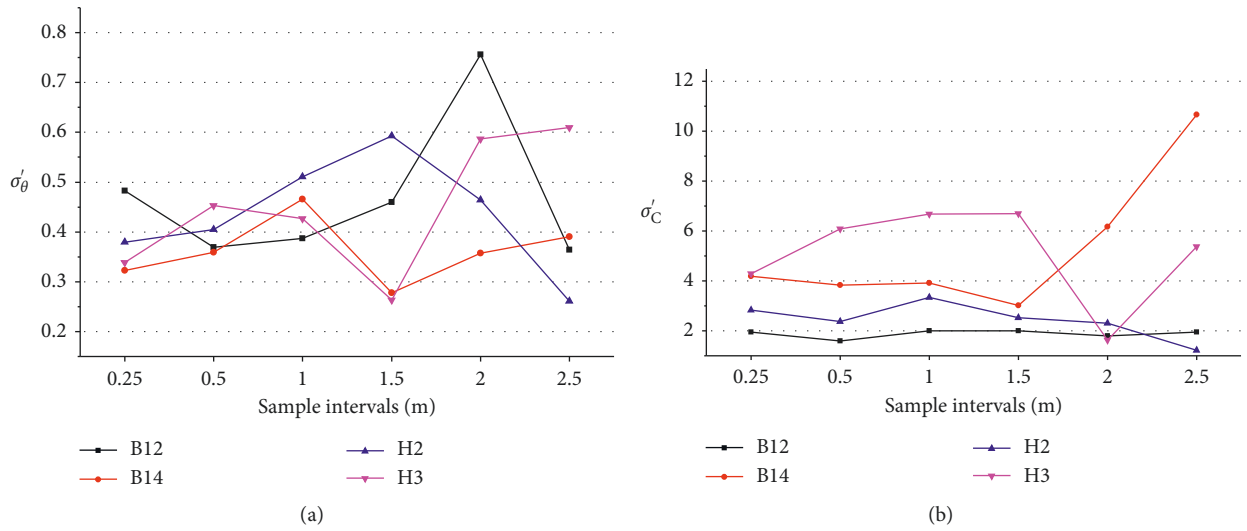


(b)

FIGURE 5: Station distribution (a) and point cloud top view map (b) of Beichuan and Hanwang.

TABLE 2: Sample information of the buildings.

ID	Location	Height (m)	Block	Structural system	Damage degree
B1	Beichuan	16.67	3	Masonry building	Medium
B10		14.46	3	RC frame	Medium
B11		24.42	1	RC frame	Slight
B12		21.40	2	RC frame	Medium
B14		14.32	3	RC frame	Medium
B16		15.81	1	Masonry building	Serious
B2		24.02	2	RC frame	Medium
B3		13.48	1	Masonry building	Medium
B4		24.35	2	RC frame	Serious
B6		21.53	1	RC frame	Slight
B7	20.80	2	RC frame	Slight	
B8	22.37	1	RC frame	Serious	
B9	12.69	2	Masonry building	Serious	
D1	Dujiangyan	24.14	5	RC frame	Intact
H1	Hanwang	16.07	2	RC frame	Serious
H2		18.27	2	RC frame	Medium
H3		9.81	2	Masonry building	Serious
H4		19.78	3	RC frame	Slight
H8		13.39	2	Masonry building	Slight
H9	27.70	3	RC walls	Slight	
J1	Beijing	29.37	7	RC walls	Intact

FIGURE 6: Plot of the response of σ'_θ (a) and σ'_C (b) to different sample intervals.

for shape analysis. However, small sample intervals will increase the error of the shape dispersion parameters because of noise within the point cloud. After experimenting with the data, 0.5 m was selected as the ideal sample interval.

4.2. Clustering Segmentation Results for Irregular Buildings.

The TLS-BSAM divides irregular buildings using the K -means clustering method, which makes the shape dispersion parameters truly reflect the extent of building damage. For this analysis, buildings B8 and H4 were used as examples (Figure 7); B8 is a regular building that was badly

damaged, while H4 is an irregular building that was slightly damaged.

In order to test the clustering results of the TLS-BSAM, we calculated the shape dispersion parameters of H4 before (1 block) and after (3 blocks) clustering (Table 3).

As shown in Figure 8, the σ'_r , σ'_θ , σ'_R , σ'_C , and σ'_{dis} values for H4 before clustering were greater than the corresponding values after clustering, and the σ'_r , σ'_θ , σ'_C , and σ'_{dis} values were even greater than the values for B8, which was badly damaged. However, after clustering, the shape dispersion parameters for H4 were all smaller than those for B8. In other words, the clustering method helped the parameters to reflect the real building damage.

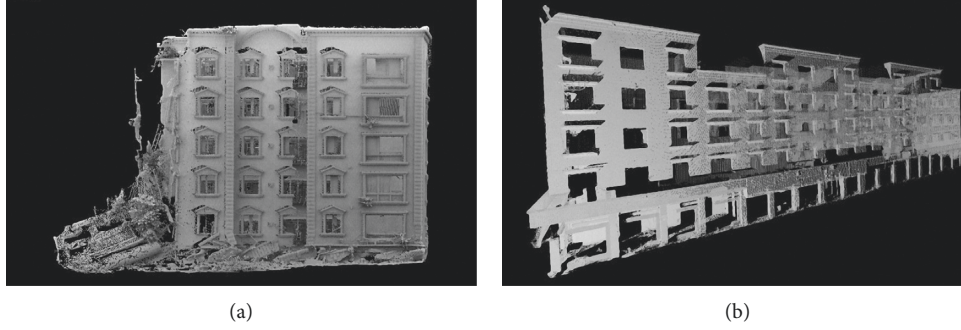


FIGURE 7: Buildings with different degrees of earthquake-induced damage. (a) B8 is a regular building that was badly damaged, while (b) H4 is an irregular building that was slightly damaged.

TABLE 3: Shape dispersion parameters of B8 and H4.

ID	Damage degree	Block	σ'_r	σ'_θ	σ'_R	σ'_C	σ'_{dis}
B8	Serious	1	0.038	0.471	0.123	4.232	0.784
H4	Slight	3	0.027	0.286	0.027	1.358	0.349
		1	0.206	0.545	0.074	13.349	1.245

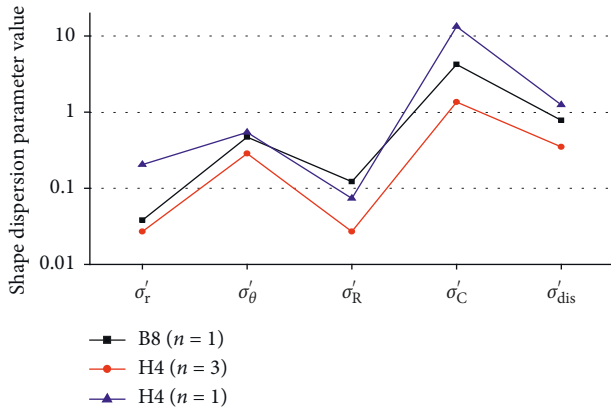


FIGURE 8: Shape dispersion parameter comparison plot before (H4 and B8, $n = 1$) and after (H4, $n = 3$) clustering for the badly damaged (B8) and slightly damaged (H4) buildings.

4.3. Comparative Analysis of Shape Dispersion Parameters of Buildings Damaged to Different Extents. By comparing the parameters of buildings damaged to different extents (Figure 9), it can be seen that slightly damaged buildings generally have low values, while seriously damaged buildings have high values and medium damaged buildings have medium values. Only one exception to this trend was detected, i.e., the σ'_r value of seriously damaged buildings was not significantly higher than that of medium damaged buildings. This suggests that at least σ'_θ , σ'_R , σ'_C , and σ'_{dis} values are able to reflect the extent of building damage.

In order to compare the different parameters, we drew box plots (Figure 10). For a given parameter, flatter boxes are indicative of more concentrated values. In addition, the larger the boxes' distance from the horizontal axis, the greater the difference in the extent of damage between buildings. If a parameter can meet both conditions at the same time, it

suggests that this parameter can better reflect the extent of damage to the buildings.

As shown in Figure 10, except for σ'_r , the values of the other four parameters change from large values to small values in correspondence with the changes in the extent of damage from serious to slight. In other words, the greater the value, the more extensive the damage. The larger boxes of σ'_C and σ'_{dis} allow for distinguishing the extent of the damage.

4.4. Discriminant Analysis of a Building's Damage Extent. A multifactor analysis method is needed to express the relationship between the shape dispersion parameters and the damage extent to buildings. Here, based on the existing sample data, we used Fisher's discriminant analysis method to obtain the linear discrimination functions relevant to the damage extent. According to the statistical results in Table 4, the parameters that can effectively identify the buildings' damage extent are σ'_C and σ'_{dis} , while the other parameters were eliminated from the analysis because they show values of $F \leq 2.71$.

Fisher's linear discrimination functions are shown as follows:

- (i) Slight damage: $F1 = 6.528\sigma'_C + 17.956\sigma'_{dis} - 9.761$.
- (ii) Medium damage: $F2 = 9.675\sigma'_C + 27.530\sigma'_{dis} - 20.560$.
- (iii) Serious damage: $F3 = 16.961\sigma'_C + 41.302\sigma'_{dis} - 55.945$.

By substituting the σ'_C and σ'_{dis} values into the three functions above, the buildings' damage extent was classified into respective categories according to the maximum values obtained, i.e., if the maximum value was obtained with the slight damage function, then that building was classified as slightly damaged. According to the space distribution scatter plots (Figure 11), the three damage extent centers were far apart and the sample points within the same damage extent area were relatively concentrated. One medium damaged building was wrongly classified as slightly damaged, and one seriously damaged building was wrongly classified as medium damaged. The discriminant results were generally accurate.

In summary, among all the parameters discussed above, σ'_C and σ'_{dis} are best suited for use in combination to distinguish the extent of building damage of the existing building samples. These findings prove that the proposed

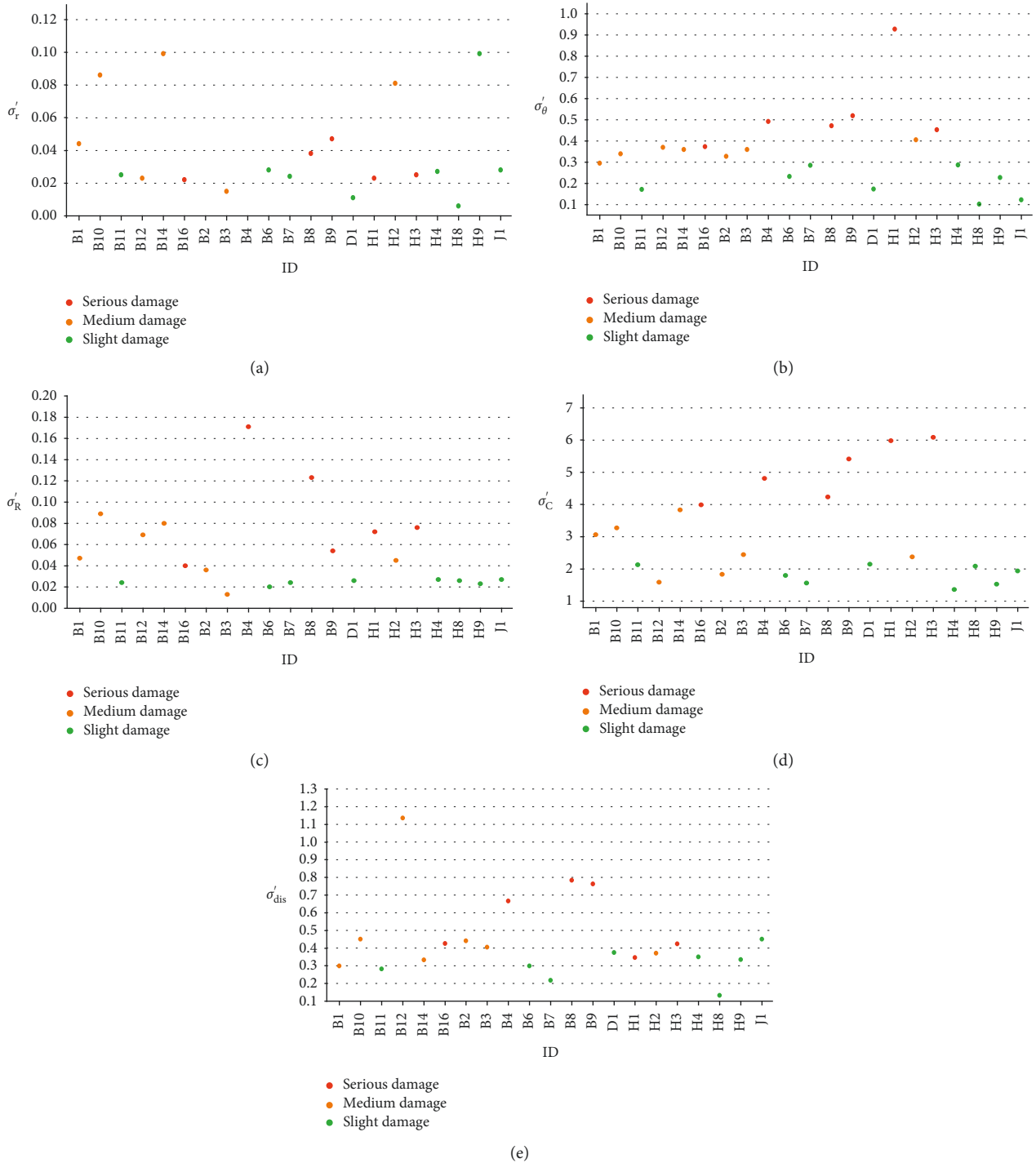


FIGURE 9: Shape dispersion parameter comparison plots for different buildings.

TLS-BSAM is capable of extracting and analyzing building earthquake damage extents.

5. Conclusions

In order to realize building earthquake damage analysis based on TLS point cloud data, TLS-BSAM was proposed. This model is based on shape analysis theory, which solves the problems of EPA extraction, shape dispersion parameter

calculations, irregular building clustering segmentation, and damage analysis. We used 21 buildings as samples to carry out our experiments. The main conclusions are as follows:

- (1) The “dimension reduction” method, which uses the EPA to express three-dimensional building data, is an effective way to carry out shape analysis, and 0.5 m is a reasonable sampling interval for the EPA during building earthquake damage analysis.

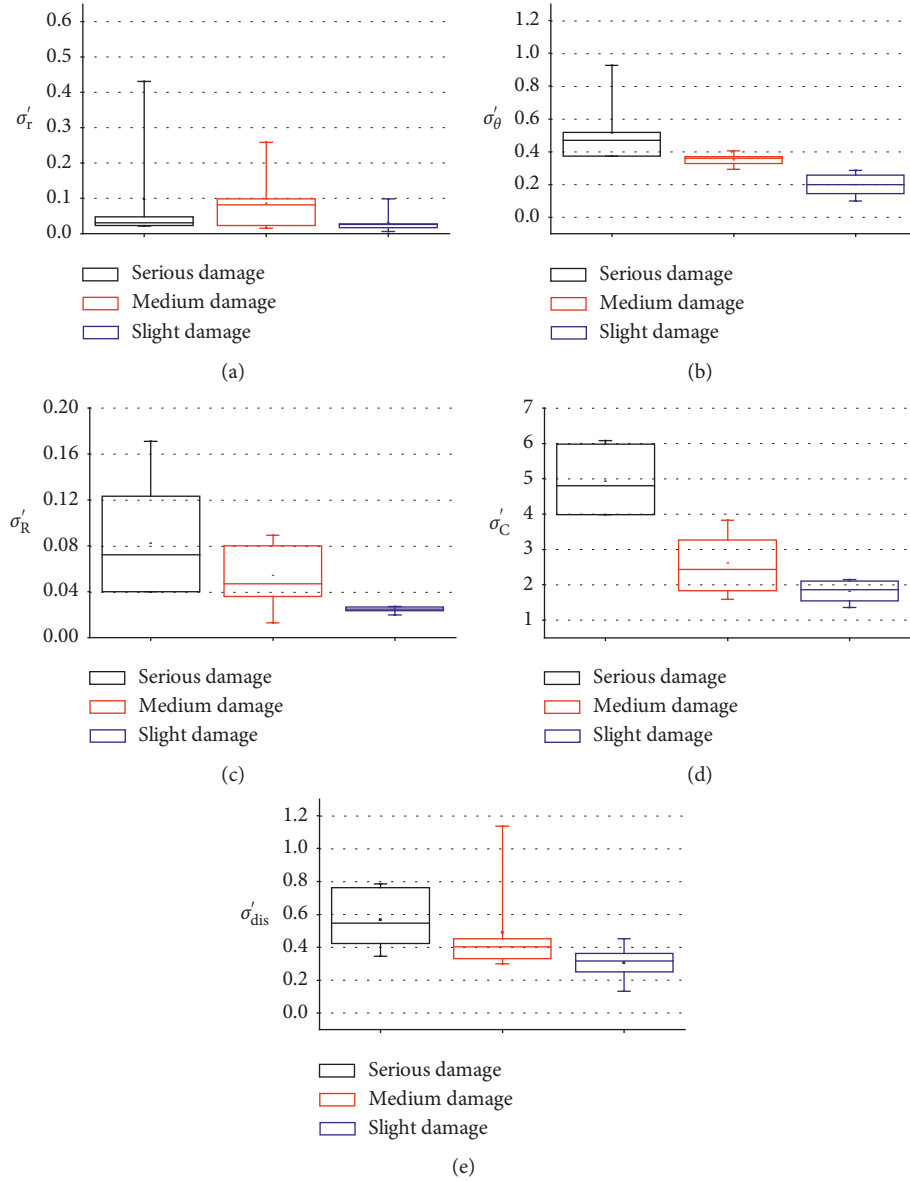


FIGURE 10: Shape dispersion parameter box plots.

TABLE 4: Statistical results for selection of different variables.

Variable	Tolerance	F	Wilks' lambda
σ'_r	0.971	0.643	0.099
σ'_θ	0.939	1.043	0.094
σ'_R	0.858	0.085	0.106
σ'_C	0.760	50.639	0.742
σ'_{dis}	0.760	5.844	0.180

(2) Using the length-width ratio of the polygon r , the inclination direction θ , rectangularity R , compactness C , and the center point (x, y) as the characteristic parameters to carry out K -means clustering, one can efficiently divide irregular buildings into regular blocks. Then, by use of the weighted averages, shape dispersion parameters can be calculated to express the damage extent to individual buildings.

Among the shape dispersion parameters, at least σ'_θ , σ'_R , σ'_C , and σ'_{dis} values are suitable to reflect the extent of a building's damage. Higher values are indicative of more serious damage.

(3) On the basis of existing data collected in the Wenchuan earthquake zone, σ'_C and σ'_{dis} were used to establish discrimination functions that can effectively distinguish the damage extent to buildings.

The TLS-BSAM is a new model by which laser scanning measurement technology can be used safely in the field to conduct building earthquake damage analysis. When combined with earthquake field survey work, the resulting information can be used as a valuable guide for assessments of the seismic intensity based on damage extents and prioritization of earthquake relief and disaster area reconstruction efforts. In addition, the obtained point cloud

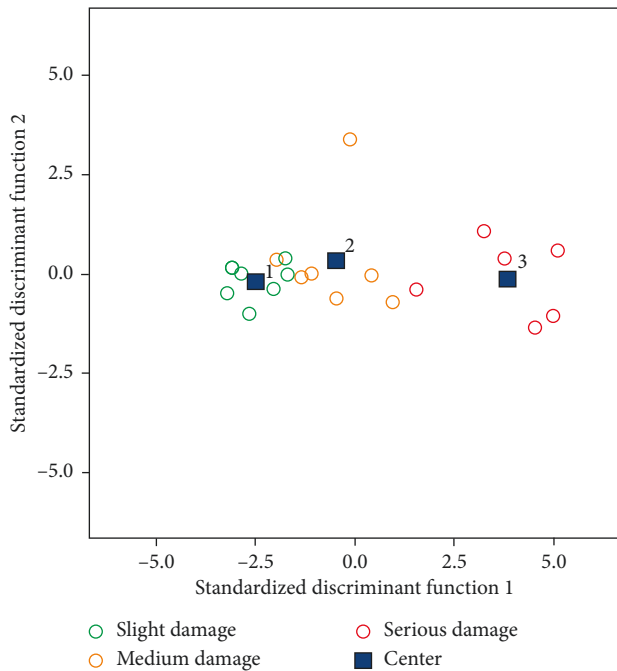


FIGURE 11: Fisher's linear discriminant results (function 1: $f(x) = 1.126\sigma'_C + 0.743\sigma'_{dis}$; function 2: $f(x) = -0.219\sigma'_C + 0.874\sigma'_{dis}$).

data provide important basic data for future building damage process numerical simulations and analyses. However, as the TLS-BSAM is a new model, it is still in the experimental stage. The model proposed in the paper is better used for buildings with structural or structural element damage. Presently, because of the few sample data points used in the experiments, the discriminant functions cannot yet be widely applied to building damage analyses in other areas. We plan on collecting more point cloud data for earthquake-damaged buildings to validate and improve the existing functions in the future, which would make them more widely applicable.

Data Availability

The TLS point cloud data used to support the findings of this study are available from the corresponding author upon request.

Conflicts of Interest

The authors declare that they have no conflicts of interest.

Acknowledgments

The authors thank all the developers of CloudCompare, which is a GPL three-dimensional point cloud and mesh processing software. This work was supported by the research grant from the Institute of Crustal Dynamics, China Earthquake Administration (grant no. ZDJ2017-29).

References

- [1] K. Saito, R. J. S. Spence, C. Going, and M. Markus, "Using high-resolution satellite images for post-earthquake building damage assessment: a study following the 26 January 2001 Gujarat earthquake," *Earthquake Spectra*, vol. 20, no. 1, pp. 145–169, 2004.
- [2] S. Stramondo, C. Bignami, M. Chini, N. Pierdicca, and A. Tertuliani, "Satellite radar and optical remote sensing for earthquake damage detection: results from different case studies," *International Journal of Remote Sensing*, vol. 27, no. 20, pp. 4433–4447, 2006.
- [3] T. Balz and M. Liao, "Building-damage detection using post-seismic high-resolution SAR satellite data," *International Journal of Remote Sensing*, vol. 31, no. 13, pp. 3369–3391, 2010.
- [4] X. Lin, J. Zhang, X. Ning, M. Duan, and Y. Zang, "Filtering of point clouds using fusion of three types of primitives including points, objects and key points," *Acta Geodaetica et Cartographica Sinica*, vol. 45, no. 11, pp. 1308–1317, 2016.
- [5] M. He, Q. Zhu, Z. Du, H. Hu, Y. Ding, and M. Chen, "A 3D shape descriptor based on contour clusters for damaged roof detection using airborne LiDAR point clouds," *Remote Sensing*, vol. 8, no. 3, p. 189, 2016.
- [6] M. Li, L. Cheng, J. Gong et al., "Post-earthquake assessment of building damage degree using LiDAR data and imagery," *Science in China Series E: Technological Sciences*, vol. 51, no. 2, pp. 133–143, 2008.
- [7] H. Ma, C. Yao, and S. Zhang, "Some technical issues of airborne LiDAR system applied to Wenchuan earthquake relief works," *Journal of Remote Sensing*, vol. 12, no. 6, pp. 925–932, 2008.
- [8] Y. Shao, H. Gong, S. Wang, F. Zhang, and W. Tian, "Multi-source SAR remote sensing data for rapid response to Wenchuan earthquake damage assessment," *Journal of Remote Sensing*, vol. 12, no. 6, pp. 865–870, 2008.
- [9] X. Tong, Z. Hong, S. Liu et al., "Building-damage detection using pre- and post-seismic high-resolution satellite stereo imagery: a case study of the May 2008 Wenchuan earthquake," *ISPRS Journal of Photogrammetry and Remote Sensing*, vol. 68, pp. 13–27, 2012.
- [10] A. Biasion, L. Bornaz, and F. Rinaudo, "Laser scanning applications on disaster management," in *Proceedings of the 1st International Symposium on Geo-Information for Disaster Management (Gi4DM)*, Delft, Netherlands, March 2005.
- [11] M. Alba, F. Roncoroni, and M. Scaioni, "Application of TLS for change detection in rock faces," *International Archives of the photogrammetry, Remote Sensing and Spatial Information Sciences*, vol. 38, no. 3, pp. 99–104, 2009.
- [12] A. Abellán, J. Calvet, J. M. Vilaplana, and J. Blanchard, "Detection and spatial prediction of rockfalls by means of terrestrial laser scanner monitoring," *Geomorphology*, vol. 119, no. 3-4, pp. 162–171, 2010.
- [13] N. A. Haddad, "From ground surveying to 3D laser scanner: a review of techniques used for spatial documentation of historic sites," *Journal of King Saud University—Engineering Sciences*, vol. 23, no. 2, pp. 109–118, 2011.
- [14] F. Pirotti, A. Guarnieri, and A. Vettore, "Ground filtering and vegetation mapping using multi-return terrestrial laser scanning," *ISPRS Journal of Photogrammetry and Remote Sensing*, vol. 76, pp. 56–63, 2013.
- [15] M. J. Olsen, K. F. Cheung, Y. Yamazaki et al., "Damage assessment of the 2010 Chile earthquake and tsunami using terrestrial laser scanning," *Earthquake Spectra*, vol. 28, no. 1, pp. S179–S197, 2012.

- [16] M. J. Olsen and R. Kayen, "Post-earthquake and tsunami 3D laser scanning forensic investigations," *Forensic Engineering*, pp. 477–486, 2012.
- [17] S. Loncaric, "A survey of shape analysis techniques," *Pattern Recognition*, vol. 31, no. 8, pp. 983–1001, 1998.
- [18] D. Zhang and G. Lu, "Review of shape representation and description techniques," *Pattern Recognition*, vol. 37, no. 1, pp. 1–19, 2004.
- [19] F. P. Preparata and S. J. Hong, "Convex hulls of finite sets of points in two and three dimensions," *Communications of the ACM*, vol. 20, no. 2, pp. 87–93, 1977.
- [20] R. L. Graham and F. Frances Yao, "Finding the convex hull of a simple polygon," *Journal of Algorithms*, vol. 4, no. 4, pp. 324–331, 1983.